Investigating past and present continental earthquakes with high-resolution optical imagery

Yu Zhou

Thesis submitted to the University of Oxford

for the degree of Doctor of Philosophy

in

Earth Sciences



Department of Earth Sciences

and St Cross College

University of Oxford

Hilary Term, 2016

Supervised by Prof. Barry Parsons and Prof. Richard Walker

Declaration

The contents of this thesis are all my own work, except where otherwise stated. The views and opinions expressed herein are mine and not necessarily those of any other person or body unless so attributed.

Citation: Zhou, Y. (2016), Investigating past and present continental earthquakes with high-resolution optical imagery, D.Phil. thesis, University of Oxford, Department of Earth Sciences, Oxford, UK.

Keywords: High Resolution, Optical Imagery, Continental Earthquakes, Faulting, Active Tectonics, Mexico, Pakistan, Iran, China.

This thesis has been typeset using LaTeX 2_ε, released under the LaTeX Project Public License (LPPL), and references were compiled using BibTeX. Most of the figures were produced using the open source Generic Mapping Tools (GMT) software, released under the GNU General Public License.

Copyright ©, by Yu Zhou, 2016.
All rights reserved.

No part of the material protected by this copyright notice may be reproduced or utilised in any form or by any means, electronic or mechanical, including photocopying, recording or by any information storage and retrieval system, without written permission from the copyright owner.

Printed in the United Kingdom.

Abstract

Investigating past and present continental earthquakes with high-resolution optical imagery

Yu Zhou
Department of Earth Sciences, Oxford

Hilary Term, 2016

Over the past few decades, remote sensing has emerged as a powerful tool for studying active faulting in continental regions. However, the commonly used remote sensing techniques, including radar interferometry, visual inspection of imagery, and image matching, cannot measure three-dimensional (3D) surface displacements in earthquakes, limiting our ability to investigate faulting. The improvement of very high-resolution (VHR) optical imaging systems (stereo in particular) in recent years has made it possible for earth scientists to measure 3D surface deformation remotely. In this thesis, I contribute to assessing the capability of VHR optical imagery, by determining earthquake deformation from four different types of earthquakes (different in sense of slip and date of the event). In the case of the 2010 M_w 7.2 El Mayor-Cucapah, Mexico earthquake, I show that digital elevation models (DEMs) derived from Pleiades stereo imagery are comparable to light detection and ranging (LiDAR) surveys, and differencing pre- and post-earthquake DEMs can measure 3D displacements, which will be very useful for studying future earthquakes. For the 2013 M_w 7.7 Balochistan, Pakistan earthquake, I determine the vertical motion from a post-earthquake Pleiades DEM and find constant fault kinematics throughout the Late Quaternary. This study has resolved a current controversy of the Balochistan earthquake, in which it has been argued that kinematics of the Hoshab fault switches between strike-slip and dip-slip. Applying historical aerial, KH-9 Hexagon spy satellite, SPOT-2 and modern SPOT-6 images to the 1978 M_w 7.3 Tabas-e-Golshan earthquake, I measure the coseismic and postseismic displacements, and show that the Tabas fold system in eastern Iran may exhibit characteristic slip behaviour. Combining Pleiades imagery, fieldwork and geological dating techniques, I determine slip in the 1556 Huaxian earthquake in China and the recurrence interval for similar events. These examples demonstrate the usefulness of high-resolution optical imagery in investigating past and present earthquakes.

Extended Abstract

Investigating past and present continental earthquakes with high-resolution optical imagery

Yu Zhou

Department of Earth Sciences, Oxford

Hilary Term, 2016

The increasing number of earthquake-related deaths over the centuries has highlighted the importance of continued research towards understanding earthquake mechanics. Large (moment magnitude (M_w) ≥ 7) continental earthquakes often occur on faults that were previously unmapped or poorly studied, often due to the long recurrence times between events and their subtle geomorphological expression in the landscape. Understanding the mechanisms of faulting and quantifying the associated seismic hazard are limited by inadequate knowledge of fault behaviour in continental regions. Over the past few decades, remote sensing has emerged as a powerful tool for studying active faulting over large spatial scales. However, the commonly used remote sensing techniques including radar interferometry (InSAR), visual inspection of imagery, and optical and radar image matching cannot measure three-dimensional (3D) surface displacements in earthquakes. Insufficient observations may create difficulties in understanding faulting and continental deformation. Recently, light detection and ranging (LiDAR) surveys have been a valuable tool for determining 3D offset in earthquakes, but its applicability is limited by its relatively high cost and low availability. The improvement of high-resolution imaging systems in the past five years, stereo imagery in particular, has made it possible for earth scientists to remotely measure surface deformation in 3D at sub-metre scale. The utility

of new generations of very high-resolution (VHR) stereo imagery (including satellite and aerial photos) in active tectonics has not yet been fully assessed. I contribute to assessing the capability of VHR imagery, by determining earthquake deformation from four different types of earthquakes (different in slip-sense, in age, and in the type of data used) in Mexico, Pakistan, Iran and China.

The 2010 M_w 7.2 El Mayor-Cucapah, Mexico earthquake

In Chapter 3, I use the 2010 M_w 7.2 El Mayor-Cucapah earthquake to demonstrate the capability of Pleiades stereo imagery to measure coseismic vertical ground displacement. Post-earthquake Pleiades tri-stereo imagery from backward, near-nadir and forward orientations was tasked for acquisition for a 45 km × 7 km portion of the epicentral area, to coincide with previous LiDAR surveys. 1-m resolution digital elevation models (DEMs) were produced with the four different combinations of incidence angles and compared to the post-earthquake LiDAR DEM. Elevations from tri-stereo have slightly (∼15%) smaller uncertainties than bi-stereo as the tri-stereo DEM incorporates more observations. Elevation differences between the Pleiades and post-earthquake LiDAR DEMs show that the vertical accuracy of the Pleiades DEMs is ∼0.3 m. By differencing the Pleiades DEM and the pre-earthquake, 5-m resolution LiDAR DEM, I was able to map metre and sub-metre offsets along the faults, obtaining results comparable to a previous study that differenced the two LiDAR DEMs. This is the first case study of assessing VHR satellite stereo imagery to determine sub-metre vertical ground displacement in an earthquake. By extension, I expect it to be possible to measure sub-metre vertical offsets occurring in earthquakes using pre- and post-earthquake VHR stereo imagery.

The 2013 M_w 7.7 Balochistan, Pakistan earthquake

The 2013 M_w 7.7 Balochistan earthquake, a predominantly strike-slip event, occurred on the arcuate Hoshab fault in the eastern Makran linking an area of mainly left-lateral shear in the east to one of shortening in the west. The difficulty of reconciling predominantly strike-slip motion with this shortening has led to a wide range of unconventional kinematic and dynamic models. In Chapter 4, I determine the vertical component of motion on the fault using a 1-m-resolution DEM derived from post-earthquake Pleiades satellite imagery. I find a constant local ratio of vertical to horizontal slip through multiple past earthquakes,

suggesting the kinematic style of the Hoshab fault has remained constant throughout the Late Quaternary.

I then apply the classic structural geology approach of calculating fault dip from the surface trace as it crosses undulating topography to the Pleiades DEM, in order to re-examine the fault geometry. I find a switch from northward to southward dipping at the southern end of the main trace within a stepover. This previously unidentified geometrical complexity may act as the endpoint of earthquake ruptures for the southern end of the Hoshab fault. In addition, I also find evidence for active faulting on a series of nearby, subparallel faults, showing that failure in large, distributed and rare earthquakes is the likely method of faulting across the eastern Makran, reconciling geodetic and long-term records of strain accumulation.

The 1978 M_w 7.3 Tabas-e-Golshan, Iran earthquake

In Chapter 5, I use historical aerial photographs, and pre-earthquake and modern satellite images to investigate the 1978 M_w 7.3 Tabas-e-Golshan, Iran earthquake. Cross-correlation of images from 1974 and 1991 reveals a near-surface shortening component of ∼2.9 m across the margin of the Tabas fold, which is a combination of coseismic and postseismic deformation. Cross-correlation of images from 1991 and 2013 shows a further ∼0.3 m of postseismic shortening. Using six pre-earthquake aerial photographs acquired in 1956 and a SPOT-6 stereo data set in 2013, I also generate pre- and post-earthquake DEMs of one of the main fold segments, and by differencing the two DEMs, I measure a height change of ∼4.7 m. Models of the surface deformation field imply a total slip of 7 m from 1974 to 2013 on a 50° dipping fault, extending from a depth of 0.1 km to 6 km at its base, the majority of which (∼6.5 m) occurred prior to 1991. The results, combined with previous InSAR observations, indicate time-decaying shallow postseismic afterslip, with a best-fitting power law exponent of 0.02. The slip appears to dissipate in the near surface, and is accommodated as a narrow band of flexural slip on bedding planes. Comparison of the fault slip model with terrace heights measured from the SPOT-6 DEM suggests that the Tabas fold system may exhibit a characteristic slip behaviour. Such behaviour would require a magnitude M_w 7.3 earthquake every ∼3500 years with the previously estimated shortening rate of ∼1.0 mm/yr.

The 1556 Huaxian, China earthquake

The January 23rd, 1556, Huaxian earthquake is the most destructive seismic event known in history, killing an estimated 830,000 people and causing heavy damage across the Weihe graben, central China. Seismic intensities extracted from detailed historical accounts define a zone of maximum shaking sited along the Huashan and Weinan tableland faults, and with a magnitude estimated at ∼8.5 from magnitude-intensity relations. However, the Huashan and Weinan tableland faults have a combined length of only ∼90 km, and are short on their own to account for the estimated magnitude. In Chapter 6, I first use InSAR to measure the interseismic rate across the Weihe graben but did not observe any evident tectonic signals, suggesting that the slip rates across the graben are small (on the order of 1–3 mm/yr). I then perform detailed analysis of the geomorphology and palaeoseismology of the Weinan Tableland fault, and find that the fault ruptured within the last ∼900 years, involving surface slip of up to 10 m. I reestimate the magnitude for the 1556 earthquake based on various scaling relationships and obtain a range of M_w 7.3–7.9, suggesting that the previously inferred magnitude is likely an overestimate. The 1556 earthquake was the only surface rupturing event for at least 5,000 years and potentially for longer (5,500–7,500 years).

Acknowledgements

I thank my supervisors Barry Parsons (Big Boss) and Richard Walker (Little Boss), for their help and advice, for their constructive criticism, and for their endless encouragement of my work. I could not have done this PhD without their support. They helped a naughty boy to become a well-behaved man, and mean far more to me than just supervisors.

This research was funded by a PAG (formerly Pacific Alliance Group) scholarship from the University of Oxford. I also acknowledge two research grants from the Geological Society of London and the Geological Remote Sensing Group.

I am grateful to my Grandfather Philip England for always being so kind and supportive to me, John Elliott for being a wealth of practical advice, and James Hollingsworth from ISTerre, Université Grenoble Alpes for useful discussions about the Tabas earthquake. Thanks too, to Xijie Feng and Ji Ma from China Earthquake Administration Shaanxi Province, Xiaogang Song from the Institute of Geology, China Earthquake Administration, and Magali Rizza from Aix-Marseille University for their help and advice during my fieldwork in China.

Special thanks go to Peizhen Zhang, Xinjian Shan, Wenjun Zheng, Huiping Zhang, Zhikun Ren, Wenyu Gong and Jingxing Yu from the Institute of Geology, China Earthquake Administration, and Qiyun Lei and Wuxiong Cheng from China Earthquake Administration Ningxia Province, for making our visit to China so enjoyable.

Joan deserves a medal, for making my life special. I will always remember all the dinners we had, the films we watched, the places we travelled to, the adventures we experienced and the time we spent together.

I gratefully acknowledge many useful discussions on Tectonics (as well as on the "philosophy of life") over wine with Tim Middleton. I will not forget our "romantic" evenings

by the beach and on the rooftop bars. Thank you for always being there whenever I need you. Thank you also to my buddy Mike Stock for making me cross the fatal Crib Goch on the Snowdon Massif, and for giving me private "lectures" on igneous petrology in Santorini and the English people and culture. You and your families made my life in the UK memorable. Thanks also to my friends and colleagues in S4 (50.03) over the years: John Elliott, Marcus Bell, Ivana Barisin, Richard Walters, James Moore, Al Sloan, Susi Ebmeier, David Mackenzie, Eleanor Ainscoe, and more recently Austin Elliott and Marion Thomas. I would also like to thank Tim Wright (the new Lord of COMET), Jean-Philippe Avouac, Alex Copley, Zhenhong Li, David Bekaert and members of the COMET group with whom I have had discussions.

The Department of Earth Sciences has been wonderful. I thank the computing, administrative and technical staff for their great efforts in keeping everything running. Cheers to the Postgrad12 comrades: Joan, Weimu, Helen, Nikita, Hanne, Renee, Fern, Brendan (van der) Dyck, Mr. Nash, Qingfeng, Ash, Dave, Brook, Tim and Mike, with whom I have gone through all the "battles" over PhD. I cannot imagine my the PhD without you guys.

Thanks too, to everybody else who is always by my side and made my life so much fun: Shu, Juliane, Feifei, Yujia, Claire, Xiaofei, Steven, Weidi (80K), Xingwei, Micha, Peilin, Yishu, Jinchao, Tao, Kimi, Fan, Liang, Philip (Navy Seal), Tom (Big Old Man), and Kyle (Big Brother). I have a cast of thousands more to thank, and I hope you will forgive me if I miss anybody out.

Finally, my love and thanks go to my parents and granny without whose encouragement and support none of this would have happened.

Contents

Declaration . . . iii

Abstract . . . vii

Extended Abstract . . . ix

Acknowledgements . . . xiii

Contents . . . xviii

List of Figures . . . xxiii

List of Tables . . . xxv

1 Introduction **1**

1.1 Continental Tectonics . . . 2

1.2 The Earthquake Cycle . . . 4

1.3 Types of Faulting . . . 5

1.3.1 Strike-slip Faulting . . . 5

1.3.2 Thrust Faulting . . . 6

1.3.3 Normal Faulting . . . 7

1.4 Quantifying Earthquake Deformation: Methods and Challenges . . . 8

1.4.1 Global Positioning System (GPS) . . . 8

1.4.2 Interferometric Synthetic Aperture Radar (InSAR) . . . 9

1.4.3 Optical Image Matching . . . 10

1.4.4 Light Detection And Ranging (LiDAR) . . . 11

1.5 Aims and Overview of Thesis . . . 12

1.6 Publications . . . 13

2 Photogrammetry Technique **15**

2.1 Introduction . . . 15
2.2 Sensor Models: Single View Geometry . . . 16
2.2.1 Rigorous Models . . . 17
2.2.2 Generic Models . . . 23
2.3 Epipolar Geometry: Stereo View Geometry . . . 28
2.4 3D Reconstruction . . . 31
2.4.1 Satellite Stereo Imagery . . . 32
2.4.2 Frame Photos . . . 36
2.5 Orthorectification . . . 49
2.6 Summary . . . 50

3 Earthquake Height Changes from Pleiades 51
3.1 Introduction . . . 51
3.2 Overview of the 2010 El Mayor-Cucapah Earthquake . . . 53
3.3 Data and Methods . . . 55
3.3.1 Data Sets . . . 55
3.3.2 DEM Generation . . . 56
3.4 Evaluation of the Pleiades DEMs . . . 58
3.4.1 Point Clouds . . . 58
3.4.2 Accuracy of the Pleiades DEMs . . . 58
3.5 Surface Deformation Using the Pleiades DEM and Discussion of Fault Geometry . . . 65
3.5.1 Biased Measurements of Height Changes . . . 65
3.5.2 Correcting for Horizontal Displacement . . . 66
3.5.3 Estimation of Fault Dip . . . 69
3.6 Discussion and Conclusions . . . 71

4 The 2013 Balochistan earthquake in Pakistan 73
4.1 Introduction . . . 73
4.2 Tectonic Background . . . 74
4.3 Data and Results . . . 77

4.3.1 Surface Slip in the 2013 Earthquake . . . 77
4.3.2 Cumulative Surface Slip . . . 81
4.3.3 Fault Dip . . . 83
4.4 Discussion . . . 84
4.4.1 Endpoint of Earthquake Ruptures on the Hoshab Fault . . . 84
4.4.2 Long-term Fault Kinematics . . . 85
4.4.3 Distributed Faulting in the Eastern Makran . . . 88
4.5 Conclusions . . . 93

5 The 1978 Tabas-e-Golshan Earthquake in Iran 95
5.1 Introduction . . . 95
5.2 Tectonic Background of the 1978 Tabas Earthquake . . . 97
5.3 Image Processing . . . 101
5.3.1 SPOT-6 Images Obtained in 2013 . . . 101
5.3.2 KH-9 Image Obtained in 1974 . . . 102
5.3.3 SPOT-2 in 1991 . . . 103
5.3.4 Aerial Photographs Obtained in 1956 . . . 103
5.4 Results . . . 104
5.4.1 Horizontal Displacement from Cross-correlation . . . 104
5.4.2 Height Changes from DEM Differencing . . . 107
5.5 Discussion . . . 109
5.5.1 Models of Fault Slip . . . 109
5.5.2 Timescale of the Deformation . . . 111
5.5.3 Faulting in the Tabas Region . . . 113
5.5.4 Long-term Surface Folding: Characteristic Slip Behaviour . . . 119
5.6 Conclusions . . . 121

6 The 1556 Huaxian Earthquake in China 123
6.1 Introduction . . . 123
6.2 Interseismic Rate Map for the Weihe Graben . . . 126
6.3 The 1556 Huaxian Earthquake . . . 129

6.4 Geomorphology of the Chishui Catchment . . . 133
6.4.1 Generation and Validation of the Pleiades DEM . . . 133
6.4.2 Geomorphic Analysis and Geological Dating . . . 134
6.4.3 Quarry Exposure . . . 140
6.5 Borehole Cross-section . . . 147
6.6 Discussion . . . 148
6.6.1 Landscape Evolution of the Chishui River Catchment . . . 148
6.6.2 Re-estimating the Magnitude . . . 150
6.7 Conclusions . . . 152
6.8 Contributions . . . 153

7 Conclusions and Discussion **155**
7.1 Compilation of Earthquake Deformation Studied with Optical Image Matching . . . 156
7.1.1 Image Resolution and Surface Displacement . . . 156
7.1.2 Coseismic Shallow Slip Deficit? . . . 158
7.2 Future Work and Possibilities . . . 160
7.2.1 Towards 3D Mapping of Earthquake Deformation . . . 161
7.2.2 Historical Earthquakes . . . 161

Bibliography **163**

Appendices **183**

A Cumulative Surface Slip along the Hoshab Fault **183**

B Estimating Fault Dip with High-resolution Topography **189**

C Additional Correlation Results for the 1978 Tabas-e-Golshan Earthquake **197**

D Orthorectification-induced Horizontal Displacement **205**

E Radiocarbon Samples from the Chishui Site **209**

List of Figures

1.1 Earthquake deaths over the past century. 2
1.2 Global plate boundaries. 3
1.3 Elastic rebound theory. 5
1.4 Types of faulting. 5
1.5 Coseismic deformation of the 2008 Wenchuan earthquake from GPS. 8
1.6 Coseismic deformation of the 2008 Wenchuan earthquake from InSAR. . . 9
1.7 Coseismic surface displacement in the 2010 El-Mayor Cucapah earthquake from optical imagery. 10
1.8 3D displacement in the 2010 El-Mayor Cucapah earthquake from LiDAR DEM differencing. 11

2.1 Remote sensing systems. 16
2.2 Perspective projection. 18
2.3 Camera distortion. 22
2.4 An example of calibration for camera distortion. 23
2.5 Grid interpolation model. 25
2.6 Epipolar geometry. 28
2.7 Epipolar lines. 31
2.8 3D reconstruction. 32
2.9 Pleiades stereo imagery with correspondences used for 3D reconstruction. . 34
2.10 Template matching. 35
2.11 An example of fiducial markers in old aerial photos. 37
2.12 SfM workflow. 39
2.13 SIFT image features. 41

2.14 Connectivity graph. 42
2.15 Relative orientation. 44
2.16 Sparse reconstruction. 45
2.17 Dense reconstruction. 46
2.18 3D reconstruction of a scarp from field photos. 48
2.19 Direct and indirect orthorectification. 50

3.1 Tectonic setting of the El Mayor-Cucapah earthquake rupture. 55
3.2 Statistics of point cloud density. 59
3.3 Point clouds from Pleiades stereo imagery. 60
3.4 An example of mostly featureless desert salt flats with few matching points. 61
3.5 Coregistration of the Pleiades tri-stereo and post-earthquake LiDAR DEMs. 62
3.6 Figure 3.5 (Continued). 63
3.7 Elevation difference map between the tri-stereo Pleiades and post-earthquake LiDAR DEMs. 64
3.8 Elevation difference with ground slope. 65
3.9 Direct differencing of the Pleiades tri-stereo and pre-earthquake LiDAR DEMs. 67
3.10 3D displacements derived from the Pleiades tri-stereo and pre-earthquake LiDAR DEMs. 69
3.11 Vertical and fault-normal displacements along the 2010 El Mayor-Cucapah rupture. 71

4.1 Tectonic setting of the 24 September 2013 Balochistan earthquake. 76
4.2 Coseismic displacements along the Hoshab fault. 78
4.3 Surface fault slip measured from Pleiades stereo imagery. 79
4.4 Vertical displacement in the 2013 Balochistan earthquake. 80
4.5 An example of cumulative displacements along the Hoshab fault. 82
4.6 Dip estimates along the Hoshab fault. 84
4.7 Stepovers along the Hoshab fault. 86
4.8 Termination of the 2013 rupture at the southern end of the Hoshab fault. . 87

4.9 Google Earth imagery showing preserved fault scarps. 89
4.10 Across-fault topographic relief along the southern segment of the Hoshab fault. 92
4.11 An example of long-term thrust motion recorded across the alluvial fans. . 92

5.1 Tectonic setting of Iran. 99
5.2 Surface ruptures of the 1978 Tabas earthquake mapped in the field. 100
5.3 E-W displacement from cross-correlating the KH-9 and SPOT-6 images. . . 105
5.4 E-W displacement from cross-correlating the KH-9 and SPOT-2, and SPOT-2 and SPOT-6 images. 106
5.5 Height changes from direct differencing of the pre-earthquake aerial DEM and the post-earthquake SPOT-6 DEM. 108
5.6 As for Figure 5.3c, but modelled with different top depths. 110
5.7 Modelled surface displacements assuming slips on different faults at depth. 111
5.8 Time dependent postseismic afterslip and power law fits for the 1978 Tabas earthquake. 114
5.9 Schematic cross-section along the Tabas fold summarising the sub-surface structure. 115
5.10 Long-term surface folding of the Espakh fold. 117
5.11 Schematic cross-section of faults in the Tabas region. 118
5.12 Long-term surface folding of the Tabas fold. 120

6.1 Active faults around the Ordos plateau. 124
6.2 Triangular facets along the range front of Huashan. 125
6.3 Expansion of Xi′an. 125
6.4 Baseline plot for track 161. 127
6.5 Rate map across the Weihe graben. 129
6.6 Isoseismal map of the 1556 Huaxian earthquake. 131
6.7 SRTM shaded-relief topography of the eastern Weihe graben. 131
6.8 GCPs used in DEM generation. 134
6.9 3D perspective view of Pleiades imagery. 135

6.10 Surface geomorphology of the Chishui catchment. 137
6.11 Radiocarbon samples collected at the Chishui site. 139
6.12 Pottery and bones collected from T2. 140
6.13 3D model of the quarry exposure near Chishui village. 141
6.14 Western wall of the trench at the Chishui site. 144
6.15 Eastern wall of the trench at the Chishui site. 145
6.16 Radiocarbon samples collected from the Chishui trench. 146
6.17 Borehole cross-section at the Chishui site. 148
6.18 Cartoon showing the landscape evolution of the Chishui river catchment. . 150

7.1 Comparison of surface displacements from different images in the Balochistan earthquake. 159
7.2 Coseismic shallow slip deficit. 160
7.3 Surface displacement from the 1976 M_w 7.3 Chaldiran, Turkey earthquake. 162

A.1 Cumulative displacements along the Hoshab fault (at Site 3). 184
A.2 Cumulative displacements along the Hoshab fault (at Site 4). 185
A.3 Cumulative displacements along the Hoshab fault (at Site 5). 186
A.4 Cumulative displacements along the Hoshab fault (at Site 6). 187

B.1 Measuring fault dip by fitting a plane (in yellow) to the surface rupture. . . 190
B.2 Estimates of fault dip along the Hoshab fault. 195

C.1 Displacement fields from cross-correlating the pre-earthquake KH-9 and post-earthquake SPOT-6 images. 198
C.2 Cross-correlation results using different parameters in COSI-Corr. 199

D.1 Apparent horizontal displacement due to vertical motion. 207

E.1 Calibrated age ranges (95%) for sample RC1. 211
E.2 Calibrated age ranges (95%) for sample RC2. 211
E.3 Calibrated age ranges (95%) for sample RC3. 212
E.4 Calibrated age ranges (95%) for sample RC4. 212
E.5 Calibrated age ranges (95%) for sample C1. 213

E.6 Calibrated age ranges (95%) for sample C2. 213
E.7 Calibrated age ranges (95%) for sample C3. 213
E.8 Calibrated age ranges (95%) for sample C4. 214
E.9 Calibrated age ranges (95%) for sample C5. 214
E.10 Calibrated age ranges (95%) for sample C6. 214
E.11 Calibrated age ranges (95%) for sample C7. 215
E.12 Calibrated age ranges (95%) for sample C8. 215
E.13 Calibrated age ranges (95%) for sample C9. 215
E.14 Calibrated age ranges (95%) for sample C10. 216
E.15 Calibrated age ranges (95%) for sample C11. 216

List of Tables

2.1 Estimation of the scale factor in the Helmert transformation. 49

4.1 Cumulative displacements along the Hoshab fault. 81

5.1 Imagery used for determining surface displacements from the 1978 Tabas earthquake. 101

6.1 Intensity scale for the 1556 Huaxian earthquake. 132

6.2 Comparison between the RTK measurements and Pleiades DEM. 134

6.3 Fault parameters and magnitude estimates. 151

7.1 Compilation of earthquake deformation studied with optical image matching 157

B.1 Estimates of fault dip along the Hoshab fault. 191

E.1 Radiocarbon material, ages, and calibration for samples collected at the Chishui site. 210

Chapter 1

Introduction

The increasing number of earthquake-related deaths over the centuries has highlighted the importance of continued research towards understanding earthquake mechanics. Large earthquakes occur in two major settings: on plate boundaries and within continents. Great earthquakes that take place on subduction zones can kill large numbers of people, e.g. the 2004 Sumatra earthquake killed more than 300,000. However, if we take account of all the earthquake deaths in the past 120 years, the total number of deaths within continental interiors is about 2 times larger than on the plate boundaries, as shown in Figure 1.1 (*England and Jackson*, 2011). In contrast to the plate boundaries, whose locations have been precisely mapped, the locations of faults within the continents are less well known, often due to the long recurrence times between events and their subtle geomorphological expression in the landscape. It is, therefore, more difficult to evaluate and mitigate the seismic hazard within continental interiors. During the past 30 years, our ability to identify active faults and quantify the associated hazard has improved significantly (*Tapponnier and Molnar*, 1977; *Fialko et al.*, 2005; *Funning et al.*, 2005; *Walker*, 2006; *Klinger et al.*, 2011; *Oskin et al.*, 2012). The advances in fault mapping come from lessons learnt in recent earthquakes, combined with a continued increase in the resolution, availability, and capability of satellite imaging techniques. Since the 1992 Landers earthquake, radar interferometry has been widely used to determine earthquake deformation over a spatial scale of hundreds of kilometres, e.g. *Massonnet et al.* (1993); *Wright et al.* (2004b); *Fialko et al.* (2005); *Elliott et al.* (2012). Recent developments in geodesy, notably photogrammetry, a technique that allows the direct measurement of

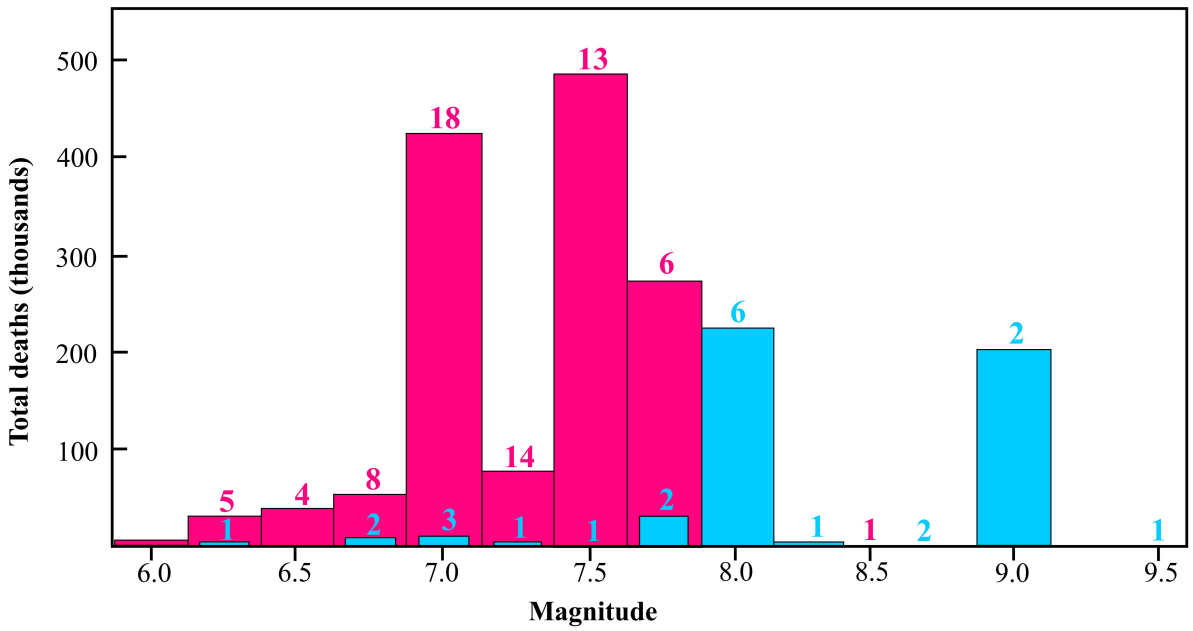


Figure 1.1: Earthquake deaths over the past century, modified from *England and Jackson* (2011). The total number of deaths within continental interiors (red) is about 2 times larger than on the plate boundaries (blue).

the deformation of the Earth's surface in three dimensions (3D), have opened up new opportunities for studies of past and present earthquakes. By combining the information from photogrammetry, radar interferometry, and geophysical models, we can gain new insights into earthquake mechanics and continental deformation, including going back in time, to re-examine earthquakes that occurred before the advent of techniques such as radar interferometry.

1.1 Continental Tectonics

Plate tectonics quantitatively describes the kinematics of the lithosphere (the outer shell of Earth) (*Molnar*, 1988). It states that the Earth's surface is composed of a number of rigid plates that are in relative motion which can be described as rotations about Euler poles (*McKenzie and Parker*, 1967). This theory requires that the deformation occurs only in narrow zones (a few tens of kilometres) around the edges of plates, with little internal deformation within the plate. Plate tectonics is very useful for explaining the kinematics of oceanic lithosphere, where earthquakes– a proxy for lithospheric deformation, are concentrated along plate boundaries, transform faults and subduction zones

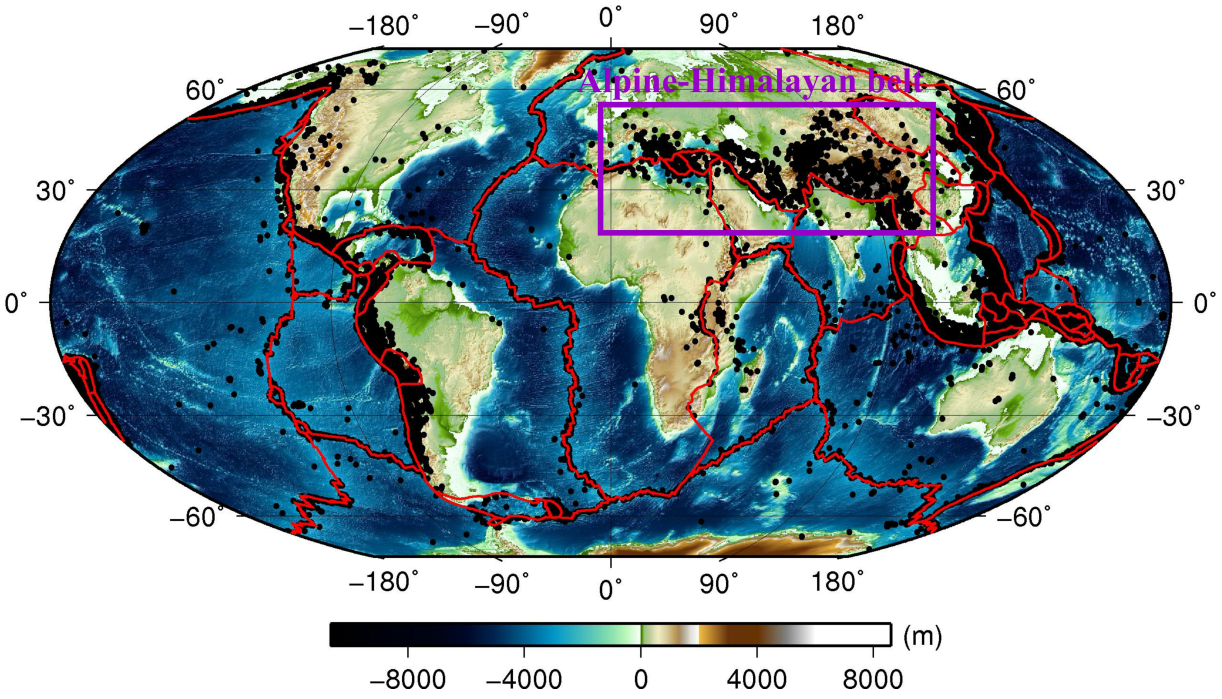


Figure 1.2: Gobal plate boundaries (red lines) from *Bird* (2003) with earthquakes M_w 5.5+ (1976–2008) from the Global CMT catalogue (black dots). In the oceanic plates, earthquakes are concentrated along plate boundaries, but distributed over hundreds to thousands of kilometres in some continental regions like the Alpine-Himalayan belt (marked by the purple box).

(*Turcotte and Schubert*, 2014) (Figure 1.2). However, it fails to characterise the behaviour of some continental regions. For example, as shown in Figure 1.2, shallow seismicity is distributed over hundreds to thousands of kilometres in the Alpine-Himalayan belt (*Molnar and Tapponnier*, 1975; *England and Molnar*, 1997).

Why continental deformation is spread over wide zones remains controversial (*Bürgmann and Dresen*, 2008), but it is evident that the oceanic and continental lithosphere have distinctive rheologies. The oceanic lithosphere, with only a few kilometres of dense crust overlying the more dense mantle, is rich in olivine and largely anhydrous; this composition suggests that the oceanic lithosphere behaves in a brittle/elastic manner to depths of ∼40 km (temperatures of ∼600°C) and undergoes ductile flow beneath the brittle upper part (*Chen and Molnar*, 1983; *Molnar*, 1988; *McKenzie et al.*, 2005; *Turcotte and Schubert*, 2014). In contrast, the continental lithosphere has a much thicker (a mean thickness of ∼40 km) and lighter crust, which makes it gravitationally stable and keeps it afloat (*Molnar*, 1988; *Turcotte and Schubert*, 2014). The quartzose material comprising the crust also makes the continental lithosphere weaker than the oceanic lithosphere. Brittle

deformation is confined to the upper-crustal layer (typically 15–20 km) where fault zones (pre-existing weaknesses) deform at lower stresses (*Zoback et al.*, 1987). Beneath this, the lower crust is deforming by ductile flow with a nearly complete absence of earthquakes, apart from occasional earthquakes in the continental lithospheric mantle (*Molnar*, 1988; *McKenzie et al.*, 2005).

1.2 The Earthquake Cycle

The governing mechanism of the overall style of continental deformation is debatable (*Bürgmann and Dresen*, 2008). Study of shallow earthquakes, i.e. deformation of the brittle upper crust by overcoming the frictional stresses on faults, enables us to gain an understanding of the nature of continental tectonics. After the 1906 San Francisco earthquake, *Reid* (1910) developed the elastic rebound theory based on measurements of deformation both during the 1906 earthquake (coseismic) and in the time between earthquakes (interseismic) to explain fault motion and strain accommodation. The elastic rebound theory (as illustrated in Figure 1.3) states that in the interseismic period, the fault is locked by friction and thus elastic strain is accumulated, until the elastic stresses overcome the frictional stresses so that the fault is able to move. In the coseismic period, all of the stored elastic strain is released by rapid slip on the fault. The process of interseismic strain accumulation and coseismic strain release defines an 'earthquake cycle'. The elastic rebound theory forms a good basis for the study of continental deformation, but its simple view does not explain all the features of the earthquake cycle. For example, many earthquakes show that fault slip decreases towards the surface, or remains buried at depth, and the gradients of slip are relaxed by afterslip, e.g. the 1989 Loma Prieta (*Segall et al.*, 2000) and 1978 Tabas-e-Golshan (*Zhou et al.*, 2016b) earthquakes. Other phenomena including viscoelastic relaxation and poroelastic rebound (*Jonsson et al.*, 2003) have also been observed following large continental earthquakes, e.g. the 1992 Landers *Savage and Svarc* (1997) and 2002 Denali (*Pollitz*, 2005) earthquakes. These observations give rise to the idea of postseismic deformation. It is important to measure deformation throughout the entire seismic cycle in order to fully characterise the mechanisms of continental deformation.

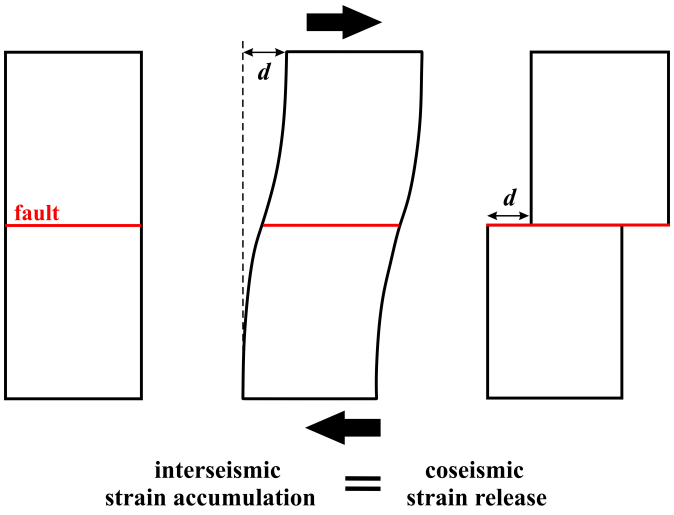


Figure 1.3: Schematic of the elastic rebound theory by *Reid* (1910). Elastic strain is accumulated in the crust in the interseismic period as the fault is locked by friction. In the coseismic period, all of the stored elastic strain is released by rapid slip on the fault.

1.3 Types of Faulting

Depending on the state of stress in the lithosphere, faulting is categorised into three types (Figure 1.4): strike-slip, thrust and normal (*Turcotte and Schubert*, 2014). In most earthquakes, slip is oblique between theses cases, or may vary along strike.

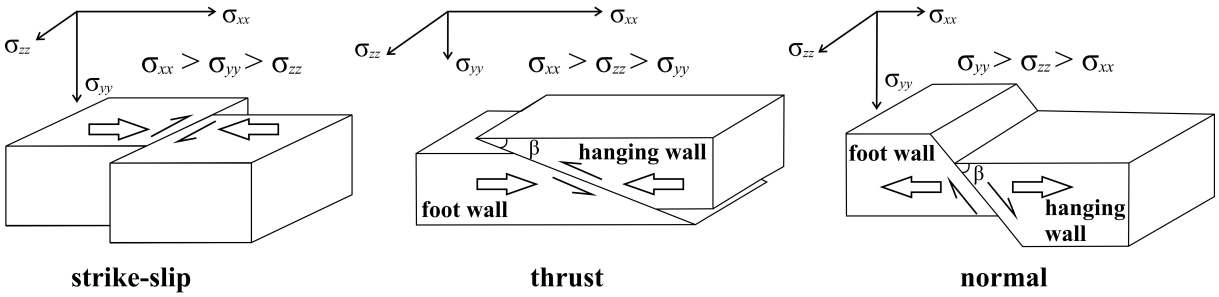


Figure 1.4: Cartoon showing three types of faulting, depending on the state of stress in the lithosphere. (*left*) Strike-slip faulting. (*middle*) Thrust faulting. (*right*) Normal faulting.

1.3.1 Strike-slip Faulting

Strike-slip faulting is the case where the displacement is strictly horizontal. As shown in Figure 1.4, the state of stress is composed of a vertical lithostatic stress $\sigma_{yy} = \rho g h$ and two horizontal deviatoric principal stresses, i.e. the compressional deviatoric stress $\Delta\sigma_{xx} > 0$ and the tensional deviatoric stress $\Delta\sigma_{zz} < 0$.

The horizontal compressional stress in the x direction is:

$$\sigma_{xx} = \rho g h + \Delta\sigma_{xx} \tag{1.1}$$

The horizontal tensional stress in the z direction is:

$$\sigma_{zz} = \rho g h + \Delta\sigma_{zz} \tag{1.2}$$

Therefore, we have $\sigma_{xx} > \sigma_{yy} > \sigma_{zz}$. For strike-slip faulting, the vertical lithostatic stress is always the intermediate stress. Actual strike-slip earthquakes always involve some vertical motion. For example, the 2010 M_w 7.2 El-Mayor Cucapah earthquake (in Chapter 3) is a combination of right-lateral strike-slip and normal faulting, and the 2013 M_w 7.7 Balochistan earthquake (in Chapter 4) is predominately a left-lateral strike-slip faulting event with some thrust motion.

1.3.2 Thrust Faulting

Thrust faulting will cause horizontal compressional strain to accommodate the compression of the lithosphere. The elevated block is referred to as the hanging wall, and the depressed block is called the foot wall. The state of stress in thrust faulting consists of a vertical lithostatic stress $\sigma_{yy} = \rho g h$ and a compressional deviatoric horizontal stress in the x direction $\Delta\sigma_{xx} > 0$ (Figure 1.4).

The horizontal stress in the x direction σ_{xx} is:

$$\sigma_{xx} = \rho g h + \Delta\sigma_{xx} \tag{1.3}$$

The deviatoric stress in the z direction $\Delta\sigma_{zz}$ is proportional to $\Delta\sigma_{xx}$, i.e. $\Delta\sigma_{zz} = \nu\Delta\sigma_{xx}$, where $0 < \nu < 1$.

The horizontal stress in the z direction σ_{zz} is:

$$\sigma_{zz} = \rho g h + \nu\Delta\sigma_{xx} \tag{1.4}$$

Therefore, for thrust faulting, we have $\sigma_{xx} > \sigma_{zz} > \sigma_{yy}$. The vertical stress is always

the minimum compressive stress. Based on the Anderson theory of faulting, the typical dipping angle of a thrust fault (β in Figure 1.4) is ~25° (*Anderson*, 1905).

It is common for thrust faults to remain buried at depths. As many thrust faults do not reach the surface, it is often very difficult to map and understand the behaviour of thrust faulting. In Chapter 5, I show a study of the September 16, 1978 M_w 7.3 Tabas-e-Golshan earthquake in eastern Iran, one of the examples that occurred on a series of previously unrecognised blind thrust faults, which has completely demolished the oasis town of Tabas and killed ~11000 people (85% of its population) (*Berberian*, 1979).

1.3.3 Normal Faulting

Normal faulting can accommodate horizontal extensional strain by motion on a dipping fault plane. The elevated block is referred to as the foot wall, and the depressed block is called the hanging wall (Figure 1.4). The state of stress in normal faulting consists of a vertical lithostatic stress $\sigma_{yy} = \rho g h$ and a tensional deviatoric horizontal stress $\Delta\sigma_{xx} < 0$. The horizontal stress in the x direction σ_{xx} is:

$$\sigma_{xx} = \rho g h + \Delta\sigma_{xx} \tag{1.5}$$

The deviatoric stress in the z direction $\Delta\sigma_{zz}$ is proportional to $\Delta\sigma_{xx}$, i.e. $\Delta\sigma_{zz} = \nu\Delta\sigma_{xx}$, where $0 < \nu < 1$.

The horizontal stress in the z direction σ_{zz} is:

$$\sigma_{zz} = \rho g h + \nu\Delta\sigma_{xx} \tag{1.6}$$

Therefore, for normal faulting, we have $\sigma_{yy} > \sigma_{zz} > \sigma_{xx}$. The vertical stress is always the maximum compressive stress. Based on the Anderson theory of faulting, the typical dipping angle of a normal fault is ~65° (*Anderson*, 1905). Normal faulting often bounds continental basins where the crust is being stretched. Chapter 6 shows an example of large continental normal faulting events, i.e. the 1556 Huaxian earthquake, with a fault slip of 10 m.

1.4 Quantifying Earthquake Deformation: Methods and Challenges

1.4.1 Global Positioning System (GPS)

The Global Positioning System (GPS) that launched in the early 1980s has provided revolutionised means for the accurate measurements of crustal motions in tectonically active regions (*Dixon*, 1991). For example, Figure 1.5 shows the coseismic displacements of the 2008 Wenchuan earthquake measured from a few GPS stations. There are two typical modes of data collection. The continuous GPS (cGPS), which operates on permanent GPS receivers, offers unprecedented precision (on the order of mm/yr) and time resolution (e.g. *D'Agostino et al.* 2005; *Hsu et al.* 2006). The campaign mode consists of periodic resurveys of GPS sites that are set up at selected localities in a region of interest. It costs much less than cGPS, and also allows rapid acquisition for a larger area (such as the Himalayan-Tibetan orogen), so it is usually combined with cGPS to measure crustal deformation at very large spatial scales, e.g. China (*Wang et al.*, 2001). However, GPS has four major limitations: (1) GPS data in some countries like China are not open-access; (2) to measure small strains, it requires a minimum of two years of cGPS data or three occupations of campaign data; (3) GPS only measures displacement of points; (4) it requires operators to go out for data collection.

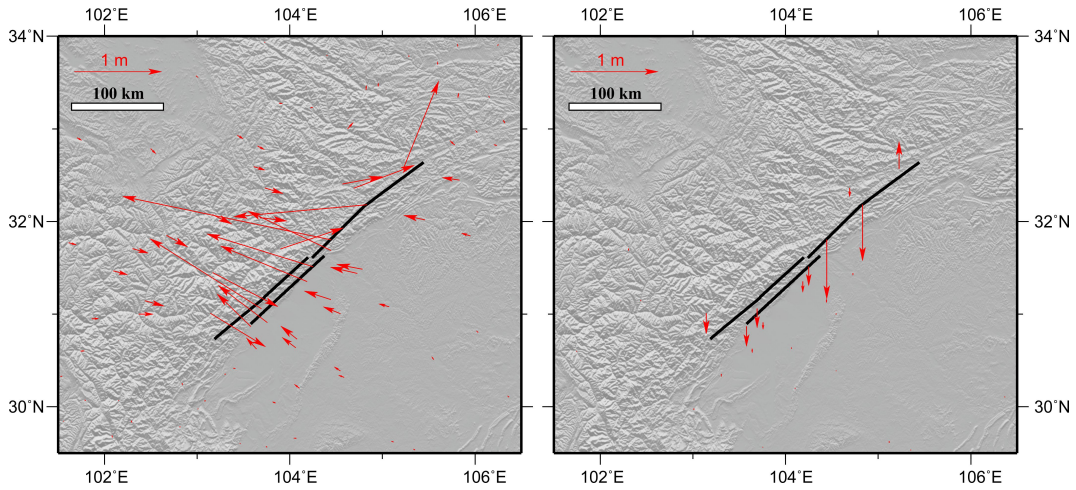


Figure 1.5: Coseismic deformation of the 2008 Wenchuan earthquake estimated from GPS. GPS data were from *Shen et al.* (2009). (*left*): Horizontal displacements. (*right*): Vertical displacements. Black lines denote the fault.

1.4.2 Interferometric Synthetic Aperture Radar (InSAR)

Interferometric Synthetic Aperture Radar (InSAR) has been widely used to measure ground displacement since the 1992 M_w 7.3 Landers earthquake (*Massonnet et al.*, 1993). It uses phase differences between different radar acquisitions to retrieve small ground displacement (readers are referred to the classic textbook by *Hanssen* (2001) for a more comprehensive understanding of the InSAR technique). With pre- and post-earthquake radar images, it is possible to map decimetric surface displacement at a spatial resolution of tens of metres over hundreds of kilometres (as shown in Figure 1.6). Recent InSAR studies have also detected small interseismic and postseismic deformation (a few mm/yr) using a time succession of images (e.g. *Pollitz et al.* 2001; *Wright et al.* 2004b). However, unlike GPS that can measure motion in three dimensions, InSAR only measures displacement in the line-of-sight (LOS) direction. Decorrelation between two images (e.g. the epicentral areas in Figure 1.6) and atmospheric noises create additional challenges for measuring ground deformation with InSAR.

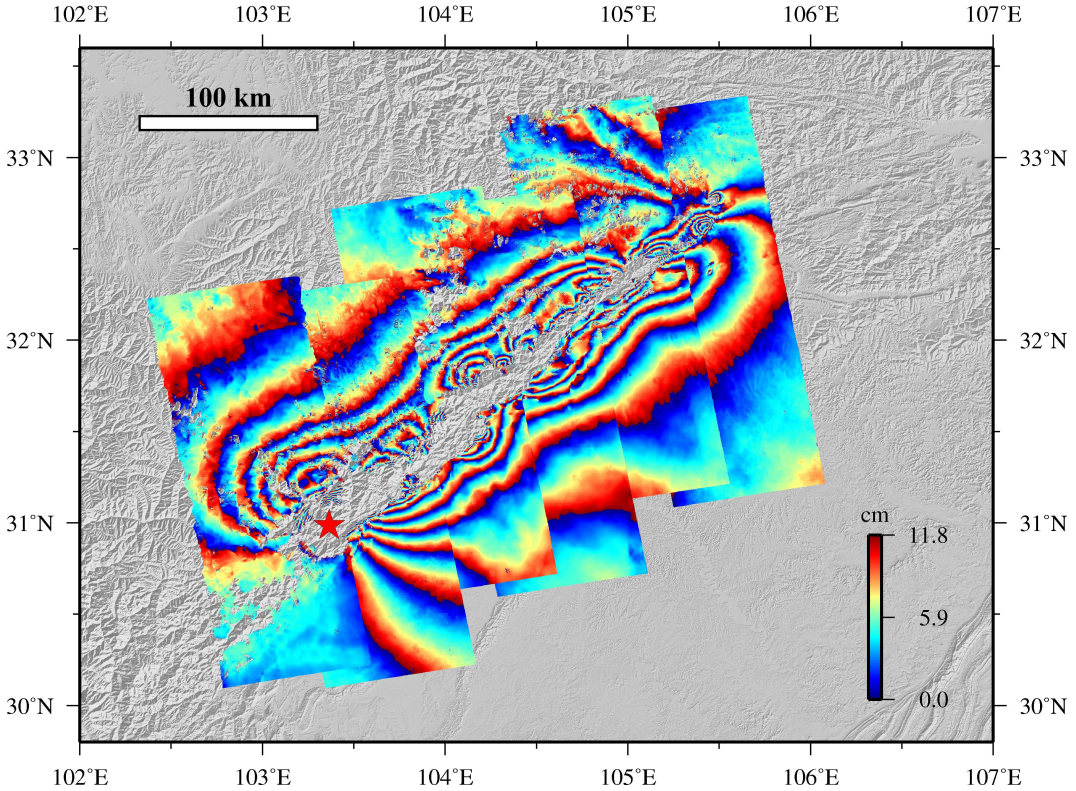


Figure 1.6: Coseismic deformation of the 2008 Wenchuan earthquake estimated from InSAR, modified from *Xu et al.* (2010). The interferograms are displacements in the LOS direction. Each cycle from blue to red means 11.8 cm displacement. Red star indicates the epicentre. It is decorrelated in the near-field due to very large surface deformation in the earthquake.

1.4.3 Optical Image Matching

Matching of pre- and post-earthquake optical imagery of the epicentral region has the potential to measure horizontal surface displacements at sub-pixel accuracy (*Michel and Avouac*, 2002, 2006; *Leprince et al.*, 2007; *Rosu et al.*, 2015) and is often used to investigate coseismic deformation. In the past decades, a wide range of optical images, such as ASTER, SPOT and Landsat, have been used to map coseismic surface displacements, e.g., the 1999 Izmit (*Michel and Avouac*, 2002), 2003 Bam (*Binet and Bollinger*, 2005), 2005 Kashmir (*Avouac et al.*, 2006), 2010 El-Mayor Cucapah (*Barišin et al.*, 2015) and 2013 Balochistan (*Barnhart et al.*, 2015) earthquakes. The image matching method can resolve surface horizontal displacements down to 1/20 of the image resolution (i.e. input pixel size) (*Leprince et al.*, 2007). Note that the uncertainties in the measured displacements are usually determined from fitting line to the data and do not include the uncertainties associated with the original image matching. Therefore, these uncertainties might be underestimates. Image matching does not normally cause decorrelation in the near-field deformation (see Figure 1.7), which is a common case for InSAR. However, due to a lack of both pre- and post-earthquake topography for orthorectifying the optical images, the derived displacements are usually contaminated by changes in topography (*Hollingsworth et al.*, 2012). Moreover, optical image matching cannot measure height changes directly.

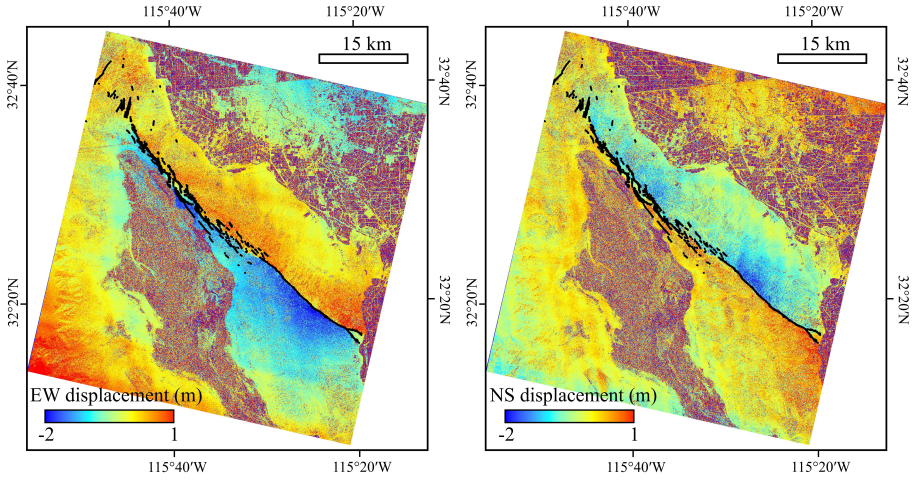


Figure 1.7: Coseismic surface displacement fields of the epicentral area of the 2010 El-Mayor Cucapah earthquake from cross-correlating pre- and post-earthquake SPOT-5 images, modified from *Barišin et al.* (2015). Black lines indicate surface ruptures mapped in the field by *Fletcher et al.* (2014) and *Teran et al.* (2015). Optical image matching can measure displacements in two dimensions and does not normally decorrelate in the near-field.

1.4.4 Light Detection And Ranging (LiDAR)

Given the disadvantage that both InSAR and optical image matching cannot measure vertical displacements directly, light detection and ranging (LiDAR) surveys have been shown to be a valuable tool for determining vertical offsets in earthquakes in recent years, e.g. the 2010 El-Mayor Cucapah (*Oskin et al.*, 2012), 2010-2011 Canterbury (*Elliott et al.*, 2012), 2008 Iwate-Miyagi and 2011 Fukushima-Hamadori earthquakes (*Nissen et al.*, 2014). Matching of pre- and post-earthquake LiDAR topography can reveal accurate 3D surface displacements (on the order of decimetres), as shown in Figure 1.8, but its relatively high cost and low availability has limited its applicability, particularly as pre-earthquake LiDAR acquisitions are rare (*Nissen et al.*, 2014). In addition, there are many areas in the world where airborne LiDAR measurements are difficult.

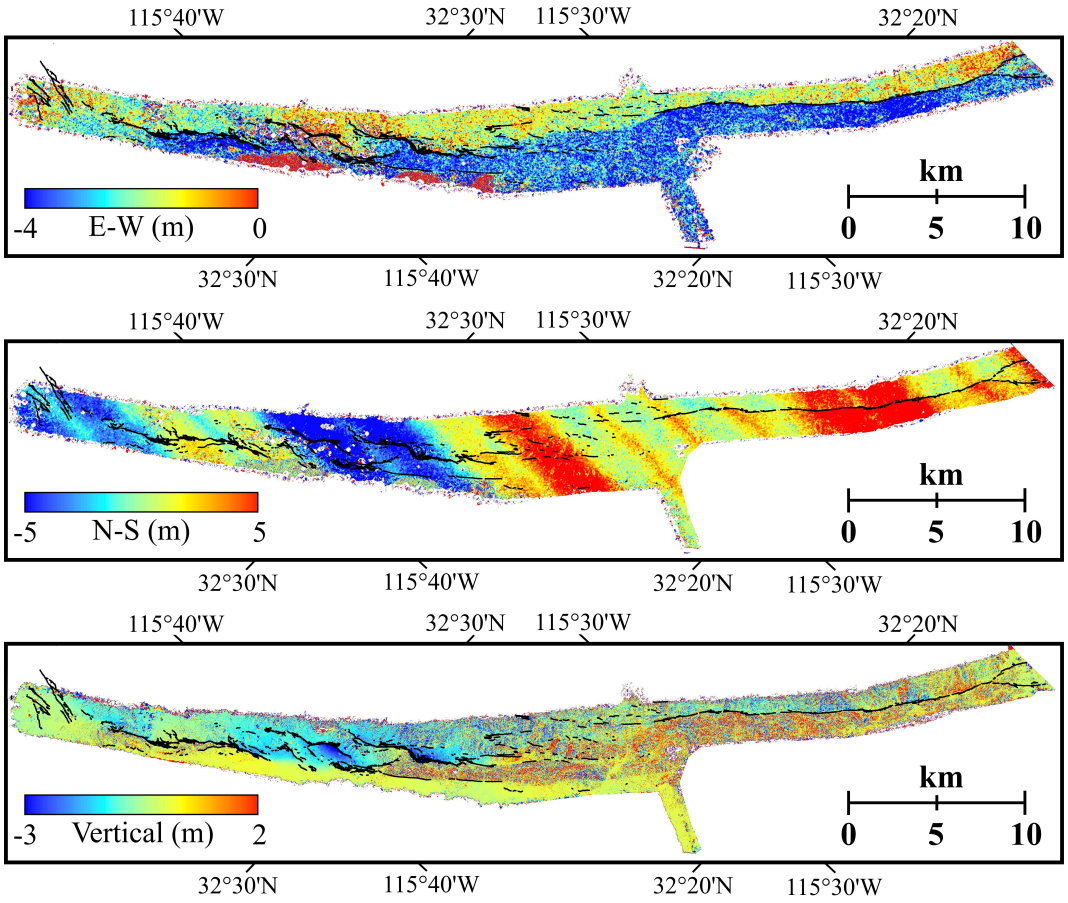


Figure 1.8: 3D coseismic surface displacement fields of the epicentral area of the 2010 El-Mayor Cucapah earthquake from differencing pre- and post-earthquake LiDAR DEMs. Black lines indicate surface ruptures mapped in the field by *Fletcher et al.* (2014) and *Teran et al.* (2015). (*top*): E-W displacements. (*middle*): N-S displacements. Stripping effects are due to laser beam misalignment in the pre-earthquake LiDAR DEM (*Glennie et al.*, 2014). (*bottom*): Vertical displacements.

1.5 Aims and Overview of Thesis

The aim of this thesis is to seek a more efficient alternative of measuring earthquake deformation in 3D. Various high-resolution optical images are explored, ranging from modern satellite imagery, to historical aerial photographs. I choose the 2013 Balochistan (Pakistan), 1978 Tabas-e-Golshan (Iran) and 1556 Huaxian (China) earthquakes as three case studies where no geodetic measurements of coseismic displacement exist, since InSAR and GPS monitoring were not available at the time of the earthquakes. High-resolution optical images provide a unique opportunity for studying these earthquakes, thus improving our ability to investigate faulting.

Chapter 2 describes the technique of photogrammetry as applied to measurements of the 3D ground surface.

Chapter 3 evaluates the capability of Pleiades stereo imagery (50 cm resolution) to measure coseismic vertical ground displacement. I compare the satellite-derived results with a previous study that uses costly LiDAR surveys (*Oskin et al.*, 2012).

Chapter 4 is concerned with the 2013 Balochistan, Pakistan earthquake. Previous studies have suggested a wide range of unconventional kinematic and dynamic models (*Avouac et al.*, 2014; *Barnhart et al.*, 2014, 2015). I use the post-earthquake Pleiades stereo imagery and the topography derived from it to determine the 3D coseismic displacements so as to resolve the current controversy of this earthquake.

Chapter 5 presents a case study of using historical and modern imagery to investigate past earthquakes. I employ historical aerial stereo, KH-9 Hexagon spy satellite, SPOT-2 and modern SPOT-6 images to study the 1978 Tabas-e-Golshan, Iran earthquake, which highlights the usefulness of historical imagery in investigating past earthquakes, thus providing new information about faulting in continental regions.

Chapter 6 consists of a palaeoseismic study of the 1556 Huaxian earthquake in the Weihe graben in central China. High-resolution topographic data, fieldwork and geological dating techniques are combined to study tectonic geomorphology in the graben, and determine slip of the 1556 event and recurrence intervals for similar events.

Chapter 7 discusses the contributions of the research to an improved understanding of earthquake deformation, and the future applications of high-resolution stereo imagery in

continental tectonics.

1.6 Publications

The work in Chapter 3 has been published in *Zhou et al.* (2015b):

- Zhou, Y., B. Parsons, J. R. Elliott, I. Barisin, and R. T. Walker (2015b), Assessing the ability of Pleiades stereo imagery to determine height changes in earthquakes: A case study for the El Mayor-Cucapah epicentral area, *Journal of Geophysical Research: Solid Earth, 120*(12), 8793-8808, doi:10.1002/2015JB012358.

The work that constitutes the majority of Chapter 4 has been published in *Zhou et al.* (2015a) and *Zhou et al.* (2016a):

- Zhou, Y., J. R. Elliott, B. Parsons, and R. T. Walker (2015a), The 2013 Balochistan earthquake: an extraordinary or completely ordinary event?, *Geophysical Research Letters, 42*, 6236–6243, doi:10.1002/2015GL065096.
- Zhou, Y., R. T. Walker, J. R. Elliott, and B. Parsons (2016), Mapping 3D fault geometry in earthquakes using high-resolution topography: Examples from the 2010 El Mayor-Cucapah (Mexico) and 2013 Balochistan (Pakistan) earthquakes, *Geophysical Research Letters, 43*, doi:10.1002/2016GL067899.

The study of the 1978 M_w 7.3 Tabas-e-Golshan, Iran earthquake in Chapter 5 has been published in *Zhou et al.* (2016b):

- Zhou, Y., R. T. Walker, J. Hollingsworth, M. Talebian, X. Song and B. Parsons (2016), Coseismic and postseismic displacements from the 1978 M_w 7.3 Tabas-e-Golshan earthquake in eastern Iran, *Earth and Planetary Science Letters*, doi: 10.1016/j.epsl.2016.07.38.

The material in Chapter 6 is a contribution to a collaborative study with researchers at the China Earthquake Administration Shaanxi Province through the Earthquake without Frontiers (EwF) project, which will be submitted to *Earth and Planetary Science Letters*:

- Feng, X., J. Ma, Y. Zhou, R. T. Walker, B. Parsons, P. England and M. A. Rizza (in prep.), Repeated high stress-drop ruptures on the 1556 Huaxian earthquake normal fault, Shaanxi, central China, *Earth and Planetary Science Letters*.

I have also worked on InSAR studies of ice dynamics in Antarctica, which have been published in *Zhou et al.* (2014) and *Zhou et al.* (2015c):

- Zhou, Y., C. Zhou, D. E and Z. Wang (2014), A Baseline-Combination Method for Precise Estimation of Ice Motion in Antarctica, *IEEE Transactions on Geoscience and Remote Sensing, 52*(9), 5790-5797, doi:10.1109/TGRS.2013.2292815.
- Zhou, Y., C. Zhou, F. Deng, D. E, H. Liu and Y. Wen (2015c), Improving InSAR elevation models in Antarctica using laser altimetry, accounting for ice motion, orbital errors and atmospheric delays, *Remote Sensing of Environment 162*, 112-118, doi:10.1016/j.rse.2015.01.017.

Chapter 2

Photogrammetry Technique

2.1 Introduction

Our capability of measuring the Earth's surface in three dimensions (3D) has been greatly improved by recent developments in the remote sensing technique of photogrammetry, which uses a series of photographs to recover positions on the Earth's surface (*Eisenbeiss et al.*, 2004; *Snavely et al.*, 2008a; *Tong et al.*, 2010; *Westoby et al.*, 2012; *Johnson et al.*, 2014; *Zhou et al.*, 2015a). New generations of very high-resolution (VHR) satellites (*de Lussy et al.*, 2005; *Fraser and Ravanbakhsh*, 2009; *Mitchell and MacNabb*, 2010; *Poli and Toutin*, 2012; *Bernard et al.*, 2012) have stimulated photogrammetric products to become widely used in earth sciences in recent years, for example, mapping surface displacements in earthquakes (e.g. *Barnhart et al.* 2015; *Zhou et al.* 2015b; *Middleton et al.* 2016) and landslides (e.g. *Stumpf et al.* 2014), and measuring metre-scale elevation changes of glaciers (e.g. *Berthier et al.* 2014). In my thesis, a wide range of imagery, including modern VHR satellite images (Pleiades and SPOT), old film-based satellite and aerial images, and field photos from compact cameras, has been used to study earthquake deformation and active tectonics.

This chapter focuses on the photogrammetry technique and is split into two parts: firstly I will outline the sensor models for images acquired from different platforms, for example, rigorous models for aerial and ground-based photos, and the rational function model for most satellite images (Pleiades, WorldView and SPOT-6/7); secondly I will describe

photogrammetric processing including 3D reconstruction and orthorectification.

2.2 Sensor Models: Single View Geometry

In imaging systems (as shown in Figure 2.1), a sensor model (also termed "geometric model") is used to describe the geometric relationship between 2D image coordinates (x, y) and the 3D ground (or object) coordinates (X, Y, Z). A well-designed sensor model is essential for photogrammetric processing including 3D reconstruction and orthorectification (*Tao and Hu*, 2002). There are two broad categories of sensor models (*McGlone*, 1996): the rigorous models which are derived directly from the image sensor physics (*Tao and Hu*, 2002), and the generic models which are approximations to the rigorous models and do not have any physical meaning (*OGC*, 1999; *Tao and Hu*, 2002; *Fraser and Hanley*, 2005). Both film-based and digital frame cameras use a rigorous model whereas most modern optical satellites use a"pushbroom" sensor with a generic model for simplicity.

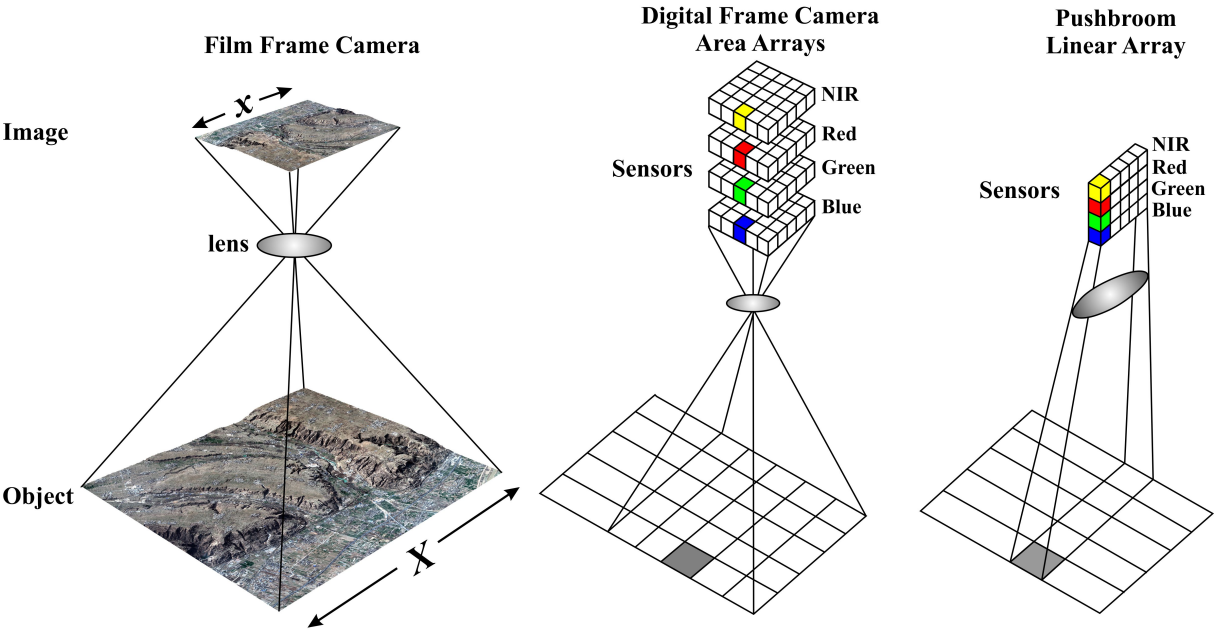


Figure 2.1: Remote sensing systems used to collect images. The most commonly used cameras are area arrays (typical for airborne sensors) and linear arrays (typical for spaceborne imaging systems).

2.2.1 Rigorous Models

Most commercial digital cameras are frame cameras that use 2D arrays of sensors to capture the scene over a large area. The mathematical relationship between the 3D world and the 2D image plane can be rigorously modelled with a perspective projection, i.e. the pinhole camera model (*Ballard and Brown*, 1982; *Dawson-Howe and Vernon*, 1994). For linear pushbroom cameras where the pixels on the same scan line are captured with a linear (1D) array rather than an area (2D) array, each scan line can be modelled with a pinhole camera model. Rigorous pushbroom camera models focus mainly on the interpolation of the attitude of the platform as a function of time (*Lee et al.*, 2000).

The basis of the pinhole model is collinear equations derived from the spatial relationship between the image point, the perspective centre and the object point. As shown in Figure 2.2, the image point ($\mathbf{x}$) lies on the line defined by the perspective centre ($\mathbf{p}$) and the object point ($\mathbf{X}$). In the camera (sensor) coordinate system (with its origin at the perspective centre), the projection from a 3D point (X_c, Y_c, Z_c) ($_c$ means the camera coordinate system) to the image plane (x, y, $-f$) yields the equation (*Mikhail et al.*, 2001):

$$\lambda \begin{pmatrix} x - x_0 \\ y - y_0 \\ -f \end{pmatrix} = \begin{pmatrix} X_c \\ Y_c \\ Z_c \end{pmatrix} \tag{2.1}$$

where λ is a scale factor, f is the focal length, (x_0, y_0) is the position of the image centre, Z axis represents the principal axis (the line passing through the optical centre and perpendicular to the image plane), and the other two axes along the edge of the image are chosen to form a right-hand coordinate system.

x_0, y_0 and f are termed the "interior orientation parameters" of a camera. Theoretically, these parameters are known constants if the camera settings used in data collection are fixed, but due to the geometric limitations of cameras, the values of the parameters given usually contain small errors. Accurate knowledge of the parameters requires camera calibration in a professional 3D calibration field (a room with a large number of targets surrounding the camera and the positions of each target are accurately known) (*Brown*, 1971; *Fraser*, 1997). Such calibration is very accurate, but requires special equipment

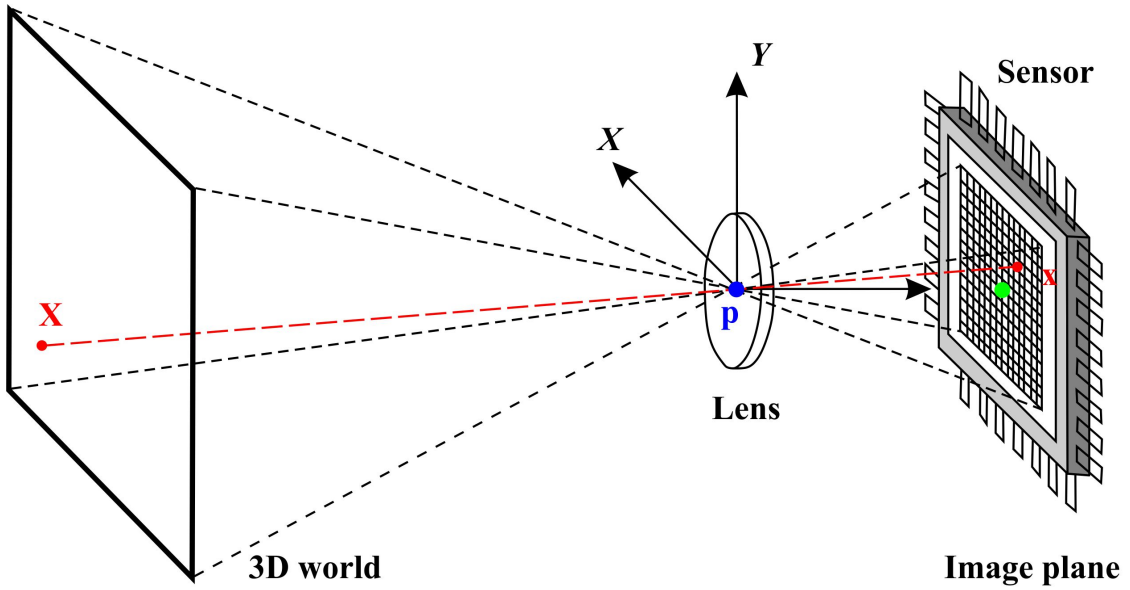


Figure 2.2: Perspective projection describes the mathematical relationship between the 3D world and the 2D image plane. The image point ($\mathbf{x}$) lies on the line defined by the perspective centre ($\mathbf{p}$) and the object point ($\mathbf{X}$). This spatial relationship serves as the principle of the pinhole model. Green dot denotes the image centre (x_0, y_0).

and regular maintenance. Instead, the planar pattern-based calibration method (*Zhang*, 2000), which only requires the camera to capture a few images of a planar pattern from different orientations, has been widely used in close-range photogrammetry and computer vision due to its simplicity and flexibility.

It should be noted that the coordinates of an object are usually given in a predefined coordinate system which is not normally located at the camera perspective centre. Thus, an additional rigid-body transformation is needed to transform the coordinates of a point in the predefined object coordinate system $\mathbf{X} = (X, Y, Z)^T$ to the camera coordinate system $\mathbf{X_c} = (X_c, Y_c, Z_c)^T$.

$$\mathbf{X_c} = \begin{pmatrix} X_c \\ Y_c \\ Z_c \end{pmatrix} = \mathbf{R} \left[\begin{pmatrix} X \\ Y \\ Z \end{pmatrix} - \begin{pmatrix} X_0 \\ Y_0 \\ Z_0 \end{pmatrix} \right] \tag{2.2}$$

where $\mathbf{C} = (X_0, Y_0, Z_0)^T$ is the position of the perspective centre in the predefined object coordinate system, and $\mathbf{R}$ is a rotation matrix (Equation 2.3) that can be determined by three rotation angles about the X, Y and Z axes (known as roll, pitch and yaw, i.e. ω, ϕ and κ respectively). These six parameters are termed the "exterior orientation

parameters" (*Beyer*, 1992).

$$\begin{aligned}\mathbf{R} &= \begin{pmatrix} R_{11} & R_{12} & R_{13} \\ R_{21} & R_{22} & R_{23} \\ R_{31} & R_{32} & R_{33} \end{pmatrix} \\ &= \begin{pmatrix} \cos\phi\cos\kappa & -\cos\phi\sin\kappa & \sin\phi \\ \cos\omega\sin\kappa + \sin\omega\sin\phi\cos\kappa & \cos\omega\cos\kappa - \sin\omega\sin\phi\sin\kappa & -\sin\omega\cos\phi \\ \sin\omega\sin\kappa - \cos\omega\sin\phi\cos\kappa & \sin\omega\cos\kappa + \cos\omega\sin\phi\sin\kappa & \cos\omega\cos\phi \end{pmatrix}\end{aligned} \tag{2.3}$$

Equations 2.1 and 2.2 describe the relationship between the 3D object coordinates and the 2D image coordinates. Rearrangement of the two equations yields the general form of the collinearity equations (*Luhmann et al.*, 2006):

$$x - x_0 = -f\frac{R_{11}(X - X_0) + R_{12}(Y - Y_0) + R_{13}(Z - Z_0)}{R_{31}(X - X_0) + R_{32}(Y - Y_0) + R_{33}(Z - Z_0)} \tag{2.4}$$

$$y - y_0 = -f\frac{R_{21}(X - X_0) + R_{22}(Y - Y_0) + R_{23}(Z - Z_0)}{R_{31}(X - X_0) + R_{32}(Y - Y_0) + R_{33}(Z - Z_0)} \tag{2.5}$$

Direct Linear Transform (DLT)

Control points are needed to solve for the orientation parameters (x_0, y_0, f, X_0, Y_0, Z_0, ω, ϕ and κ) in Equations 2.4 and 2.5. Since the equations are non-linear, the first step in the solution is to obtain initial estimates of these parameters. For this purpose, the direct linear transform (DLT) (*Abdel-Aziz*, 1971) has been derived relating a 3D object and its 2D projection in a linear form.

The collinear equations (Equation 2.4) can be rearranged as:

$$\begin{aligned} x &= x_0 - f\frac{R_{11}(X - X_0) + R_{12}(Y - Y_0) + R_{13}(Z - Z_0)}{R_{31}(X - X_0) + R_{32}(Y - Y_0) + R_{33}(Z - Z_0)} \\ &= \frac{x_0R_{31} - fR_{11}}{R_{31}X + R_{32}Y + R_{33}Z - (R_{31}X_0 + R_{32}Y_0 + R_{33}Z_0)} \cdot X \\ &\quad + \frac{x_0R_{32} - fR_{12}}{R_{31}X + R_{32}Y + R_{33}Z - (R_{31}X_0 + R_{32}Y_0 + R_{33}Z_0)} \cdot Y \\ &\quad + \frac{x_0R_{33} - fR_{13}}{R_{31}X + R_{32}Y + R_{33}Z - (R_{31}X_0 + R_{32}Y_0 + R_{33}Z_0)} \cdot Z \\ &\quad + \frac{x_0R_{31}X_0 + x_0R_{32}Y_0 + x_0R_{33}Z_0 + fR_{11}X_0 + fR_{12}Y_0 + fR_{13}Z_0}{R_{31}X + R_{32}Y + R_{33}Z - (R_{31}X_0 + R_{32}Y_0 + R_{33}Z_0)} \end{aligned} \tag{2.6}$$

A general form for Equation 2.6 is:

$$x = \frac{L_1X + L_2Y + L_3Z + L_4}{L_9X + L_{10}Y + L_{11}Z + 1} \tag{2.7}$$

where

$$L_1 = -\frac{x_0R_{31} - fR_{11}}{R_{31}X_0 + R_{32}Y_0 + R_{33}Z_0} \tag{2.8}$$

$$L_2 = -\frac{x_0R_{32} - fR_{12}}{R_{31}X_0 + R_{32}Y_0 + R_{33}Z_0} \tag{2.9}$$

$$L_3 = -\frac{x_0R_{33} - fR_{13}}{R_{31}X_0 + R_{32}Y_0 + R_{33}Z_0} \tag{2.10}$$

$$L_4 = -\frac{x_0R_{31}X_0 + x_0R_{32}Y_0 + x_0R_{33}Z_0 + fR_{11}X_0 + fR_{12}Y_0 + fR_{13}Z_0}{R_{31}X_0 + R_{32}Y_0 + R_{33}Z_0} \tag{2.11}$$

$$L_9 = \frac{-R_{31}}{R_{31}X_0 + R_{32}Y_0 + R_{33}Z_0} \tag{2.12}$$

$$L_{10} = \frac{-R_{32}}{R_{31}X_0 + R_{32}Y_0 + R_{33}Z_0} \tag{2.13}$$

$$L_{11} = \frac{-R_{33}}{R_{31}X_0 + R_{32}Y_0 + R_{33}Z_0} \tag{2.14}$$

Similarly, Equation 2.5 can be rewritten as:

$$y = \frac{L_5X + L_6Y + L_7Z + L_8}{L_9X + L_{10}Y + L_{11}Z + 1} \tag{2.15}$$

where

$$L_5 = -\frac{y_0R_{31} - fR_{21}}{R_{31}X_0 + R_{32}Y_0 + R_{33}Z_0} \tag{2.16}$$

$$L_6 = -\frac{y_0R_{32} - fR_{22}}{R_{31}X_0 + R_{32}Y_0 + R_{33}Z_0} \tag{2.17}$$

$$L_7 = -\frac{y_0R_{33} - fR_{23}}{R_{31}X_0 + R_{32}Y_0 + R_{33}Z_0} \tag{2.18}$$

$$L_8 = -\frac{y_0R_{31}X_0 + y_0R_{32}Y_0 + y_0R_{33}Z_0 + fR_{21}X_0 + fR_{22}Y_0 + fR_{23}Z_0}{R_{31}X_0 + R_{32}Y_0 + R_{33}Z_0} \tag{2.19}$$

Equations 2.7 and 2.15 define the DLT that describes the relationship between the image point and the object point in a linear form:

$$\lambda\widetilde{\mathbf{x}} = \mathbf{L}\widetilde{\mathbf{X}} \tag{2.20}$$

where

$$\lambda = L_9X + L_{10}Y + L_{11}Z + 1 \tag{2.21}$$

$$\widetilde{\mathbf{x}} = (x, y, 1)^T \tag{2.22}$$

$$\widetilde{\mathbf{X}} = (X, Y, Z, 1)^T \tag{2.23}$$

$\mathbf{L}$, which incorporates the orientation parameters (x_0, y_0, f, X_0, Y_0, Z_0, ω, ϕ and κ), is a 3×4 perspective projection matrix:

$$\mathbf{L} = \begin{pmatrix} L_1 & L_2 & L_3 & L_4 \\ L_5 & L_6 & L_7 & L_8 \\ L_9 & L_{10} & L_{11} & 1 \end{pmatrix} \tag{2.24}$$

To estimate the perspective matrix $\mathbf{L}$, a minimum of 6 points with known object coordinates (X, Y, Z) and the corresponding image coordinates (x, y) are needed. The least squares inversion is given by:

$$\begin{pmatrix} X & Y & Z & 1 & 0 & 0 & 0 & 0 & -xX & -xY & -xZ \\ 0 & 0 & 0 & 0 & X & Y & Z & 1 & -yX & -yY & -yZ \end{pmatrix} \begin{pmatrix} L_1 \\ L_2 \\ L_3 \\ L_4 \\ L_5 \\ L_6 \\ L_7 \\ L_8 \\ L_9 \\ L_{10} \\ L_{11} \end{pmatrix} = \begin{pmatrix} x \\ y \end{pmatrix} \tag{2.25}$$

Camera Distortion

In theory, a straight line in the 3D world will remain a straight line in the 2D image under perspective projection. However, due to lens imperfections, a straight line is usually

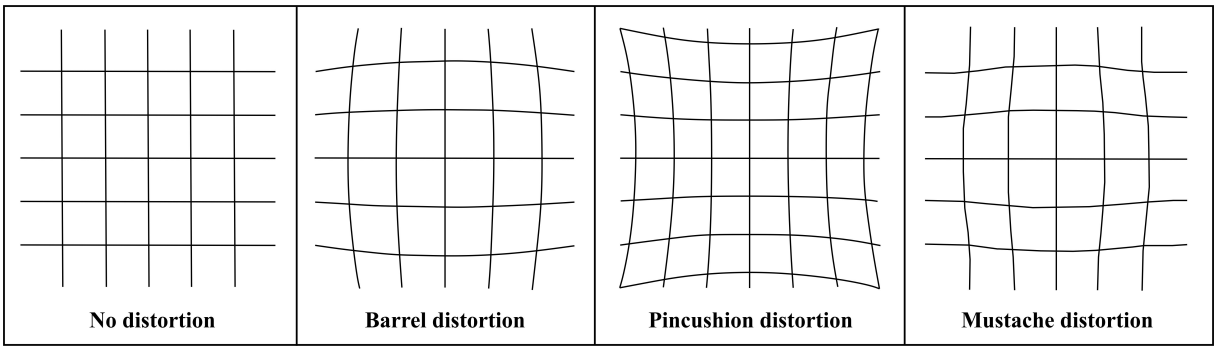


Figure 2.3: Camera distortion. In theory, a straight line in the 3D world will remain a straight line in the 2D image in the perspective projection. However, distortion occurs due to lens imperfections. The radial distortion is usually categorised as the barrel, pincushion and mustache styles. The mustache style is a combination of the barrel distortion near the centre and the pincushion distortion at the edges.

distorted when projected into the image. In that sense, the pinhole model described in Equations 2.1 and 2.2 is only an approximation of the real camera projection unless the systematic distortion has been corrected (*Fleck*, 1995; *Heikkila and Silvén*, 1997). Camera distortion occurs in both the radial and tangential directions, but the most common distortion is the radial distortion. Based on the shape of the distortion, radial distortion is usually divided into the barrel, pincushion and mustache styles (as shown in Figure 2.3) (*Jenkins and White*, 1957).

The Brown-Conrady model is widely used to correct for camera distortion (*Conrady*, 1919; *Brown*, 1971; *Heikkila and Silvén*, 1997; *Wang et al.*, 2008). The transformation between the distorted (x_d, y_d) and undistorted images (x_u, y_u) is given as (*Weng et al.*, 1992; *Wang et al.*, 2008):

$$\begin{aligned} x_d = x_u(1 + K_1 r^2 + K_2 r^4 + K_3 r^6 + \cdots) + \\ (P_2(r^2 + 2x_u^2) + 2P_1 x_u y_u)(1 + P_3 r^2 + P_4 r^4 + \cdots) \end{aligned} \tag{2.26}$$

$$\begin{aligned} y_d = y_u(1 + K_1 r^2 + K_2 r^4 + K_3 r^6 + \cdots) + \\ (P_1(r^2 + 2y_u^2) + 2P_2 x_u y_u)(1 + P_3 r^2 + P_4 r^4 + \cdots) \end{aligned} \tag{2.27}$$

where r is the distance in the undistorted image to the principal point, K_i ($i = 1, 2, ...$) is the ith coefficient for the radial distortion, and P_i ($i = 1, 2, ...$) is the ith coefficient for the tangential distortion. As the camera distortion is dominated by low-order components,

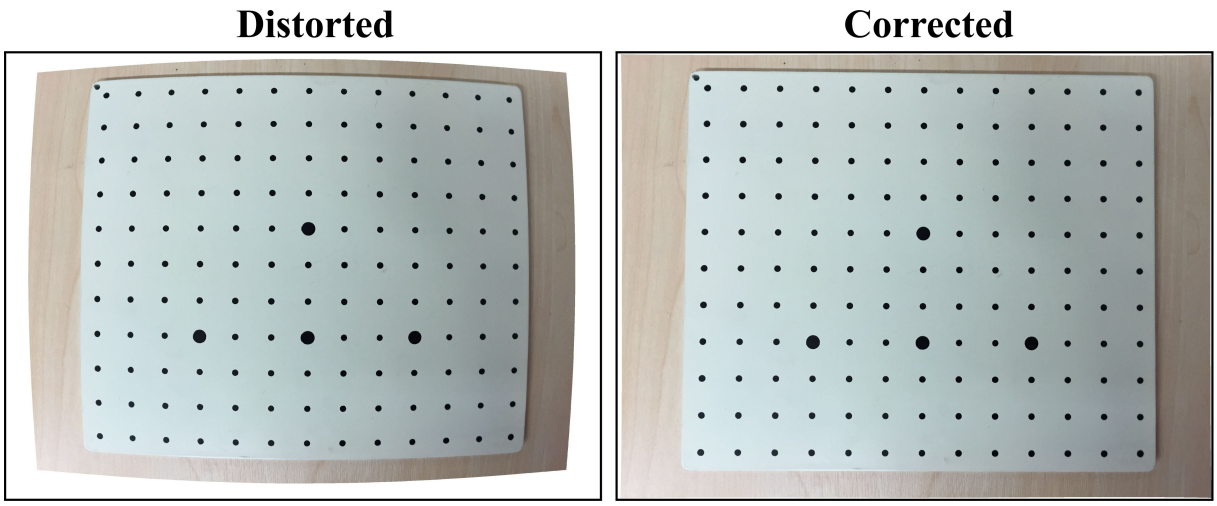


Figure 2.4: (*left*): A distorted photo. (*right*): Corrected for camera distortion. The coefficients for the distortion are: $K_1 = -0.0128992$, $K_2 = -0.035823$, $K_3 = 0$, $P_1 = 2.755246 \times 10^{-4}$, $P_2 = 1.583117 \times 10^{-4}$, $P_3 = 0$, $P_4 = 0$.

3rd- and 2nd-order corrections are accurate enough to compensate for the radial and tangential distortions (*Wang et al.*, 2008). Figure 2.4 shows an example of calibration for camera distortion. The distortion coefficients are usually calibrated along with the interior orientation parameters (before launch in the case of satellite cameras).

2.2.2 Generic Models

Rigorous models are complex and computationally intensive, particularly for pushbroom imaging systems (such as Pleiades and SPOT-6/7 satellites) in which each scanning line needs to be treated as an individual model. Different image sensors have their own specific physical model, so in order to allow users to perform photogrammetric processing based on the rigorous models, many software packages are needed to handle all the different sensors (*OGC*, 1999). In addition, developing such packages requires good knowledge of the image sensor physics. As a result, for real-time applications based on satellite imagery, simpler models have been proposed to approximate the rigorous physical sensor models (*OGC*, 1999; *Dowman and Dolloff*, 2000); these models, which are termed "generic models", do not take account of the physical interpretation of the imaging system and therefore are sensor-independent. Moreover, the generic models enable commercial satellite image companies to keep the information about the sensors, such as ephemeris and satellite attitude, confidential (*Tong et al.*, 2010). In the following sections, I will briefly describe

three main generic models. For a more comprehensive understanding of these models, readers are referred to *OGC* (1999); *Dowman and Dolloff* (2000); *Tao and Hu* (2002); *Di et al.* (2003); *Grodecki and Dial* (2003); *Hu et al.* (2004); *Fraser and Hanley* (2005); *Fraser et al.* (2006); *Tong et al.* (2010); *Poli and Toutin* (2012).

Grid Interpolation Model

The grid interpolation model uses interpolation to find the image positions (x, y) of an arbitrary ground point (X, Y, Z) based on a known regular 3D grid (the grid points are equally spaced) (*OGC*, 1999). This 3D grid is computed using a rigorous sensor model by a central facility and provided as image support data that contains both the image and ground coordinates of each grid point (*OGC*, 1999). By giving such a 3D grid, users can choose different interpolation methods to calculate the image coordinates of a specified ground point from its surrounding grid points (Figure 2.5). For example, the tri-linear interpolation method can be used to find the image coordinates (x_0, y_0) of an arbitrary ground point (X_0, Y_0, Z_0) by:

$$\begin{aligned}(x_0, y_0) = (1-\gamma)\{(1-\beta)[(1-\alpha)(x_1, y_1) + \alpha(x_2, y_2) + \beta[(1-\alpha)(x_3, y_3) + \alpha(x_4, y_4)]\} \\ + \gamma\{(1-\beta)[(1-\alpha)(x_5, y_5) + \alpha(x_6, y_6)] + \beta[(1-\alpha)(x_7, y_7) + \alpha(x_8, y_8)]\}\end{aligned} \tag{2.28}$$

where (X_i, Y_i, Z_i, x_i, y_i) (i = 1, 2, ..., 8) are the grid points surrounding the arbitrary point (X_0, Y_0, Z_0), and α, β and γ are the scaling parameters calculated by:

$$\alpha = \frac{X_0 - X_1}{X_2 - X_1} \tag{2.29}$$

$$\beta = \frac{Y_0 - Y_1}{Y_3 - Y_1} \tag{2.30}$$

$$\gamma = \frac{Z_0 - Z_1}{Z_5 - X_1} \tag{2.31}$$

The grid interpolation model is relatively simple and robust, and can be easily applied to all sensor types (*OGC*, 1999). The accuracy of this model depends on the interpolation method and the spacing of the given grid. Higher-order interpolation can increase the positioning accuracy but is more computationally intensive. Smaller spacing grid (i.e. denser grid points) also provides higher accuracy, but requires larger image support data.

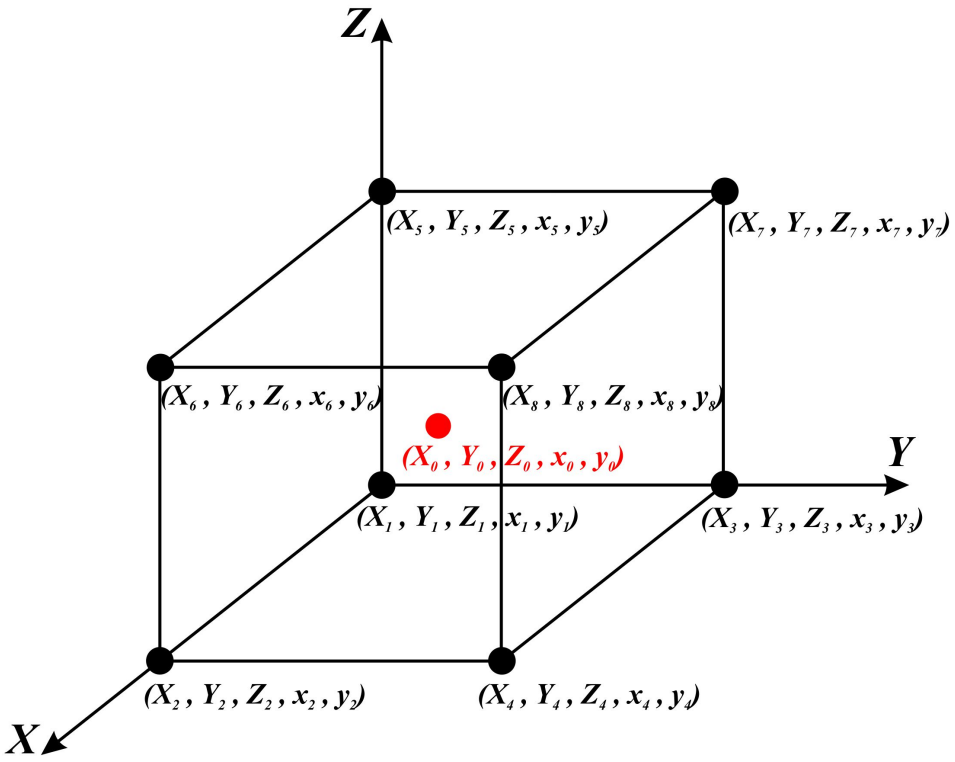


Figure 2.5: Grid interpolation model using the tri-linear interpolation method modified from *OGC* (1999). Black dots denote the equally spaced grid points recorded in the image support data in the form of (X, Y, Z, x, y), where (X, Y, Z) and (x, y) are the ground and image coordinates computed using some rigorous sensor model. The red dot is an arbitrary ground point (X_0, Y_0, Z_0) within a grid cell, whose image coordinates (x_0, y_0) need to be estimated.

The large size of the image support data is the major disadvantage of the grid interpolation model (*OGC*, 1999).

Rational Function Model

The rational function model (RFM) was initially used in the U.S. military and has now become one of the most commonly used generic models (*Dowman and Dolloff*, 2000; *Tao and Hu*, 2002; *Fraser and Hanley*, 2005). The RFM uses the ratio of two polynomial functions to relate the image (x, y) and ground (X, Y, Z) coordinate systems in two forms: the forward form transforms the ground coordinate system to the image coordinate system (*Tao and Hu*, 2002; *Fraser and Hanley*, 2005; *Fraser et al.*, 2006) and the inverse form defines the image-to-ground transformation (*Yang*, 2000). The forward RFM takes the

following form:

$$x = \frac{P_1(X,\, Y,\, Z)}{P_2(X,\, Y,\, Z)} \tag{2.32}$$

$$y = \frac{P_3(X,\, Y,\, Z)}{P_4(X,\, Y,\, Z)} \tag{2.33}$$

where P_i ($i = 1,\, 2,\, 3,\, 4$) is a polynomial function with its maximum power limited to 3. For a 3rd-order case, the case for most high-resolution satellite imagery (such as Pleiades, SPOT-6/7, WorldView and GeoEye), each function P is a 20-term polynomial:

$$\begin{aligned} P &= \sum_{i=0}^{3}\sum_{j=0}^{3}\sum_{k=0}^{3} c_{ijk} X^i Y^j Z^k \\ &= a_0 + a_1 X + a_2 Y + a_3 Z + a_4 X^2 + a_5 XY + a_6 XZ + a_7 Y^2 + a_8 YZ + a_9 Z^2 \\ &\quad + a_{10} X^3 + a_{11} X^2 Y + a_{12} X^2 Z + a_{13} XY^2 + a_{14} XYZ + a_{15} XZ^2 + a_{16} Y^3 \\ &\quad + a_{17} Y^2 Z + a_{18} YZ^2 + a_{19} Z^3 \end{aligned} \tag{2.34}$$

where a_0, a_1, ..., a_{19} are termed as rational polynomial coefficients (RPCs).

The inverse RFM determines the ground planar coordinates in terms of the image coordinates and the ground vertical coordinate:

$$X = \frac{P_5(x,\, y,\, Z)}{P_6(x,\, y,\, Z)} \tag{2.35}$$

$$Y = \frac{P_7(x,\, y,\, Z)}{P_8(x,\, y,\, Z)} \tag{2.36}$$

where P_i ($i = 5,\, 6,\, 7,\, 8$) is a polynomial function that has the same form as Equation 2.34.

Usually, a total of 160 RPCs (80 coefficients for the forward RFM and 80 for the inverse RFM) are provided for customers as an approximation to the rigorous physical model. The generation of the RPCs is based on a 3D regular grid of the ground whose image coordinates are first calculated using a rigorous sensor model (*Poli and Toutin*, 2012). Then the ground and image coordinates of each grid point are used as input to solve for the RPCs. The RFM does not adequately account for the true spatial orientation of each scan line and the attitude, position and velocity of the sensor, which will affect the accuracy of ground point determination (*Zhou et al.*, 2015b). To account for such effects,

the sensor errors are modelled as biases in image coordinates– shifts to compensate for small attitude errors, and drift or an affine (linear function) distortion to compensate for time-dependent errors (*Fraser and Hanley*, 2005; *Fraser et al.*, 2006; *Tong et al.*, 2010; *Zhou et al.*, 2015b).

Taking account of such shift and drift terms, Equations (2.32) and (2.33) can be rewritten as:

$$x + A_1 + A_2 \cdot x + A_3 \cdot y = \frac{P_1(X, Y, Z)}{P_2(X, Y, Z)} \tag{2.37}$$

$$y + B_1 + B_2 \cdot x + B_3 \cdot y = \frac{P_3(X, Y, Z)}{P_4(X, Y, Z)} \tag{2.38}$$

where A_i and B_i $(i = 1, 2, 3)$ are additional parameters that describe an affine transformation to compensate for the errors in sensor orientation (*Fraser and Hanley*, 2005; *Fraser et al.*, 2006). Ground control points (GCPs) are needed to calculate these additional parameters. Only 1 GCP is required to calculate the shift parameters A_1 and B_1; to calculate all the parameters, a minimum number of 4 GCPs is required in practice (*Fraser and Hanley*, 2005; *Fraser et al.*, 2006). Higher-order functions may also be used in the case of severe geometric distortions (*Toutin*, 2006; *Tong et al.*, 2010). This error compensation method could also be applied to the inverse RFM in a similar way.

As discussed in *Tao and Hu* (2002); *Fraser and Hanley* (2005); *Toutin* (2006); *Tong et al.* (2010), the RFM presents a very high accuracy of fitting and is easy for non-expert users to understand. It is implemented in almost all commercial photogrammetric software packages such as ERDAS IMAGINE, PCI Geomatica, ENVI and Barista. The major disadvantage of the RFM is that the accuracy of the RPCs is difficult to evaluate since they do not have any physical meaning (*Poli and Toutin*, 2012).

Universal Real-time Image Geometry Model

The universal real-time image geometry model is an extension of the RFM, which aims to accurately describe all sensor types including frame, panoramic, pushbroom and SAR sensors (*OGC*, 1999). In this model, one image can be split into several sections and the geometry model of each section is represented by an RFM. It also allows higher-order

(up to 5th-order) polynomials, as well as higher-order functions to compensate for the sensor errors. The universal real-time image geometry model offers extensive future use for satellite imagery (*OGC*, 1999).

2.3 Epipolar Geometry: Stereo View Geometry

The epipolar geometry describes the geometric relationship between a stereo pair of images (*Zhang et al.*, 1995b). For two perspective images of an object taken from two different viewpoints (e.g. left view and right view in Figure 2.6, O_l and O_r are the perspective centres), the epipolar geometry determines the locations of the corresponding image points. Based on the pinhole model, lines $O_l x_l X$ and $O_r x_r X$ intersect at the object point X, and therefore are coplanar. This plane (i.e. $O_l x_l X x_r O_r$ in Figure 2.6) is called the "epipolar plane". The epipolar plane intersects the image plane in a straight line, termed the "epipolar line".

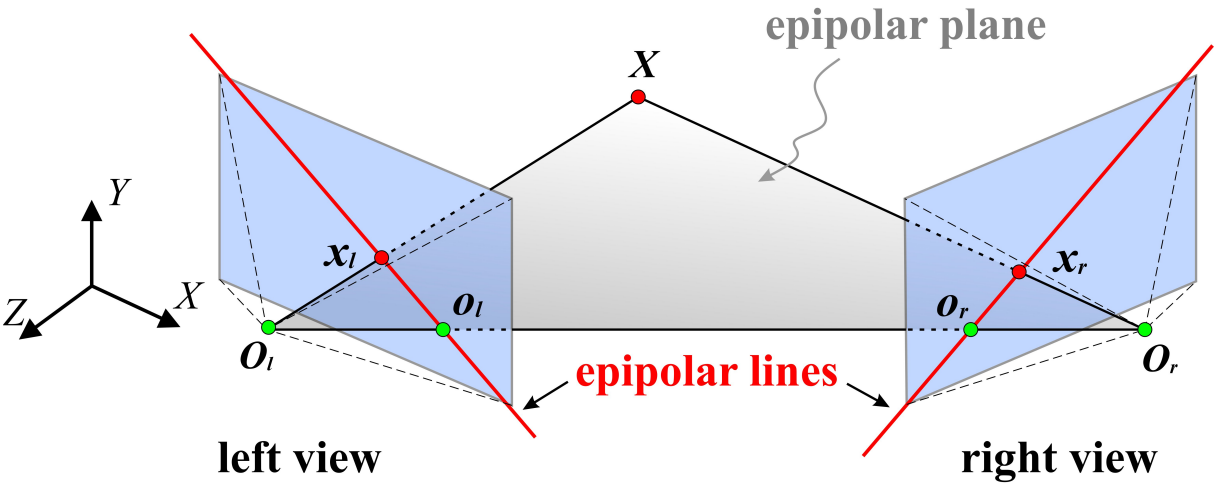


Figure 2.6: Epipolar geometry describes the spatial relationship between the correspondences (different image points that correspond to the same object point, e.g. points x_l and x_r correspond to the same object point X). O_l (perspective centre of the left view), x_l and X are collinear, as are O_r (perspective centre of the right view), x_r and X. The two lines determines a plane ($O_l x_l X x_r O_r$), i.e. the epipolar plane. The epipolar plane intersects the image plane in a straight line, i.e. the "epipolar line", as shown in red. o_l and o_r, which are the intersections of the baseline $O_l O_r$ and the images, are termed the "epipoles".

Assume $\mathbf{L_l}$ and $\mathbf{L_r}$ are the perspective projection matrices of the left and right views (see Section 2.48). From Equation 2.20, the projections of the object point ($\mathbf{X}$) onto the left

($\mathbf{x_l}$) and right ($\mathbf{x_r}$) views are:

$$\lambda_l \widetilde{\mathbf{x_l}} = \mathbf{L_l} \widetilde{\mathbf{X}} \tag{2.39}$$

$$\lambda_r \widetilde{\mathbf{x_r}} = \mathbf{L_r} \widetilde{\mathbf{X}} \tag{2.40}$$

where $\widetilde{\mathbf{x_l}} = (x_l, y_l, 1)^T$, and $\widetilde{\mathbf{x_r}} = (x_r, y_r, 1)^T$.

As both image points $\mathbf{x_l}$ and $\mathbf{x_r}$ are linearly related to $\mathbf{X}$, we can find a linear transformation $\mathbf{H}$ that can map $\mathbf{x_l}$ to $\mathbf{x_r}$:

$$\widetilde{\mathbf{x_r}} = \mathbf{H} \widetilde{\mathbf{x_l}} \tag{2.41}$$

Note that point $\mathbf{x_r}(x_r, y_r)^T$ lies on line $o_r x_r$ (see Figure 2.6). Assuming that a line in the plane of the right view is represented by a vector $(a, b, c)^T$, satisfying $ax + by + c = 0$, we have:

$$\widetilde{\mathbf{x_r}}^T \cdot o_r \vec{x}_r = 0 \tag{2.42}$$

Similarly,

$$\widetilde{\mathbf{o_r}}^T \cdot o_r \vec{x}_r = 0 \tag{2.43}$$

Note $\mathbf{o_r}$ is also the projection of $\mathbf{O_l}$ onto the right view:

$$\lambda_r \widetilde{\mathbf{o_r}} = \mathbf{L_r} \widetilde{\mathbf{O_l}} \tag{2.44}$$

As the epipolar line joins points $\mathbf{o_r}$ and $\mathbf{x_r}$, $o_r \vec{x}_r$ can be determined by:

$$o_r \vec{x}_r = \widetilde{\mathbf{o_r}} \times \widetilde{\mathbf{x_r}} = \frac{1}{\lambda_r} (\mathbf{L_r} \widetilde{\mathbf{O_l}}) \times \widetilde{\mathbf{x_r}} = \frac{1}{\lambda_r} [\mathbf{L_r} \widetilde{\mathbf{O_l}}]_\times \widetilde{\mathbf{x_r}} \tag{2.45}$$

where $[\mathbf{L_r} \widetilde{\mathbf{O_l}}]_\times$ is a 3×3 skew-symmetric matrix, defined as:

$$[\mathbf{L_r} \widetilde{\mathbf{O_l}}]_\times = \begin{pmatrix} 0 & -a_3 & a_2 \\ a_3 & 0 & -a_1 \\ -a_2 & a_1 & 0 \end{pmatrix} \tag{2.46}$$

assuming $\mathbf{L_r} \widetilde{\mathbf{O_l}} = (a_1, a_2, a_3)^T$.

Substitution $\mathbf{x_r}$ with Equation 2.41 yields:

$$o_r\vec{x}_r = \frac{1}{\lambda_r}[\mathbf{L_r}\widetilde{\mathbf{O_l}}]_\times(\mathbf{H}\widetilde{\mathbf{x_l}}) = \mathbf{F}\widetilde{\mathbf{x_l}} \tag{2.47}$$

where $\mathbf{F}$ is called the fundamental matrix (*Zhang et al.*, 1995b; *Hartley and Zisserman*, 2003):

$$\mathbf{F} = \frac{1}{\lambda_r}[\mathbf{L_r}\widetilde{\mathbf{O_l}}]_\times\mathbf{H} \tag{2.48}$$

Substitution $o_r\vec{x}_r$ in Equation 2.42 with Equation 2.47 yields:

$$\widetilde{\mathbf{x_r}}^T\mathbf{F}\widetilde{\mathbf{x_l}} = \mathbf{0} \tag{2.49}$$

Without knowing the perspective matrices $\mathbf{L_l}$ and $\mathbf{L_r}$, the fundamental matrix $\mathbf{F}$ can be derived with at least 8 control points identified based on image features. If we choose a point on the left view, Equation 2.49 gives a line (i.e. the epipolar line). Therefore, the fundamental matrix can constrain the positions of the correspondences. See Figure 2.7 for an example. It is usually used after intensity- or texture-based image matching to remove false matches (*Zhang et al.*, 1995b).

The fundamental matrix $\mathbf{F}$ also reduces the traditional correlation-based image matching from 2D searching in the image plane to 1D searching along epipolar lines (see Section 2.4.1 for matching). Due to the convenience and significant improvement in the computational efficiency, $\mathbf{F}$ is widely used in stereo mapping and dense reconstruction (*Zhang et al.*, 1995b; *Furukawa et al.*, 2010).

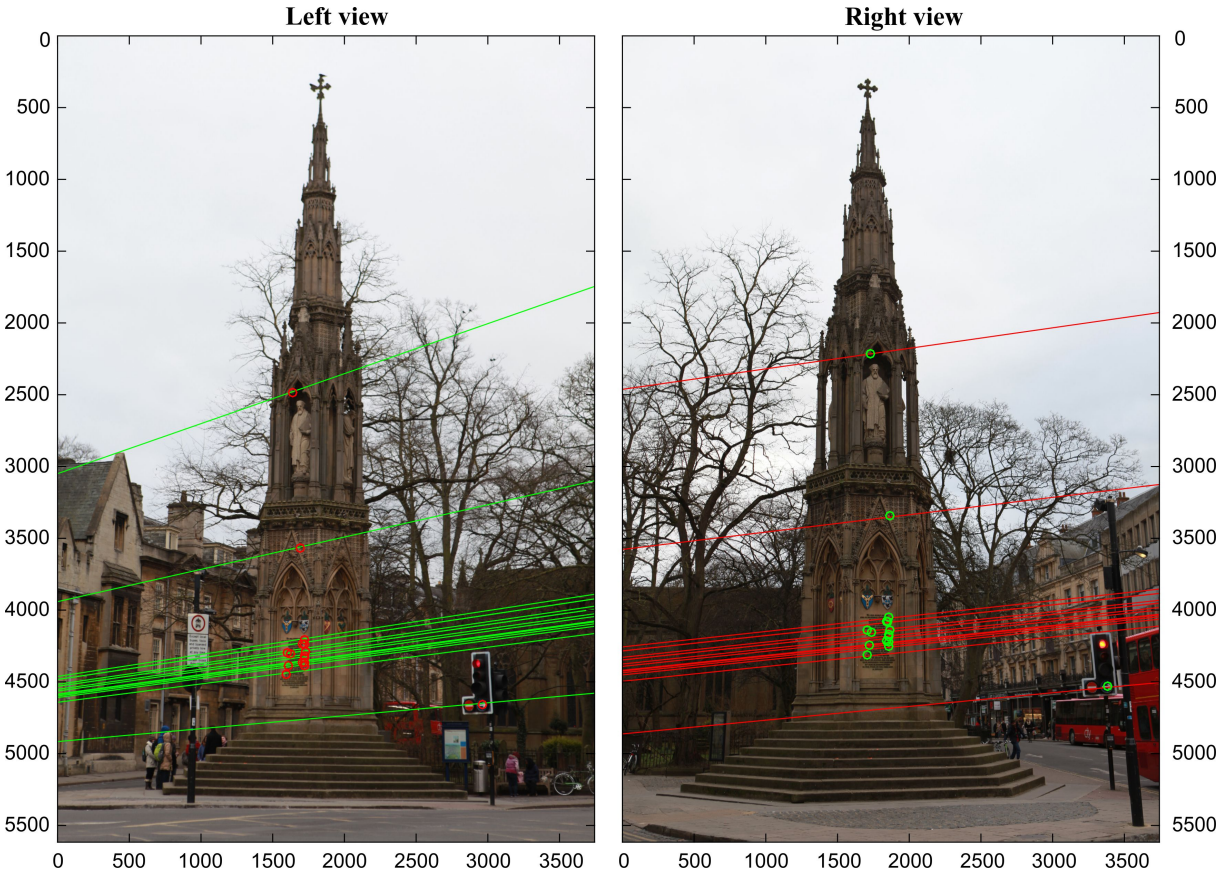


Figure 2.7: Epipolar lines in two photos of the Martyrs' Memorial in central Oxford taken from different viewpoints. A feature in the left view (red points) corresponds to a line in the right view (red lines, i.e. epipolar line), and the matching feature in the right view (green points) lies on the epipolar line. This geometric relationship is determined by the fundamental matrix **F**.

2.4 3D Reconstruction

Photogrammetry can be used to construct high-resolution digital elevation models (DEMs), from which earth scientists are able to measure offsets of geomorphological features and retrieve the 3D deformation in earthquakes. In principle, a pair of stereo images are needed for 3D reconstruction. As shown in Figure 2.8, two images covering the same area are acquired with sensors S_1 and S_2. Image points $a_1(x_1, y_1)$ and $a_2(x_2, y_2)$ are related to the corresponding ground point $A(X, Y, Z)$ via some sensor model:

$$x_1 = \mathcal{F}_1(X, Y, Z),\ y_1 = \mathcal{F}_2(X, Y, Z) \tag{2.50}$$

$$x_2 = \mathcal{F}_3(X, Y, Z),\ y_2 = \mathcal{F}_4(X, Y, Z) \tag{2.51}$$

where $\mathcal{F}_i$ $(i = 1, 2, 3, 4)$ denotes the sensor model.

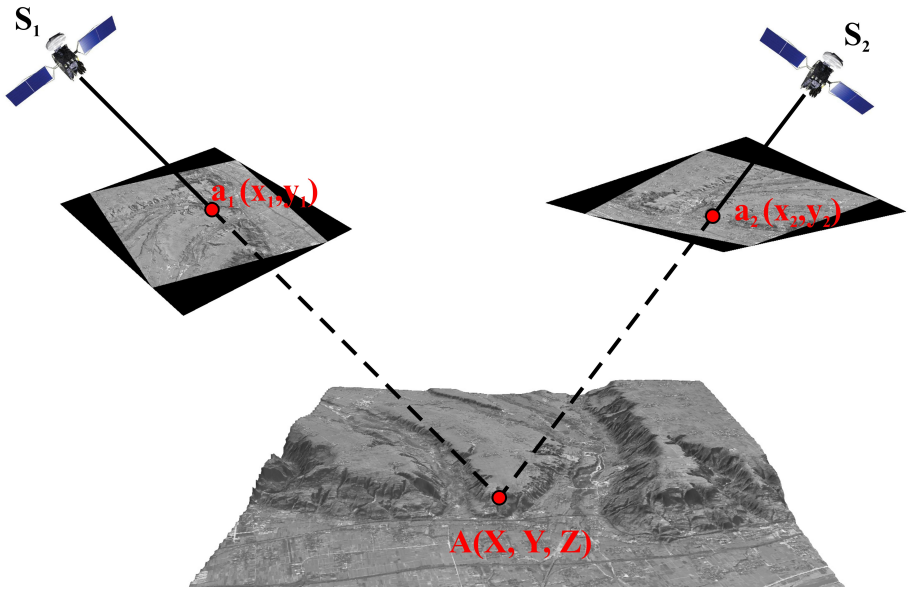


Figure 2.8: 3D reconstruction based on two images. S_1 and S_2 indicate the optical centre of the sensors. Perspective projection means that the object A, the optical centre of the camera S_1 and the corresponding image point a_1 are collinear (A, S_2 and a_2 are collinear as well). The ground coordinates of A can be estimated by finding the intersection of the lines S_1a_1 and S_2a_2.

The ground coordinates of point A(X, Y, Z) can be estimated by solving the four equations using a least squares adjustment. In practice, three or more images may be used. As explained in Section 2.2, ground- or aerial-based photos use rigorous sensor models while most satellite images use the RFM, so the algorithms for 3D reconstruction from these different data sets are different. Furthermore, to investigate historical earthquakes (e.g., the 1978 Tabas earthquake in Iran) where photos are non-digital, additional processing is needed.

2.4.1 Satellite Stereo Imagery

Most satellite images including Pleiades, SPOT-6/7, WorldView and GeoEye use the RFM. In this section, I focus on the forward RFM because it has been shown by *Tao and Hu* (2002) that 3D reconstruction based on the forward form is more accurate than the inverse form. Using the forward RFM, Equations 2.50 and 2.51 can be rewritten as:

$$x_1 = \frac{P_{1,1}(X,\, Y,\, Z)}{P_{2,1}(X,\, Y,\, Z)},\; y_1 = \frac{P_{3,1}(X,\, Y,\, Z)}{P_{4,1}(X,\, Y,\, Z)} \tag{2.52}$$

$$x_2 = \frac{P_{1,2}(X,\, Y,\, Z)}{P_{2,2}(X,\, Y,\, Z)},\; y_2 = \frac{P_{3,2}(X,\, Y,\, Z)}{P_{4,2}(X,\, Y,\, Z)} \tag{2.53}$$

where P is a polynomial function defined as Equation 2.34.

Using a Taylor expansion, the first-order approximations can be derived:

$$x_1 = \hat{x}_1 + \frac{\partial x_1}{\partial X}dX + \frac{\partial x_1}{\partial Y}dY + \frac{\partial x_1}{\partial Z}dZ,\ y_1 = \hat{y}_1 + \frac{\partial y_1}{\partial X}dX + \frac{\partial y_1}{\partial Y}dY + \frac{\partial y_1}{\partial Z}dZ \tag{2.54}$$

$$x_2 = \hat{x}_2 + \frac{\partial x_2}{\partial X}dX + \frac{\partial x_2}{\partial Y}dY + \frac{\partial x_2}{\partial Z}dZ,\ y_2 = \hat{y}_2 + \frac{\partial y_2}{\partial X}dX + \frac{\partial y_2}{\partial Y}dY + \frac{\partial y_2}{\partial Z}dZ \tag{2.55}$$

where

$$\frac{\partial x}{\partial X} = \frac{\frac{\partial P_1}{\partial X}P_2 - P_1\frac{\partial P_2}{\partial X}}{P_2^2},\ \frac{\partial y}{\partial X} = \frac{\frac{\partial P_3}{\partial X}P_4 - P_3\frac{\partial P_4}{\partial X}}{P_4^2} \tag{2.56}$$

$$\frac{\partial x}{\partial Y} = \frac{\frac{\partial P_1}{\partial Y}P_2 - P_1\frac{\partial P_2}{\partial Y}}{P_2^2},\ \frac{\partial y}{\partial Y} = \frac{\frac{\partial P_3}{\partial Y}P_4 - P_3\frac{\partial P_4}{\partial Y}}{P_4^2} \tag{2.57}$$

$$\frac{\partial x}{\partial Z} = \frac{\frac{\partial P_1}{\partial Z}P_2 - P_1\frac{\partial P_2}{\partial Z}}{P_2^2},\ \frac{\partial y}{\partial Z} = \frac{\frac{\partial P_3}{\partial Z}P_4 - P_3\frac{\partial P_4}{\partial Z}}{P_4^2} \tag{2.58}$$

and $\hat{x}$ and $\hat{y}$ are the initial approximate image coordinates that are determined by the initial approximate ground coordinates $(\hat{X},\ \hat{Y},\ \hat{Z})$:

$$\hat{x} = \frac{P_1(\hat{X},\ \hat{Y},\ \hat{Z})}{P_2(\hat{X},\ \hat{Y},\ \hat{Z})},\ \hat{y} = \frac{P_3(\hat{X},\ \hat{Y},\ \hat{Z})}{P_4(\hat{X},\ \hat{Y},\ \hat{Z})} \tag{2.59}$$

The weighted least squares inversion is given by:

$$\begin{pmatrix} \frac{\partial x_1}{\partial X} & \frac{\partial x_1}{\partial Y} & \frac{\partial x_1}{\partial Z} \\ \frac{\partial y_1}{\partial X} & \frac{\partial y_1}{\partial Y} & \frac{\partial y_1}{\partial Z} \\ \frac{\partial x_2}{\partial X} & \frac{\partial x_2}{\partial Y} & \frac{\partial x_2}{\partial Z} \\ \frac{\partial y_2}{\partial X} & \frac{\partial y_2}{\partial Y} & \frac{\partial y_2}{\partial Z} \end{pmatrix} \begin{pmatrix} dX \\ dY \\ dZ \end{pmatrix} = \begin{pmatrix} x_1 - \hat{x_1} \\ y_1 - \hat{y_1} \\ x_2 - \hat{x_2} \\ y_2 - \hat{y_2} \end{pmatrix} \tag{2.60}$$

$$\mathbf{Ax} = \mathbf{b}$$

$$\mathbf{A}^T\mathbf{\Sigma^{-1}Ax} = \mathbf{A}^T\mathbf{\Sigma^{-1}b}$$

$$\mathbf{x} = \left[\mathbf{A}^T\mathbf{\Sigma^{-1}A}\right]^{-1}\mathbf{A}^T\mathbf{\Sigma^{-1}b}$$

where $\mathbf{\Sigma^{-1}}$ is the covariance matrix for errors in image coordinates.

The initial approximation of the coordinates $(\hat{X},\ \hat{Y},\ \hat{Z})$ can be calculated using the inverse RFM (*Tao and Hu*, 2002). The corrections dX, dY and dZ are computed iteratively via Equation 2.60 until the changes drop below a predefined threshold. The workflow is

illustrated in the following sections.

Matching points

The first step in 3D reconstruction from satellite stereo imagery is to find matching points, i.e. (x_1, y_1) and (x_2, y_2). This can be done in two ways: feature-based and pixel-by-pixel. Feature-based matching first selects distinctive "features" in images with automated feature detection algorithms, and then find the corresponding pixels (i.e. correspondences) in other images. These feature detection algorithms commonly use intensity, colour and texture of an object, e.g. corners of buildings and intersections of roads. Figure 2.9 shows an example of automatically identified image features. Pixel-by-pixel matching is done on each individual pixel, without pre-selecting image features and thus giving more points. For each feature or pixel, various matching methods can be applied to find its correspondence in another image.

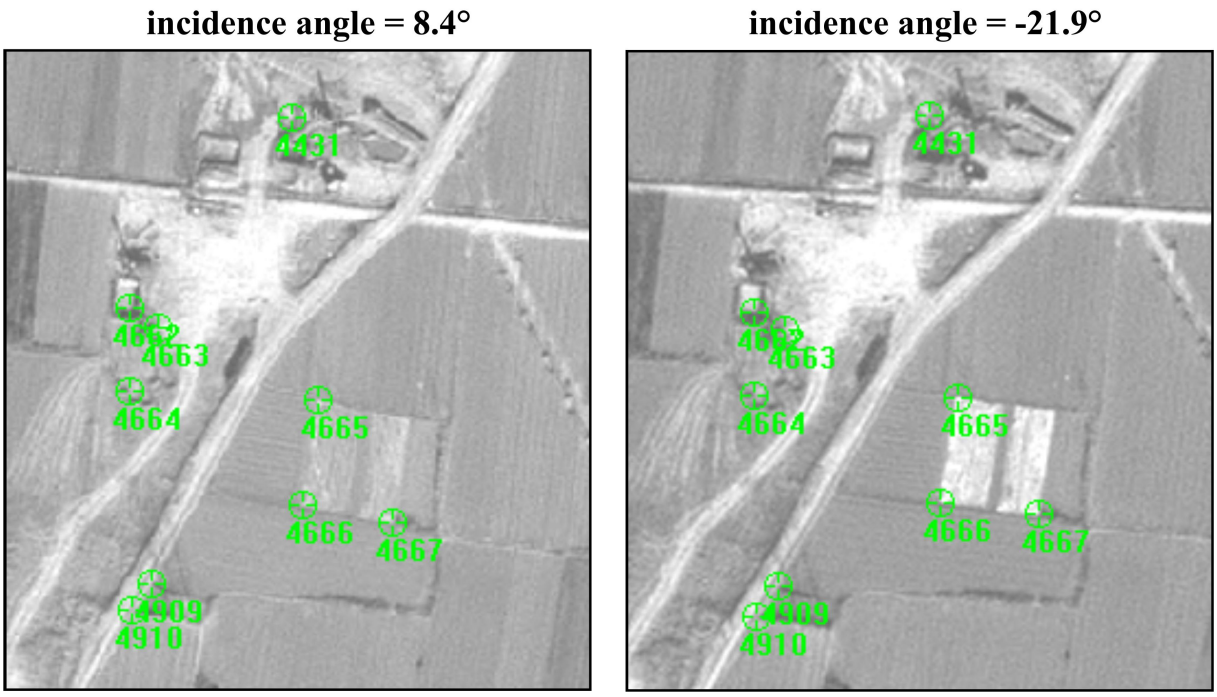


Figure 2.9: Matching features (i.e. correspondences) in a pair of Pleiades stereo imagery that cover part of the Weihe graben in northern China. The correspondences are used to estimate the 3D ground coordinates via Equations 2.54–2.60.

In the procedure of matching, a pixel (x', y') to be matched (template pixel, $\mathbf{T}$) is described by its surrounding pixels within a window (template) (Figure 2.10), usually 3×3 to 9×9 pixels. Note that the images can be intensity images or their Fourier transforms. A specific

algorithm (listed below) treats every pixel (x, y) in the other image (source image, **I**) as a potential candidate, and by "sliding" the template across the source image, it finds the best match through evaluating the "closeness" between the template pixel and the candidates. The closeness can be defined by the normalised cross-correlation (*Gonzales et al.*, 2004):

$$C(x,y) = \frac{\sum(T(x',y') \cdot I(x,y))}{\sqrt{\sum T(x',y')^2 \cdot \sum I(x,y)^2}} \tag{2.61}$$

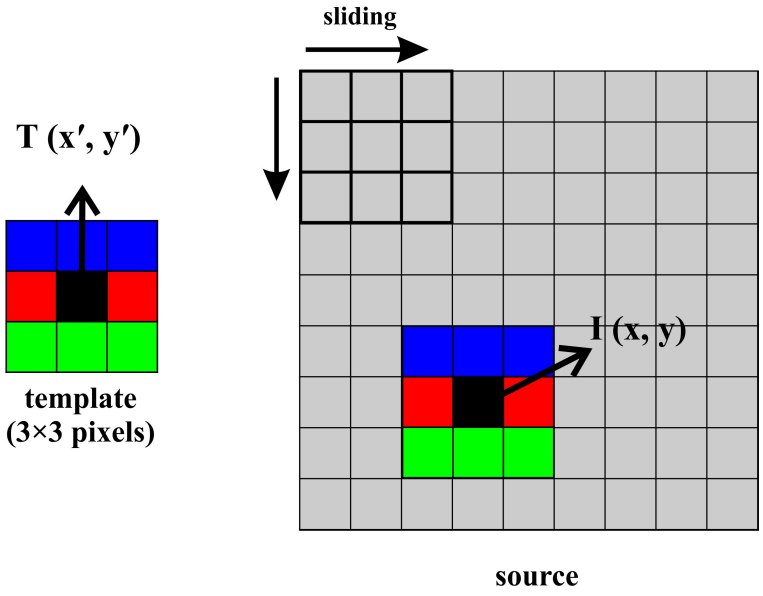


Figure 2.10: Template matching. The correspondence of a point (x', y') on the other image is found by "sliding" the template across the source image. The "closeness" (can be defined by Equations 2.61) is computed between the template pixel and every pixel in the source image. If the "closeness" is above a predefined threshold, e.g. 0.7 for cross-correlation, then the pixel in the source image is regarded as a matching point, $I(x, y)$.

A perfect match results in a normalised cross-correlation of 1. In practice, a cross-correlation of 0.7 is usually used as a threshold for a good match in satellite-based photogrammetry.

Estimation of ground coordinates

After obtaining the correspondences, the corresponding ground coordinates can be determined by solving Equation 2.60. As the RFM is non-linear, the initial estimates of the ground coordinates $(\hat{X}, \hat{Y}, \hat{Z})$ are needed in the solution. For each matching point, the

inverse RFM is used to estimate the initial ground coordinates:

$$\hat{X} = \frac{P_{51}(x_1, y_1, \hat{Z})}{P_{61}(x_1, y_1, \hat{Z})}, \hat{Y} = \frac{P_{71}(x_1, y_1, \hat{Z})}{P_{81}(x_1, y_1, \hat{Z})} \tag{2.62}$$

$$\hat{X} = \frac{P_{52}(x_2, y_2, \hat{Z})}{P_{62}(x_2, y_2, \hat{Z})}, \hat{Y} = \frac{P_{72}(x_2, y_2, \hat{Z})}{P_{82}(x_2, y_2, \hat{Z})} \tag{2.63}$$

where $\hat{Z}$ is assumed constant.

With the initial ground coordinates ($\hat{X}$, $\hat{Y}$, $\hat{Z}$), the forward RFM is used to calculate the corresponding image coordinates ($\hat{x_1}$, $\hat{y_1}$) and ($\hat{x_2}$, $\hat{y_2}$) via Equation 2.59. Because the initial ground coordinates are inaccurate, the estimated image coordinates ($\hat{x_1}$, $\hat{y_1}$) and ($\hat{x_2}$, $\hat{y_2}$) are different from their true positions (x_1, y_1) and (x_2, y_2). This difference is used to calculate the corrections of the ground coordinates (dX, dY, dZ) via Equation 2.60. New estimates of the ground coordinates ($\hat{X}+dX$, $\hat{Y}+dY$, $\hat{Z}+dZ$) are used to refine the estimation of the image coordinates ($\hat{x_1}$, $\hat{y_1}$) and ($\hat{x_2}$, $\hat{y_2}$). The optimal estimation of the ground coordinates (i.e. changes in dX, dY and dZ drop below a predefined threshold) is normally achieved after a few iterations.

2.4.2 Frame Photos

Ground- and aerial-based photos provide alternative means of recovering the 3D ground surface. Old aerial photos also allow us to study earthquakes back to the early 1970s (*Burnett*, 2012; *Zhou et al.*, 2016b). The mathematical theory of 3D reconstruction based on frame photos is similar to that described in Section 2.4.1 (but with the rigorous sensor models described in Section 2.2.1). In the case of 2 or 3 frame photos, they can be treated as "satellite stereo images", but more often, tens or even hundreds of photos are collected and used to produce a very high-resolution DEM. In the past decade, many algorithms have been developed to deal with the increasingly large data sets. In this section, I will use some examples to illustrate the state-of-the-art algorithms for 3D reconstruction from frame photos.



Figure 2.11: An example of fiducial markers in a KH-9 image of Tabas (Iran) acquired on the 26th November, 1974. The centre of the white crosses at the four corners of the image can be used to derive the coefficients in Equations 2.64 and 2.65.

Digitisation

As digital cameras are innovations from the end of the last century, there will be situations in which the photos are film-based rather than digital. In order to process these film-based photos with modern automated approaches, they are usually digitised with high-resolution photo scanners. Scanning error would occur due to the misalignment of the scanline and the photo on the scanner. As a result, the digitised image is usually misoriented. Interior orientation needs to be done to eliminate such error in the scanning process. The error can be modelled with an affine transformation as:

$$x_s = a_0 + a_1 x + a_2 y \tag{2.64}$$

$$y_s = b_0 + b_1 x + b_2 y \tag{2.65}$$

where a_0, a_1, a_2, b_0, b_1, and b_2 describe a linear transformation between the original scan (x, y) and the corrected image coordinates (x_s, y_s).

The parameters can be estimated by using the fiducial markers at the corners of a photo (e.g. in Figure 2.11) as control information. Knowing their positions in the predefined photo coordinate system and the measured positions in the digitised image, the parameters (a_0, a_1, a_2, b_0, b_1, and b_2) can be derived using at least 4 markers with a least squares estimation.

Sparse Reconstruction

To handle large data sets in 3D reconstruction, the key technique is Structure-from-Motion (SfM) (*Bolles et al.*, 1987), which uses a large sequence of photos acquired from multiple viewpoints to construct a 3D model of the target. The basic theory is similar to that described in traditional photogrammetry (Equations 2.50 and 2.51), but instead of using the given parameters in the sensor model (Equations 2.4 and 2.5), or manually selected feature points and their correspondences, SfM estimates the orientation parameters using automatically identified matching points (*Lowe*, 1999; *Triggs et al.*, 2000). In the development of SfM algorithms, Bundler (*Snavely et al.*, 2008b) became the most well-known SfM software for automated 3D reconstruction from large, unstructured internet photo collections. The major contribution of *Snavely et al.* (2006, 2008b) is the pipeline proposed for sorting unstructured images which is a critical step in processing close-range photos. As a brief summary, the proposed workflow of Bundler is given in Figure 2.12.

For unstructured photo collections, the first step is to build the relationship between these photos through correspondences. To obtain correspondences, pixels with good features need to be extracted and related to the corresponding pixels in other photos. A good feature should have the following properties: repeatability (the same feature can be detected in many different photos of the same scene), distinctiveness (distinguishable from a large database of objects), locality (features are local so that they are robust to occlusion), quantity (hundreds or thousands in a single image), and invariance to geometric and photometric differences between two views. For aerial and satellite images, as the flying height and view angle do not change significantly during the flight, the variation in the scale of objects in different images is ignorable, so it is common to use intensity, colour and texture for describing image features (Figure 2.9). However, due to the significant variation in view angles and distances to an object in close-range photos (Figure 2.7), the intensity, scale and shape of the object also show significant variations in different photos (*Tuytelaars and Mikolajczyk*, 2008). Therefore, the invariance to geometric and photometric differences between two views becomes important for describing features in close-range photos. Many invariant feature detection methods have been proposed to address this issue, among which scale invariant feature transform (SIFT) feature is re-

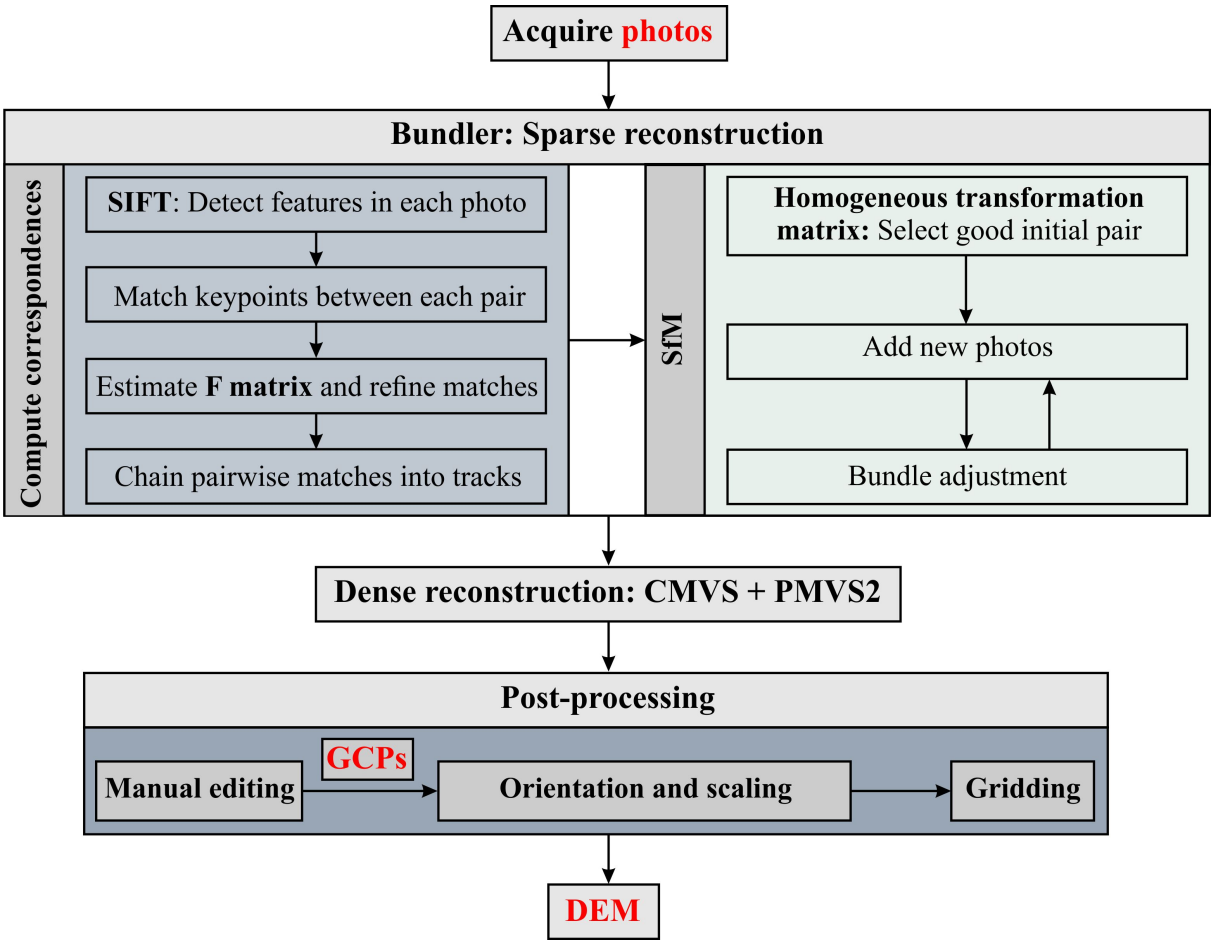


Figure 2.12: The workflow of 3D reconstruction from frame photos. Scale invariant feature transform (SIFT) applies a 4-stage approach to describe image features (*Lowe*, 2004). **F matrix** is the fundamental matrix defined by Equation 2.48 in Section 2.3. A **homogeneous transformation matrix** is computed for each pair of photos using the correspondences. The pair with the largest misfit is selected as the initial pair in SfM. The remaining photos are added successively. After sparse reconstruction, Clustering view for Multi-View Stereo (**CMVS**) and Patch-based Multi-View Stereo (**PMVS2**) are used to reconstruct a denser point cloud. Post-processing including manual editing, orientation and scaling to generate a DEM from the point cloud.

garded the best feature descriptor (an example of SIFT features in a photo is shown in Figure 2.13).

The SIFT algorithm is a 4-stage approach (readers are referred to *Lowe* (2004) for more details of SIFT):

(1) Scale-space extrema detection

This step defines a "scale space" function for identifying the locations and scales of potential features (keypoints):

$$L(x, y, \sigma) = G(x, y, \sigma) * I(x, y) \tag{2.66}$$

where $*$ is the convolution operator, $I(x, y)$ is the input image, and $G(x, y, \sigma)$ is a Gaussian function using $\sigma = \sqrt{2}$:

$$G(x, y, \sigma) = \frac{1}{\sqrt{2\pi}\sigma} e^{-x^2/2\sigma^2} \tag{2.67}$$

One technique to detect stable keypoints is based on the difference of Gaussians between two images $D(x, y, \sigma)$ and $D(x, y, k\sigma)$, with scale k times the other:

$$D(x, y, \sigma) = L(x, y, k\sigma) - L(x, y, \sigma) \tag{2.68}$$

If $D(x, y, \sigma)$ for a point is the minimum or maximum compared to its 8 neighbours at the same scale $k\sigma$, and 9 neighbours at scales $(k-1)\sigma$ and $(k+1)\sigma$, this point is an "extremum" and thus a potential "keypoint".

(2) Keypoint localisation

The points extracted in the first step may have low contrast or be poorly localised on an edge; these points need to be excluded. All extrema with a function value $D(x, y, \sigma) \leq 0.03$ are discarded as they may be unstable with low contrast. For poorly defined extrema in $D(x, y, \sigma)$, the principal curvature across the edge would be much larger than that along it. If the ratio of the two principle curvatures at a point is larger than a threshold (10 in *Lowe* (2004)), the point is rejected. The principle curvatures are found by solving for the eigenvalues of the second-order Hessian matrix, $\overline{\mathbf{H}}$:

$$\overline{\mathbf{H}} = \begin{pmatrix} \frac{\partial^2 D}{\partial x^2} & \frac{\partial^2 D}{\partial x \partial y} \\ \frac{\partial^2 D}{\partial y \partial x} & \frac{\partial^2 D}{\partial y^2} \end{pmatrix} \tag{2.69}$$

(3) Orientation Assignment

This step assigns consistent orientations to the keypoints from the previous step. As the keypoints are described by their gradient magnitude $m(x, y)$ and orientation $\theta(x, y)$, they become invariant to geometric differences in different views:

$$m(x, y) = \sqrt{(L(x+1, y) - L(x-1, y))^2 + (L(x, y+1) - L(x, y-1))^2} \tag{2.70}$$

$$\theta(x, y) = \tan^{-1} \frac{L(x, y+1) - L(x, y-1)}{L(x+1, y) - L(x-1, y)} \tag{2.71}$$

The calculations are done for every pixel in a neighboring region around the keypoint. An orientation histogram with 36 bins is formed (each bin covers 10°). Each pixel is weighted by its gradient magnitude and by a Gaussian-weighted circular window with 1.5σ and added to the histogram (*Lowe*, 2004). The peaks in the histogram is the dominant orientation, which will be assigned to the image pixel.

(4) Keypoint descriptor

Previous steps determine keypoints at a particular scale $\sigma = \sqrt{2}$ and assign orientations $\theta(x, y)$ to its neighbouring pixels. The next step is to generate a descriptor vector for each keypoint, which should be highly distinctive and partially invariant to the remaining variations such as illumination. Firstly, a 16×16 neighbourhood around a keypoint is divided into 16 subblocks of 4×4 size. For each subblock, a 8-bin orientation histogram covering the 360° range of orientations is calculated. A total of 128 (8 bin values per subblock $\times$ 16 subblocks) bin values are used to represent the keypoint descriptor (a vector that consists of those 128 elements). These resulting vectors are termed "SIFT keys" and used for matching.

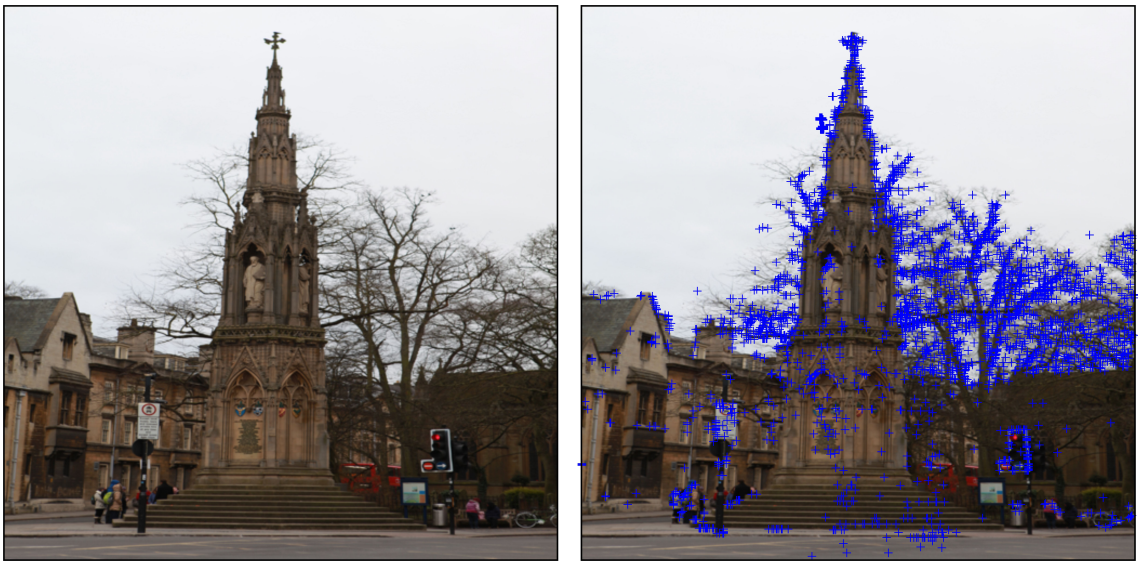


Figure 2.13: SIFT features in a photo (blue crosses) after eliminating those with low contrast or poorly localised on an edge.

Bundler first detect SIFT features in all photos, and match these features based on their "SIFT keys" (see Section 2.4.1 for matching). To refine the matches, the fundamental matrix (see Section 2.3) of each pair of photos is derived and applied to filter false matches. The filtered correspondences are connected through an image "connectivity graph", which



Figure 2.14: Connectivity graph. Coloured dots represent correspondences. If the number of correspondences between two images exceeds a threshold, an undirected arc is drawn to connect the two images. In the end, an image "connectivity graph" will be created to track all the correspondences.

is an undirected graph indicating the overlap information between images. The connectivity graph takes each image as a node. An undirected arc is created between two images if there is enough overlap between them (as shown in Figure 2.14). Usually the number of correspondences is used to decide whether the two images should be connected or not.

Bundler also adopts an incremental approach for SfM, i.e. adding the photos sequentially based on the connectivity graph generated in the first stage (*Snavely et al.*, 2008b). The most critical step in this approach is selecting the first pair of photos (*Snavely et al.*, 2008b). Because the connectivity between the processed photos and the remaining photos may be broken due to an insufficient number of correspondences, the initial pair should include as many correspondences as possible (at least 100, *Snavely et al.* (2008b)). A stereo

pair with short baseline may lead to very low reconstruction accuracy. The extreme case is that photos captured at the same locations (i.e. zero baseline) cannot reconstruct the 3D scene. Therefore, long baseline is preferred for the first pair. Given that the correspondences in the photos captured at the same location would yield a homogeneous transformation, the homogeneous transformation matrix of the correspondences is used to evaluate the length of the baseline. Large errors in the fit for the homogeneous transformation matrix indicate long baselines. In addition, a flat scene would also result in a homogeneous transformation, so the homogeneous transformation matrix can also be used to exclude photos with less depth. Consequently, the selection of first pair is also based on the error in the fit for the homogeneous transformation matrix (*Snavely et al.*, 2008b).

The initial pair is selected based on the criterion that the error in the fit for the homogeneous transformation matrix is the largest among all the pairs with more than 100 matches. The following step is to reconstruct the initial 3D scene. As shown in Figure 2.15, images 1 and 2 are the initial pair. O_1 and O_2 indicate the perspective centres. X_1 and X_2 are the matching points. In the camera coordinate system of the left view, vector $\overrightarrow{O_1X_1}$ can be written as:

$$\overrightarrow{O_1X_1} = \begin{pmatrix} x_1 - x_1^0 \\ y_1 - y_1^0 \\ -f_1 \end{pmatrix} \tag{2.72}$$

where x_1^0, y_1^0 and f_1 are the interior orientation parameters of camera 1.

Similarly, in the camera coordinate system of the right view, we have:

$$\overrightarrow{O_2X_2} = \begin{pmatrix} x_2 - x_2^0 \\ y_2 - y_2^0 \\ -f_2 \end{pmatrix} \tag{2.73}$$

The camera coordinate system of the right view can be transformed to the coordinate

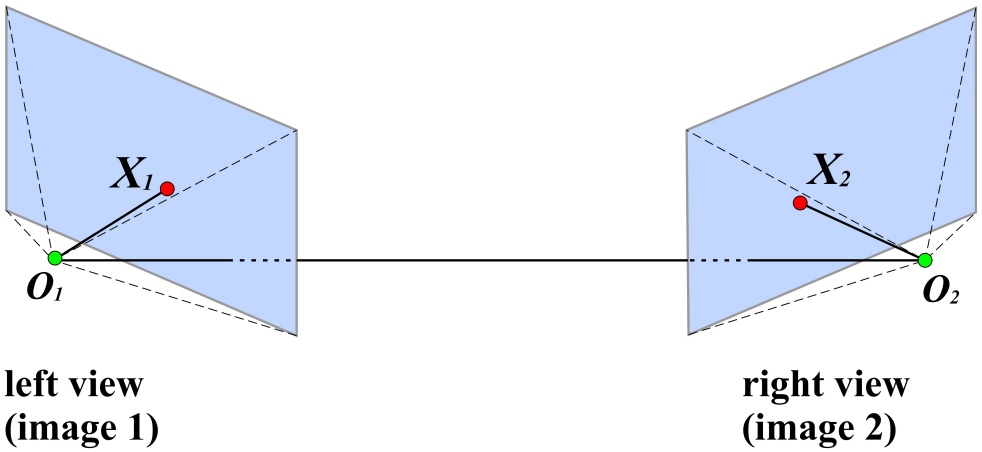


Figure 2.15: Relative orientation. O_1 and O_2 indicate the perspective centres. X_1 and X_2 are the matching points. As $\overrightarrow{O_1X_1}$ and $\overrightarrow{O_2X_2}'$ must intersect, $\overrightarrow{O_1O_2}$, $\overrightarrow{O_1X_1}$, and $\overrightarrow{O_2X_2}'$ are coplanar.

system of the left view via a rigid-body transformation, i.e.

$$\overrightarrow{O_2X_2}' = \mathbf{R}^{-1} \cdot \overrightarrow{O_2X_2} + \overrightarrow{O_1O_2} \tag{2.74}$$

where $\overrightarrow{O_2X_2}'$ is $\overrightarrow{O_2X_2}$ expressed in the coordinate system of the left view, $\overrightarrow{O_1O_2}$ is the baseline between the two cameras, $\mathbf{R}$ is a rotation matrix that can be determined by three rotation angles of the right view with respect to the left view.

As X_1 and X_2 are the matching points, $\overrightarrow{O_1X_1}$ and $\overrightarrow{O_2X_2}'$ must intersect, and hence they are coplanar. Therefore, we have:

$$(\overrightarrow{O_1O_2} \times \overrightarrow{O_1X_1}) \cdot \overrightarrow{O_2X_2}' = 0 \tag{2.75}$$

$$(\overrightarrow{O_1O_2}_{\times} \cdot \overrightarrow{O_1X_1})^T \cdot \mathbf{R}^T \cdot \overrightarrow{O_2X_2} = 0 \tag{2.76}$$

$$\overrightarrow{O_2X_2}^T \cdot (\mathbf{R} \cdot \overrightarrow{O_1O_2}_{\times}) \cdot \overrightarrow{O_1X_1} = 0 \tag{2.77}$$

In practice, we select the camera coordinate system of the first camera to be the reference coordinate system, and determine the positions and attitudes of all other cameras in this system. After estimating the exterior orientation parameters of camera 2 via Equation 2.77, we can triangulate the object for each matching point in the first pair and reconstruct the initial 3D scene.

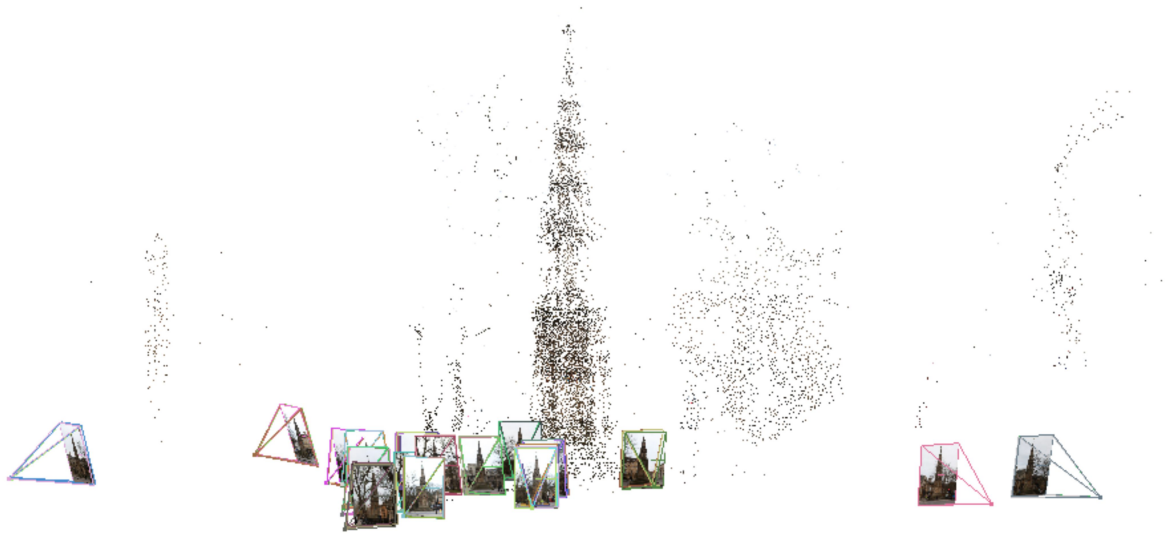


Figure 2.16: Sparse reconstruction solves the orientation parameters of all the cameras and generates a sparse point cloud. The example is from the Martyrs' Memorial in central Oxford.

The remaining photos are added successively based on the number of reconstructed correspondences in the existing scene. The photo with the largest number of correspondences in the scene is added first. Since we have estimated the ground coordinates of the correspondences in the first pair, we can use those correspondences to estimate the orientation of the third image with the Direct Linear Transform (DLT in Section 2.2.1) algorithm directly. To enhance the robustness of the estimation, a random sample consensus (RANSAC, *Fischler and Bolles* (1981)) procedure is applied on the DLT algorithm to find the best estimate and remove the outliers simultaneously. With known exterior orientations, features with more than two correspondences can be reconstructed and new features will be added to the 3D scene. Furthermore, bundle adjustment is applied each time after adding one photo to improve the accuracy of the existing estimates through global optimisation. In the end, the orientation parameters of all the cameras are solved, and a sparse point cloud representing the 3D scene (Figure 2.16) is generated.

Dense Reconstruction

SfM is able to recover the orientations of the cameras and generate a sparse point cloud of the scene. However, a denser point cloud would be needed in order to generate a high-resolution DEM. Dense reconstruction aims to find more matching points and generate a dense point cloud (Figure 2.17). This is done based on the epipolar geometry (Section 2.3),

which requires that the corresponding point of a pixel in one image lies on the epipolar line in another image. Dense reconstruction finds matching points through one-dimensional searching along the epipolar lines. In the past two decades, many dense reconstruction algorithms have been developed. Given the large data sets (hundreds to thousands of photos), the efficiency (time and space) of the algorithms is critical. Based on an on-line evaluation (`http://vision.middlebury.edu/mview/eval/`) (*Seitz et al.*, 2006), the algorithms proposed by *Furukawa and Ponce* (2010) and *Furukawa et al.* (2010) show consistently good accuracy and completeness for all different data sets.



Figure 2.17: Dense reconstruction generates a denser point cloud to represent the 3D object. The example is from the Martyrs' Memorial in central Oxford.

In order to reduce the computational and memory costs, *Furukawa and Ponce* (2010) used the connectivity graph produced in sparse reconstruction to divide the images into

small clusters based on the computational capacity of the computer, i.e. the Clustering Views for Multi-view Stereo (CMVS) module. Points are matched within each cluster in parallel. The resulting clusters are aligned after matching and thus giving a large number of correspondences. Then the Patch-based Multi-view Stereo (PMVS2) module divides the photos into cells and reconstructs at least one patch (a 3D rectangle) using the correspondences in each cell (*Furukawa et al.*, 2010). The density of the reconstructed point cloud depends on the size of the cells.

Post-processing

Manual editing of the dense point cloud is often needed in order to remove false matches and unwanted objects such as trees (Figure 2.18). To recover the absolute 3D coordinates of the object (X_T, Y_T, Z_T) in the ground space, a few control points are needed to solve the scale factor (μ), rotation (R_{ij}, i, $j = 1, 2, 3$) and translation (C_X, C_Y, C_Z) matrices in Equation 2.78. This process is called the Helmert transformation or seven-parameter transformation in geodesy (*Watson*, 2006). With a minimum of 3 points, the dense point cloud can be georeferenced, and then gridded to obtain a DEM.

$$\begin{bmatrix} X_T \\ Y_T \\ Z_T \end{bmatrix}_{absolute} = \mu \begin{bmatrix} R_{11} & R_{12} & R_{13} \\ R_{21} & R_{22} & R_{23} \\ R_{31} & R_{32} & R_{33} \end{bmatrix} \begin{bmatrix} X \\ Y \\ Z \end{bmatrix}_{relative} + \begin{bmatrix} C_X \\ C_Y \\ C_Z \end{bmatrix} \tag{2.78}$$

There are occasions when only heights of fault scarps or rectified image of palaeoseismic trench walls are wanted. In such cases, only the scale factor μ is needed. The simplest way to estimate μ would be identifying an object with known dimensions in the dense point cloud. For example, I used an orange notebook (20.8 cm long and 14.6 cm wide in Table 2.1) as the control information (Figure 2.18) to scale the 3D model of the scarp to the absolute ground space (7.5 m). The result shows that for a ∼10 m scarp, 3D reconstruction from field photos without any accurate ground control points can obtain an accuracy of ∼30 cm in that example.

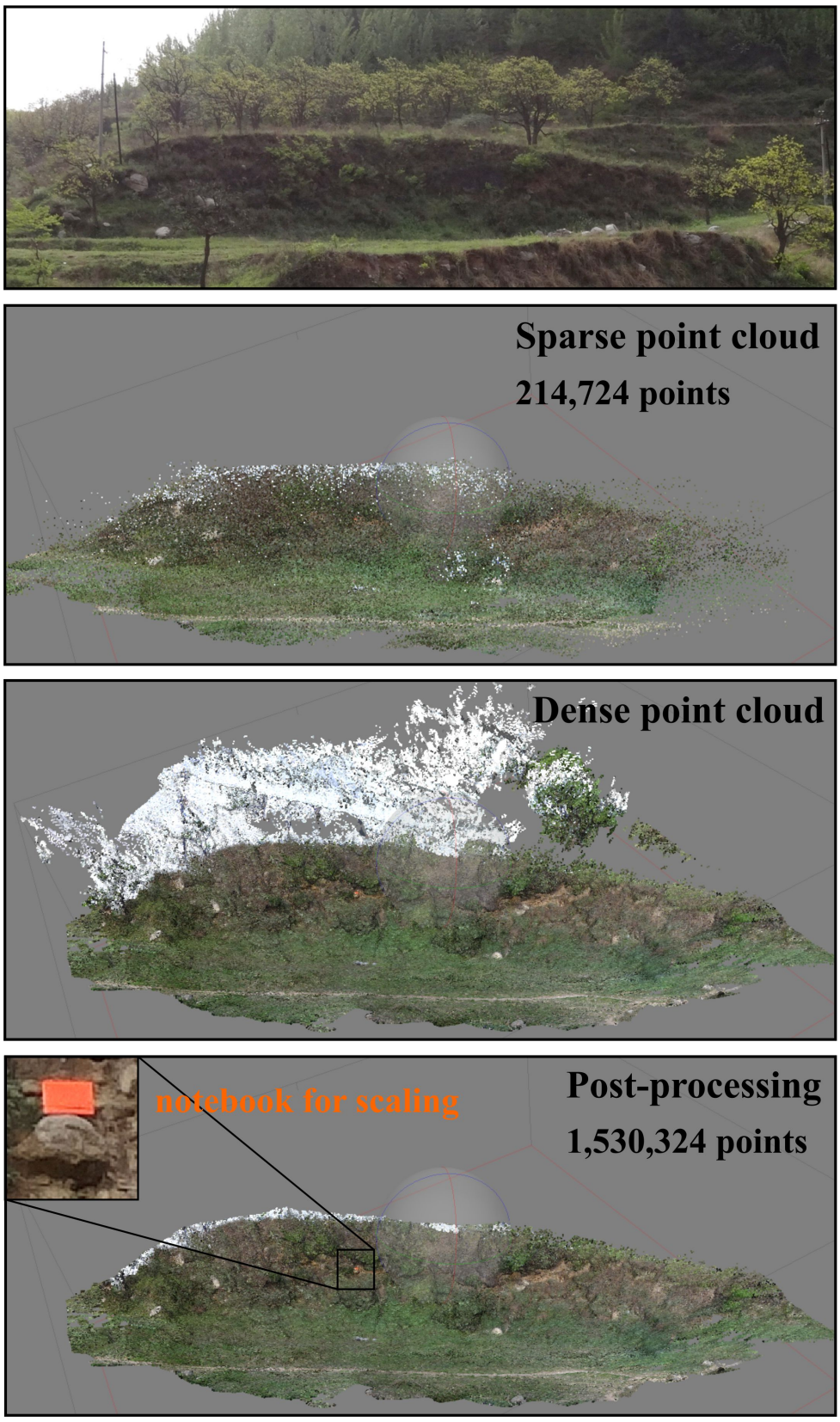


Figure 2.18: 3D reconstruction of a scarp from field photos. The scarp (34°01′24.874″N, 108°56′39.799″E) is located on the North Qinling fault in the Weihe graben in China. After dense reconstruction, manual editing is usually needed in the post-processing stage to remove false matches and unwanted objects. An orange notebook was used to estimate the scale factor μ. The height of the scarp is estimated to be ∼7.5 m.

Table 2.1: Scale factor estimated from a notebook (in Figure 2.18) of 20.8 cm long and 14.6 cm wide. The size of the notebook in the point cloud is 0.41 p and 0.28 p.

Length in point cloud (p)	True length (cm)	Scale factor (cm/p)	
0.282	14.6	51.7	50.8±1.5
0.417	20.8	49.9	
0.284	14.6	51.4	
0.414	20.8	50.2	

2.5 Orthorectification

Orthorectification is the process of projecting image points (x, y) onto the ground surface (X, Y), hence removing the effects of image perspective and terrain (*Novak*, 1992). This step is necessary before using the imagery for visual analysis. It can be done by either a direct or an indirect transformation (Figure 2.19). The direct orthorectification calculates the ground coordinates of each image pixel and fills that ground pixel with the grey value of the given image pixel. This method does not change the contrast and intensity of the original image, but it may result in gaps and overlaps in the ground grid, in which case resampling is needed to obtain a regular grid. The indirect orthorectification (which is more commonly used) defines a regular grid of the imaged ground first and then calculates the image coordinates of each ground pixel. The resulting image pixel is not necessarily in an integer position (as shown in Figure 2.19), so the grey value of that pixel is computed by interpolation of the grey values of the surrounding pixels.

For a given sensor model, taking the RFM for example, the direct orthorectification uses the inverse RFM (Equations 2.35 and 2.36), whereas the indirect orthorectification uses the forward RFM (Equations 2.32 and 2.33) (*Tao and Hu*, 2002). In both methods, elevation Z is needed. For stereo imagery, the elevation can be directly taken from the derived DEM. For monoscopic imagery, the elevation can be either assumed as constant or derived from an external DEM such as the Shuttle Radar Topography Mission (SRTM) DEM (*Farr et al.*, 2007).

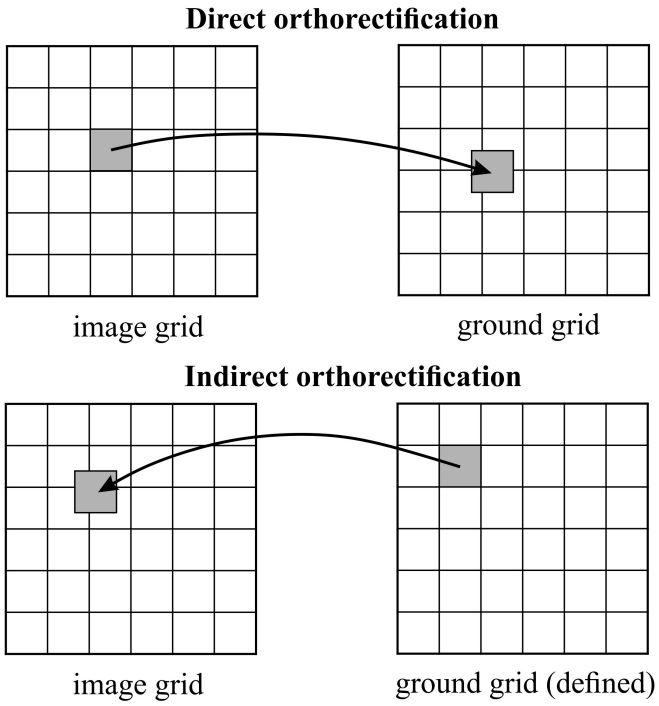


Figure 2.19: Cartoon showing the direct (top) and indirect (bottom) orthorectification, modified from *Novak* (1992).

2.6 Summary

Photogrammetry has been widely used in surveying and computer vision for the last 30 years, but its application in tectonic studies is relatively recent. The improvement of high-resolution imaging systems in the past 5 years, stereo imagery in particular, has made it possible for earth scientists to remotely measure 3D surface deformation at sub-metre scale. However, the utility of VHR stereo imagery (including satellite and aerial photos) in active tectonics has not yet been fully assessed. I contribute to assessing the capability of VHR stereo imagery, by determining earthquake deformation from four different types of earthquakes (different in sense of slip and date of the event) in Mexico (Chapter 3), Pakistan (Chapter 4), Iran (Chapter 5) and China (Chapter 6).

Chapter 3

Assessing the Ability of Pleiades Stereo Imagery to Determine Height Changes in Earthquakes

Adapted from Zhou, Y., B. Parsons, J. R. Elliott, I. Barisin, and R. T. Walker (2015), Assessing the ability of Pleiades stereo imagery to determine height changes in earthquakes: A case study for the El Mayor-Cucapah epicentral area, *Journal of Geophysical Research: Solid Earth, 120*(12), 8793-8808, doi:10.1002/2015JB012358.

3.1 Introduction

Late Quaternary fault activity is recorded in the landscape in the form of fault scarps (*Wallace*, 1977; *Hanks et al.*, 1984; *Avouac and Peltzer*, 1993; *Oskin et al.*, 2007), and displacements of landforms such as river channels and terraces (*Wesnousky et al.*, 1999; *Cowgill*, 2007); these pieces of evidence provide important information about past earthquakes and potentially characterise future seismic events that are likely to occur (*Gold and Cowgill*, 2011; *Oskin et al.*, 2012). Until relatively recently, such evidence could only be investigated in the field, but the short spatial scale field observations may have limited our understanding of fault behaviour in continental regions and therefore the estimation of the associated seismic hazard (*Jackson*, 2001; *England and Jackson*, 2011; *Oskin et al.*, 2012; *Zhang*, 2013). In the last few decades, remote sensing has emerged as a powerful tool

for studying active faulting over large scales. Satellite imagery (e.g., Landsat, ASTER and SPOT) has been used to identify fault geometries, surface ruptures and offsets in recent and ancient earthquakes (e.g., *Molnar and Tapponnier* 1975; *Fialko et al.* 2001; *Dominguez et al.* 2003; *Klinger et al.* 2005; *Avouac et al.* 2006; *Campbell et al.* 2015).

Matching of pre- and post-earthquake optical and radar imagery of the epicentral region has the potential to measure horizontal surface displacements at sub-pixel accuracy (*Leprince et al.*, 2007) and is often used to investigate coseismic deformation (e.g., *Fialko et al.* 2001; *Michel and Avouac* 2002; *Binet and Bollinger* 2005; *Avouac et al.* 2014). However, these approaches cannot measure height changes directly. Light detection and ranging (LiDAR) surveys have been a valuable tool for determining vertical offsets in earthquakes (*Oskin et al.*, 2012; *Elliott et al.*, 2012; *Ren et al.*, 2015), but its relatively high cost and low availability has limited its applicability, particularly as pre-earthquake LiDAR acquisitions are rare (*Nissen et al.*, 2014).

New generations of very high-resolution (VHR) satellites, e.g. Pleiades 1A/1B (0.7 m panchromatic), GeoEye-1 (0.41 m panchromatic), WorldView-1/2 (0.46 m panchromatic), and WorldView-3 (0.31 m panchromatic), allow rapid 3D reconstruction due to their short revisit time and stereo capability (*de Lussy et al.*, 2005; *Fraser and Ravanbakhsh*, 2009; *Mitchell and MacNabb*, 2010; *Poli and Toutin*, 2012; *Bernard et al.*, 2012). VHR stereo imagery can in principle measure surface topography with decimetric precision, comparable to LiDAR surveys, but at a much lower cost and with higher availability. Recent studies have evaluated the ability of VHR imagery to trace horizontal displacements (*Barnhart et al.*, 2011; *Stumpf et al.*, 2014) and Pleiades stereo imagery to map metre-scale elevation changes of glaciers (*Berthier et al.*, 2014). It is an open question as to how well 3D mapping based on VHR stereo imagery captures sub-metre height changes occurring in an earthquake in order to characterise 3D surface slip (*Zhou et al.*, 2015a) and fault geometry. The aim of this study is to assess the capability of the Pleiades satellites to determine such height changes.

The 2010 M_w 7.2 El Mayor-Cucapah earthquake (*Wei et al.*, 2011; *Oskin et al.*, 2012) is chosen as a case study because it is the first time that an earthquake rupture has been completely captured by differential LiDAR (*Oskin et al.*, 2012). We explore whether the

Pleiades stereo imagery also has the ability to capture the vertical ground displacement resulting from the earthquake at a decimetric level of accuracy. In addition, because the Pleiades satellite system is capable of acquiring 3 along-track images of the same area in a single pass (i.e. the tri-stereo mode) due to its steerable platform, we want to compare the quality of DEM generation from tri-stereo and bi-stereo modes, in order to compare their relative ability to accurately capture height changes in earthquakes.

Therefore, we requested acquisitions of Pleiades tri-stereo imagery for a 45 km × 7 km portion of the epicentral area of the El Mayor-Cucapah earthquake to coincide with the post-earthquake LiDAR DEM (Figure 3.1). We first produce 1-m resolution DEMs with the three combinations of bi-stereo images and the single tri-stereo mode. The uncertainties in the Pleiades DEMs are estimated using the post-earthquake LiDAR DEM assuming this is the most accurate. By differencing the Pleiades and pre-earthquake LiDAR DEMs, we map the surface deformation occuring in the earthquake, and then compare our result to the previous study that differenced the two LiDAR DEMs (*Oskin et al.*, 2012). Using the near-field surface deformation, we are also able to examine the fault geometry.

3.2 Overview of the 2010 El Mayor-Cucapah Earthquake

The 4 April 2010 El Mayor-Cucapah earthquake (Mexico) occurred on a complex, multi-segment fault system that forms part of the right-lateral transform boundary of the Pacific and North America plates in southern California (Figure 3.1) (*Hauksson et al.*, 2011). Geological and geodetic studies indicate that more than ∼90% of the plate motion (∼46 mm/yr) in the vicinity of the 2010 rupture is accommodated on the Laguna Salada, Cañada David, Cerro Prieto and Imperial fault systems (*Bennett et al.*, 1996; *Fletcher et al.*, 2014). However, the 2010 earthquake did not rupture any of these four, well-known faults (*Fletcher et al.*, 2014). Instead, the highly segmented rupture occurred on a series of obscure and, in part, previously unidentified faults (such as the Indiviso fault that is covered by thick sediments). Geodetic and seismological observations indicate that the rupture initiated with a normal faulting sub-event on the Indiviso fault and propagated

bi-laterally northward and southward with predominantly strike-slip motion (*Wei et al.*, 2011). The average right-lateral surface slip over the 120 km rupture length was 2 m (*Wei et al.*, 2011).

A low-resolution LiDAR survey (with a point density of 0.02 points/m^2) was undertaken from 31 July to 7 August 2006 by the Instituto Nacional de Estadistica y Geografia (INEGI) of Mexico, and 4 months after the earthquake in August 2010, high-resolution LiDAR data (with a point density of 9.12 points/m^2) were collected along the fault rupture by the National Center for Airborne Laser Mapping (NCALM) (*Oskin et al.*, 2012; *Glennie et al.*, 2014). The relative height accuracy of the post-earthquake LiDAR data is estimated to be 4-9 cm by comparing the elevation differences within areas of swath overlap (*Oskin et al.*, 2012). Elevation changes from differencing the two LiDAR DEMs reveal large distributed deformation over the structurally complex Sierra Cucapah area (*Oskin et al.*, 2012; *Glennie et al.*, 2014). The pre-earthquake LiDAR DEM was reprocessed by *Glennie et al.* (2014). Both the corrected pre- and post-earthquake LiDAR DEMs are freely available from `http://www.opentopography.org/`. In addition to the image-based studies of this earthquake, *Fletcher et al.* (2014) and *Teran et al.* (2015) investigated the surface rupture and fault structure in the field.

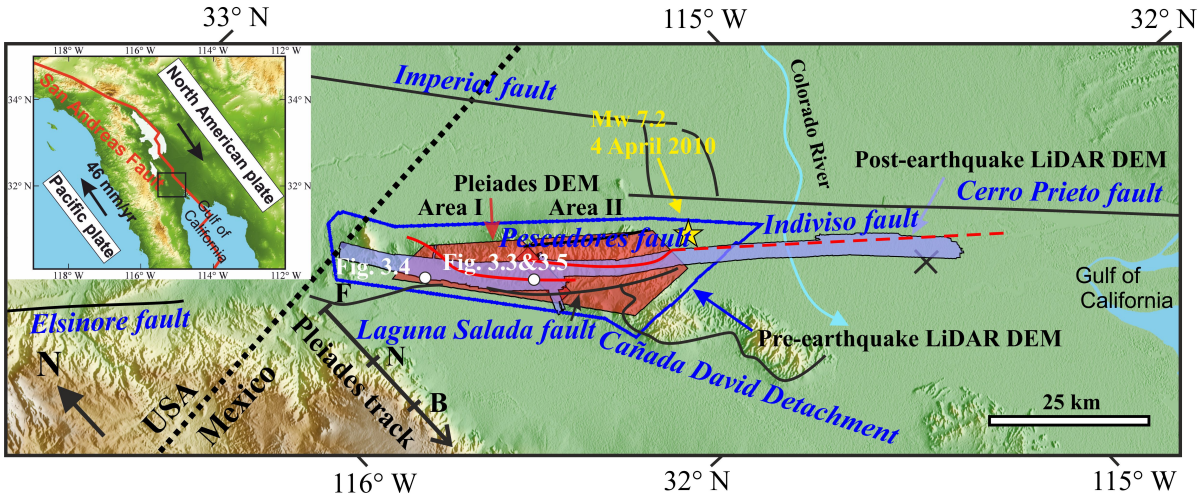


Figure 3.1: Tectonic setting of the El Mayor-Cucapah earthquake rupture. The 2010 El Mayor-Cucapah earthquake occurred on a complex, multisegment fault system which forms the right-lateral transform boundary of the Pacific and North America plates in southern California. The earthquake initiated on the Indiviso fault (yellow star) and ruptured bi-laterally. Two sets of Pleiades tri-stereo imagery were acquired in this study (marked as Area I and II by filled red polygon). These two sets of Pleiades imagery overlap at the northwestern end of the Pescadores fault (the dark red area). Forward (F) /Nadir (N) /Backward (B) orientations are marked on the Pleiades track. Pre- and post-earthquake LiDAR DEMs (downloaded from http://www.opentopography.org/) are marked by blue outline and filled purple polygons. White dots indicate the areas in Figures 3.3–3.5. Faults from *Fletcher et al.* (2014) are marked by red (the 2010 rupture) and black lines.

3.3 Data and Methods

3.3.1 Data Sets

The Pleiades satellite constellation consists of two identical satellites launched on 17/12/2011 (Pleiades 1A) and 02/12/2012 (Pleiades 1B), in sun-synchronous orbits (98.2° inclination) offset 180° from each other, which provide VHR optical images worldwide with a revisit interval of 24 h due to steering ability of platform (*de Lussy et al.*, 2006). Panchromatic images are acquired with a 70 cm nadir resolution and delivered with a nominal resolution of 50 cm over a swath footprint of 20 km. Multi-spectral images are acquired simultaneously and delivered with a nominal resolution of 2 m. The Pleiades satellite system is capable of acquiring 3 images of the same area in a single pass with B/H ratios (Baseline/Height, Height ≈ 694 km) of 0.1 to 0.5 with the tri-stereo mode, i.e. ∼70–350 km separation and corresponding stereo angles of ∼6–28° (*de Lussy et al.*, 2006). In this study, tri-stereo data were acquired by Pleiades 1B over a 45 km × 7 km area on 17 March

2014 (Figure 3.1). Images are acquired with a 20 km × 20 km footprint, so the region was tasked in two areas. The along-track incidence angles of the forward (F)/near-nadir (N)/backward (B) orientations for the NW and SE data sets are -13.4°/-1.2°/11.3° (I) and -9°/3.6°/15.8° (II) respectively.

3.3.2 DEM Generation

The tri-stereo data were processed using the Leica Photogrammetry Suite (LPS). The initial task was to define the geometric model. In remote sensing systems, a geometric model is used to describe the relationship between image (x, y) and ground (X, Y, Z) coordinate systems. For traditional frame cameras, the geometric model can be represented with a standard pinhole model (*Gremban et al.*, 1988) and the derivation is relatively simple. However, for pushbroom imaging systems (such as the Pleiades satellites), although each scanning line could be represented rigorously with the pinhole model, such a model would be rather complex as each line needs to be treated as an individual pinhole model with different attitude parameters. Therefore, a single set of rational polynomial functions (RPFs) are introduced to approximate all of these rigorous sensor models (*Hu et al.*, 2004; *Fraser and Hanley*, 2005). The RPFs take the following form:

$$x = \frac{P_1(X, Y, Z)}{P_2(X, Y, Z)} \tag{3.1}$$

$$y = \frac{P_3(X, Y, Z)}{P_4(X, Y, Z)} \tag{3.2}$$

where P_i (i = 1, 2, 3, 4) is a 3rd-order polynomial function. The coefficients of these polynomial functions are given as 80 rational polynomial coefficients (RPCs) (20 coefficients for each polynomial function). However, the RPC model does not have any physical meaning, and does not adequately take account of the true spatial orientation of each scan line and the attitude, position and velocity of the sensor (*Fraser and Hanley*, 2005). The sensor errors can be modelled as biases in image coordinates– shifts to compensate for small attitude errors, and drift or an affine (linear function) distortion to compensate for time-dependent errors (*Fraser and Hanley*, 2005).

To compensate for such shift and drift terms, Equations (3.1) and (3.2) can be rewritten as:

$$x + a_1 + a_2 \cdot x + a_3 \cdot y = \frac{P_1(X,\, Y,\, Z)}{P_2(X,\, Y,\, Z)} \tag{3.3}$$

$$y + b_1 + b_2 \cdot x + b_3 \cdot y = \frac{P_3(X,\, Y,\, Z)}{P_4(X,\, Y,\, Z)} \tag{3.4}$$

where a_i and b_i $(i = 1, 2, 3)$ describe an affine transformation to correct for the errors in sensor orientation.

Given that in our case we had no ground control points (GCPs), we identified more than 40 tie points, evenly distributed over the imagery, to calculate both the shift parameters a_1 and b_1, and the ground coordinates of each tie point simultaneously (i.e. bundle adjustment) (*Grodecki and Dial*, 2003); the residuals of the tie points are less than 0.2 pixels. After applying the simple shift corrections to the RPC model, a pixel-by-pixel matching procedure based on a least-squares adjustment was implemented with a relatively small window size of 5×5 pixels to avoid strong smoothing of the topographic surface (*Stumpf et al.*, 2014). We used 0.3 as the minimum correlation coefficient for matching. A lower correlation coefficient threshold generates more matching points, but the matching is less reliable. The correspondence (i.e. two points in different images $(x_1,\, y_1)$ and $(x_2,\, y_2)$ corresponding to the same point $(X,\, Y,\, Z)$ on the ground) from pairwise matching was used to estimate the ground coordinates via Equations (3.3) and (3.4). The resulting point cloud $(X,\, Y,\, Z)$ was filtered by averaging within a cell of 1 m and then gridded with a pixel spacing of 1 m (WGS84 UTM 11N) using continuous curvature splines in tension with a tension factor of 0.75 (*Smith and Wessel*, 1990). The spline interpolation yields a root-mean-square (RMS) error of ∼0.3 m. Following the same procedure, point clouds and DEMs have been produced with four different combinations of incidence angles (B-N, N-F, B-F and B-N-F).

3.4 Evaluation of the Pleiades DEMs

3.4.1 Point Clouds

The density of a point cloud determines the ground resolution of the raster DEM. To evaluate the ground resolution of the Pleiades DEMs, we calculated the densities of the point clouds. The raw point cloud has the lowest average point density of ∼0.7 points/m^2 for B-F, ∼1.0 points/m^2 for B-N and N-F, and the greatest average density of ∼3.0 points/m^2 for tri-stereo (B-N-F). However, given that the points are unevenly distributed due to vegetation and topography, average point density may be an inadequate measure for evaluating the ground resolution of the DEMs. Therefore, we examined the number of points within a grid cell of 1 m (the statistics are shown in Figure 3.2). ∼47% of the point cloud from B-N and N-F has a point density of ≥1 points/m^2 whilst ∼35% of the point cloud from B-F reaches this resolution. For tri-stereo, ∼65% of the point cloud has a point density of ≥1 points/m^2. The point densities of the various point clouds suggest that tri-stereo improves the spatial resolution of the DEMs by 50% compared to bi-stereo (Figure 3.3 shows an example of the advantage of incorporating images from three viewing angles). The wide stereo angle (B-F) makes matching difficult and generates a very sparse point cloud especially over the mountainous areas. B-N and N-F work well for the majority of the area, but each is affected by topographic shadowing in different ways. Tri-stereo makes full use of all three viewing angles, and provides a very dense point cloud. However, ∼5% of the imagery is covered by mostly featureless areas, e.g., shadows or desert salt flats (Figure 3.4), where the point density is lower than 0.04 points/m^2, even for the tri-stereo.

3.4.2 Accuracy of the Pleiades DEMs

The accuracy of the Pleiades DEMs is evaluated through a comparison with the post-earthquake LiDAR DEM. Due to errors in the sensor models, the absolute location accuracy of Pleiades 1A and 1B based on the RPFs only is reported to be 8.5 m and 3.5 m respectively (*Oh and Lee*, 2014). This location error will result in large elevation differences between the two DEMs. As shown in Figure 3.5a, elevation differences be-

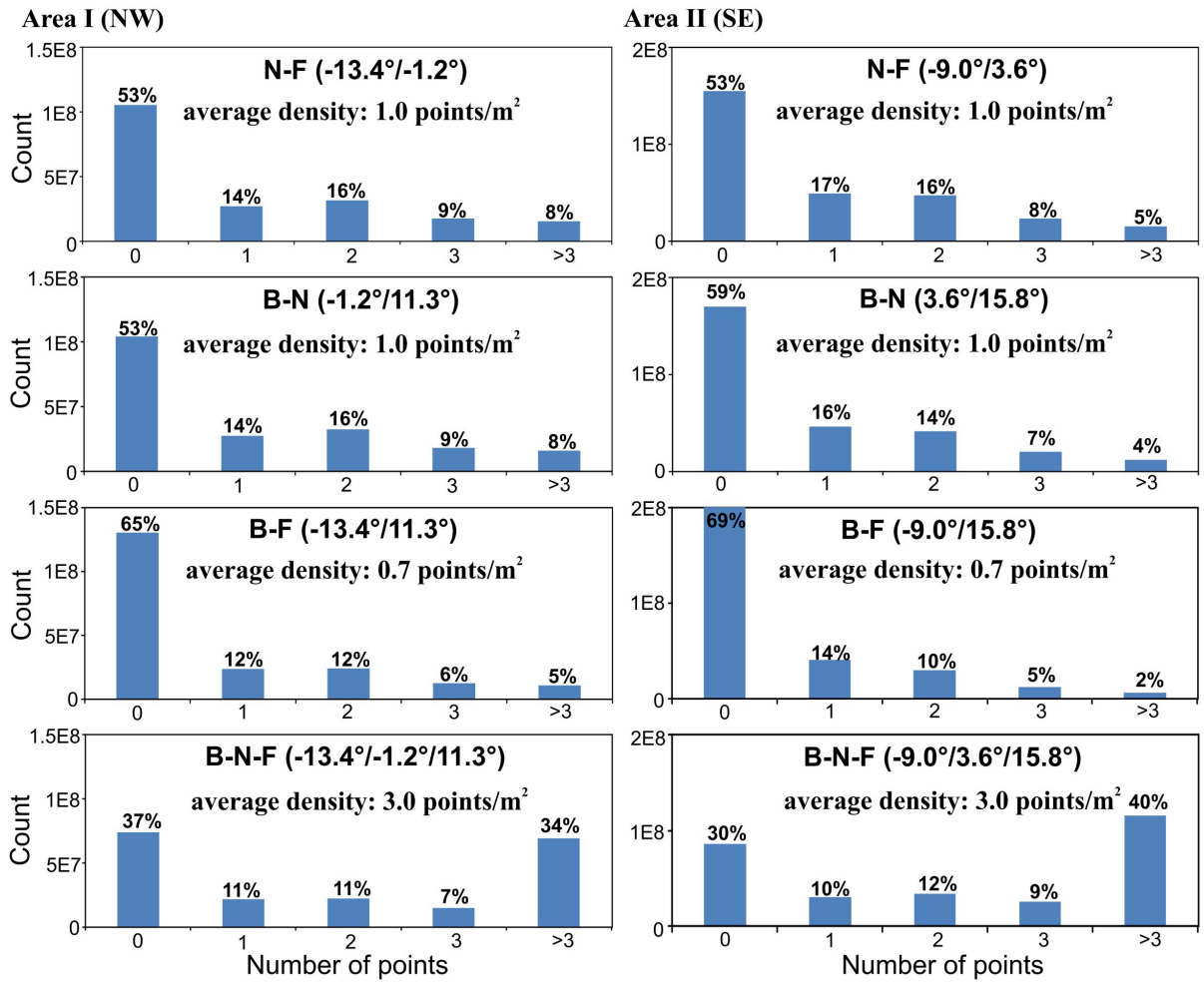


Figure 3.2: Statistics of the number of points within a grid cell for a grid spacing of 1 m for B-N, N-F, B-F and B-N-F combinations for the two tri-stereo datasets (Area I and II, see Figure 3.1). If the number of points is greater than or equal to 1, the cell has at least 1 measurement and therefore can be gridded with a spacing of 1 m. For tri-stereo, ∼65% of the DEM can reach a spatial resolution of 1 m.

tween the non-coregistered Pleiades and LiDAR DEMs are strongly correlated with the slope facing direction. Therefore, before comparing the Pleiades and LiDAR DEMs, they need to be coregistered. Different image matching algorithms including cross-correlation (*Leprince et al.*, 2007) and iterative closest point (ICP) (*Besl and McKay*, 1992; *Nissen et al.*, 2012) can reduce the misregistration between the two DEMs. We ran ICP with a square window of 100 m, 200 m and 500 m, and compared the results with those from the cross-correlation and ICP methods using the whole imagery. Figure 3.5 shows the elevation differences after coregistration with different methods have been largely reduced, but still increase with surface slope. This observation suggests that there is a residual coregistration error of ∼0.5 m that cannot be removed by either a simple shift in x and y

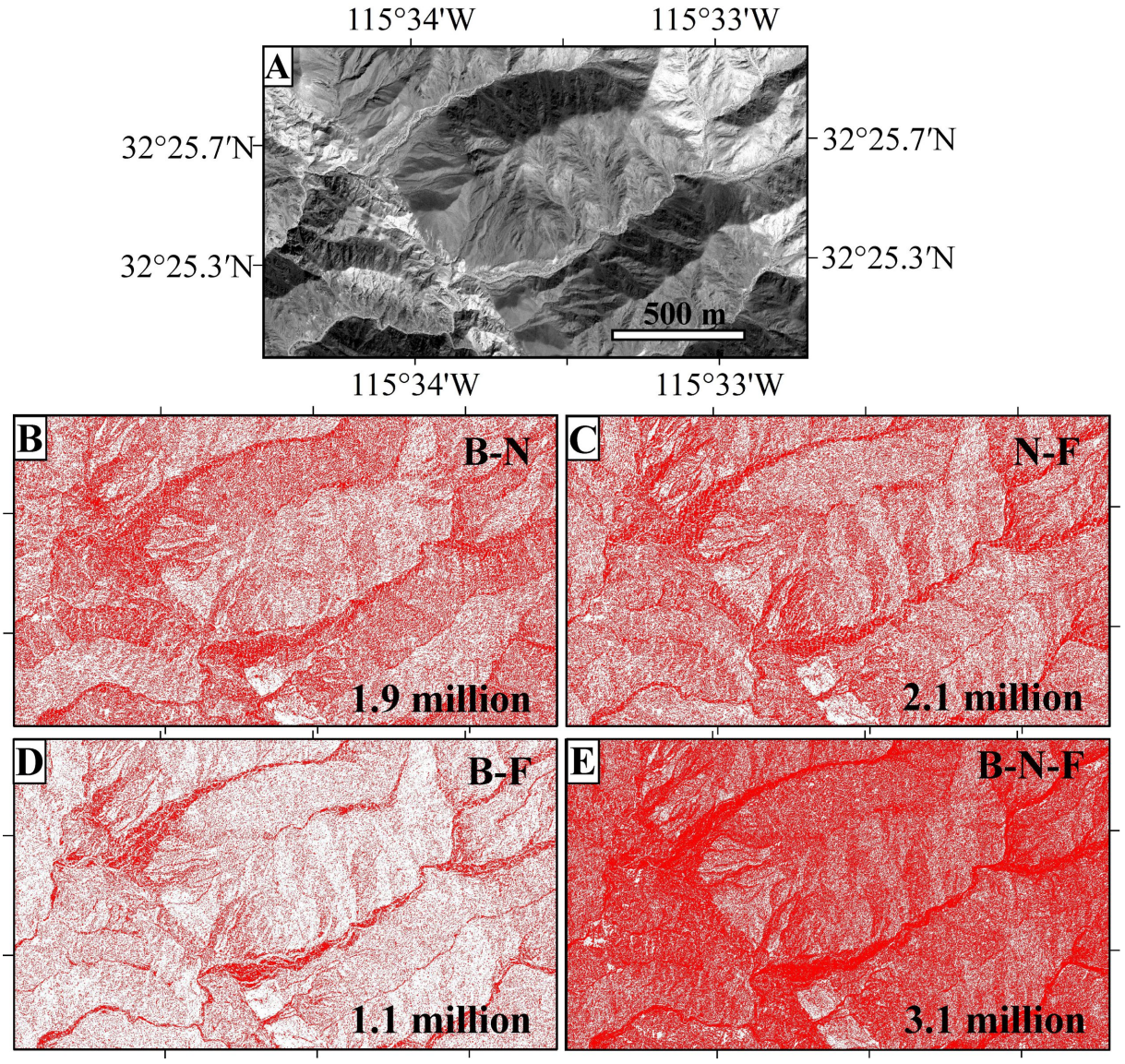


Figure 3.3: Point clouds generated from Pleiades stereo imagery (see Figure 3.1 for location). (a) An orthorectified image (covering an area of ∼4.5 million m^2). Red dots are the gridded matching points from (b) B-N (1.9 million), (c) N-F (2.1 million), (d) B-F (1.1 million) and (e) tri-stereo (3.1 million). Each dot indicates at least 1 point within a grid of 1 m.

directions or a rigid body transformation, as the positioning error is a function of surface topography. The cross-correlation result is similar to the results from the ICP method. We prefer the cross-correlation method as the ICP algorithm is very computationally intensive. Moreover, ICP may distort the geometry of the Pleiades DEM. Our test on ICP with a window size of 100 m shows a much larger rotation (an order of magnitude or more) than those with a window size of 200 m and 500 m; such distortion results in the larger elevation difference after coregistration (Figure 3.5e). Small windows of <200 m are therefore not recommended.

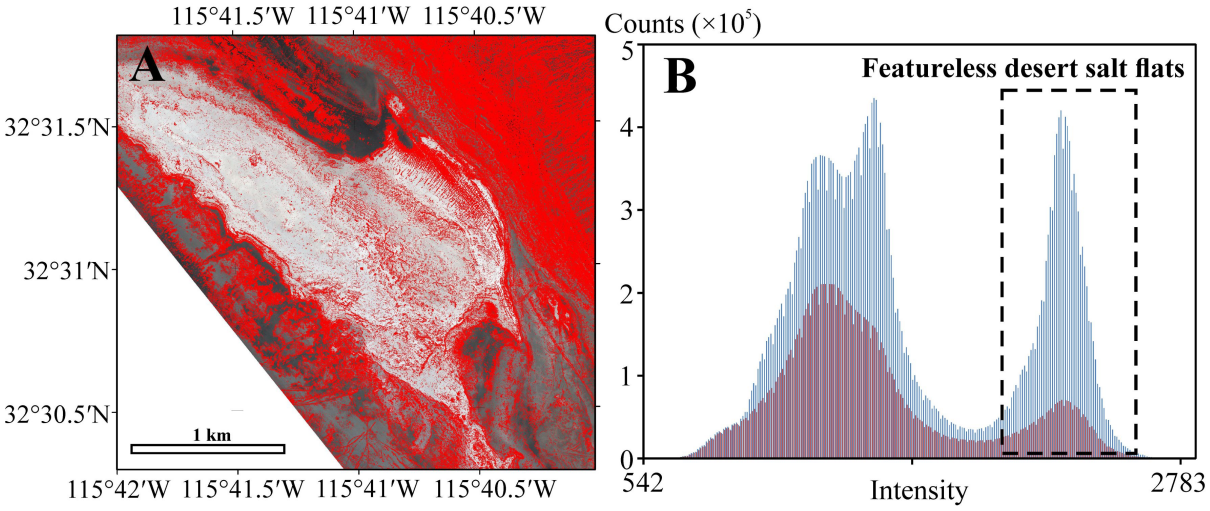


Figure 3.4: (a) An example of mostly featureless desert salt flats with few matching points (red points) from tri-stereo data with image below (see Figure 3.1 for location). (b) Histogram of the image is shown in blue. Histogram in red shows the areas where matching points have been found. In most areas, over 50% of the pixels can be matched, whereas in mostly featureless desert salt flats (bright area in (a)), only 20% of the pixels were matched.

After transforming the Pleiades DEMs to the LiDAR coordinate system, we differenced the Pleiades and post-earthquake LiDAR DEMs. When compared to the post-earthquake LiDAR DEM, the Pleiades DEMs have a mean elevation difference of 1 m to 4 m, with a standard deviation of 0.5 m to 0.7 m (Figure 3.7). Fortunately the mean difference, caused by a lack of GCPs for absolute calibration of the Pleiades DEMs, is not an issue in terms of determining relative height changes in earthquakes. The tri-stereo DEM has a smaller uncertainty (0.53-0.62 m) than the bi-stereo DEMs (0.55-0.71 m). Figure 3.8 shows that the elevation difference between the DEMs increases with surface slope due to topography-related misregistration. With topographic slopes of less than 10°, the standard deviation of the elevation difference is 0.30 m; this is mainly caused by the elevation errors in the Pleiades DEM. For topographic slopes of 30°-50°, the standard deviation is 0.56 m for tri-stereo, resulting from a combination of the elevation error in the Pleiades DEM and the residual misregistration error between the LiDAR and Pleiades systems. The DEMs from B-F and tri-stereo show a very good agreement in flat areas although the point cloud from B-F is very sparse; this suggests that the wide stereo angle provides a good geometric accuracy. With steep slopes, the standard deviation of the DEM from B-F becomes much larger, because the sparse point cloud cannot represent

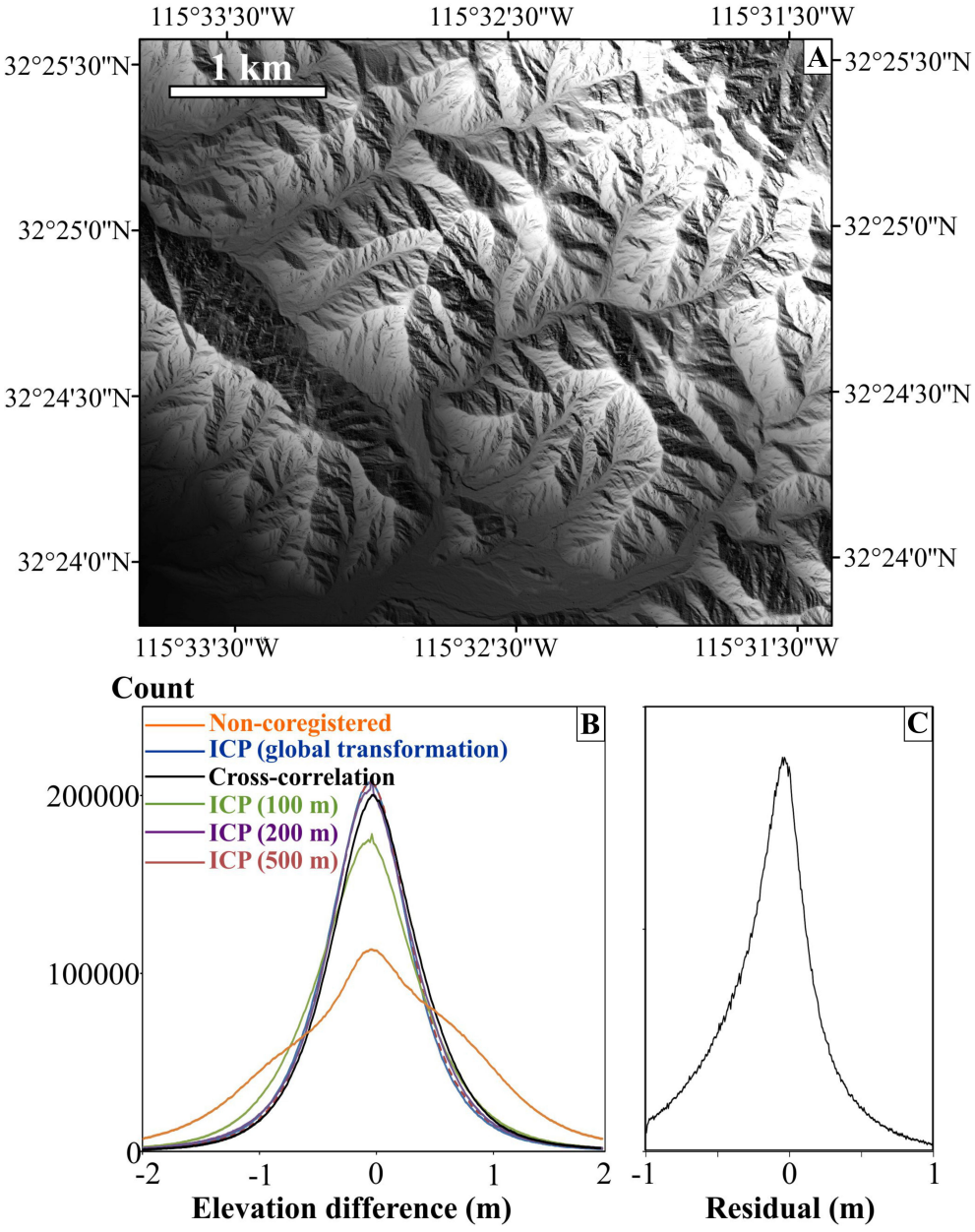


Figure 3.5: Coregistration of the Pleiades tri-stereo and post-earthquake LiDAR DEMs (See Figure 3.1 for location). (a) Shaded-relief Pleiades tri-stereo DEM. (b) Histograms of the elevation differences. (c) Histogram of the interpolation error in gridding with a pixel spacing of 1 m using continuous curvature splines in tension with a tension factor of 0.75. The spline interpolation has an RMS error of ∼0.3 m. (d) Elevation difference map between the non-coregistered DEMs. Elevation difference maps after coregistration using (e) cross-correlation (translation in X and Y directions), (f) ICP (a single transformation for the image, 3 translation, 3 rotation and 1 scaling parameters), (j) ICP with a window size of 100 m, (k) ICP with a window size of 200 m and (l) ICP with a window size of 500 m. (g-i) and (m-o) Elevation differences as a function of surface slope.

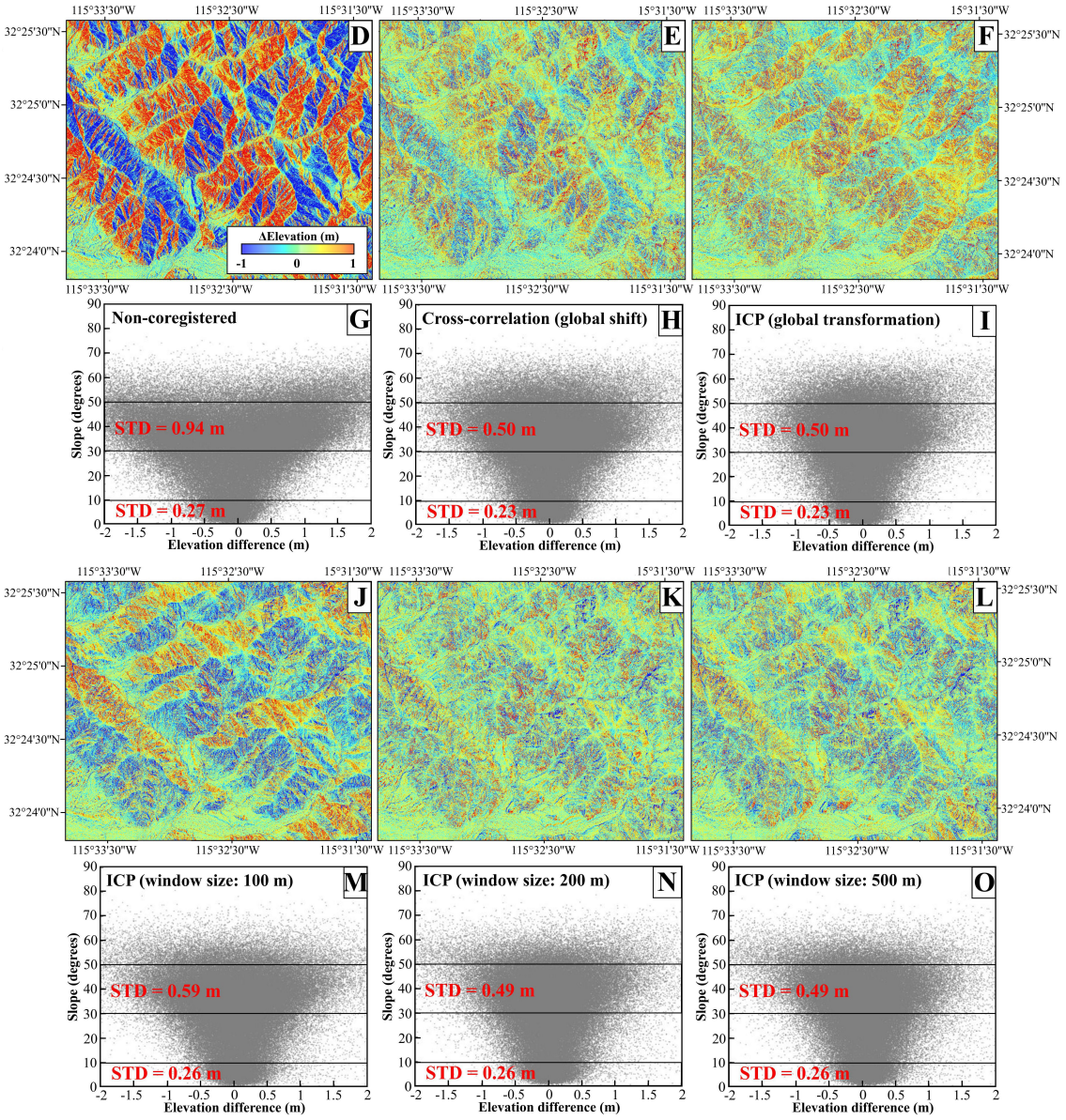


Figure 3.6: Figure 3.5 Cont.

the rough topography well. Therefore, for mountainous areas, a wide stereo angle of ∼25° is not as suitable. To avoid the contamination of the residual misregistration error, we evaluate the vertical accuracy of the Pleiades DEMs within areas with slopes of less than 10° only. The two DEMs are independent measurements, and the post-earthquake LiDAR DEM was suggested to have a vertical uncertainty of less than 0.1 m (*Oskin et al.*, 2012); therefore the relative vertical accuracy of the Pleiades DEMs is ∼0.3 m. It should be noted that over a large spatial scale (≥20 km), it may be difficult to capture this level of height change since GCPs would be needed for coregistration.

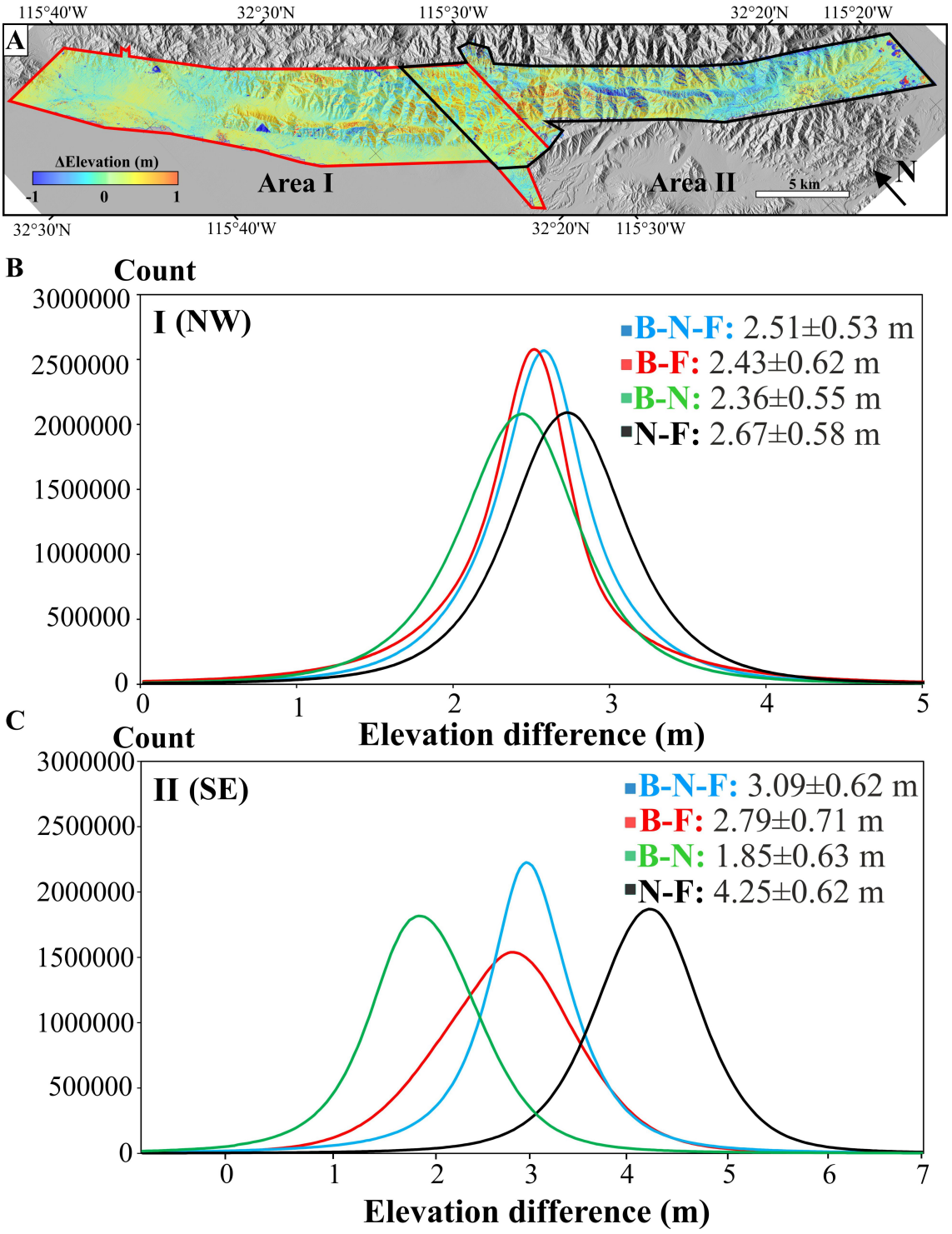


Figure 3.7: (a) Elevation difference map between the tri-stereo Pleiades and post-earthquake LiDAR DEMs. (b) and (c) Histograms of the elevation difference between the Pleiades (Area I and II marked in red and black polygons in Figure 3.7a) and post-earthquake LiDAR DEMs. Compared to the post-earthquake LiDAR DEM, the Pleiades DEMs have a mean elevation difference of 1 m to 4 m, with a standard deviation of 0.5 m to 0.7 m. Tri-stereo has a slightly smaller uncertainty (0.53-0.62 m) than bi-stereo (0.55-0.71 m). The mean elevation difference is due to a lack of ground control points for absolute calibration.

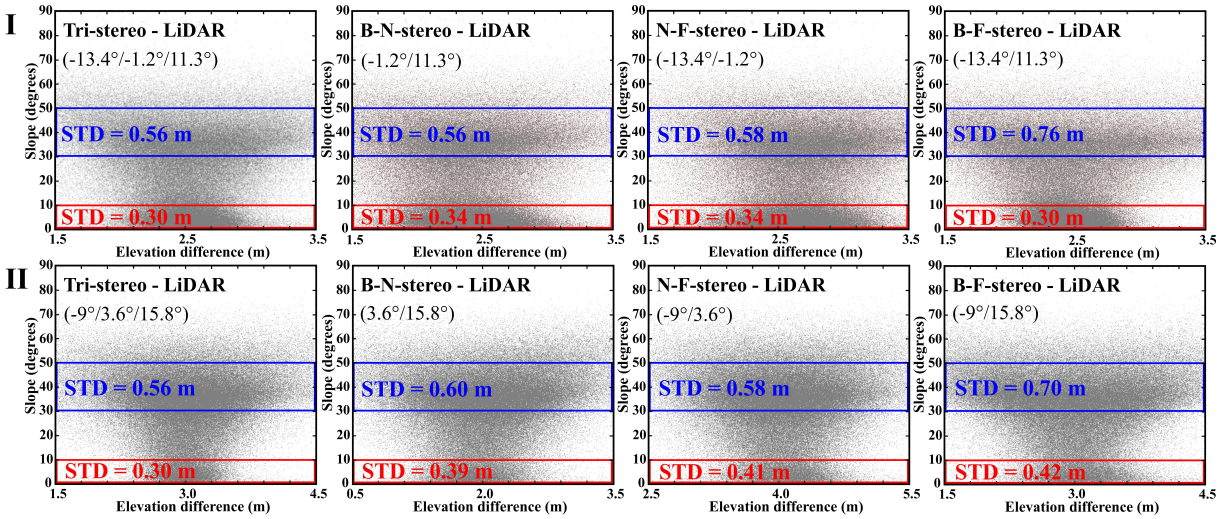


Figure 3.8: The elevation difference between the Pleiades and LiDAR DEMs increases with ground slope. For topographic slopes of less than 10°, the standard deviation of the elevation difference is ∼0.30-0.40 m for all four combinations; for topographic slopes of 30°-50°, the standard deviation is ∼0.56 m for B-N, N-F, and tri-stereo.

3.5 Surface Deformation Using the Pleiades DEM and Discussion of Fault Geometry

Our analysis of the accuracy of the Pleiades DEM shows that it is capable of capturing sub-metre height changes over a length scale of ≤20 km. To estimate the height changes occurring in the earthquake, we differenced the Pleiades and pre-earthquake LiDAR DEMs. As there is an average of 2 m right-lateral surface slip, direct differencing without accounting for such lateral slip will yield biased measurements of height changes. In order to show the biases and make a direct comparison with the result from *Oskin et al.* (2012), we first differenced the two DEMs without correcting for the lateral slip. In the following section, we calculate the horizontal displacements and corrected for these displacements before differencing the two DEMs.

3.5.1 Biased Measurements of Height Changes

For a direct comparison with the study by *Oskin et al.* (2012), we first differenced the 1-m tri-stereo Pleiades DEM and the pre-earthquake, lower-resolution (5-m) LiDAR DEM without accounting for the horizontal displacement. The pre-earthquake LiDAR DEM that we used in the study has been reprocessed by *Glennie et al.* (2014) by removing the

majority of systematic errors due to the mirror/laser beam misalignment. The elevation difference map (Figures 3.9a and 3.9b) shows metre and sub-metre offsets along the faults, directly comparable to the result obtained by differencing the two LiDAR DEMs (*Oskin et al.*, 2012). For example, profile X-X′ (Figure 3.9d) shows a vertical displacement of 1.1 m across the Paso Inferior Accommodation Zone and an offset of 0.6 m across the Borrego fault, in good agreement with the previous study by *Oskin et al.* (2012) (Figure 3.9c); the profile also shows a ∼0.2 m vertical displacement across the Laguna Salada fault. When differencing the post-earthquake LiDAR and Pleiades DEMs, we got a difference of 0.3 m, consistent with the errors in flat areas in Figure 3.8. We also differenced the bi-stereo Pleiades DEMs and the pre-earthquake LiDAR DEM, and obtained very similar results. The level of consistency found between offsets measured in our study using the Pleiades DEM and the previous study using the LiDAR DEM (*Oskin et al.*, 2012) demonstrates the capability of the Pleiades DEM in measuring sub-metre vertical offsets with decimetric relative accuracy. *Oskin et al.* (2012) focused on the Paso Inferior Accommodation Zone where topographic slopes are less than 3°. Away from flat areas, the height changes are biased and strongly correlated with surface slope due to the large right-lateral coseismic slip (Figure 3.9a).

3.5.2 Correcting for Horizontal Displacement

To estimate unbiased height changes, we need to account for the right-lateral slip in the earthquake. We first estimated the horizontal displacements from the Pleiades and pre-earthquake LiDAR DEMs using the COSI-Corr software package (freely available from `www.tectonics.caltech.edu/slip_history/spot_coseis/index.html`), which measures horizontal surface displacements with sub-pixel accuracy (i.e. the degree to which the result of a measurement matches the true value is smaller than a pixel) (*Leprince et al.*, 2007; *Ayoub et al.*, 2009; *Hollingsworth et al.*, 2012). The Pleiades DEM was downsampled to 5 m to match the pre-earthquake LiDAR DEM. The sub-pixel matching procedure estimates horizontal displacements by cross-correlating the pre- and post-earthquake DEMs in small windows. The cross-correlation is implemented in the frequency domain and the displacement retrieved from the phase difference of their Fourier transform (*Leprince*

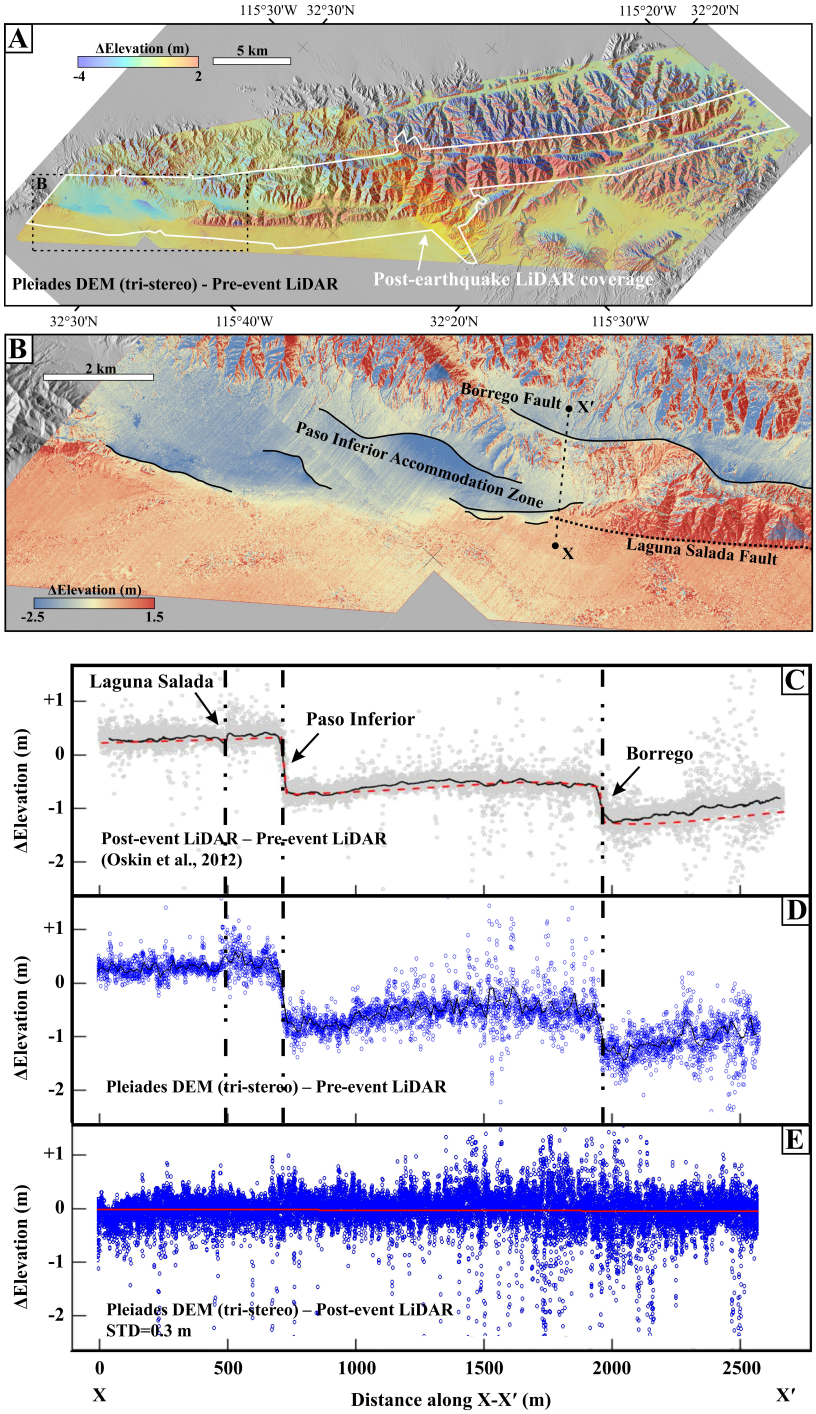


Figure 3.9: (a) Elevation difference map derived from differencing the Pleiades tri-stereo and pre-earthquake LiDAR DEMs without accounting for the horizontal displacement. With large topographic relief, elevation difference is strongly effected by surface slope due to the large right-lateral surface slip. Our Pleiades imagery covers a wider area than the post-earthquake LiDAR DEM (the latter indicated by the white polygon). (b) The elevation differences estimated in this study show distributed deformation in the Paso Inferior accommodation zone (indicated by the box in a). (c) Swath profile of elevation difference along line X-X′ from *Oskin et al.* (2012) obtained by differencing the two LiDAR DEMs. (d) Swath profile of elevation difference along line X-X′ of this study by differencing the Pleiades tri-stereo and pre-earthquake LiDAR DEMs. The elevation difference map shows metre and sub-metre offsets along the faults, comparable to the result by differencing the two LiDAR DEMs. (e) Elevation difference of the Pleiades and post-earthquake LiDAR DEMs. Outliers result from noise and vegetation.

et al., 2007; *Ayoub et al.*, 2009). We used a correlation window of 64 pixels as a first step, followed by 32 pixels, with a step of 4 pixels (20 m). The resulting east-west and north-south components of the horizontal displacement were filtered using the non-local means algorithm (Figures 3.10a and b) (*Ayoub et al.*, 2009). Although *Glennie et al.* (2014) had corrected for processing errors in the pre-earthquake LiDAR DEM and such corrections can remove the artifacts in the east-west displacement (Figure 3.10a), the north-south displacement (Figure 3.10b) still shows large systematic deviations, resulting from remaining errors in the laser beam alignment in the pre-earthquake LiDAR DEM. When differencing the Pleiades and pre-earthquake LiDAR DEMs, we also need to account for these laser beam alignment errors as well as the horizontal motion. It would be possible to correct for the horizontal motion using the displacement field from cross-correlating pre- and post-earthquake SPOT-5 images (*Barišin et al.*, 2015), but we would then need to do an additional correction to take account of the alignment errors in the pre-earthquake LiDAR DEM. It is therefore simplest to apply both corrections at once using the horizontal displacements shown in Figures 3.10a and 3.10b to the Pleiades DEM, and then difference the corrected Pleiades and pre-earthquake LiDAR DEMs to obtain unbiased measurements of height changes.

Compared to the biased elevation difference, the resulting elevation difference map (Figure 3.10c) shows no evident correlation with surface slope. Profile Y-Y′ reveals a vertical displacement of ∼1.5 m across the Pescadores fault from the corrected elevation difference map (Figure 3.10e), which cannot be seen in the biased height changes (Figure 3.10d). We estimated an average vertical displacement of 1.2 m over the epicentral area from the corrected elevation difference (Figure 3.11a). Thus, in order to reliably determine height changes in earthquakes using pre- and post-earthquake DEMs, horizontal displacement needs to be estimated and removed first. Whereas *Oskin et al.* (2012) compared their LiDAR measurements with an elastic model over the Paso Inferior Accommodation Zone, here we focus on the Pescadores fault where topographic slopes are larger than 30°. We reproduced the vertical displacements across the Pescadores fault using a three-dimensional elastic model for a rectangular dislocation (*Okada*, 1985) with oblique-normal fault slip of 4 m on a fault plane with a strike, dip and rake of 312°/75°/-150° (*Wei et al.*, 2011)

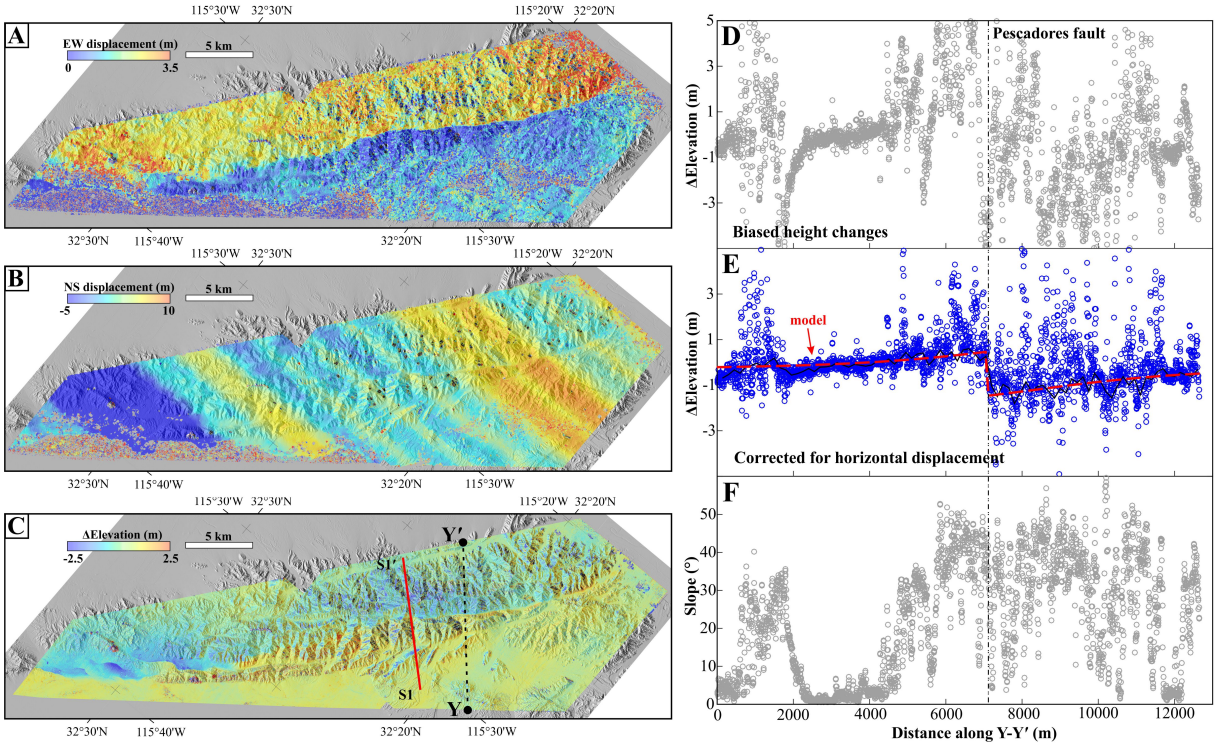


Figure 3.10: (a) East-west component of the horizontal displacement derived from the Pleiades tri-stereo and pre-earthquake LiDAR DEMs. (b) North-south component of the horizontal displacement. Note striping artefacts due to laser beam misalignment of the pre-earthquake LiDAR. (c) Elevation difference map after correcting for the horizontal displacement. S1-S1′ is the swath profile in Figure 3.11. (d) Profile of elevation difference along line Y-Y′ from the biased measurements of height changes. (e) Profile of elevation difference along line Y-Y′ after correcting for the horizontal displacement (blue circles). Because the horizontal displacement fields used to correct for the apparent motion contain some errors, the corrected elevation difference would be contaminated by such errors particularly in areas with large topographic relief, resulting in the noises in the profile. Red dashed line shows the elastic dislocation model. (f) Surface slope along line Y-Y′. In flat areas (with surface slopes of less than 5°), the biased height changes agree well with those after correcting for the horizontal displacement; with steep slopes, the influence of the horizontal displacement is significant.

(equivalent to a dip slip of 2 m with a throw of 1.9 m), a length of 100 km, top/bottom depths of 0.001/6 km, and Lamé parameters ($\lambda = \mu$) of 3.23×10^{10} Pa. As shown in Figure 3.10e, the elastic model agrees well with the height changes determined from the Pleiades and pre-earthquake LiDAR DEMs.

3.5.3 Estimation of Fault Dip

The detailed 3D near-field deformation enables us to estimate fault dip (δ) along the rupture using Equation (3.5)

$$\delta = \tan^{-1}\frac{V}{N} \tag{3.5}$$

where V and N are vertical and fault-normal offsets, i.e. throw and heave at the fault. The vertical and fault-normal offsets in the 2010 earthquake can be obtained from differencing and cross-correlating the pre- and post-earthquake DEMs (Figure 3.10). However, as the DEM-derived displacement in the north-south direction was contaminated by the large systematic deviations in the pre-earthquake LiDAR DEM (as shown in Figure 3.10b), here we used the horizontal displacement field from *Barišin et al.* (2015). Swath profiles (1-km-wide) were taken to calculate the dip along the Pescadores fault where the surface rupture is linear. We resolved the east-west and north-south components of the surface displacement onto the fault-normal direction, and calculated the fault-normal and vertical offsets by fitting lines on both sides of the fault (see Figure 3.11). Applying Equation (3.5), the dip was estimated to be 76° for profile S1-S1′ (Figures 3.11b and 3.11c) with an average of 72° for the Pescadores fault (Figure 3.11a).

Our estimates of fault dip agree very well with both the field measurements by *Teran et al.* (2015), and the modelling result (75°) from seismological and remote sensing observations by *Wei et al.* (2011). The consistent results suggest that accurate measurements of 3D near-field deformation provides an additional means of constraining fault geometry.

The El Mayor-Cucapah earthquake has been well-studied using remote sensing, seismology, LiDAR and field observations, so we focused on comparing our result and results from other well-established studies (*Wei et al.*, 2011; *Oskin et al.*, 2012; *Fletcher et al.*, 2014; *Teran et al.*, 2015; *Barišin et al.*, 2015). In other areas where field or airborne LiDAR measurements are difficult, our method based on VHR stereo imagery will be essential for investigating fault geometry. For example, we used Pleiades stereo imagery to study the fault zone deformation of the 2013 M_w 7.7 Balochistan earthquake and found that the 200-km-long north-dipping Hoshab fault in the eastern Makran switches to south-dipping at its southern end, which may act as the endpoint of earthquake ruptures like the 2013 event (*Zhou et al.*, 2016a).

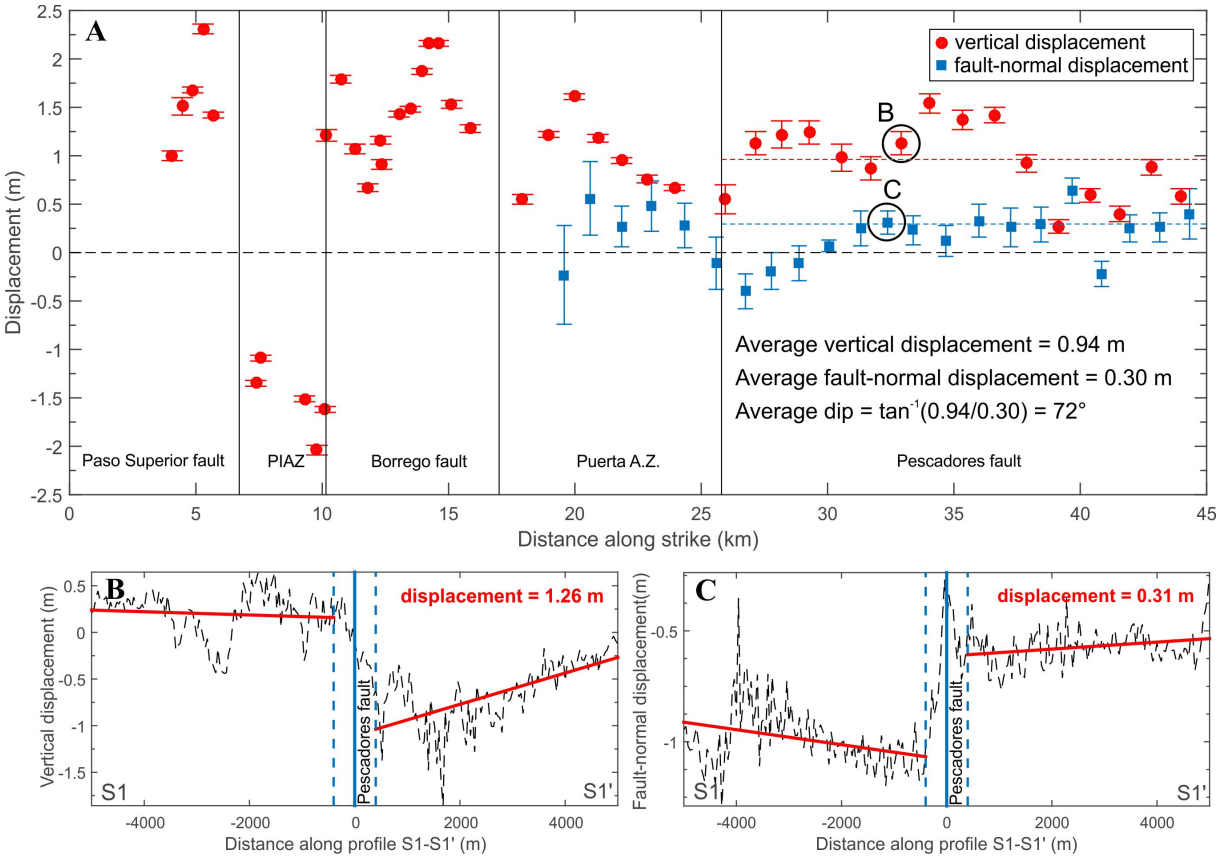


Figure 3.11: (a) Vertical (red dots, positive for south-side-up) and fault-normal (blue squares, positive for extension) displacements along the 2010 rupture. PIAZ: Paso Inferior Accommodation Zone. Puerta A.Z.: Puerta Accommodation Zone. The average vertical displacement along the Pescadores fault is 0.94 m (red dashed line) and the average fault-normal displacement is 0.30 m (blue dashed line), from which we estimate an average fault dip of 72°. Circles indicate the locations of Figures 3.11b and 3.11c. (b) Swath profile (swath width is 1 km) S1-S1′ showing a vertical displacement of 1.26 m (see Figure 3.10 for location). Blue line denotes the Pescadores fault. Black lines are the measurements. Red lines are the best-fitting lines to the measurements on both sides of the fault. We excluded the measurements in the near-fault zone (bounded by blue dashed lines). (c) Swath profile S1-S1′ showing a fault-normal displacement of 0.31 m.

3.6 Discussion and Conclusions

This study assesses the capability of the new Pleiades satellites to determine height changes in earthquakes. Two Pleiades tri-stereo pairs covering part of the 2010 M_w 7.2 El Mayor-Cucapah epicentral area were acquired and processed to generate 1-m resolution DEMs. Results from four different combinations of incidence angles (B-N, N-F, B-F and B-N-F) were compared. Tri-stereo (B-N-F) can improve the point cloud density by 50% compared to bi-stereo as it makes full use of all three viewing angles, although with additional costs in acquisition and processing. The tri-stereo DEM, which incorporates more observations, also has slightly smaller uncertainties than bi-stereo, and thus is more

robust and reliable for measuring surface height. The wide stereo angle, e.g. the B-F pair (∼25° corresponding to a B/H ratio of 0.44) makes matching difficult and generates a sparse point cloud (≤0.4 points/m^2), which cannot represent rough topography well, resulting in large uncertainties with increasing slopes above ∼30°. If we ignore the contamination of misregistration error due to the different coordinate systems of the Pleiades satellites and LiDAR, the intrinsic vertical accuracy of the Pleiades DEMs is estimated to be ∼0.3 m.

By differencing the 1-m Pleiades DEM and the pre-earthquake, lower resolution LiDAR DEM, we have demonstrated that Pleiades stereo imagery has the capability to determine sub-metre height changes, e.g., ∼0.2 m vertical displacement across the Laguna Salada fault; this result is comparable to a previous study that differenced two LiDAR DEMs (*Oskin et al.*, 2012). With sub-pixel matching using the COSI-Corr software package, we can recover the 3D surface displacements from the Pleiades and pre-earthquake LiDAR DEMs. By extension, we expect it to be possible to measure sub-metre vertical offsets occurring in earthquakes using pre- and post-earthquake VHR stereo imagery (such as Pleiades and WorldView), without the necessity to conduct a costly LiDAR survey. Tasking of optical stereo imagery can be relatively rapid, but is subject to constraints of cloud cover. Also the advantages over LiDAR will be lost in areas that are heavily vegetated, mountainous or mostly featureless desert salt flats.

In this study, 3D surface displacements were calculated in two steps. In the first step, we used the pre- and post-earthquake DEMs to resolve the horizontal displacement. In the second step, we removed the horizontal displacement from the post-earthquake Pleiades DEM, and differenced the corrected Pleiades and pre-earthquake LiDAR DEMs. Recently, *Leprince et al.* (2013) developed a new method that uses mutli-temporal VHR stereo images to extract topography and derive 3D ground motion simultaneously. Such a method offers extensive future use for measuring earthquake surface deformation in places where pre- and post-earthquake images are available.

Chapter 4

The 2013 M_w 7.7 Balochistan, Pakistan Earthquake

Adapted from Zhou, Y., J. R. Elliott, B. Parsons, and R. T. Walker (2015), The 2013 Balochistan earthquake: an extraordinary or completely ordinary event?, *Geophysical Research Letters, 42*, 6236–6243, doi:10.1002/2015GL065096.

Zhou, Y., R. T. Walker, J. R. Elliott, and B. Parsons (2016), Mapping 3D fault geometry in earthquakes using high-resolution topography: Examples from the 2010 El Mayor-Cucapah (Mexico) and 2013 Balochistan (Pakistan) earthquakes, *Geophysical Research Letters, 43*, doi:10.1002/2016GL067899.

4.1 Introduction

The 24 September 2013 M_w 7.7 Balochistan earthquake, the only modern large upper-crustal earthquake in the southwestern India-Eurasia boundary zone (Figure 4.1), provides a valuable opportunity for studying the ongoing deformation resulting from the accommodation of the relative motion between India and Eurasia. This strike-slip earthquake is very unusual when compared to other well-studied large continental earthquakes worldwide (*Lin et al.*, 2002; *Wright et al.*, 2004a; *Oskin et al.*, 2012; *Elliott et al.*, 2012), in that it ruptured a 225-km long section of the curved and moderately dipping (50-70°N) Hoshab fault (*Avouac et al.*, 2014; *Jolivet et al.*, 2014) while appearing to show consistent and predominantly strike-slip behaviour along its entire length, its slip vector rotating dra-

matically along-strike by ∼60°. This striking observation, and the difficulty of reconciling the largely strike-slip motion with the shortening to the west, has led to the suggestion that previous events on the fault must have displayed a different ratio of shortening to strike-slip motion. To explain this atypical faulting behaviour, a wide range of hypotheses has been proposed, including: (1) dynamic stresses during rupture promoting sustained strike-slip failure on a curved fault in the 2013 event (*Avouac et al.*, 2014; *Barnhart et al.*, 2015); (2) time-varying fault kinematics leading to rupture histories which alternate between pure strike-slip and dip-slip (*Avouac et al.*, 2014; *Zinke et al.*, 2014; *Barnhart et al.*, 2015); (3) bimodal slip behaviour on different segments along strike accommodating strain partitioning through time (*Barnhart et al.*, 2015); and (4) a ball-and-socket rigid rotation south of the fault that can also account for the complexity at the fault termination point in the Chaman fault system to the northeast (*Barnhart et al.*, 2014). These ideas largely arise from the interpretation of surface observations of horizontal displacements determined from optical satellite imagery through visual analysis and digital image matching, and from very sparse global positioning system (GPS) data (*Avouac et al.*, 2014; *Jolivet et al.*, 2014; *Zinke et al.*, 2014; *Barnhart et al.*, 2014, 2015). We seek to test these complex ideas by additional constraints from the vertical component of motion on the fault. In addition, we also re-examine the fault geometry for the Balochistan earthquake, where it has been argued from rupture mapping using image-matching correlations that there is no clear geometrical control on the 200+ km surface rupture (*Avouac et al.*, 2014), but where no field access is possible for testing.

4.2 Tectonic Background

The Hoshab fault that ruptured in the 2013 Balochistan earthquake is part of a kinematic transition zone between subduction of the Ormara oceanic plate beneath Eurasia at ∼3 cm/yr in the west (*Kukowski et al.*, 2000; *Bilham et al.*, 2007), and northward motion of the Indian plate with respect to Eurasia at ∼3 cm/yr in the east (Figure 4.1) (*Mohadjer et al.*, 2010; *Ader et al.*, 2012; *Avouac et al.*, 2014; *Zinke et al.*, 2014). High interseismic coupling (*Lin et al.*, 2015) and several large earthquakes, including the 1945 M_w 8.1 earthquake (*Byrne et al.*, 1992) in the eastern Makran subduction zone, suggest that a

large fraction ($\geq$ 70%) of the convergence between Arabia and Eurasia is accommodated on the Makran megathrust (*Lin et al.*, 2015). The rate of shortening to be accommodated by internal deformation in the eastern Makran is uncertain. Deformed river terraces and GPS measurements in the western Makran show a shortening rate of 6-8 mm/yr in the Makran accretionary wedge (*Haghipour et al.*, 2012), about 30% of the rate of convergence, and we use this figure as the rate of shortening for the eastern Makran as well. A recent geodetic study consisting of 5 GPS sites (Figure 4.1) reveals ~2.5 cm/yr left-lateral motion in the eastern Makran, ~1.5 cm/yr of which it is suggested is accommodated on the Ornach-Nal fault (*Szeliga et al.*, 2012). GPS velocities from stations PANG, BEDI and ZHAO indicate ~1 cm/yr left-lateral motion to be accommodated within the transition zone (Figure 4.1).

The 2013 Balochistan rupture was bilateral, but propagated much further to the south of the epicentre than to the north where fault creep (~3 mm/yr) has released a large fraction of the accumulated stress (*Fattahi et al.*, 2014a). Sub-pixel matching of pre- and post-earthquake Landsat-8 imagery reveals an average of ~8 m left-lateral strike-slip motion during the earthquake (*Avouac et al.*, 2014).

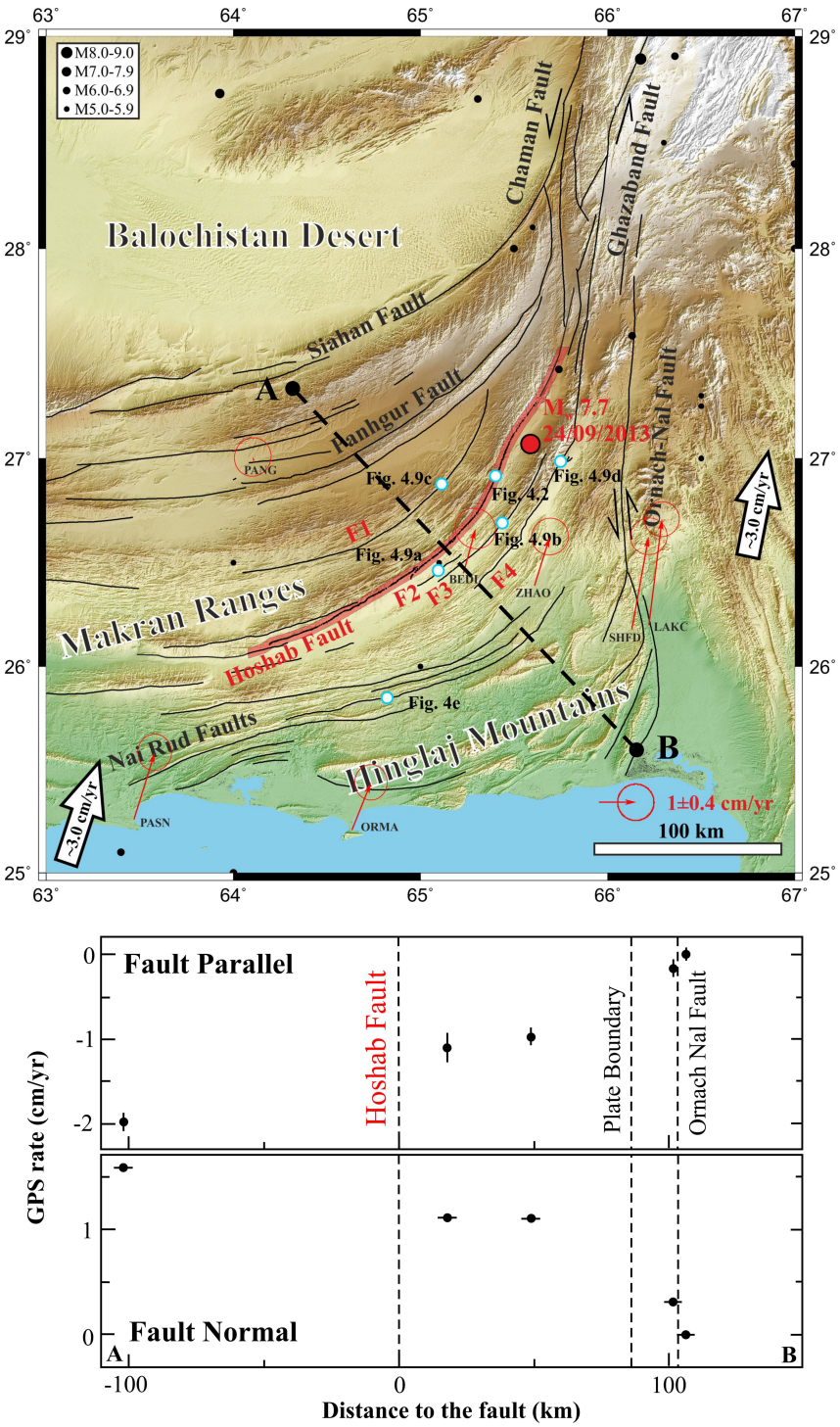


Figure 4.1: Tectonic setting of the 24 September 2013 Balochistan earthquake. (top) Regional active faults are remapped through our own geomorphic analysis of the landscape. The elongate red polygon denotes the extent of the post-earthquake Pleiades stereo imagery (5 km wide × 240 km long). Red arrows are GPS velocities relative to Eurasia measured at 7 campaign sites (*Szeliga et al.*, 2012; *Lin et al.*, 2015). White arrows indicate relative plate motion. The Arabian oceanic plate subducts beneath Eurasia at ∼3 cm/yr and the Indian plate moves northward with respect to Eurasia at ∼3 cm/yr. F1-F5 are unnamed faults, on which we find evidence for active faulting at the locations indicated by the blue circles. Black dots are historical earthquakes in the region (*Song*, 2012). (bottom) GPS-derived displacement rates projected into the fault-parallel and the fault-normal directions. The convergence that needs to be taken up by the Hoshab and nearby faults is ∼0.5 cm/yr.

4.3 Data and Results

4.3.1 Surface Slip in the 2013 Earthquake

The Pleiades satellite constellation provides 50-cm panchromatic imagery worldwide and allows rapid three-dimensional (3D) reconstruction due to its stereo capability (*Poli and Toutin*, 2012). To quantify the 3D surface slip, we constructed a high-resolution (1-m) digital elevation model (DEM) from Pleiades stereo imagery for the entire 225-km-long surface rupture over an area of more than 1000 km^2 (Figure 4.1). The method was illustrated in Chapter 3. By visual analysis of geomorphic features (e.g. Figure 4.2b), we measured 150 strike-slip offsets (Figure 4.3) that mainly agree well with similar measurements made previously from WorldView imagery (*Zinke et al.*, 2014; *Barnhart et al.*, 2015) and also measurements from subpixel image correlation of pre- and post-earthquake Landsat-8 images (*Avouac et al.*, 2014). Where this is not the case is within young alluvial sediments where measurements of the strike-slip offset at the fault are typically less than that seen in image correlations, suggesting that unconsolidated, immature materials do not localise fault slip near the surface (*Oskin et al.*, 2012; *Dolan and Haravitch*, 2014; *Zinke et al.*, 2014). In addition, we measured 236 vertical displacements from offset river channels and alluvial fans observed in the post-earthquake DEM (Figure 4.3). The measurements reveal an average of 1.9 m vertical component of motion, with local maximum up to 5.6 m due to localised bending of the fault trace (Figure 4.4). The dominant sense of fault motion is north-side-up sinistral-thrusting slip, but some portions of the fault also show south-side-up sinistral-normal slip due to rupture complexity and local changes in strike (Figure 4.4). Given an average fault dip of ~50°N (*Avouac et al.*, 2014; *Jolivet et al.*, 2014), the average shortening in the 2013 event is 1.6 m.

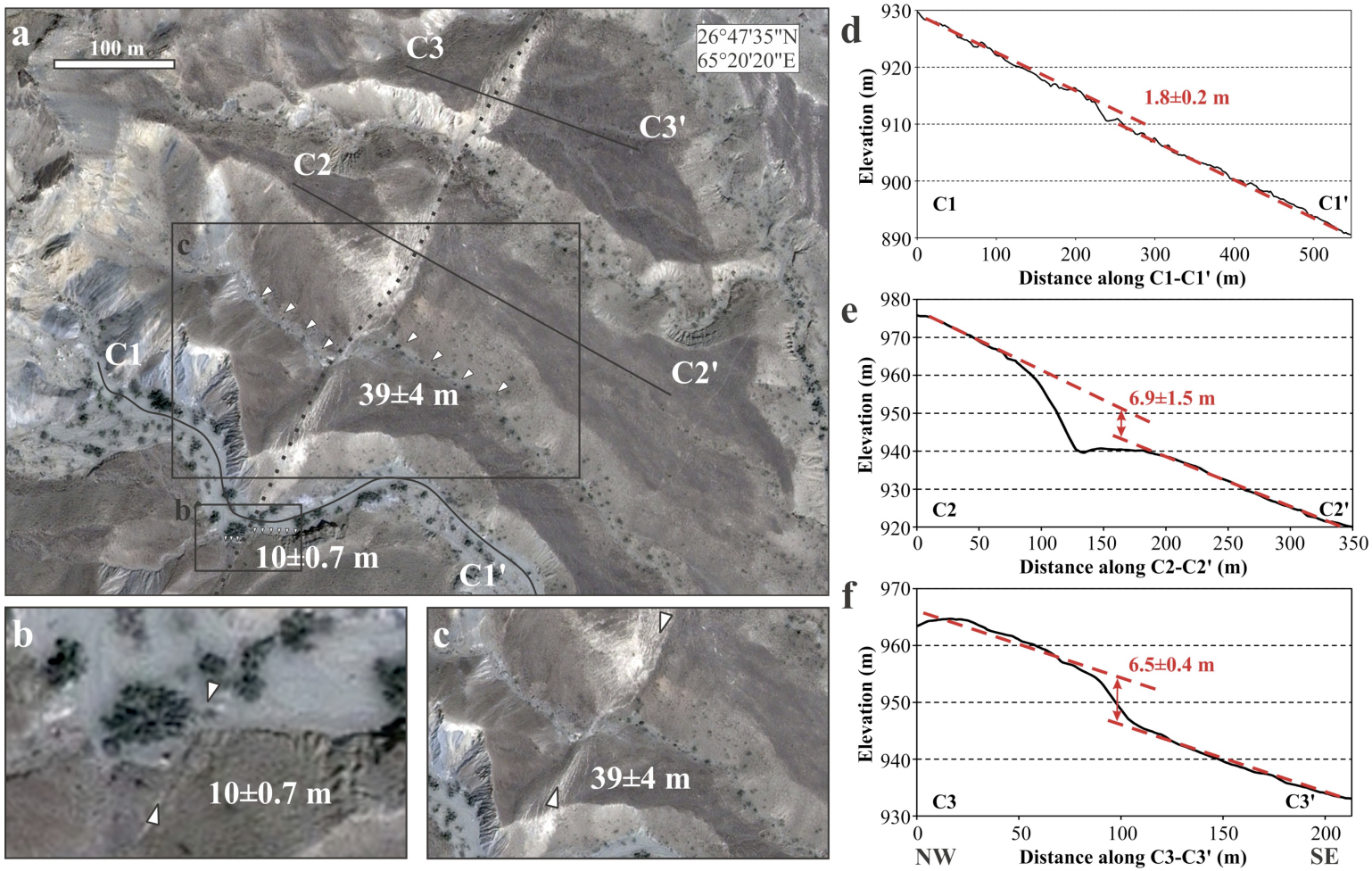


Figure 4.2: Displacements along the Hoshab fault (see Figure 4.1 for location). (b) The lateral offset in the 2013 earthquake at this location is 10 m. (c) A gully within an older fan surface is laterally offset by 39 m. (d) Elevation profile C1-C1′ from our Pleiades derived 1 m DEM along the old fan surface shows that the vertical displacement in the 2013 earthquake at this location is 1.8 m (north-side-up). (e) Elevation profile C2-C2′ shows a cumulative vertical displacement of 6.9 m (north-side-up). (f) Elevation profile C3-C3′ shows a cumulative vertical displacement of 6.5 m (north-side-up).

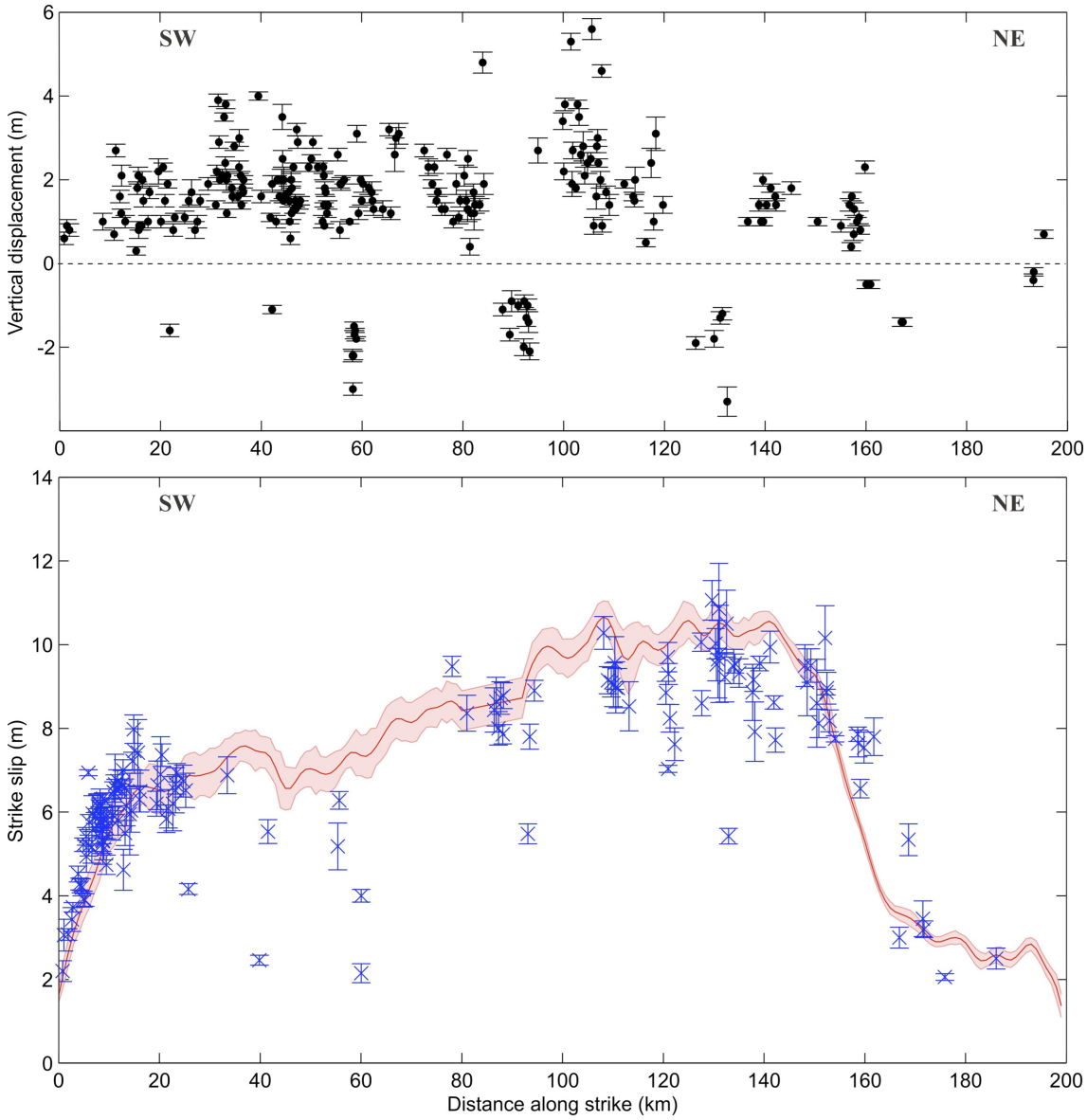


Figure 4.3: Surface fault slip measured from Pleiades stereo imagery (points) and Landsat-8 image correlation (red band). Black dots show the vertical displacements measured from the Pleiades DEM (positive for north-side-up). Blue crosses denote the lateral displacements measured by visual analysis of Pleiades imagery (positive for left-lateral). Red line and error band is the strike-slip displacement from correlating pre- and post-earthquake Landsat-8 imagery (*Avouac et al.*, 2014) (positive for left-lateral). Some of the scatter in vertical measurements including short sections with south-side-up displacements arises from local complexities of bending of the fault trace.

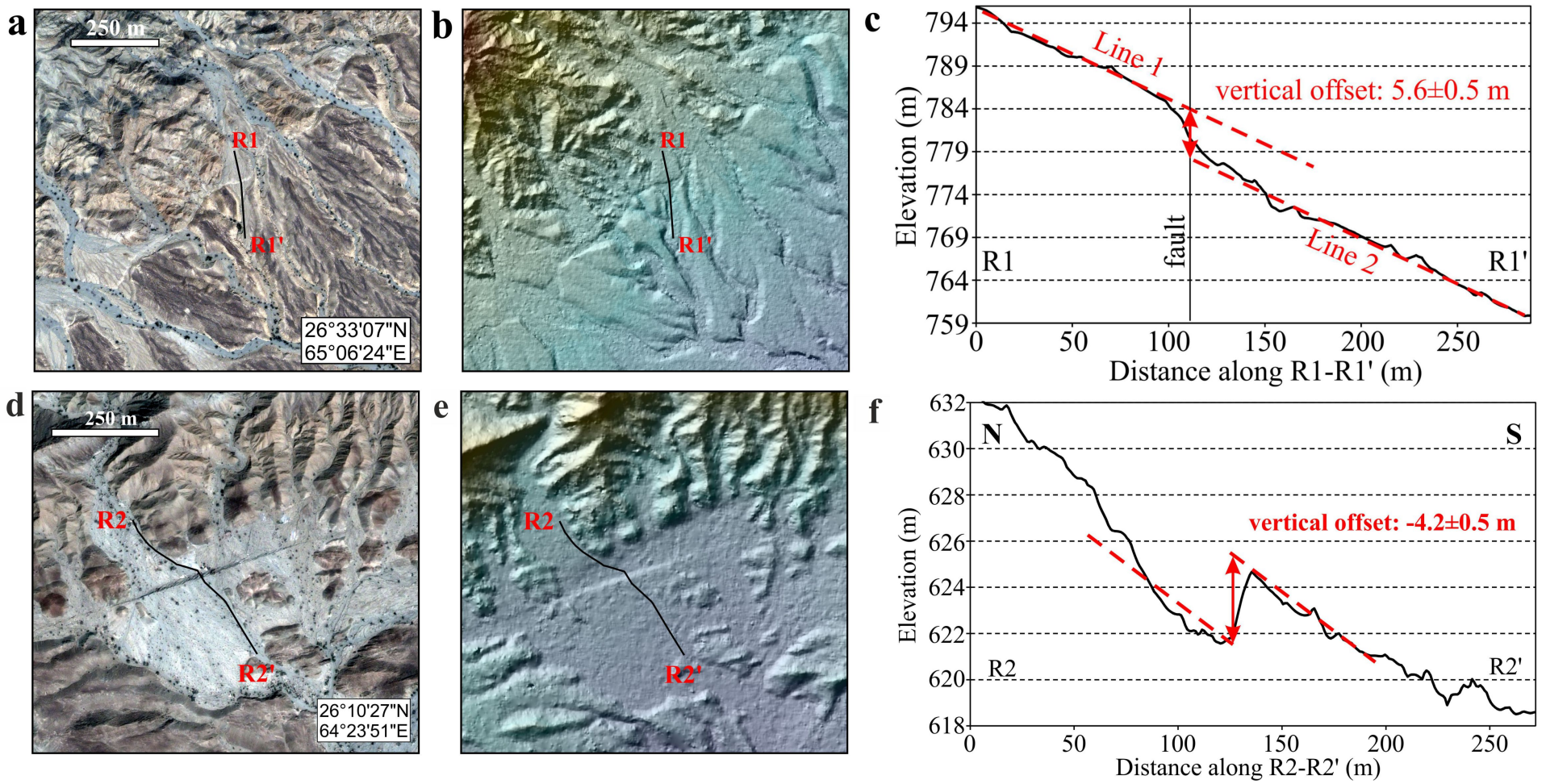


Figure 4.4: (top) Maximum vertical displacement in the 2013 Balochistan earthquake. (a) Pleiades imagery showing the earthquake rupture. (b) Shaded-relief Pleiades DEM. (c) Elevation profile R1-R1′ across the alluvial fan surface shows the vertical offset at this location is 5.6 m (north-side-up), the maximum vertical offset in the 2013 earthquake. (bottom) An example of south-side-up vertical motion due to rupture complexity. (a) Post-earthquake Pleiades imagery showing the surface rupture. (b) Shaded-relief Pleiades DEM. (c) Elevation profile R2-R2′ across the river channel shows the vertical offset at this location is 4.2 m (south-side-up).

4.3.2 Cumulative Surface Slip

To test the hypothesis that the kinematics of the Hoshab fault switches between thrust and strike-slip faulting through successive earthquake cycles (*Avouac et al.*, 2014; *Zinke et al.*, 2014; *Barnhart et al.*, 2015), we located 6 sites in the post-earthquake Pleiades imagery and DEM where there is convincing evidence for lateral and vertical displacements accumulated in past earthquakes (Figures 4.2 and 4.5, Table 4.1, and Appendix A). The cumulative surface slip through multiple earthquakes has a consistent sense with that found for the 2013 earthquake, with a constant local ratio of vertical to horizontal slip (Table 4.1). For example, a gully in Figure 4.2c shows a 39-m lateral offset with 7-m north-side-up vertical motion, which is approximately four times larger than the slip found for the 2013 earthquake at this location (10-m lateral offset with 1.8-m north-side-up vertical motion). An alluvial fan surface is offset by 21 m laterally and 4.3 m vertically (south-side-up) (Figure 4.5), which is twice the slip in the 2013 event at this site (10-m lateral and 2.2-m south-side-up vertical offsets).

Table 4.1: Sites showing cumulative lateral (positive for left-lateral strike-slip) and vertical (positive for north-side-up) displacements on the Hoshab fault. Sites 3–6 are presented in Appendix A.

Site	Location		2013 earthquake displacements			Cumulative displacements		
	Latitude	Longitude	Lateral (m)	Vertical (m)	Ratio	Lateral (m)	Vertical (m)	Ratio
Figure 4.2	26°47'35"N	65°20'20"E	10.0± 0.7	1.8± 0.2	5.6	39± 4	6.5± 0.4	6.0
Figure 4.5	26°41'50"N	65°15'50"E	10.1± 0.3	-2.2± 0.2	5.1	21± 4	-4.3± 0.2	4.9
Site 3	27°04'05"N	65°28'18"E	3.3± 0.7	0.3± 0.3	11.0	40± 5	4.3± 0.2	9.3
Site 4	26°10'43"N	64°25'05"E	6.7± 0.7	1.4± 0.4	4.8	41± 6	7.4± 0.6	5.5
Site 5	26°47'12"N	65°20'07"E	10.0± 1.0	1.4± 0.3	7.1	61± 7	10.5± 0.2	5.8
Site 6	26°11'17"N	64°26'22"E	6.6± 2.5	0.9± 0.4	7.3	40± 5	4.7± 1.9	8.5

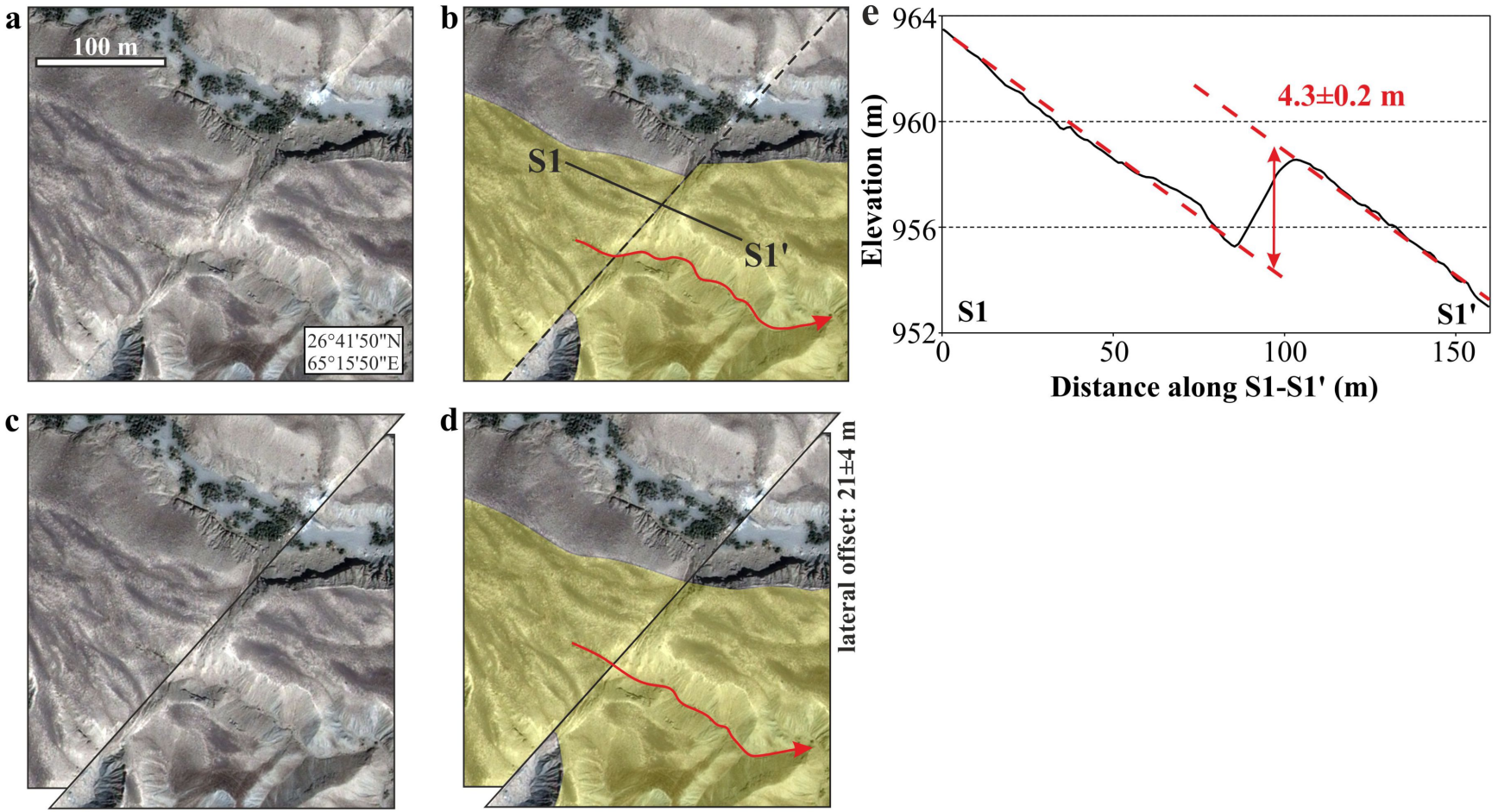


Figure 4.5: Cumulative displacements along the Hoshab fault. (a) Post-earthquake Pleiades imagery. (b) Annotation showing the offset alluvial fan surface (yellow polygon) and gully (red line). (c) Restoration of the alluvial fan surface and gully. (d) The cumulative lateral offset at this site is 21 m. (e) Elevation profile S1-S1′ across the fan surface shows the cumulative vertical offset at this site is 4.3 m (south-side-up). Surface displacement of the 2013 event (10.1 m lateral and 2.2 m vertical) was measured 2 km southwest of this location.

4.3.3 Fault Dip

We applied the classic structural geology approach of calculating fault dip from the surface trace as it crosses undulating topography (*Tearpock and Bischke*, 2002) to the Pleiades topography (see Appendix B for details). For each segment along the Hoshab fault that we mapped (>120 m in length and with a topographic variation of ≥15 m), we used a set of points along the rupture and ran the random subsampling described in Appendix B to estimate the best-fitting fault plane. The dip varies from 69°N in the northern section where the rupture initiated, to 62°N in the southern section, in good agreement with the joint inversion result of coseismic geodetic observations and global low frequency W-phase waveforms (*Avouac et al.*, 2014; *Jolivet et al.*, 2014) (Figure 4.6). For comparison, we also estimated the average dip (θ) of each fault segment (fault segments are defined by *Avouac et al.*, 2014) by combining vertical (V) and fault-normal (N) offsets using the relationship $\theta = \tan^{-1}\frac{V}{N}$ (*Zhou et al.*, 2015b). To obtain the fault-normal offsets, we resolved the east-west and north-south components of the surface displacement from *Barnhart et al.* (2015) onto the fault-normal direction. Weighting by the uncertainties of the offsets (Figure 4.6a), we obtained average vertical/fault-normal offsets of 1.4±0.6 m/1.2±0.3 m, 2.0±0.7 m/1.6±0.3 m, 2.0±0.8 m/1.4±0.2 m, 2.7±1.2 m/1.9±0.2 m, 2.0±0.8 m/1.2±0.1 m, and 1.3±0.5 m/0.8±0.1 m for each fault segment (from south to north); the corresponding dips are estimated to be 49±13°, 51±12°, 55±11°, 55±12°, 59±9° and 58±10° (Figure 4.6b). The three independent estimates are consistent within the estimated error (Figure 4.6b), except for the fifth segment (from south to north) where we found a slightly larger difference (12°) between our estimates and those of *Avouac et al.* (2014). The estimates obtained by determining a best-fitting plane show a variation from 45° to 69° along this segment, in which case average estimates of fault dip over tens of kilometres may have oversmoothed the fault structure at the surface (from $\theta = \tan^{-1}\frac{V}{N}$), as well as at depth (from *Avouac et al.* (2014)).

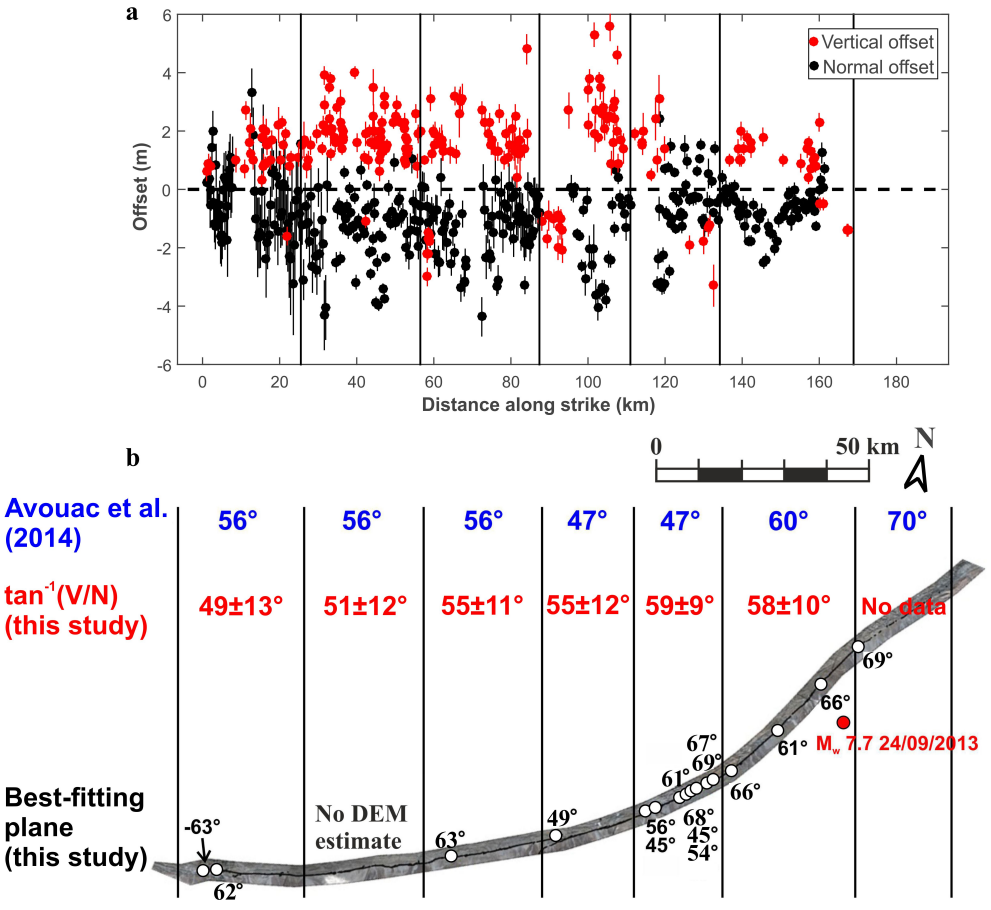


Figure 4.6: (a) Vertical and fault-normal offsets in the 2013 Balochistan earthquake. Vertical offsets are from *Zhou et al.* (2015a). Fault-normal offsets are calculated from the displacement field obtained by cross-correlating pre- and post-earthquake WorldView images (*Barnhart et al.*, 2015). (b) Dip estimates along the Hoshab fault from our study (numbers in black, positive for north-dipping), the inversion result of global low frequency W-phase waveforms (numbers in blue at the top) (*Avouac et al.*, 2014), and the method by combining the average vertical (V) and fault-normal (N) offsets along each segment (numbers in red near the top). White dots denote the sites where we calculated the fault dip from the Pleiades topography. Black vertical lines indicate fault segmentation prescribed in the modelling (*Avouac et al.*, 2014).

4.4 Discussion

4.4.1 Endpoint of Earthquake Ruptures on the Hoshab Fault

The surface trace of the 2013 earthquake appears to be relatively continuous (despite the two small restraining stepovers) (Figure 4.7) and the fault geometry (dip) appears to be smooth with gradual changes on a spatial scale of tens of kilometres (Figure 4.6b), which leads to an open question as to why the rupture suddenly stopped in the south with the surface displacement decreasing from 6 m to zero within a 12-km zone. By estimating the dip at a smaller scale with our method, we found a 3.7-km-long segment dipping

63°S with north-side-up left-lateral normal slip at the end of the main trace, which we interpret to be a response to localised extension (Figure 4.8a). On closer examination, we identified many discontinuous surface cracks within the stepover (Figures 4.8b and 4.8c), but the rupture did not propagate onto the previously unmapped western fault. The 2013 rupture ended in a stepover (3-km-wide, 12-km-long). This stepover could have resulted from the oblique orientation that the main Hoshab fault has to the regional slip vector (*Cunningham and Mann*, 2007). It is also possible that this is a relay stepover due to strike-slip motion on the overlapping western and eastern strands (*Peacock and Sanderson*, 1991). The abrupt decrease in surface slip from 6 m across the stepover (Figure 4.7c) indicates that this stepover has significantly dissipated seismic energy. The high topographic relief across the western fault shows long-term deformation (Figure 4.8d), but there is no clear evidence for surface ruptures from past earthquakes. We therefore suggest that this previously unidentified stepover (with a significant change in fault dip) may act as the endpoint of earthquake ruptures on the Hoshab fault (*King and Nábělek*, 1985; *Wesnousky*, 2006).

4.4.2 Long-term Fault Kinematics

The occurrence of the 2013 Balochistan earthquake has led to suggestions that the Hoshab fault may accommodate most of the motion between the Makran and India (*Avouac et al.*, 2014; *Jolivet et al.*, 2014; *Zinke et al.*, 2014; *Barnhart et al.*, 2014, 2015). Assuming that the observed relative motion across the eastern Makran is eventually localised on the Hoshab fault, and given an average of 8-m of strike-slip motion (ignoring the ends where slip decreases) and 1.6-m shortening in the 2013 event, it would require an M_w 7.7 earthquake every 800 years to accommodate the 1 cm/yr strike-slip motion (*Szeliga et al.*, 2012), but a much shorter recurrence interval (∼200-270 years) if the earthquakes take-up the 6 mm/yr shortening in the west. It is this shortening deficit that has led to the hypothesis that the kinematics of the Hoshab fault slip switches between thrust and strike-slip faulting in successive earthquake cycles (*Avouac et al.*, 2014; *Zinke et al.*, 2014; *Barnhart et al.*, 2015). However, our observations of the constant local ratio of vertical to horizontal slip along the fault through multiple past earthquakes indicates that the Hoshab

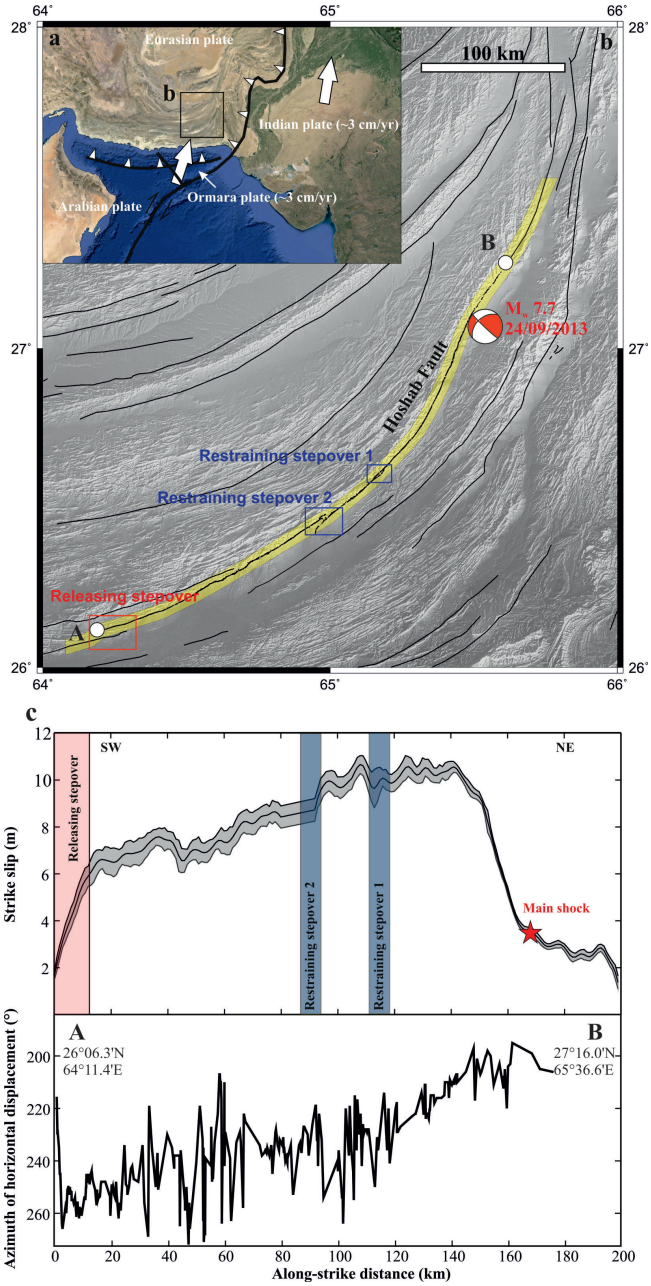


Figure 4.7: Stepovers along the Hoshab fault. (a) The eastern Makran. (b) Yellow polygon denotes the coverage of the post-earthquake Pleiades imagery. (c) Surface strike-slip displacement in the 2013 earthquake derived from cross-correlating pre- and post-earthquake Landsat-8 imagery (*Avouac et al.*, 2014). Blue boxes show two restraining stepovers, which have been identified in previous studies. These restraining stepovers did not appear to influence the rupture process. We have identified a stepover at the end of the main trace (red box). The surface slip decreased abruptly to zero from 6 m over ~15 km across this stepover. The azimuth of horizontal displacement was measured from visual analysis of offset geomorphic features.

fault has maintained the same style of faulting in the Late Quaternary. Cumulative displacements are multiples (2, 4, 5, 6 and 12 times) of the 2013 slip (Table 4.1), suggesting that this fault may have experienced characteristic-slip behaviour (*Klinger et al.*, 2003, 2011).

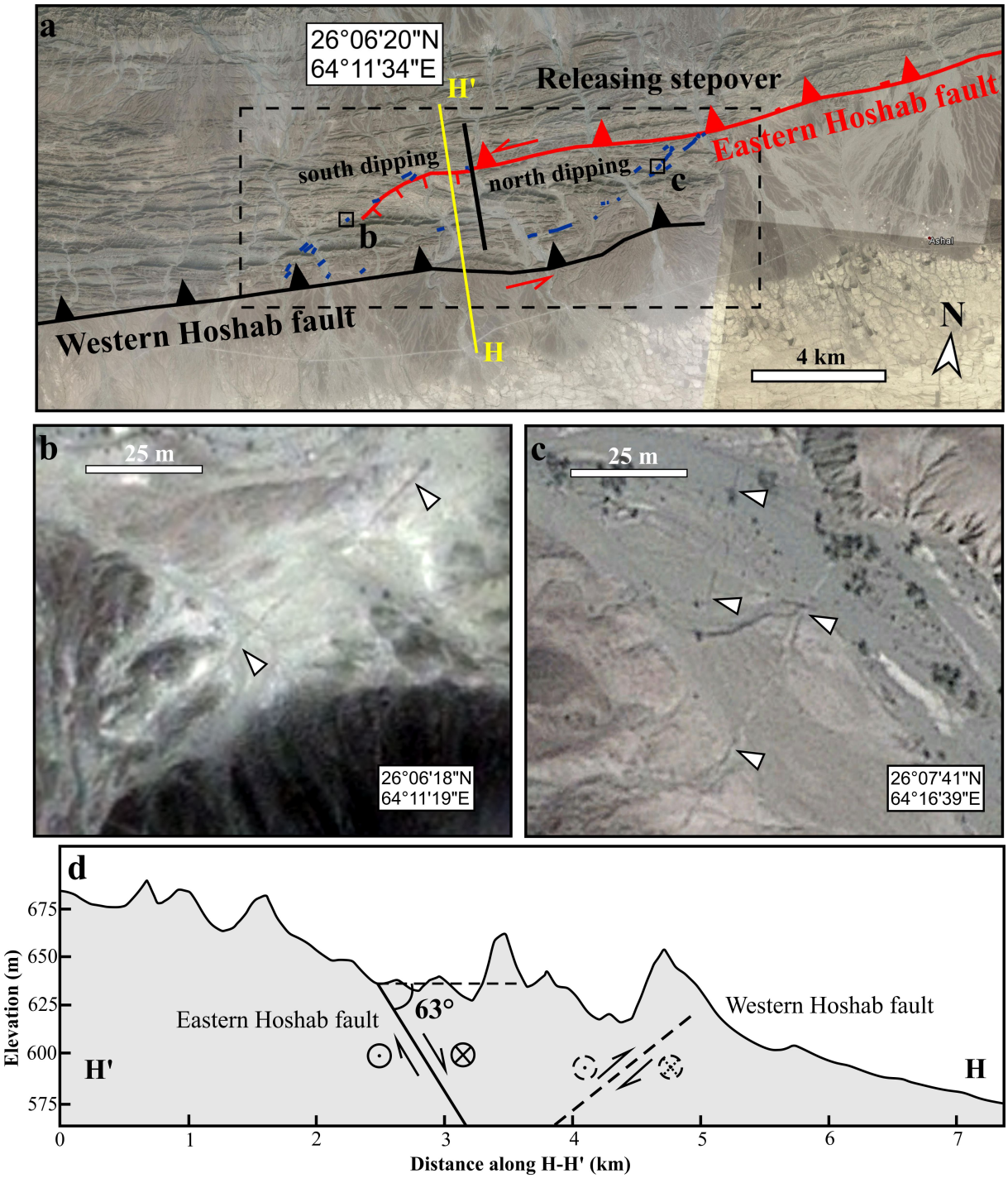


Figure 4.8: Termination of the 2013 rupture at the southern end of the Hoshab fault. (a) Google Earth imagery (17th December, 2013) showing the stepover (see Figure 4.7b for location). Red line denotes the surface rupture in the 2013 earthquake. Black line denotes the Western Hoshab fault. We did not find any clear evidence for surface ruptures on this western fault. Blue lines indicate surface cracks within the stepover. (b) and (c) are post-earthquake Pleiades imagery showing surface fractures (indicated by the white arrows) in the stepover. (d) Elevation profile (from the 90 m SRTM DEM) along H-H′ shows long-term deformation on the western Hoshab fault.

4.4.3 Distributed Faulting in the Eastern Makran

Previous arguments on the long-term fault kinematics (*Avouac et al.*, 2014; *Zinke et al.*, 2014; *Barnhart et al.*, 2015) suppose deformation is concentrated on the Hoshab fault. We remapped active faults in the eastern Makran (*Lawrence et al.*, 1981) through an analysis of the landscape using satellite imagery and topography, and found preserved fault scarps and lateral displacements in old alluvial fans and gullies on a series of regional faults (F1-F5) subparallel to the Hoshab fault (Figure 4.9). We did not observe any fault scarps in the youngest generation of alluvial fans on any of the faults, which was also the case for the Hoshab fault until 2013; in eastern parts of Iran, the youngest generation of alluvial fans are typically 8-10 kyr in age (*Walker and Fattahi*, 2011), suggesting that the last event on these faults may have occurred >8 kyr ago. The tectonic setting of these subparallel faults F1-F5 is similar to the Hoshab fault that separates a bedrock cored range in the north and a Cenozoic sedimentary basin to the south; the preserved lateral offsets on these faults (e.g., 8 m in Figure 4.9c and 4.9e, and 24 m in Figure 4.9d) are also of similar magnitude to the surface slip on the Hoshab fault. Therefore, the faults may all behave in a very similar way, together accommodating a large part of the deformation between the Makran and Peninsular India by failure in rare (every few thousand years), large ($M_w \geq$ 7.5) earthquakes.

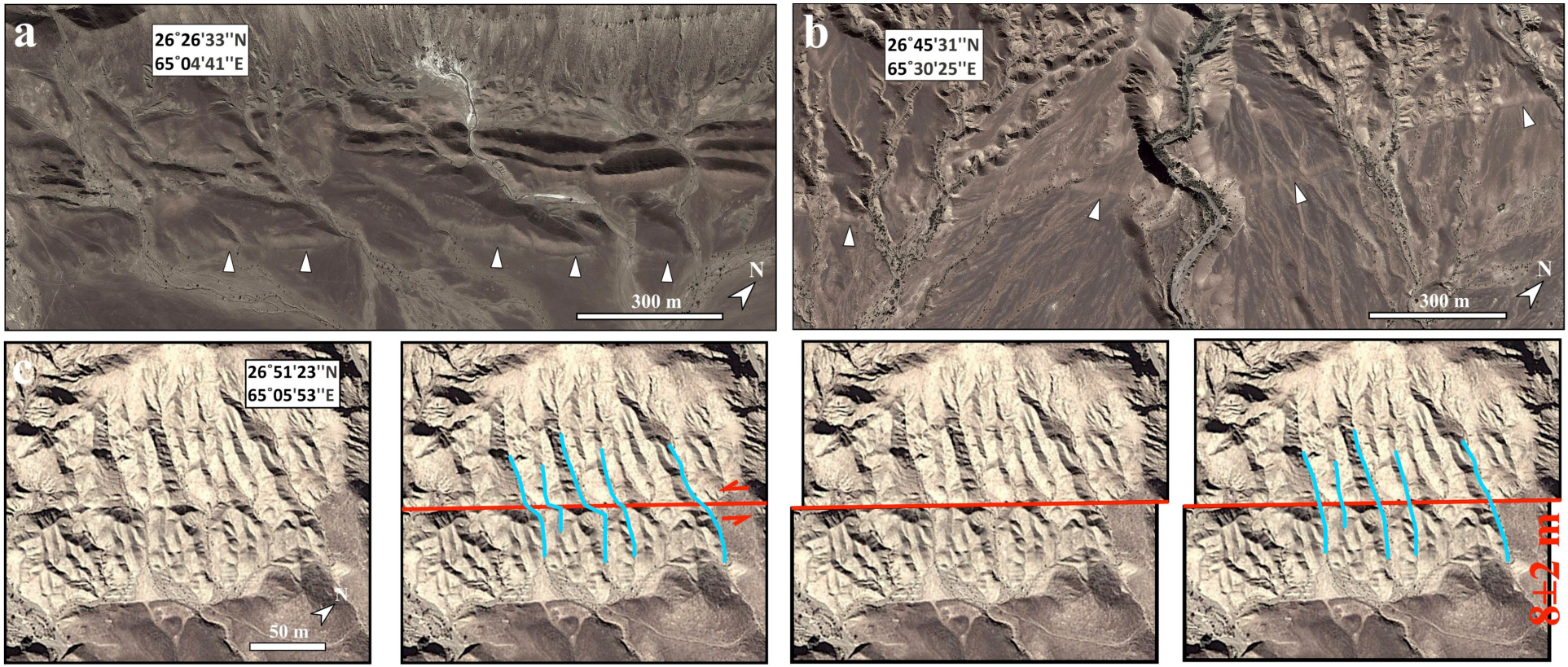


Figure 4.9: Google Earth imagery showing preserved fault scarps (indicated by white arrows) and lateral offset on faults subparallel to the Hoshab Fault (see Figure 4.1 for location). Preserved fault scarps on (a) F2 and (b) F3. (c) The 8-m lateral offset from restoring the gullies (blue lines) on F1 is of similar magnitude to the surface slip in the 2013 Balochistan earthquake.

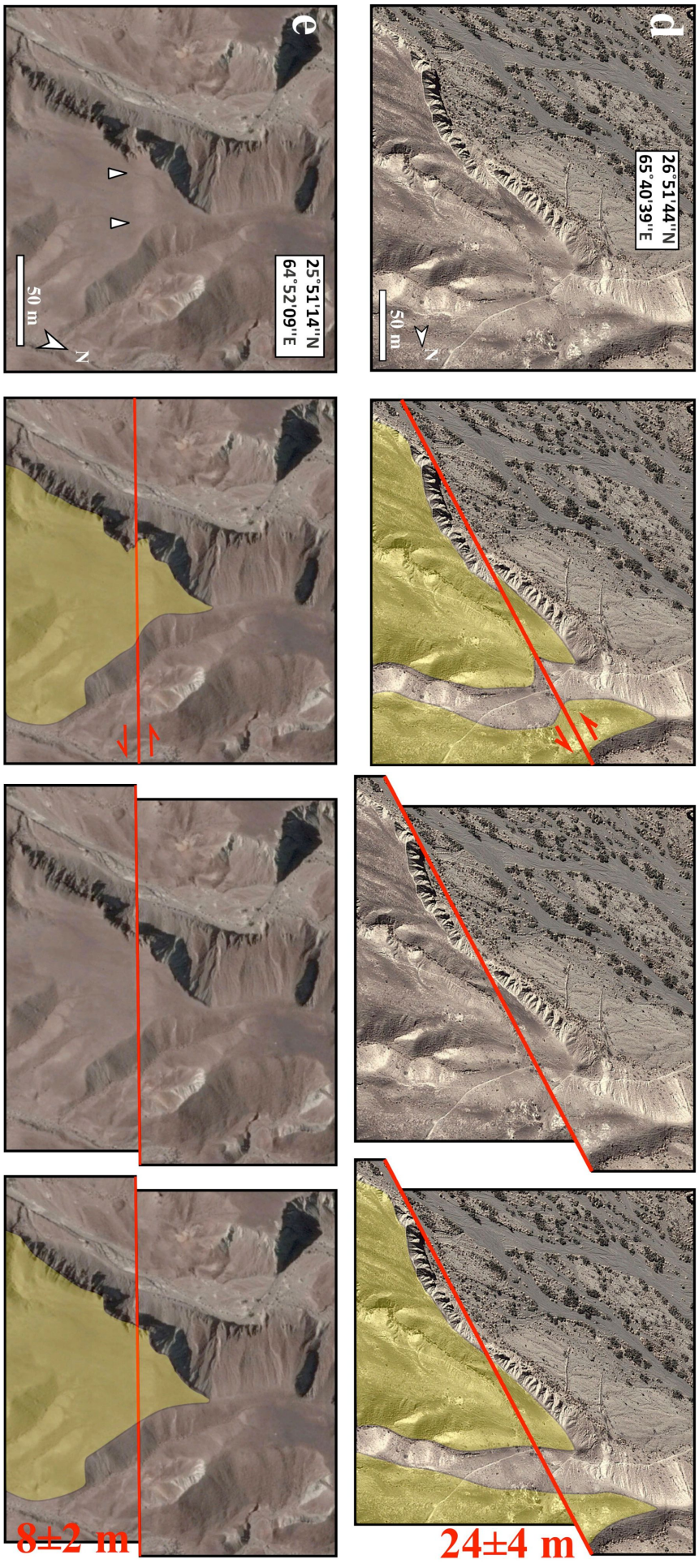


Figure 4.9 Cont.: (d) An alluvial fan surface on F4 was offset by 24 m. (e) An alluvial fan surface on F5 was offset by 8 m.

Distributed faulting makes it unlikely that the region south of the Hoshab fault rotates as rigid block about a not-too-distant pole of rotation (*Barnhart et al.*, 2014). Nonetheless, their combined effect will be to remove material laterally from the region of shortening. We note that the western end of the Hoshab fault rupture makes an angle of about 55° with respect to the shortening direction. Strike-slip motion of ∼1 cm/yr of the region south of the Hoshab fault relative to north of it (*Szeliga et al.*, 2012) therefore provides a component of motion of ∼6 mm/yr in the shortening direction (∼1 cm/yr× cos 55°). Together with thrusting on the faults similar to that in the 2013 event (∼2 mm/yr assuming an average shortening of 1.6 m in the 2013 earthquake and an earthquake recurrence interval of 800 years), this could accommodate the total shortening required.

Distributed faulting also provides other possibilities for accommodating the shortening with different faults exhibiting different ratios of strike-slip to dip-slip motion. It has been suggested that the Hoshab fault is segmented and exhibits bimodal slip behaviour (*Barnhart et al.*, 2015), with its northern segment exhibiting primarily strike-slip motion, whilst the southern segment moves mainly as a thrust except when both segments fail and strike-slip motion from the northern segment propagates to the south. It is argued that this hypothesis is supported by the large topographic relief across the southern segment of the Hoshab fault. We find that relief across the southern portion of the Hoshab fault occurs in two steps, part across the main Hoshab fault, and a part that is twice as large across the previously unidentified northern splay (Figure 4.10). Our observations of horizontal to vertical motion on the southern segment of the Hoshab fault suggest it has failed in the same manner in earlier events. However, the overall long-term shortening could be accommodated by standard slip partitioning between the main Hoshab fault and its northern splay. A few old alluvial fans were also identified by *Barnhart et al.* (2015) as providing evidence for predominant thrust motion on the southern segment of the Hoshab fault. We measured the vertical offset at one of these sites; the 9 m observed (Figure 4.11) is only approximately 6 times that of the 2013 vertical offset, and can easily be explained by a few earthquakes moving in the same way as the 2013 event.

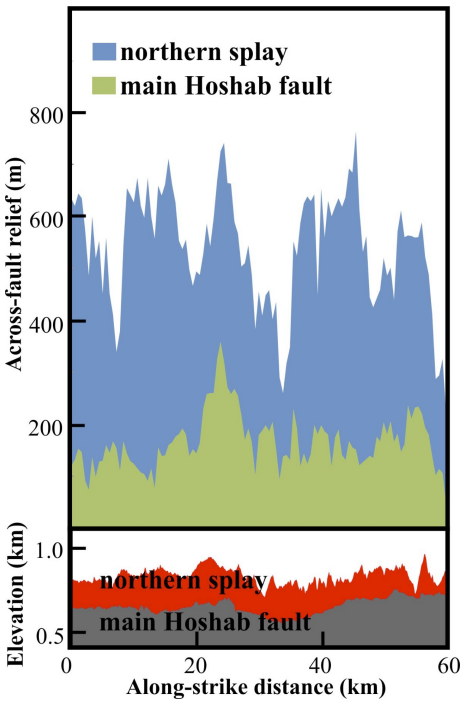


Figure 4.10: (top) Across-fault topographic relief along the southern segment of the Hoshab fault. The topographic relief is defined by the difference between the maximum and minimum elevations along a profile perpendicular to the fault trace from the Shuttle Radar Topography Mission (SRTM) DEM (*Farr et al.*, 2007). (bottom) The elevation along the main Hoshab fault and its northern splay (as shown in Figure 4.1).

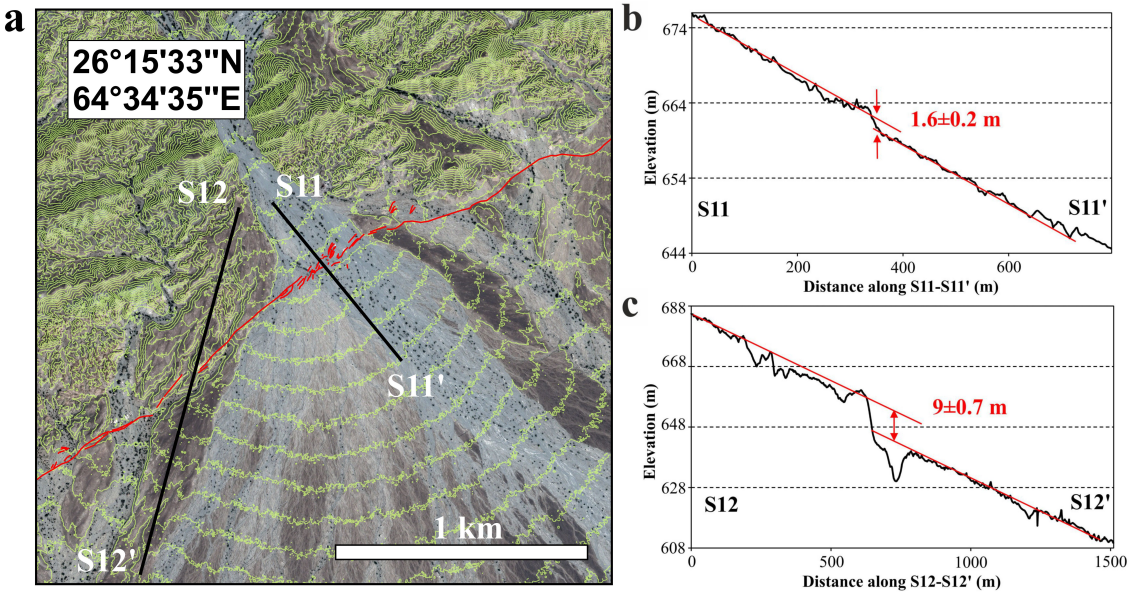


Figure 4.11: (a)An example of long-term thrust motion recorded across the alluvial fans. Red line shows the 2013 surface rupture. Yellow lines are contour lines with an interval of 5 m. Long-term strike-slip motion is not preserved at this location as surface slip is not localised to a single fault rupture trace. It has been suggested from observations of this site that the Hoshab fault alternates its behaviour between strike-slip and dip-slip in order to accommodate the shortening deficit. However, the cumulative vertical offset (9 m in c) is only 6 times larger than that in the 2013 event (1.6 m in b). This deficit does not require pure thrust faulting.

4.5 Conclusions

In this study, we use Pleiades stereo imagery to resolve a current controversy of the 2013 M_w 7.7 Balochistan earthquake, in which it has been argued that kinematics of the Hoshab fault switches between strike-slip and dip-slip (*Avouac et al.*, 2014; *Zinke et al.*, 2014; *Barnhart et al.*, 2015). By determining the vertical component of motion on the fault for the first time, we find the 2013 earthquake in fact exhibits typical behaviour for this fault. The cumulative surface displacements from past earthquakes on the Hoshab fault show a constant local ratio of vertical to horizontal slip, suggesting that the Hoshab fault has persisted with the same style of faulting in the Late Quaternary. By further mapping of subparallel faults in the eastern Makran, we also show that failure occurs in a distributed fashion and is not constrained solely to the Hoshab fault, providing an explanation for long repeat times and hence a lack of seismic events in previous decades. Based on the above arguments, we argue that the strike-slip earthquake in 2013 is not a rare event induced by dynamic stresses, but is instead a representative event on the Hoshab fault. The curvature of the fault and the rotation of its slip vector may arise from a non-uniform stress field. Although we do not have a detailed strain field for the region, single line-of-sight velocity fields observed by radar interferometry (*Fattahi et al.*, 2014a; *Lin et al.*, 2015; *Sun*, 2015) do display the same curvature as the faults. It is therefore plausible that the principal strain and stress axes also rotate along the length of the faults. The arguments depend on detailed 3D near-field observations to fully characterise the kinematics of the 2013 Balochistan earthquake. The region of the earthquake provides an example of distributed faulting in a remote and inaccessible area amenable to detailed near-field investigation by the new generation of very high-resolution satellite stereo imagery.

The case study of the 2013 Balochistan, Pakistan earthquake also suggests that small-scale features such as variations in along-strike fault dip may be essential to identify and investigate geometrical controls on earthquake ruptures. No significant geometrical complexity has been observed in previous studies of the 2013 earthquake (*Avouac et al.*, 2014; *Jolivet et al.*, 2014; *Barnhart et al.*, 2014). However, by calculating the 3D fault geometry, we found a variation in dip at the end of the main trace within a stepover. This

stepover may act as the endpoint of earthquake ruptures in the south of the Hoshab fault. Applied to future earthquakes, or any faults with traces and other planar markers (such as bedding planes) at the surface, LiDAR surveys and Pleiades as well as other (sub-metre) VHR (such as WorldView and GeoEye) stereo imagery will provide detailed information of fault geometry to complement field-based observations and modelling results, which can be very useful in dynamic modelling of earthquake rupture (*Harris*, 2004), hazard assessment of older fault zones, mapping and mining exploration.

Chapter 5

Coseismic and Postseismic Displacements from the 1978 M_w 7.3 Tabas-e-Golshan Earthquake in Eastern Iran

Adapted from Zhou, Y., R. T. Walker, J. Hollingsworth, M. Talebian, X. Song and B. Parsons (2016), Coseismic and postseismic displacements from the 1978 M_w 7.3 Tabas-e-Golshan earthquake in eastern Iran, *Earth and Planetary Science Letters*, doi: 10.1016/j.epsl.2016.07.38.

5.1 Introduction

Measurements of surface deformation in earthquakes and by postseismic creep reveals how active folds and faults evolve (*Burbank and Anderson*, 2011; *Copley*, 2014). They are the most valuable source of data for accurate description and understanding of continental tectonics, and for investigating present and future seismic hazard (*Molnar et al.*, 1973; *Berberian*, 1981; *Molnar and Lyon-Caen*, 1989; *Tapponnier et al.*, 1990; *Hubbard and Shaw*, 2009). Large (moment magnitude (M_w) $\geq$ 7) continental earthquakes often occur on faults that were previously unmapped or poorly studied, due to the long recurrence times between events and their subtle geomorphological expression in the landscape

(*Jackson*, 2001; *Fialko et al.*, 2005; *Funning et al.*, 2005; *England and Jackson*, 2011; *Oskin et al.*, 2012; *Zhang*, 2013; *Zhou et al.*, 2015a). Large blind thrust earthquakes are rare in the modern age (post 1990), but they are hazardous, and so there is a need to re-examine older events. The September 16, 1978 M_w 7.3 Tabas-e-Golshan earthquake in eastern Iran (hereafter referred to as the Tabas earthquake) is an example that occurred on a series of previously unrecognised blind thrust faults. It is the only known large event in the epicentral area for at least the last 1000 years, and completely demolished the oasis town of Tabas, killing ∼11000 people, 85% of its population (*Berberian*, 1979; *Berberian et al.*, 1979; *Walker et al.*, 2003, 2013).

Berberian (1979) mapped 85 km of discontinuous surface ruptures immediately after the 1978 earthquake. Much of the surface faulting took the form of small amounts of slip on multiple bedding planes, suggesting that much of the slip at depth failed to reach the surface and was instead accommodated as flexural-slip folding. The maximum displacement across the main frontal thrust fault on the segment south of Tabas was measured to be ∼35 cm, but adjacent bedding slip totalled ∼150 cm (*Berberian*, 1979). Because most of the coseismic slip was concentrated at depth (*Berberian*, 1982; *Walker et al.*, 2003), it is not possible to determine the seismogenic slip and the sub-surface structure from mapping of discrete surface ruptures alone. *Copley* (2014) used interferometric synthetic aperture radar (InSAR) to image shallow creep on the fold ∼6 km S-E of the town of Tabas (hereafter referred to as the Tabas fold) 30 years after the event. However, the coseismic and most of the postseismic displacements were not measurable (*Copley*, 2014), since no geodetic data, such as the Global Positioning System (GPS) and InSAR, were available at the time of the 1978 Tabas earthquake.

The declassification of Hexagon Keyhole-9 US (hereafter referred to as KH-9) images allows us to investigate historical earthquakes back to the 1970s (*Burnett*, 2012; *Hollingsworth et al.*, 2012). In this study, we first use sub-pixel correlation of KH-9 images acquired in 1974 with SPOT-2 in 1991, and also modern high-resolution SPOT-6 data, to determine the horizontal displacements associated with the 1978 Tabas earthquake, from which we invert for the fault structure and earthquake slip. We also use six pre-earthquake aerial photographs acquired in 1956 and a SPOT-6 stereo data set in 2013 to generate respec-

tively the pre- and post-earthquake topography for one of the main fold segments. By differencing the pre- and post-earthquake topography, we measure the height changes to better constrain the fault slip model. By combining the fault slip model and analysis of the long-term surface folding observed in the SPOT-6 topography, we constrain active thrust faulting in this region during the late Quaternary.

5.2 Tectonic Background of the 1978 Tabas Earthquake

The active deformation of Iran, as a result of Arabia-Eurasia convergence at a rate of ~25 mm/yr at longitude 60° (*Vernant et al.*, 2004b; *Walker and Jackson*, 2004), is characterised by distributed folding, reverse faulting, and strike-slip faulting along a series of inherited structures (*Berberian*, 1981; *Jackson et al.*, 1995; *Walker and Jackson*, 2004) (Figure 5.1a). Studies based on plate models and GPS measurements indicate that up to half of the total Arabia-Eurasia shortening (~10-15 mm/yr) is taken up by north-south shortening in the Zagros mountains of southwestern Iran (*Jackson et al.*, 1995; *Tatar et al.*, 2002; *Hessami*, 2002; *Walpersdorf et al.*, 2006) with the Alborz accommodating a further 5±2 mm/yr north-south shortening (*Vernant et al.*, 2004a), leaving ~15 mm/yr north-south right-lateral shear between central Iran and western Afghanistan (*Walker and Jackson*, 2004; *Mousavi et al.*, 2013; *Walpersdorf et al.*, 2014). This ~15 mm/yr north-south shear (*Vernant et al.*, 2004b; *Walpersdorf et al.*, 2014) is accommodated on several right-lateral strike-slip faults bordering the Dasht-e-Lut Desert, including the East Neh (1.75-2.5 mm/yr from *Meyer and Le Dortz* 2007), West Neh (1-5 mm/yr from *Meyer and Le Dortz* 2007) and Zahedan faults in the east, and the Sabzevaran (~6 mm/yr from *Regard et al.* 2006), Gowk (~3.8–5.7 mm/yr from *Walker et al.* 2013; *Fattahi et al.* 2014b) and Nayband (~1.4 mm/yr from *Walker et al.* 2009 and ~1.8 mm/yr from *Foroutan et al.* 2014) segments in the west (Figure 5.1a). The 1978 Tabas earthquake occurred at the northern end of the Nayband fault where right-lateral strike-slip motion turns into thrusting that is manifest at the surface as a series of folds within Neogene basin deposits. The Tabas region had been quiescent for at least 1100 years until the 1978 earthquake

(*Berberian*, 1979). Through detailed field mapping 10 days after the earthquake, *Berberian* (1979) mapped extensive slip on folded Neogene bedding planes along the 85 km long system of folds, and some high-angle faults within the folds that are likely tensional (Figure 5.2), consistent with coseismic fold growth (e.g. *Walker et al.* 2003). *Berberian* (1979) also measured a maximum displacement of ∼35 cm along a discrete east-dipping reverse fault at the western margin of the Kurit fold segment (Figure 5.2). Assuming a single, simple rupture event, *Walker et al.* (2003) estimated an average slip of ∼3.3 m using a rupture velocity of ∼3.5 km/s, main shock source time function duration of 18 s, and typical ratio of average slip to rupture length ($\overline{\mu}/L$) of 5×10^{-5} (*Scholz*, 1982). The relatively small surface slip measured in the field (∼35 cm) implies that most of the coseismic slip at depth failed to reach the surface (*Walker et al.*, 2003). The source parameters of the main shock indicate slip on a detachment fault dipping ∼16°E with a centroid depth of ∼9 km and with an epicentre southeast of the folding (*Walker et al.*, 2003, 2013). Analysis of 329 aftershocks shows a concentration of events around depths of 5-10 km (*Berberian et al.*, 1979). *Copley* (2014) estimated ∼5 mm/yr postseismic afterslip on a steep ramp beneath the Tabas fold, extending to a depth of 4-5 km, from modelling InSAR observations in the interval 1996–1999 (Figure 5.2). By combining all the available information, and assuming that postseismic afterslip decays with time rapidly (*Segall et al.*, 2000), *Copley* (2014) inferred that the majority of the slip gradient was relaxed aseismically prior to 1996 by postseismic motion on a high-angle thrust ramp that connects the surface anticlines to the coseismic low-angle detachment fault at depth.

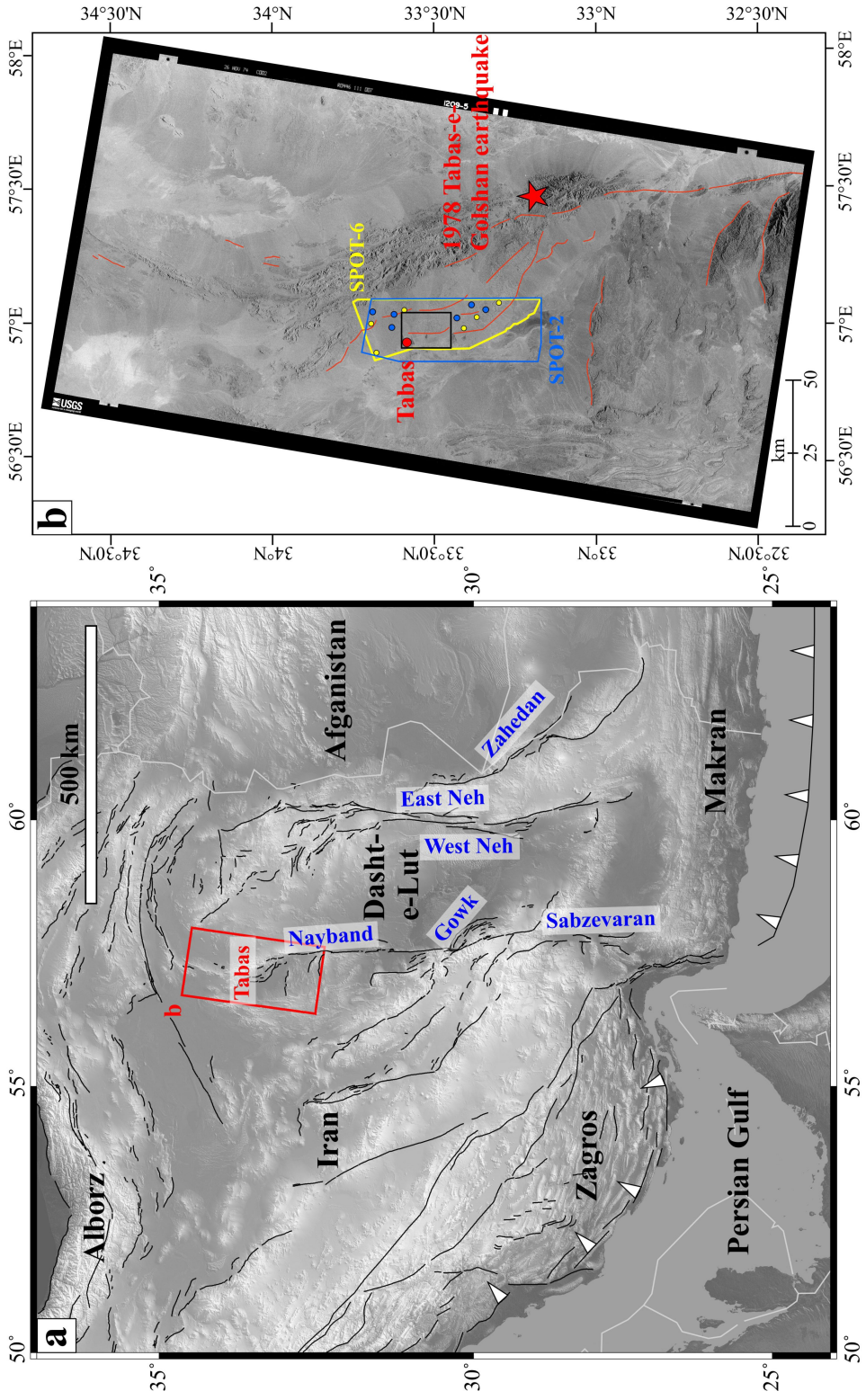


Figure 5.1: (a) Active faults (black lines) in Iran, from *Walker et al.* (2003). Red box shows the coverage of the pre-earthquake KH-9 image. (b) KH-9 image around the Tabas region. Red star indicates the epicentre of the 16 September, 1978 Tabas-e-Golshan earthquake, from *Walker et al.* (2003). Red lines are active faults. Red dot indicates the location of Tabas. Yellow polygon shows SPOT-6 stereo image coverage (Figure 5.2b). Yellow circles show the location of the GCPs used to co-register the KH-9 and SPOT-6 images. Blue polygon shows the SPOT-2 image coverage that we purchased for this study, with blue circles indicating the GCPs used to co-register the SPOT-2 and SPOT-6 images. Black box shows the area of Figure 5.3a.

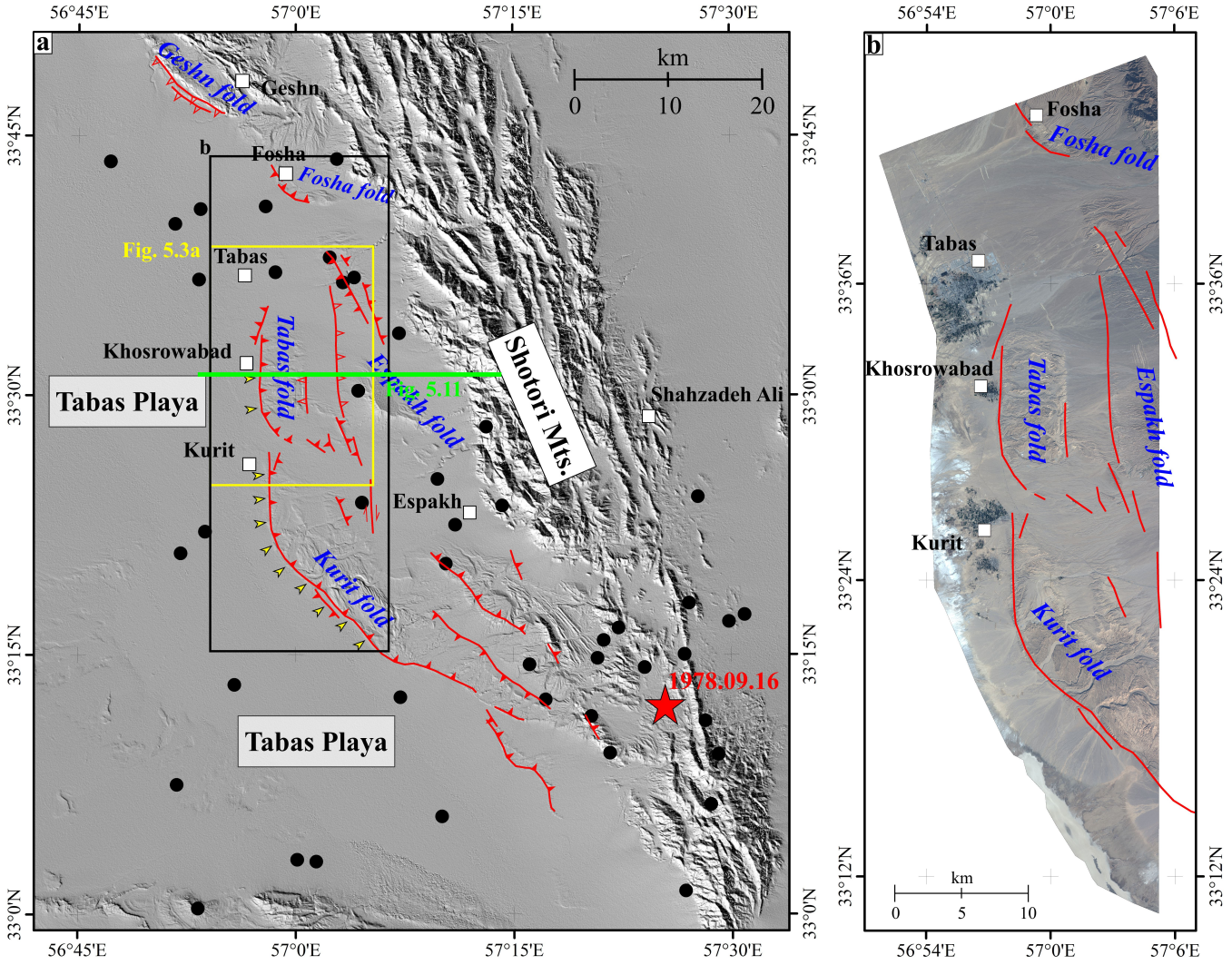


Figure 5.2: (a) Surface ruptures (red lines) observed in the field by *Berberian* (1979). Red filled triangles denote thrust faulting and open triangles are high-angle reverse faulting. Yellow arrows mark the segments that show afterslip in *Copley* (2014). Black dots are the epicentres of smaller earthquakes, from *Walker et al.* (2013). Green line shows the location of the topographic profile in Figure 5.11. (b) SPOT-6 orthoimagery showing the epicentral area of the 1978 Tabas earthquake. See (a) for location.

5.3 Image Processing

To measure the surface displacement associated with the 1978 Tabas earthquake, we acquired a KH-9 image obtained in 1974, six aerial photographs taken in 1956, a SPOT-2 image from 1991 and a SPOT-6 stereo data set from 2013 (listed in Table 5.1). Cross-correlation of the KH-9 and SPOT-2 imagery provides information about the coseismic and early postseismic motion, whereas the SPOT-2 and SPOT-6 imagery can be used to measure the horizontal motion in the later postseismic period. All cross-correlations include some component of postseismic motion. Furthermore, we use the aerial photographs to generate a pre-earthquake digital elevation model (DEM) and the SPOT-6 stereo imagery to generate a post-earthquake DEM. By differencing the two DEMs, we can also measure the height changes between 1956 and 2013. In this section, we describe the methods of processing these various images.

Table 5.1: Imagery used for determining surface displacements from the 1978 Tabas earthquake.

	Pre-earthquake		**Post-earthquake**	
	KH-9	**Aerial**	**SPOT-2**	**SPOT-6**
Time	9th Mar, 1974	13th Aug, 1956	6th Sep, 1991	29th Dec, 2013
Type	Frame camera	Frame camera	Pushbroom	Pushbroom
Resolution (m)	6-9	1-3	10	1.5
Focal length (cm)	30.5	15.524		

5.3.1 SPOT-6 Images Obtained in 2013

The SPOT-6 satellite was launched on the 9th September 2012, in a sun-synchronous orbit with a repeat cycle of 26 days (*Astrium*, 2013). It can provide 1.5 m resolution panchromatic and 6 m resolution multispectral images over a swath footprint of 60 km for high-resolution stereo mapping (*Astrium*, 2013). We purchased one tri-stereo data set tasked on the 29th December 2013 over an area of 918 km^2 (Figure 5.1b). Provided with the rational function models of the three SPOT-6 images, we processed the data using the Leica Photogrammetry Suite (LPS) with a pairwise pixel-by-pixel matching procedure (see Chapter 3 for the method). The point cloud extracted from the new automatic terrain extraction module (eATE) in LPS was filtered by averaging within a cell of 2 m and then gridded with a pixel spacing of 2 m (WGS84 UTM 40N). The SPOT-6 image was then

orthorectified using the 2 m DEM. The SPOT-6 orthoimage (Figure 5.2b) is used as the reference image for co-registration in the following sections.

5.3.2 KH-9 Image Obtained in 1974

The KH-9 mapping program consisted of 12 missions (mission numbers: 1205-1216) (*Burnett*, 2012). The first mission (1205) spanned from the 9th March to the 20th April 1973, with a duration of 42 days (*Burnett*, 2012). The program ended on the 14th October 1980 and a total of ∼29000 images with a resolution of 6-9 m were acquired. Each KH-9 image, with a footprint of 125 km × 250 km, can be purchased from the USGS (http://earthexplorer.usgs.gov/) for $30. However, the information about the camera system such as focal length, optical distortions and film size remains classified. It has been concluded from different experiments that KH-9 uses a camera similar to the NASA Large Format Camera (LFC), a 23×46 cm frame camera with a focal length of 30.5 cm (*Mollberg and Schardt*, 1988; *Surazakov and Aizen*, 2010; *Hollingsworth et al.*, 2012).

Figure 5.1b shows a KH-9 image covering the Tabas region, acquired on the 26th November 1974 in mission 1209. No post-earthquake KH-9 imagery is available on the USGS website (http://earthexplorer.usgs.gov/). The KH-9 image was processed using COSI-Corr (*Ayoub et al.*, 2009). We first used bilinear interpolation to resample the SPOT-6 orthoimage to 6 m to match the lower resolution KH-9 image. The KH-9 image was then co-registered to the 6 m SPOT-6 orthoimage using 7 ground control points (GCPs) collected 10-20 km from the Tabas fold where the maximum surface displacement was observed in both the field (*Berberian*, 1979) and the postseismic interferograms (*Copley*, 2014). Since we had no adequate pre-earthquake DEM (the DEM generated from the pre-earthquake aerial photographs contains large errors due to film distortions, discussed in Section 5.4.2), the KH-9 image was orthorectified using the post-earthquake SPOT-6 DEM. As a result, any height changes will cause an apparent horizontal signal (e.g. *Barišin et al.* (2015)). In our case, such influence (≤0.5 m) is insignificant compared to the tectonic signal (∼3.5 m), as discussed in Appendix D.

5.3.3 SPOT-2 in 1991

The SPOT-2 satellite was launched on the 22nd January 1990, and deorbited in July 2009. The products, including 10 m resolution panchromatic and 20 m resolution multispectral images, were acquired over a swath footprint of 60 km. Figure 5.1b shows the coverage (1000 km^2) of the SPOT-2 panchromatic image that we purchased for this study. It was acquired on the 6th September 1991 with an incidence angle of -2.2°. Following the same procedure as described in Section 5.3.2, we co-registered the SPOT-2 image to the SPOT-6 orthoimage using 6 GCPs (as shown in Figure 5.1b) and orthorectified it using the SPOT-6 DEM.

5.3.4 Aerial Photographs Obtained in 1956

Six aerial photographs covering the Tabas region were acquired on the 13th August, 1956, as part of a country-wide survey. The aerial photographs were scanned at a resolution of 1200 dpi × 1200 dpi using an EPSON Expression 11000XL scanner. We processed the aerial photographs based on a frame camera model in LPS to generate a pre-earthquake DEM. Interior orientation parameters consist of the focal length and the location of the principal point. The focal length (155.24 mm) is provided with the photograph, and the location of the principal point was estimated using the markers on the four edges of each image. The exterior orientation parameters (the location and three rotation angles of the camera) were estimated with a least-squares adjustment using 36 GCPs identified from the SPOT-6 imagery and DEM, along with 108 tie points (points whose ground coordinates are unknown, but can be identified over the overlapping areas between different images). After having solved the orientation parameters for all of these aerial photographs, we extracted a DEM (5 m spatial resolution) with eATE in LPS.

5.4 Results

5.4.1 Horizontal Displacement from Cross-correlation

We estimated horizontal displacements by cross-correlating the KH-9, SPOT-2 and SPOT-6 images in COSI-Corr (*Leprince et al.*, 2007). A correlation window of 64 pixels was used as a first step, followed by 32 pixels, with a step of 8 pixels (48 m). COSI-Corr outputs the E-W and N-S displacements (Figure C.1 in Appendix C) with sub-pixel accuracy (*Leprince et al.*, 2007). We also tested different parameters in the cross-correlation procedure (see Figure C.2 in Appendix C), and the results from relatively large correlation windows (32 × 32 pixels or larger) show a similar dislocation pattern, increasing our confidence in the validity of the results. In this study, we focused on the Tabas fold for three reasons: (1) the N-S displacement field was heavily contaminated by the scan artifact (Figure C.1), but the purely E-W thrust motion on the Tabas fold is free from such contamination; (2) it is located in the centre of the image, where the influence of orthorectification-induced horizontal motion is small (see Appendix D); (3) we have constraints on the structure from inversion of postseismic InSAR.

Figures 5.3a, 5.4a and 5.4d show the E-W displacement fields across the Tabas fold over different time intervals. In general, the relatively old alluvial materials within the folds preserve good coherence even 35 years after the earthquake. Despite the longer time interval, the cross-correlation result based on high-resolution imagery (Figure 5.3a) is much less noisy than that from low-resolution image matching (Figure 5.4a). To determine the displacement, we projected the measurements onto the fault-perpendicular direction (line AB in Figure 5.3a). There are some large localised westward displacements (negative values) over agricultural areas, which appears to be caused by farming, so we masked out those areas and only used the data points included in the dashed polygon. From the displacement profile in Figure 5.3b, we found an E-W offset of 3.4±0.3 m (i.e. shortening) from 1974 to 2013. Most of the displacement (2.9±0.2 m) occurred over the interval 1974-1991 (Figure 5.4b), with a small amount (0.3±0.1 m) over the interval 1991-2013 (Figure 5.4e).

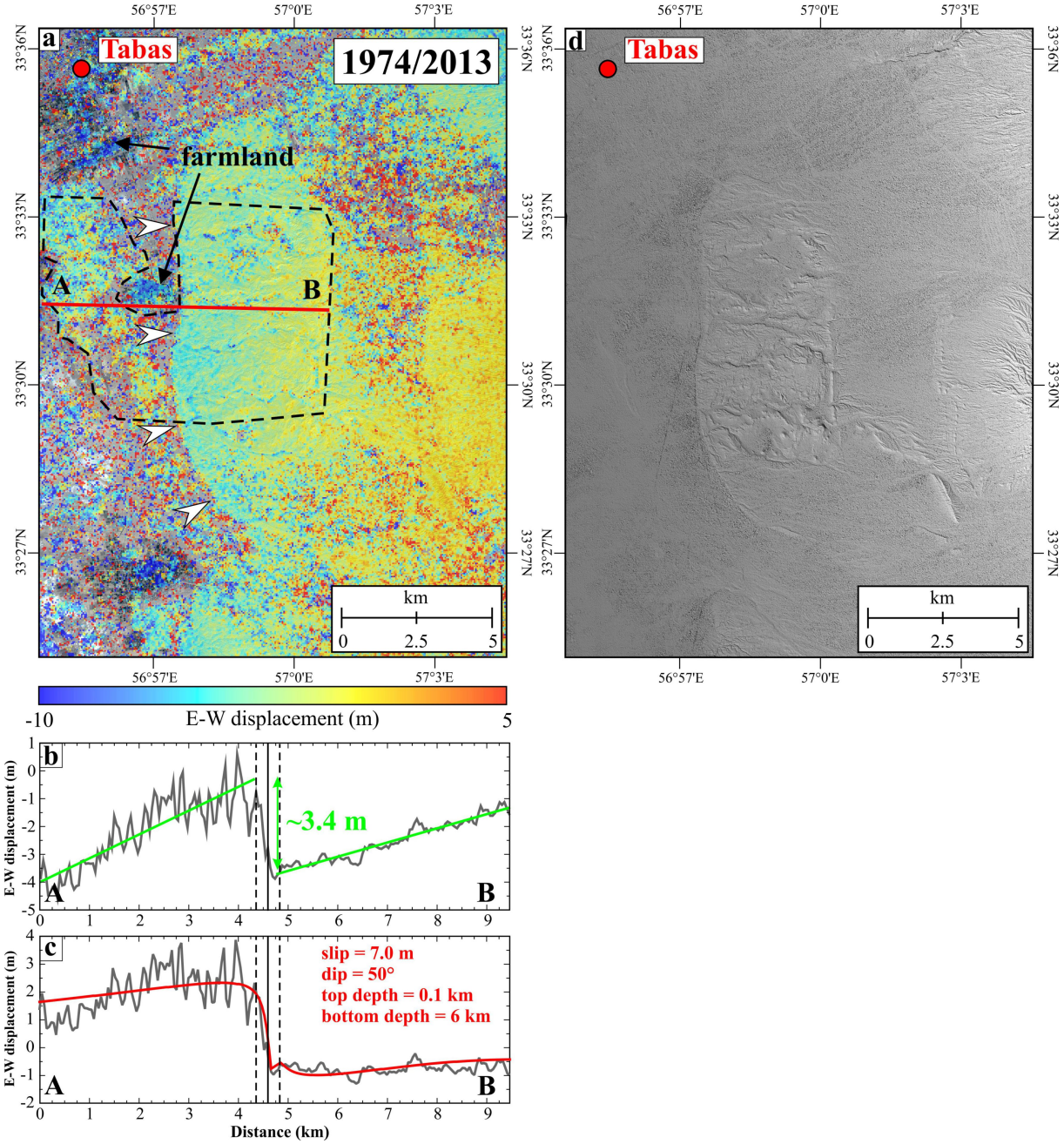


Figure 5.3: E-W displacement from cross-correlating the KH-9 and SPOT-6 images. See Figure 5.2 for location. (a) E-W displacement map. White arrows indicate the deformation front. We projected the measurements included in the dashed polygon onto line AB and took the average in along-profile bins to estimate the displacement (i.e. shortening). Large deformation signals (blue areas) in the Tabas playa are due to farming. Red circle indicates Tabas. (b) Profile AB (gray line) shows a 3.4 m E-W displacement across the fold estimated by fitting two lines (green lines) on each side of the fault. (c) Displacements predicted with the Okada model of uniform slip on a rectangular fault plane. The best-fitting model through grid search (red line) is 7 m slip on a fault, dipping 50° beneath depths of 0.1 km to 6 km at its base. (d) Shaded-relief SPOT-6 DEM showing the same region as (a).

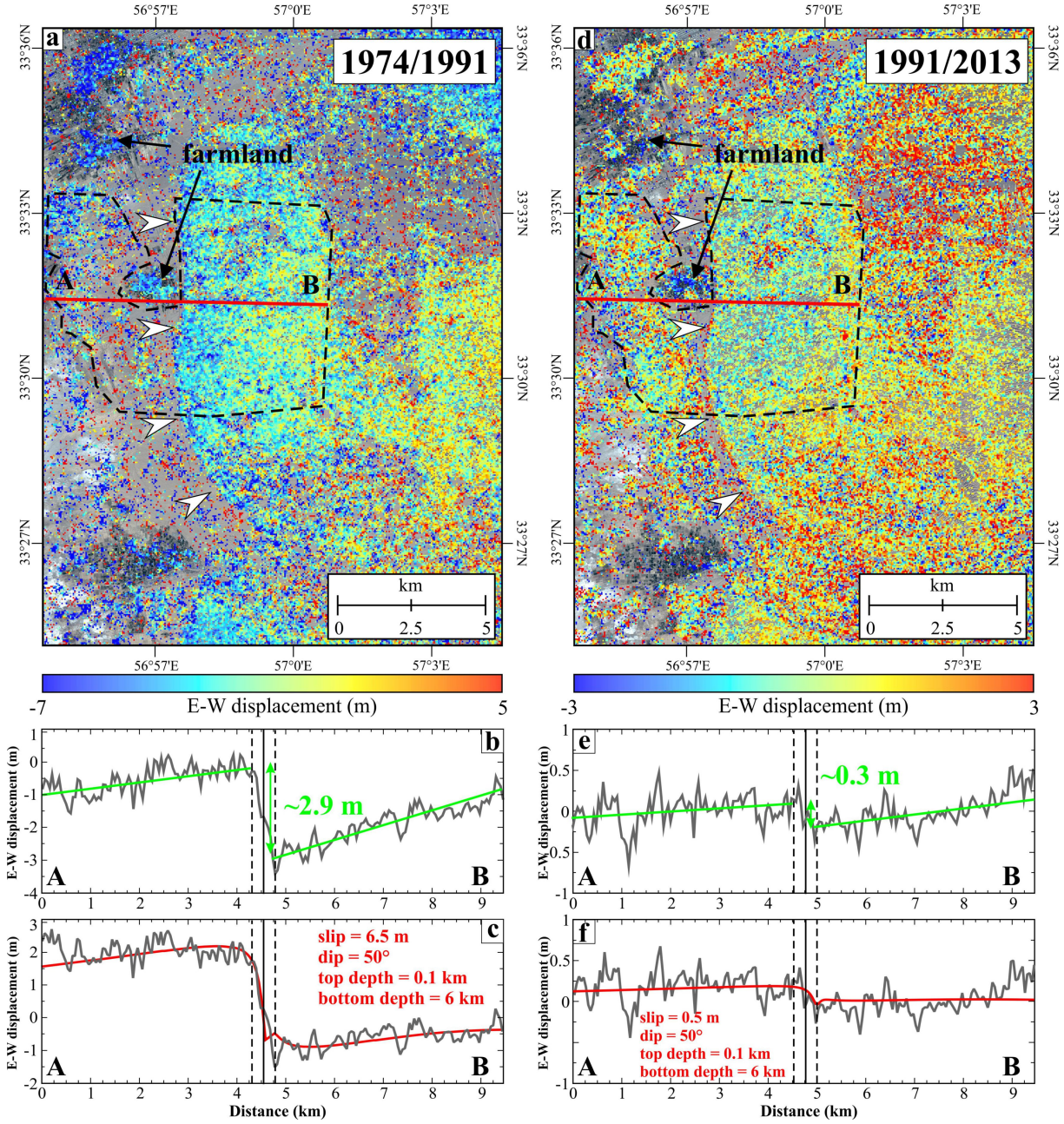


Figure 5.4: (a)–(c) As for Figure 5.3, but using the KH-9 and SPOT-2 images. Profile AB shows a 2.9±0.2 m E-W displacement. We fixed the fault geometry and varied the slip to reproduce this displacement. The best-fitting model gives a slip of 6.5 m. (d)–(f) As for Figure 5.3, but using the SPOT-2 and SPOT-6 images. Profile AB shows a 0.3±0.1 m E-W displacement. We fixed the fault geometry and varied the slip to reproduce this displacement. The best-fitting model gives a slip of 0.5 m. Note that the correlations are noisier than Figure 5.3. It is because that both the KH-9 (1974) and SPOT-6 (2013) images are forward images with a positive viewing angle whereas the SPOT-2 image is a backward image with a negative viewing angle. The intensity, scale and shape of objects change significantly in the KH-9 (SPOT-6) and SPOT-2 images, resulting in the decorrelation and noises in (a) and (d).

5.4.2 Height Changes from DEM Differencing

By differencing the pre-earthquake DEM generated from the aerial photographs and the post-earthquake SPOT-6 DEM, we also measured the height changes between 1956 and 2013. The elevation differences in Figure 5.5a show evident tilts towards the edges of each aerial photograph. These are non-tectonic signals in the pre-earthquake DEM, caused by film distortions (e.g. bending) due to duplication and storage over almost six decades. The resulting elevation errors in the pre-earthquake DEM can be as large as a few to ten metres, so we did not use the aerial photographs and the DEM for image matching. Also, we did not account for the horizontal motion in DEM differencing because (1) we cannot solve the horizontal displacements between the two DEMs, and (2) the area is relatively flat with a regional slope of $\leq 2^\circ$ (see the topographic profiles in Figure 5.12b), which means that the horizontal displacements would not cause large apparent vertical motion. Despite the large long-wavelength film distortions in Figure 5.5a, we can still measure the relatively short-wavelength dislocation at the deformation front. We projected the elevation differences in the area where we measured the horizontal displacements onto the fault-perpendicular direction (line SS′ in Figure 5.5a). Profile SS′ in Figure 5.5b shows a height change of $\sim$4.7 m at the fault over the interval 1956-2013.

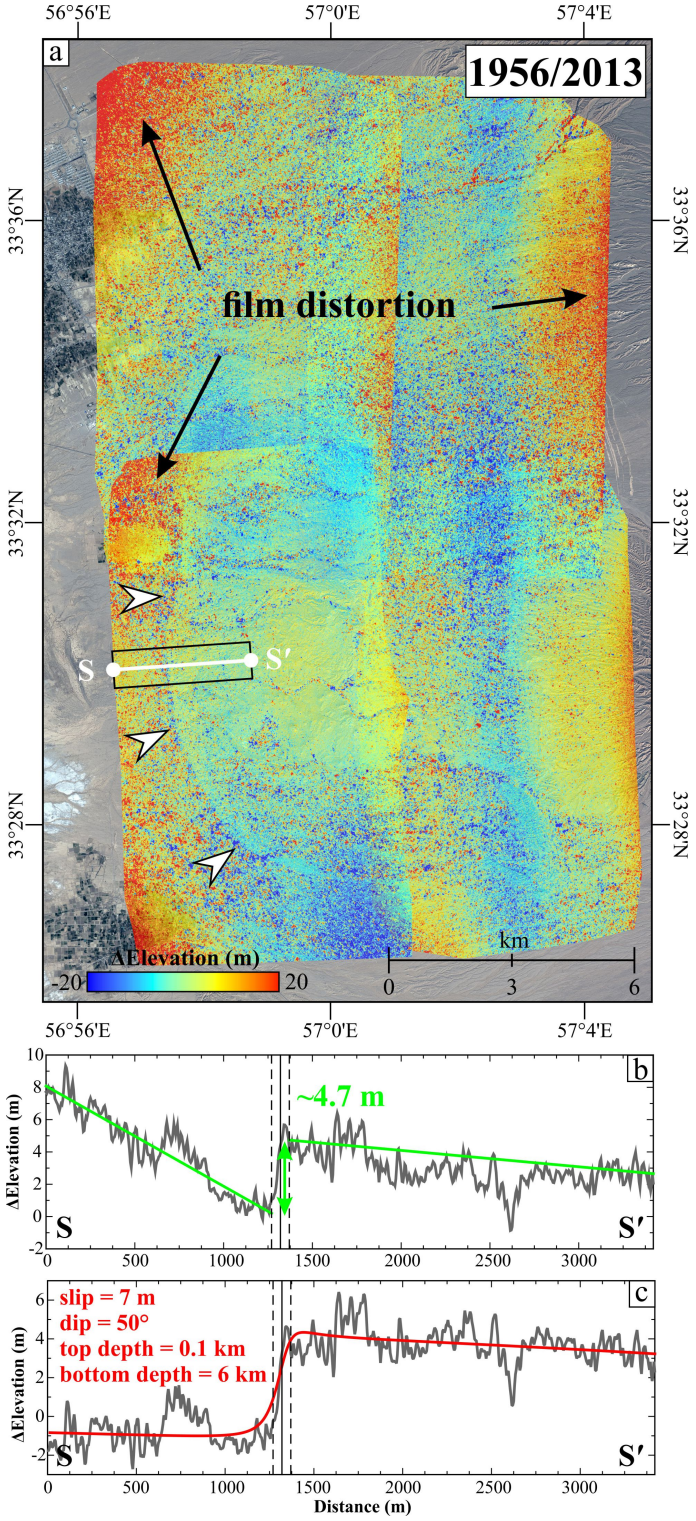


Figure 5.5: Height changes from direct differencing of the pre-earthquake aerial DEM and the post-earthquake SPOT-6 DEM. (a) Height change map. White arrows indicate the deformation front. We projected the measurements included in the polygon onto line SS′ and took the average in along-profile bins to estimate the displacement. (b) Profile SS′ shows a 4.7 m height change (gray line) estimated by fitting two lines (green lines) on each side of the fault. (c) Height changes predicted with the Okada model of 7 m slip on a rectangular fault plane, dipping 50° beneath depths of of 0.1 km to 6 km at its base. A third-order polynomial was fitted based on the residuals between the predicted displacement and the measured profile, and then removed to compensate for the film distortions. The prediction (red line) agrees well with our estimate.

5.5 Discussion

5.5.1 Models of Fault Slip

Based on the earthquake surface deformations, we are able to model the fault geometry and slip at depth. We used the routines of Okada (*Okada*, 1985) for constant slip on a rectangular plane to estimate the geometry and slip of the faulting. As the result from cross-correlating the KH-9 and SPOT-6 images presents good coherence (Figure 5.3), we used this result for determining the fault model. We varied the depth to the top of the fault plane from 0-0.5 km in steps of 0.1 km, the depth to the bottom from 4-10 km in steps of 1 km, the dip from 40-80° in steps of 5° and fault slip from 3-9 m in steps of 0.5 m. The strike and rake were fixed to 2° and 90° (i.e. pure thrust motion). We then performed a grid search to find the best fit to our measurement. Because we do not have any reference point in the displacement field, a linear trend is evident in the measured profile (Figure 5.3b). We computed the residuals between each Okada model and the measured profile, and fitted a linear trend based on the residuals. We then removed the linear trend from the measured profile, and recalculated the residuals between the predicted displacement and the new profile. The minimum misfit (the standard deviation of the residuals) gave 7±0.5 m slip on a 50±5° dipping fault, from a depth of 0.1 km to 6±1 km at its base (Figure 5.3c). This fault geometry is consistent with that obtained by modelling the postseismic deformation observed using InSAR (*Copley*, 2014), i.e. a dip of 55±10° and bottom depth of ∼4–5 km. Note that *Copley* (2014) modelled surface slip, i.e. a top depth of 0 km, but this model does not fit the displacement from image cross-correlation, as shown in Figure 5.6. Our model with a top depth of 0.1 km is more consistent with the measurement, which suggests that the main fault slip did not reach the surface.

We also calculated the theoretical height change, and compared it to the measurement from DEM differencing. As explained in Section 5.4.2, the mismatch between the modelled height change and profile SS′ is caused by a combination of a lack of reference points and film distortions in the aerial photographs. We modelled the distortion function as a third-order polynomial (*Brown*, 1971) and calculated the coefficients of the polynomial based

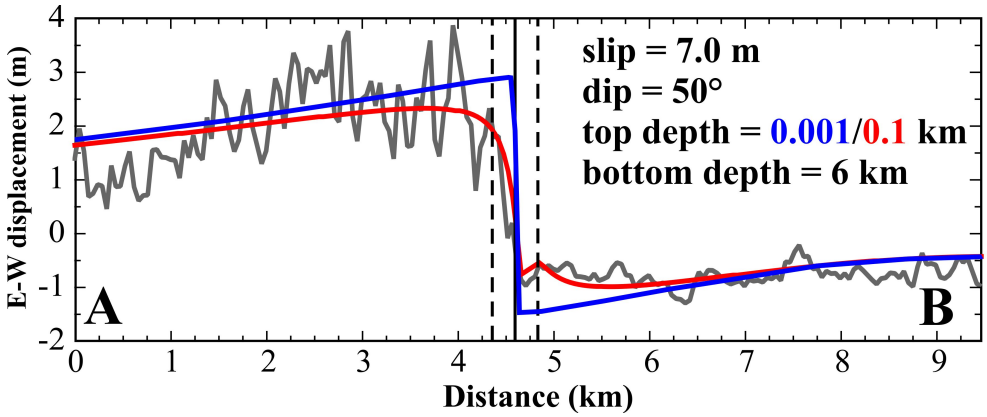


Figure 5.6: As for Figure 5.3c, but modelled with different top depths.

on the residuals between the Okada model and the measured profile. The polynomial was removed from profile SS′. Similarly, we performed a grid search procedure and obtained 7 m slip on a 50–60° dipping fault, from a depth of 0.1 km to ∼5–7 km at its base (Figure 5.5c), providing an additional constraint on the fault slip model.

We then fixed the fault geometry (a fault plane with a strike, dip, and rake of 2°/50°/90°, from a depth of 0.1 km to 6 km at its base) and repeated the modelling procedure (*Okada*, 1985) to determine the total slip in 1974-1991 and 1991-2013 by varying the magnitude of slip in steps of 0.25 m. Similarly, a linear trend was fitted based on the residuals between the prediction and the displacement profile, and removed from the displacement profile before comparing the models and the measurement. Based on the minimum misfit, we found 6.5 m slip in the coseismic and early postseismic periods (1974-1991) (Figure 5.4c), and 0.5 m slip in the late postseismic period (1991-2013) (Figure 5.4f).

Walker et al. (2003) and *Copley* (2014) suggested that the 50° dipping fault beneath the Tabas fold is connected to a low-angle (16°) fault at depth (the subsurface structure is discussed in Section 5.5.3). We also tested how much of the slip that we imaged across the Tabas fold was contributed by slip on the low-angle fault at depth. We assumed a slip of ∼3.3 m on a 16° dipping fault from a depth of 6 km to 9 km at its base, and calculated the surface displacements across the Tabas fold. As shown in Figure 5.7, both the horizontal and vertical displacements produced by slip on the low-angle fault at depth are very small (less than 5 cm). It is therefore reasonable to assume that the deformation signal measured in our study is purely due to slip on the 50° dipping fault in the inversions.

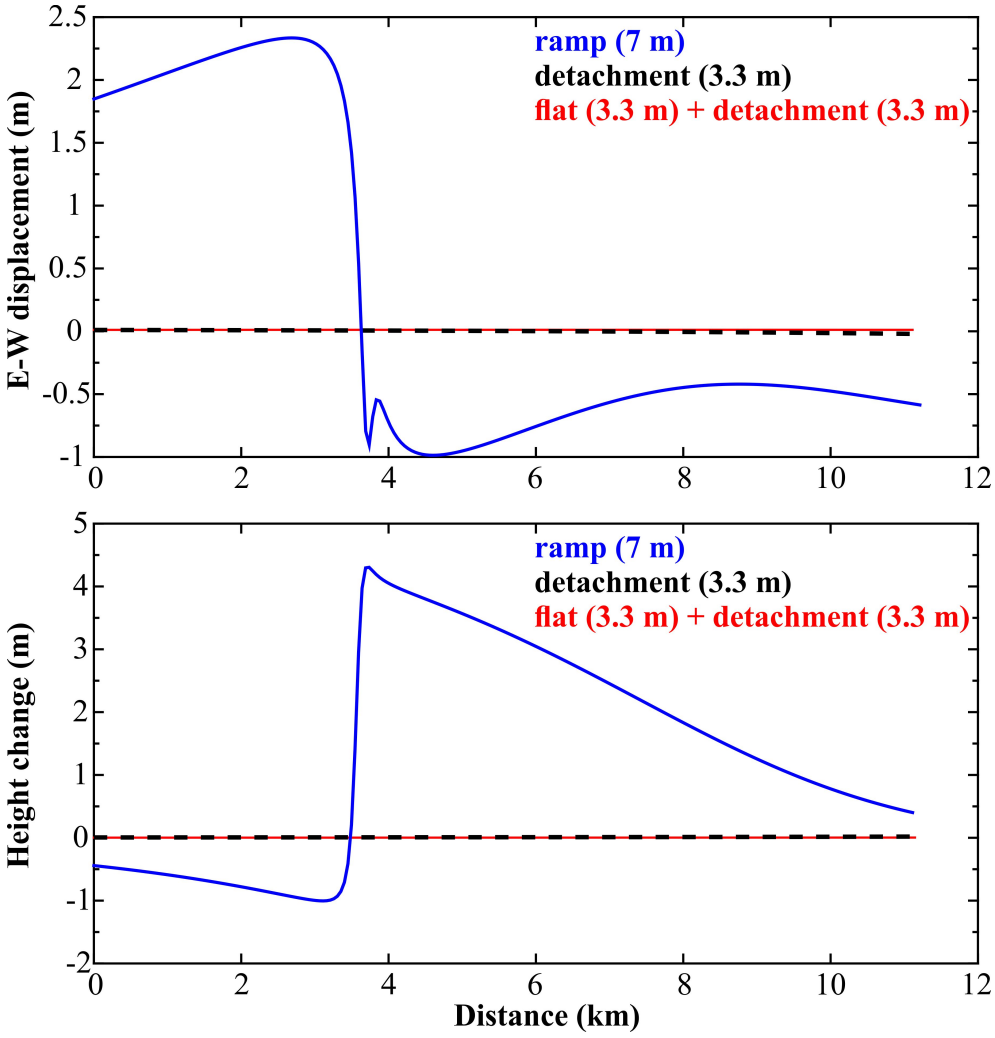


Figure 5.7: Modelled surface displacements assuming slips on different faults at depth. Blue line was produced by 7 m slip on a 50° dipping fault, from a depth of 0.1 km to 6 km at its base. Dashed black line was produced by 3.3 m slip on a 16° dipping fault, from a depth of 6 km to 9 km at its base. Red line was produced by a combination of 3.3 m slip on a flat at a depth of 6 km and 3.3 m slip on a 16° dipping fault, from a depth of 6 km to 9 km at its base.

5.5.2 Timescale of the Deformation

Both *Copley* (2014) and we have observed long-lasting shallow afterslip, which has continued for more than 30 years following the 1978 Tabas earthquake. Some other earthquakes have also presented similar long-term afterslip, e.g. afterslip continued for at least 40 years following the 1964 Alaska earthquake (*Suito and Freymueller*, 2009). Afterslip has also been suggested to markedly decay with time (*Segall et al.*, 2000). In the case of the 1978 Tabas earthquake, *Copley* (2014) discussed the features of the postseismic motion in detail based on the InSAR observations from 1996 to 2010, and speculated that most of the postseismic deformation should have occurred prior to 1996, assuming a time-decaying

rate (which was also observed from the difference between the ERS data in 1996–1999 and the Envisat data in 2003–2010). Since our observations cover an earlier period, we provide additional information about the timescale of the Tabas postseismic deformation.

Observations of laboratory experiments and many natural earthquakes have suggested that postseismic deformation following an earthquake is time-dependent, controlled by viscous flow in the lower crust and upper mantle (*Yu et al.*, 2003; *Pollitz*, 2005; *Freed et al.*, 2006; *Gratier et al.*, 2014). Laboratory derived flow laws associated with aseismic creep suggest a power law rheology (*Kirby*, 1983), and we simplify the equation to directly relate the cumulative afterslip s and time t in the form (e.g. *Çakir et al.* (2012); *Gratier et al.* (2014)): $s = \alpha t^n$, where α and n are the power law parameters. The power law exponent n was found to vary with rock type and grain size in laboratory experiments (*Gratier et al.*, 2014), and range from 0.25–0.5 in natural earthquakes (*Freed et al.*, 2006; *Çakir et al.*, 2012; *Gratier et al.*, 2014). Postseismic deformation on a fault may consist of different stages, as the effective viscosity varies as a function of time (*Freed et al.*, 2006). The viscosity after an earthquake will recover to pre-earthquake levels (after a few years to decades, e.g. ∼50 years (*Freed et al.*, 2006)). Hence, the variation in power law parameters provides information about the characteristic healing time of the fault (*Gratier et al.*, 2014).

In this study, we used the measurements of the postseismic afterslip following the 1978 earthquake to estimate the power law parameters. The 7 m slip in 1974-2013 involves both coseismic and postseismic motion, and we cannot separate these two periods directly due to a lack of data. The 1.5 m vertical displacement measured by *Berberian* (1979) provides a constraint for the coseismic slip on the Tabas fold (which is 30% of the total vertical motion), though note that the 1.5 m combines both 35 cm of primary slip, plus cumulative secondary bedding-plane slip. We estimated a maximum coseismic slip of 2.1 m (7 m×30%), and a minimum postseismic afterslip of ∼4.4 m in 1974–1991 and ∼0.5 m in 1991–2013. Also, note that the 1.5 m displacement could have all formed postseismicaly in the 10 days before they were observed by *Berberian* (1979), in which case, none of the slip is coseismic. Therefore, the maximum postseismic afterslip would be ∼6.5 m in the time interval 1974–1991 (assuming no coseismic motion). We then calculated the

power law parameters, α and n. Because the noise level of our measurements is high (∼1/20 of the pixel size), and we do not have enough data to plot points throughout the postseismic period, particularly no data in the early postseismic period (1–5 years after the earthquake), all the fits (with exponents of 0.02–0.25) are possible (as shown in Figure 5.8). Combining the afterslip rate of 5 mm/yr between 1996 and 1999 (*Copley*, 2014) and assuming it is relatively accurate, the postseismic afterslip can be best-fitted with a power law exponent of ∼0.02. Our power law exponent appears to be smaller than those observed in other natural earthquakes (the 1999 Izmit and 2004 Parkfield earthquakes), but the observations of those well-studied cases (e.g. (*Çakir et al.*, 2012; *Gratier et al.*, 2014)) cover a relatively early stage in the postseismic period compared with the 1978 Tabas earthquake. As discussed in *Freed et al.* (2006) and *Gratier et al.* (2014), the power law parameters vary with time. In the late stage of the postseismic period, the power law exponent should decrease to zero as the fault will be locked eventually (in the interseismic period). The small power law exponent observed in our study indicates a transition from the postseismic to interseismic periods.

5.5.3 Faulting in the Tabas Region

Combining all our observations and the previous work on the Tabas earthquake, e.g. *Berberian* (1979); *Berberian et al.* (1979); *Berberian* (1982); *Walker et al.* (2003, 2013); *Copley* (2014), we propose a self-consistent model of faulting in the Tabas region (Figure 5.9). Postseismic InSAR (*Copley*, 2014) and our image matching results suggest a high-angle ramp beneath the Tabas fold. It is worth noting that our modelling results show the main fault plane comes very close to the surface (∼0.1 km at depth), but did not reach the surface. We identified a ∼220 m wide zone of bedding plane slip on the surface (Figures 5.9a and 5.9b), which was reported to have ruptured in the 1978 earthquake (*Berberian*, 1979). We developed a conceptual model to reconcile the geodetic results and the geomorphological features, as illustrated in Figure 5.9c. The dip of the ramp (∼50°) starts to decrease at a depth of ∼0.1 km as it enters an upper layer of young, unconsolidated alluvial deposits, and the amount of slip dissipates, such that only 35 cm was observed on the frontal east-dipping thrust in the month after the earthquake. The

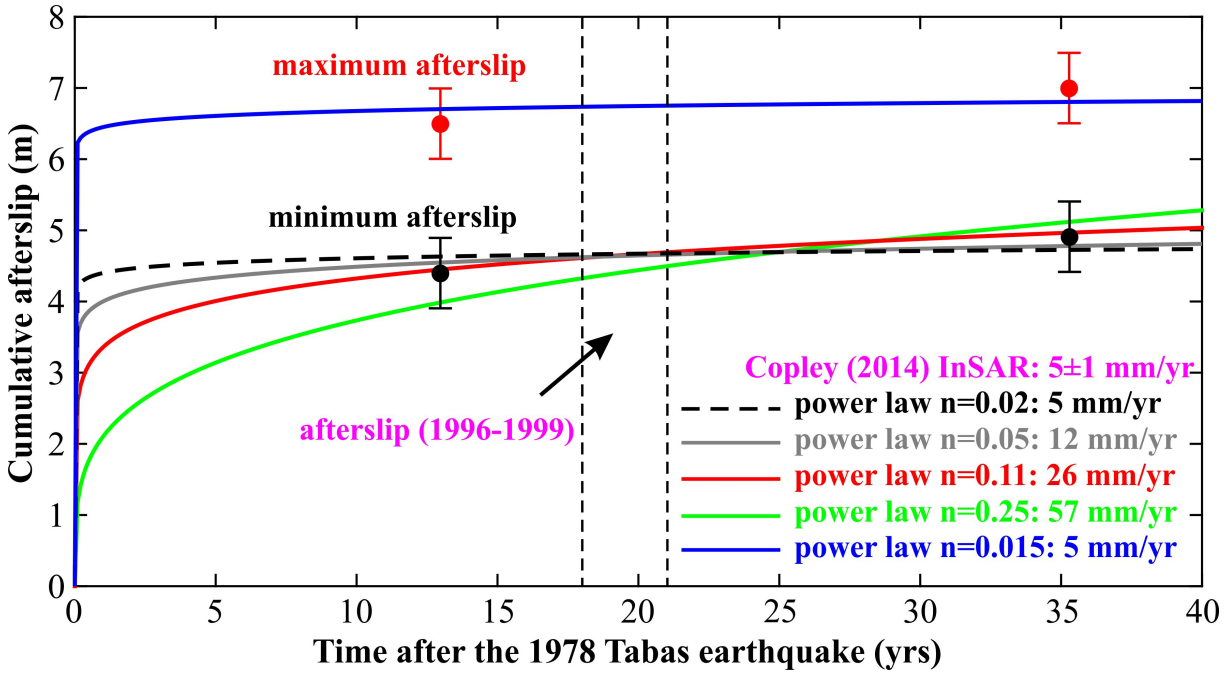


Figure 5.8: Time dependent postseismic afterslip and power law fits for the 1978 Tabas earthquake. We used $s = \alpha t^n$, where s is the cumulative afterslip, t is the time after the earthquake, and α and n (power law exponent) are the power law parameters that are related to fault healing. Black and red dots are measurements from image correlation (with an assumed error of $\sim$1/20×10 m=0.5 m). The maximum coseismic slip was estimated to be $\sim$2.1 m, leaving a minimum postseismic slip (black dots) of 4.4 m in 1978-1991 and 4.9 m in 1978-2013. The maximum postseismic slip (red dots) would be 6.5 m in the time interval 1978-1991, and 7.0 m in 1978-2013, assuming no coseismic motion. It is difficult to distinguish between different exponents in the range of 0.02–0.25 due to the noise level of our measurements and a lack of data in the early stage (0–5 years in particular). Dashed lines indicate an afterslip of 0.015 m (5 mm/yr×3 years) in 1996-1999 estimated by *Copley* (2014), which was used as a constraint for determining the power law parameters. Combining the InSAR estimate and assuming it is very accurate, the postseismic afterslip can be best-fitted with a power law exponent of $\sim$0.02.

larger part of the coseismic slip instead reaches the surface through motion on a series of small high-angle thrust faults formed between underlying Neogene beds, which is related to distributed shearing in the immediate hanging wall. As slip diminishes towards the surface, folding increases, resulting in a narrow band of bedding slip faults in the immediate hanging wall to accommodate shearing (Figure 5.9c).

The Tabas fold is only one of two active structures at that latitude. *Berberian* (1979) also observed a high-angle (80°) reverse displacement along the Espakh fold, situated east of the Tabas fold (Figure 5.2), but we did not find evidence for motion on the Espakh fold from image cross-correlation. The absence of deformation signal suggests that the surface rupture associated with the Espakh fold might be minor. It appears that the Espakh fold does not show postseismic signal in InSAR either (*Copley*, 2014). To image

the subsurface structure on the Espakh fold, we modelled the uplift of a warped river terrace (see Section 5.5.4 for the method and Figure 5.10). The best-fitting fault slip model gave 12 m slip on a 50° dipping fault, from a depth of 0.5 km to ~5–6 km at its base (Figure 5.10). However, the fault slip model is not well constrained by the uplift of the river terrace only, as there is a trade-off between the slip and fault dip, and the topography may be modified dramatically by erosion in the past few thousand years.

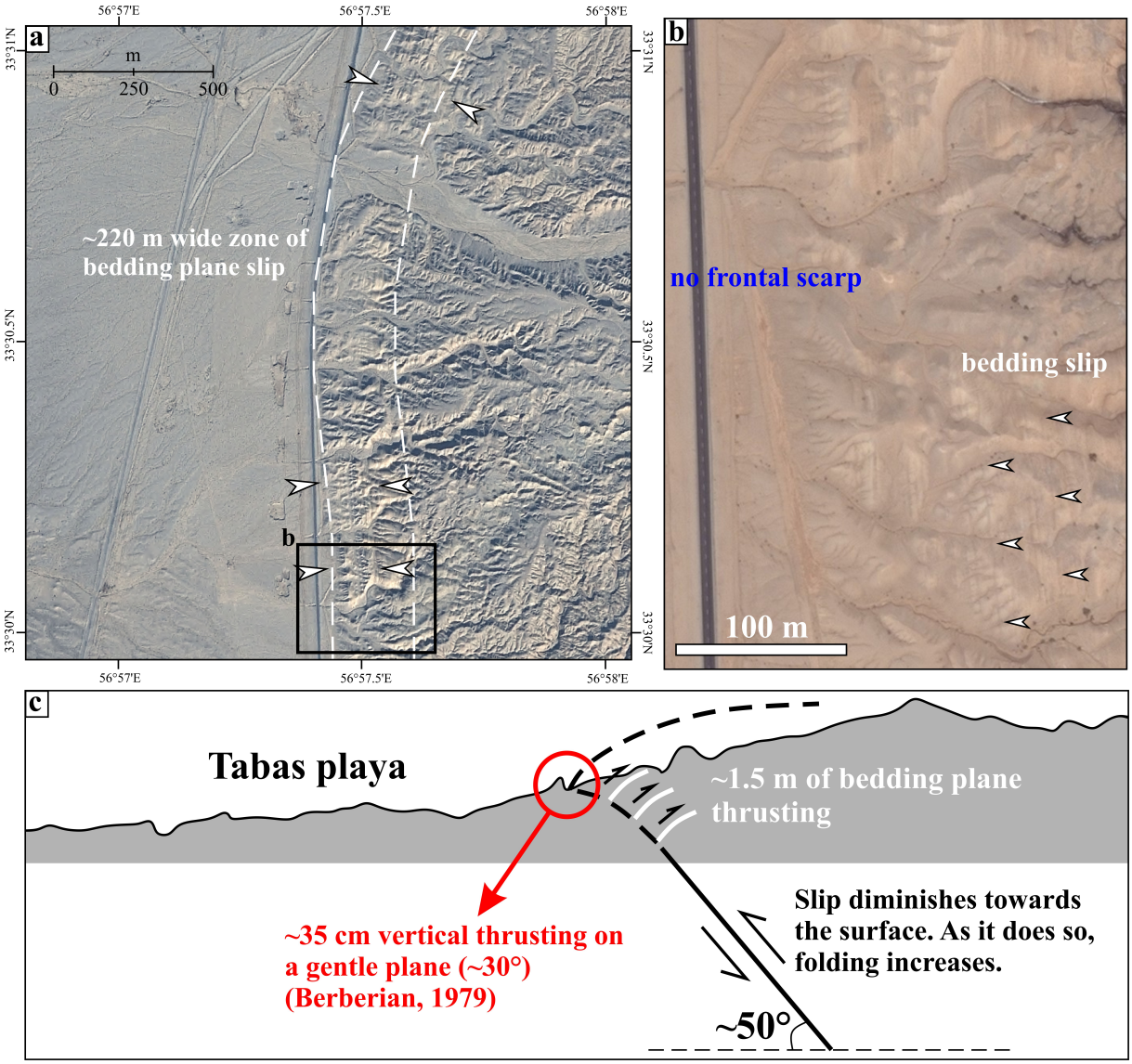


Figure 5.9: Schematic cross-section along the Tabas fold summarising the sub-surface structure. (a) SPOT-6 image showing a ~220 m wide zone of bedding plane slip (indicated by white dashed lines). (b) A close-up view (from Bing Maps, http://www.bing.com/mapspreview) of bedding plane slip. We did not find any frontal scarps from the imagery. (c) Cartoon illustrating the sub-surface fault structure. The dip of main fault decreases at a depth of ~0.1 km. *Berberian* (1979) found vertical displacement on a 30° dipping plane at surface. Most of the coseismic slip on the main fault reached the surface in the form of minor slip on a series of small thrust faults (white lines) developed between beds. As slip diminishes towards the surface, folding increases.

In summary, a cross-section (Figure 5.11) was constructed to show faulting in this region. The source parameters of the main shock indicate slip on a low-angle (16°) detachment fault with a centroid depth of 9 km with the epicentre under the Shotori Mountains (*Walker et al.*, 2003). Vertical displacements at the western margins of the Tabas and Espakh folds are the result of slip on associated ramps, which are connected by a flat at a depth of ∼5–6 km (Figure 5.11a). The flat shallows into the detachment that joins the Shotori range-front fault at a depth of ∼9 km (6 km + 12 km $\times \tan 16°$, Figure 5.11a). Given the fact that the subsurface structure of the Espakh fold is not well constrained, it is also possible that the ramps are connected by a planar detachment fault (dipping 16°) (Figure 5.11b), which would require that the Espakh fault reaches a depth of ∼7–9 km, and the Shotori range-front fault joins the detachment at a depth of ∼12 km (6 km + 20 km $\times \tan 16°$, Figure 5.11b).

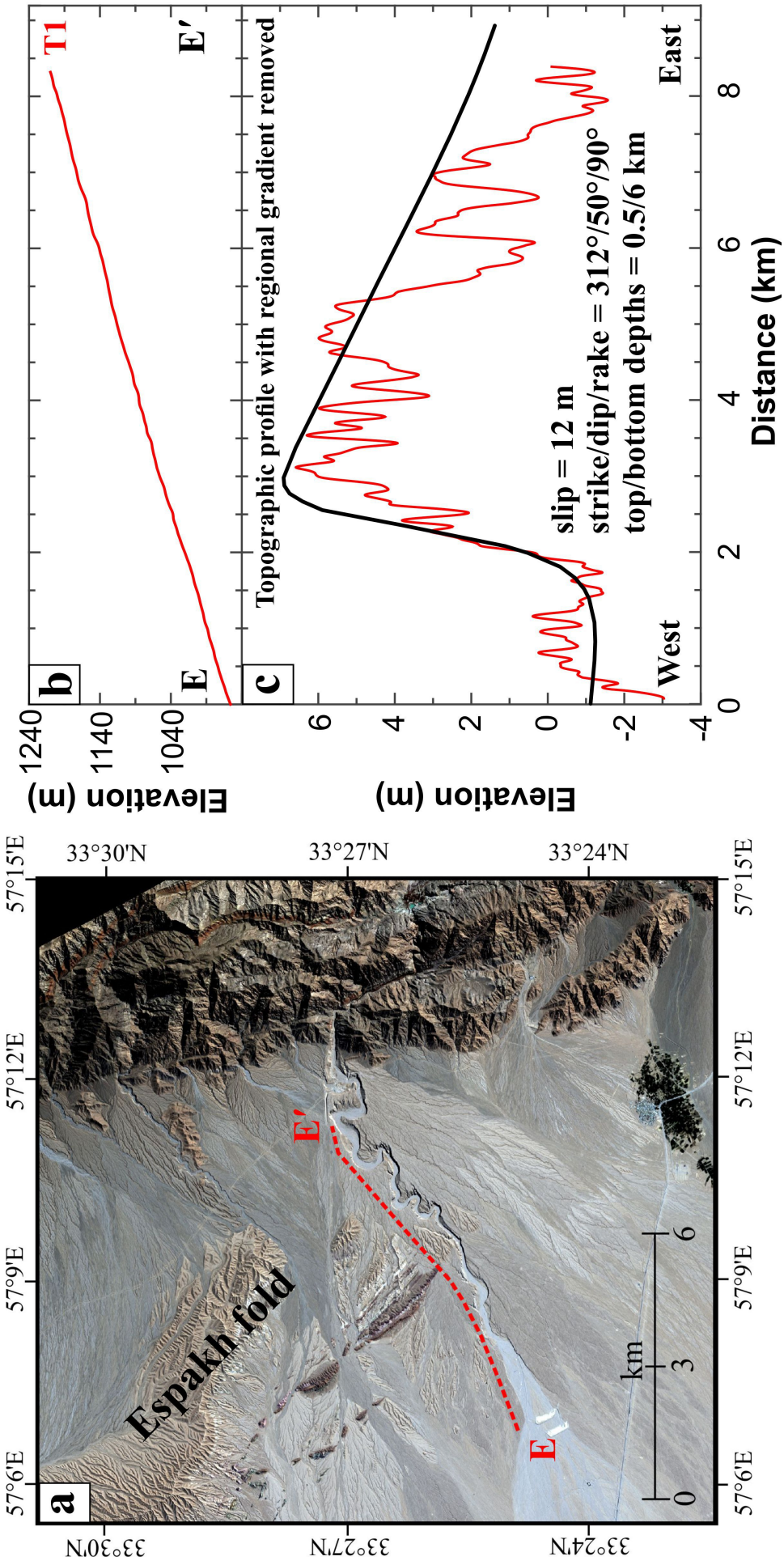


Figure 5.10: Long-term surface folding of the Espakh fold. See Section 5.5.4 for details (a) SPOT-6 orthoimage showing the Espakh fold. We only found one river terrace (T1) preserved in this area. (b) Original topographic profile E-E'. (c) Topographic profile E-E' after removing a regional gradient. The black line is the predicted topography using the Okada model (*Okada*, 1985), assuming a slip of 12 m on a 50° dipping fault, from a depth of 0.5 km to 6 km at its base.

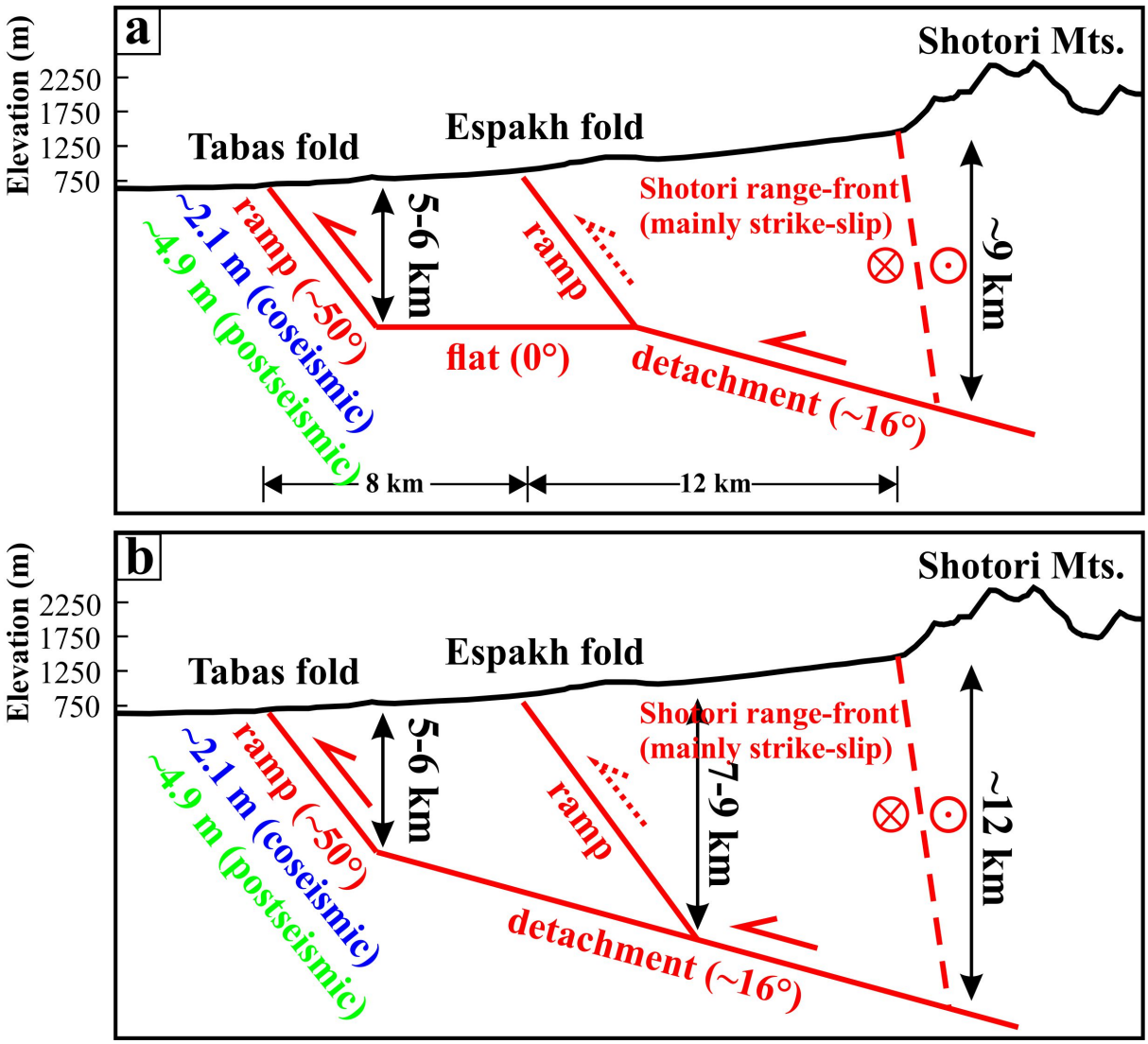


Figure 5.11: Schematic cross-section of faults in the Tabas region. See Figure 5.2 for location. As the subsurface structure of the Espakh fold is not well constrained by the uplift of the river terrace only, we show two possible scenarios of faulting in the region. (a) The Tabas and Espakh folds are connected by a flat at a depth of ∼5–6 km. The flat shallows into the detachment (dipping at ∼16° from *Walker et al.* (2003)), which joins the Shotori range-front fault at a depth of ∼9 km (6 km + 12 km × tan 16°). Vertical displacements across the Tabas fold measured by *Berberian* (1979) indicate that the coseismic slip on the Tabas ramp accounts for ∼30% of the total slip. Therefore, we speculated the coseismic slip on the fault plane is ∼2.1 m, with a postseismic afterslip of ∼4.9 m. (b) As for (a), but the Tabas and Espakh folds are connected by the detachment (dipping at ∼16°). This scenario requires the Espakh reaches a depth of 7–9 km, and the Shotori range-front fault joins the detachment at a depth of ∼12 km (6 km + 20 km × tan 16°).

5.5.4 Long-term Surface Folding: Characteristic Slip Behaviour

The SPOT-6 DEM also enables us to analyse the long-term surface folding. We identified two river terraces (a younger terrace T1 and an older one T2) associated with the growth of the Tabas fault. Figure 5.12 shows three topographic profiles, S1-S1′ along a modern river channel, S2-S2′ along the T2 surface, and S3-S3′ along the T1 surface. As the topography is dominated by a depositional slope of the alluvial surface, we removed a regional gradient from each profile, as shown in Figures 5.12c-5.12e. Note that because only a fragment of T2 is preserved, we extended S2-S2′ onto the T1 surface in order to calculate the regional surface slope. We chose river channel S1-S1′ for analysis because (1) unlike the big rivers, where the relatively young alluvial fans (T1 and T2) have been washed away, fragments of T1 are seen here (Figures 5.12a) which indicates that the river is likely to preserve recent earthquake motion, and (2) walls and dams have been built across other rivers to suppress floods and may have also changed the sedimentation and erosion patterns since the earthquake. The other rivers in the area do not show visible warping for the reasons outlined above.

The uplift profiles (Figures 5.12c-5.12e) indicate that warping of the river channel and both terraces occurs over a distance of ∼6–7 km, similar to that expected from the modelled fault geometry. The modern river channel should record the slip due to the single 1978 earthquake (∼5 m vertical motion as seen from DEM differencing and our model), whereas T1 and T2 should record a cumulative fault slip from multiple earthquakes. We used the fault model from Section 5.5.1 to predict the uplift of the river channel and terraces. If the river channel only records the motion of the 1978 earthquakes, the uplift along profile S1-S1′ can be determined from the Okada model (*Okada*, 1985) with a fault slip of 7 m. As shown in Figure 5.12c, the modelled uplift is consistent with that measured (∼5.0 m).

To estimate the fault slip responsible for the uplift of river terraces T1 and T2, we fixed the fault geometry, i.e. a fault plane dipping 50° beneath depths of 0.1 km to 6 km at its base, and varied the slip from 11-23 m in steps of 1 m (as shown in Figure 5.12). To produce the uplift of T1 (∼9.5 m), a fault slip of 13–14 m is needed. The uplift of T2 (∼14 m) requires a fault slip of 21–22 m. Note that profile S2-S2′ at the eastern end

was drawn on the T1 surface, which causes underestimation of the uplift compared to that from the model. The inferred slips appear to be multiples of the slip in the 1978 earthquake, indicating that T1 and T2 may record two and three earthquakes, with a similar magnitude to the 1978 event. It is possible that the inferred slip was caused by more than three events with smaller magnitudes. If that was the case, we would expect to see more river terraces with smaller height changes. However, as we only observed two levels of river terrace, it is plausible that T1 and T2 simply record two and three repeated earthquakes respectively.

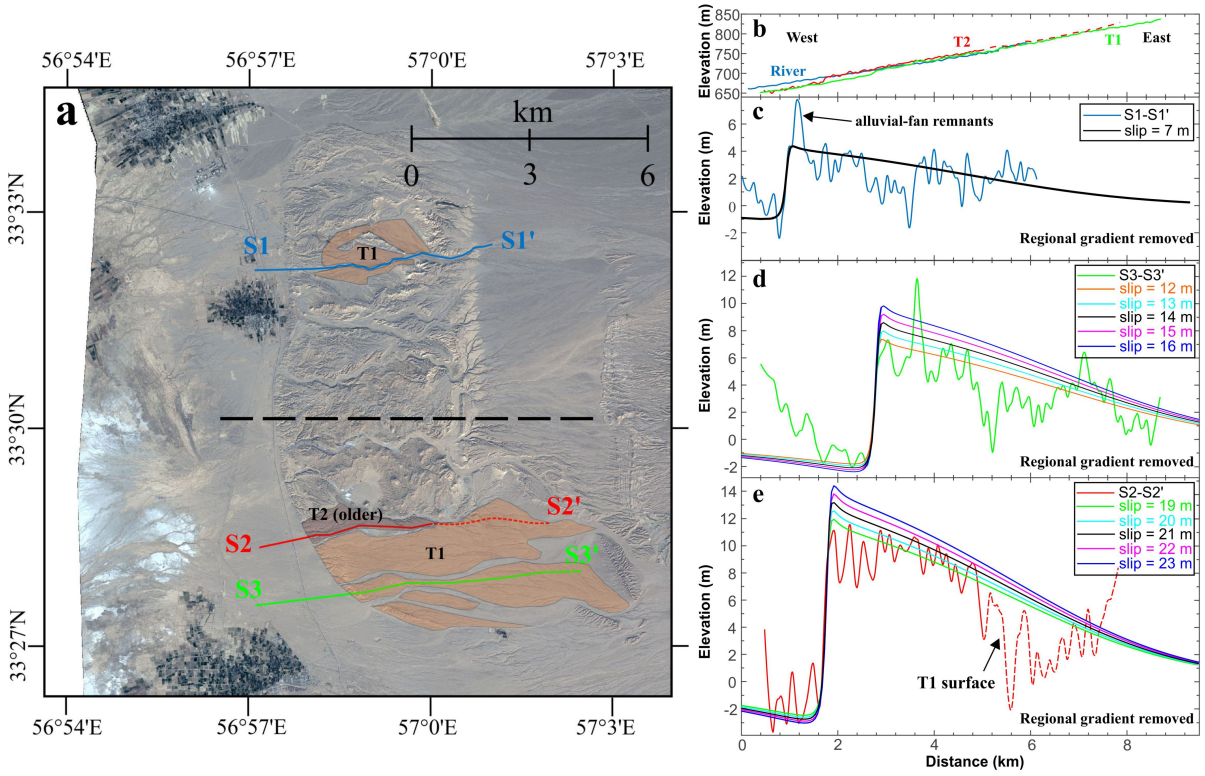


Figure 5.12: Long-term surface folding of the Tabas fold. (a) SPOT-6 orthoimage showing the Tabas fold. We identified two river terraces (T1 and T2) from the image and the DEM derived from it. Topographic profiles S1-S1′ (along a modern river channel), S2-S2′ (along the T2 surface), and S3-S3′ (along the T1 surface) were projected onto the fault-perpendicular direction (black dashed line). (b) Original topographic profiles from the SPOT-6 DEM. Blue, red and green lines indicate S1-S1′, S2-S2′ and S3-S3′ respectively. (c) Topographic profile S1-S1′ after removing a regional gradient. The black line is the predicted topography using the Okada model (*Okada*, 1985) and our estimated fault parameters (7 m slip on a 50° dipping fault, from a depth of 0.1 km to 6 km at its base). (d) Topographic profile S3-S3′ after removing a regional gradient. The predicted topography assume a model with a uniform slip (12–16 m in steps of 1 m) on a 50° dipping fault, from a depth of 0.1 km to 6 km at its base. (e) Topographic profile S2-S2′ after removing a regional gradient. The predicted topography assume a model of a uniform slip (19–23 m in steps of 1 m) on a 50° dipping fault, from a depth of 0.1 km to 6 km at its base.

The good agreement between the modelled surface uplift and the measured folding suggests that the Tabas fold may exhibit characteristic slip behaviour. Such behaviour was also observed on the Hoshab fault in the eastern Makran from an investigation of the 2013 M_w 7.7 Balochistan earthquake (*Zhou et al.*, 2015a). As we do not have any direct measurements of slip rate on the Tabas fault, we assumed that the ∼1.5 mm/yr right-lateral strike-slip on the Nayband fault (*Walker et al.*, 2009, 2013; *Foroutan et al.*, 2014) is to be absorbed by repeated thrusting on the Tabas fold system (∼1 mm/yr in the shortening direction). Given an average of ∼3.5 m shortening as observed in the 1978 earthquake, it would require a magnitude M_w 7.3 earthquake every ∼3500 years. Future palaeoseismic studies are needed to confirm this.

5.6 Conclusions

Historical images have opened up new opportunities for studies of past earthquakes. In this study, we measured the horizontal motion associated with the 1978 M_w 7.3 Tabas earthquake using KH-9, SPOT-2 and SPOT-6 images, and the vertical motion using aerial photographs and SPOT-6 stereo imagery. The results are consistent and provide insights into the coseismic and long-lasting postseismic deformation. We found time-dependent shallow postseismic afterslip, decaying as αt^n with a best-fitting power law exponent of 0.02. Although we do not have any constraints on the afterslip in the early postseismic period, it is very likely that most of the afterslip occurred prior to 1991. From comparison of terrace heights with the earthquake uplift, we also found that the Tabas fold system may exhibit a characteristic slip behaviour. This behaviour requires a magnitude M_w 7.3 earthquake every ∼3500 years to accommodate the previously estimated shortening rate of ∼1.0 mm/yr. This study potentially provides a means to investigate palaeoseismology of the Tabas folds, despite a lack of obvious surface scarps. The method may be useful more generally in regions of fault-related folding.

Chapter 6

The 1556 Huaxian Earthquake in the Weihe Graben in Central China

This chapter is a contribution to a collaborative study with researchers at the China Earthquake Administration Shaanxi Province through the Earthquake without Frontiers (EwF) project. Adapted from Feng, X., J. Ma, Y. Zhou, R. T. Walker, B. Parsons, P. England and M. A. Rizza (in prep.), Repeated high stress-drop ruptures on the 1556 Huaxian earthquake normal fault, Shaanxi, central China, *Earth and Planetary Science Letters*.

6.1 Introduction

Most great ($M_w \geq 8$) earthquakes during modern times have occurred in interplate regions or major continental collision zones, such as Sumatra (*Stein and Okal*, 2005), the Japanese island arc (*Heki et al.*, 1997; *Hashimoto et al.*, 2009; *Ozawa et al.*, 2011) or the San Andreas fault zone (*Sieh et al.*, 1989; *Stein et al.*, 1992). Although large-magnitude earthquakes are rare in continental interiors, where fault slip rates tend to be low, there is a suggestion that intraplate regions may experience high-stress drop earthquakes, such that slip is more than expected for fault length ($\bar{\mu}/L \sim 10^{-4}$), e.g. the 1897 Assam *England and Bilham* (2015) and 2001 Bhuj *Copley et al.* (2011) earthquakes. They also have the potential to be significantly deadlier than those on plate boundaries because of the long repeat times and lack of preparedness (*Butler et al.*, 1979; *Shen et al.*, 2009; *England and Jackson*,

2011; *Zhang*, 2013). The January 23rd 1556 Huaxian earthquake in Shaanxi Province, central China, is the deadliest in history with an estimated death toll of ∼830,000 from building collapse, land-sliding, famine, and disease (*Wang*, 1987; *Yuan and Feng*, 2010). The earthquake occurred in the graben of the river Wei (the Weihe graben, Figure 6.1). Geomorphological observations provide clear evidence that many of the graben-bounding normal faults around the Weihe graben are currently active (Figure 6.2). They pose a serious seismic hazard in this densely populated and rapidly expanding region, that supports over 23 million inhabitants at the present day. Between 1978 and 2014, the area covered by the city of Xi′an tripled in size, and the population reached ∼8 million in 2014 (Figure 6.3), highlighting the importance of investigating active faulting in the Weihe graben.

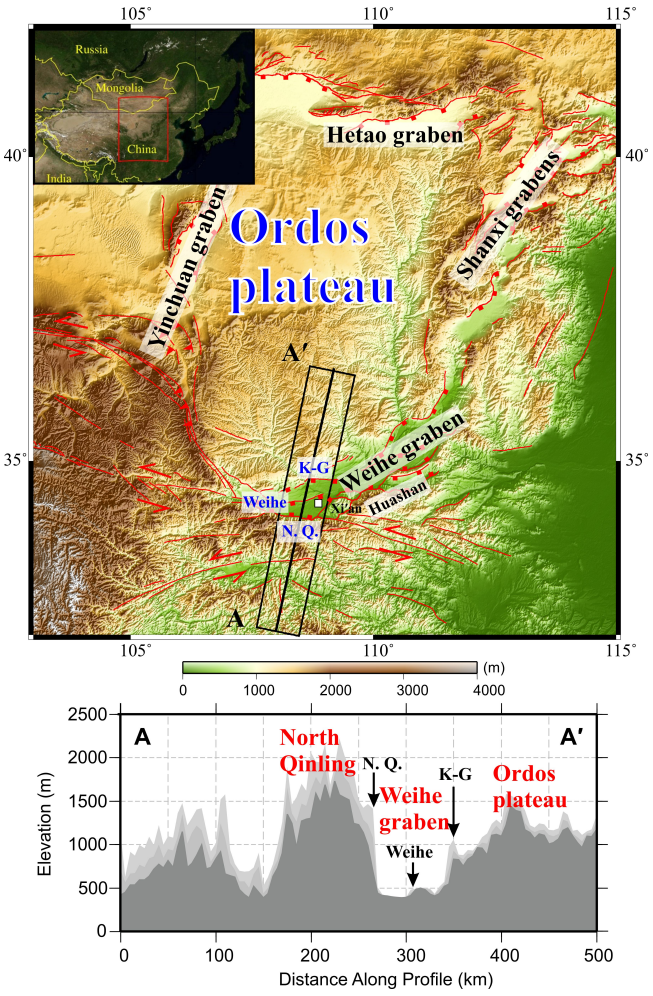


Figure 6.1: Active faults (red lines) around the Ordos plateau, mapped from satellite imagery in this study. Topographic profile A-A′ shows steep topography across the North Qinling (N. Q.), Weihe, and Kouzhen-Guanshan (K-G) faults. Black polygon indicates the InSAR data used to construct a rate map across the Weihe graben. White square marks Xi′an.

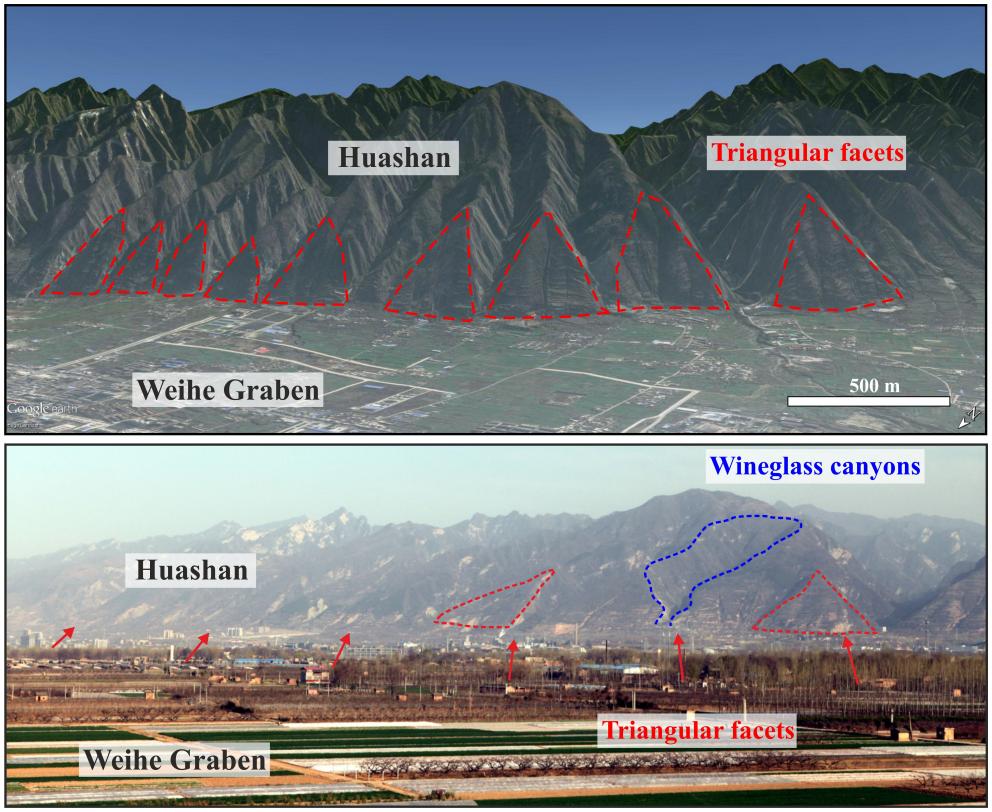


Figure 6.2: Triangular facets along the range front of Huashan (see Figure 6.1 for location). (top) Google Earth imagery (12 February, 2015). (bottom) Field photograph by Ji Ma.

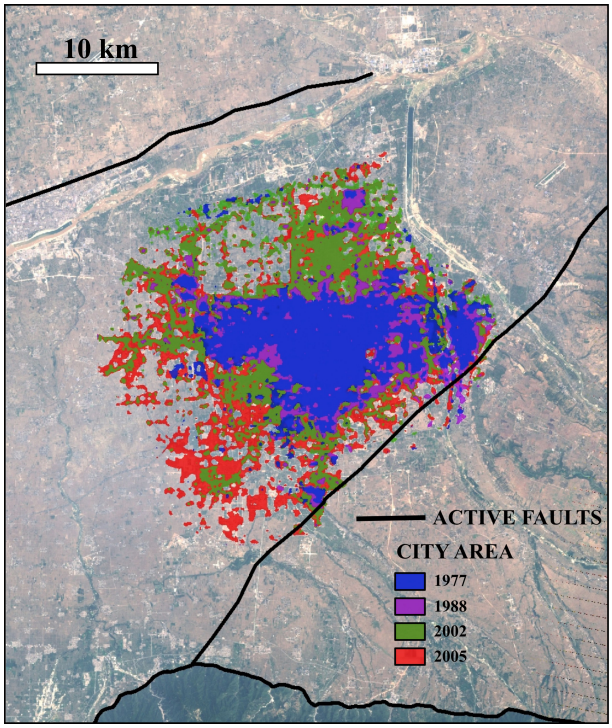


Figure 6.3: Expansion of Xi′an (see Figure 6.1 for location), with Landsat-7 image (2005) below. City areas were extracted from Landsat images using the supervised classification algorithm. From 1978 to 2014, the area of Xi′an tripled, concomitantly increasing the seismic risk.

6.2 Interseismic Rate Map for the Weihe Graben, Southern Margin of the Ordos Plateau

The Ordos plateau has been a stable block since the Mesozoic (*SSB*, 1988; *Zhang et al.*, 1998). In contrast, its margins have been tectonically active since the Eocene, when fault-bounded subsiding grabens started to form and grow (*SSB*, 1988). This extension may be associated with the Himalayan orogeny and the uplift of Tibet (*Wesnousky et al.*, 1984; *Zhang et al.*, 1998), or it could be gravitational collapse of Tibet or change in rate of Pacific subduction (*Northrup et al.*, 1995). The grabens are seismically active, with 51 earthquakes M>6 since 780 BC (*Song*, 2012). The Weihe graben forms the southern margin of the Ordos plateau (*Tapponnier and Molnar*, 1977; *Zhang et al.*, 2003) (Figure 6.1). To the north, the graben is bounded by a series of normal faults; to the south, it is bounded by the North Qinling (southwest) and Huashan (southeast). Despite the proven record of earthquakes in the Weihe graben, the distribution and rates of active faulting are relatively poorly described.

InSAR offers the potential to measure interseismic slip rates on faults at a resolution of millimetres per year (e.g. *Wright et al.* (2001)). In this study, I first used InSAR to image strain accumulation across the Weihe graben. A total of 32 Envisat SAR images were acquired from descending track 161 (Figure 6.4) that covers the central section of the graben. This section is bounded by the Kouzhen-Guanshan fault to the north and the North Qinling fault to the south. The SAR data were processed using the JPL/Caltech ROI_PAC software. The precise orbit determination from the Delft Institute for Earth-Oriented Space Research (DEOS) was applied to correct for orbital effects. The topographic contribution was simulated and removed using the 90 m resolution Shuttle Radar Topography Mission (SRTM) Digital Elevation Model (DEM) from CGIAR-SCI (http://srtm.csi.cgiar.org). Each interferogram was downsampled to 64 looks in the range direction (1280 m). Before phase unwrapping, a weighted power spectrum filter was applied to improve the signal-to-noise ratio. The branch-cut method was used for phase unwrapping. Phase unwrapping errors were checked by summing around a closed loop (*Biggs et al.*, 2007). All the major unwrapping errors were identified and corrected man-

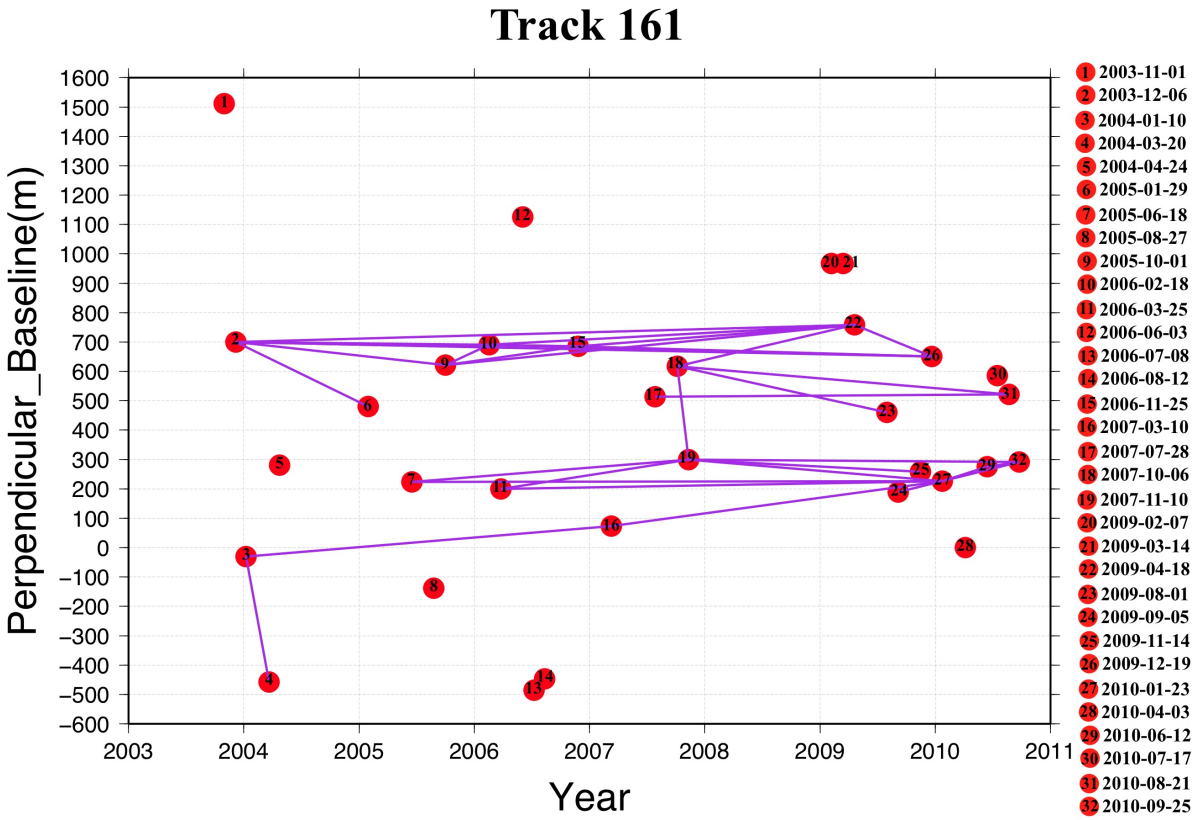


Figure 6.4: Baseline plot for track 161. See Figure 6.1 for coverage. Each red dot denotes an InSAR acquisition. Purple lines indicate interferograms that show good coherence and were used to construct a rate map.

ually. 33 interferograms were selected from the total of 98 interferograms based on their coherence. The 33 interferograms cover a time span of 75.46 years. The high relief and heavy vegetation to the south of the North Qinling fault resulted in low coherence in the interferograms.

I used the π-*RATE* (Poly-Interferogram Rate And Time-series Estimator) software package to construct a rate map from the selected interferograms. π-*RATE* (*Biggs et al.*, 2007; *Wang et al.*, 2009) uses the geocoded interferograms from ROI_PAC to create a minimum spanning tree (MST) network (*Kruskal*, 1956), from which the orbital and topographically-correlated atmospheric errors are estimated. The MST network connects all epochs with the most coherent interferograms, but which includes no closed loops of interferograms. The network approach is able to improve the estimation of orbital error by ∼9% compared to the independent interferograms approach (*Biggs et al.*, 2007), as the estimated parameters are constrained by dependent interferograms. The orbital errors are empirically modelled as planar or quadratic ramps. The quadratic orbital approximation

takes the following form:

$$\phi_{ij,k}^{orb} = (a_j - a_i)x_k^2 + (b_j - b_i)y_k^2 + (c_j - c_i)x_k y_k + (d_j - d_i)x_k + (e_j - e_i)y_k + f_{ij} \quad (6.1)$$

where $\phi_{ij,k}^{orb}$ is the orbital ramp, x_k and y_k are the x and y coordinates of pixel k, a_i, b_i, c_i, d_i and e_i are the x and y orbital coefficients for epoch i, and f_{ij} is constant for interferogram ij.

The topographically-correlated atmospheric correction (*Elliott et al.*, 2008; *Zhou et al.*, 2015c) uses:

$$\phi_{ij,k}^{atm} = (a_j - a_i)h_k + c_{ij} \quad (6.2)$$

where $\phi_{ij,k}^{atm}$ is the topographically-correlated atmospheric error at each down-sampled pixel k in each interferogram ij, elevation h_k is taken at each pixel k from the SRTM DEM, c_{ij} is a constant, and a_i and a_j are the phase-gradients which can be solved by a least squares adjustment.

The topographically-correlated atmospheric correction was applied to each interferogram after having corrected for the orbital errors. The resulting interferograms were then stacked to produce a rate map (Figure 6.5). The rate estimates were projected onto line A–A′ in Figure 6.5. Despite the apparent deformation signal around Xi′an (subsidence caused by groundwater extraction, also detected by *Qu et al.* (2014)), I did not find any clear change in the displacement rate across the major faults (Kouzhen-Guanshan, Weihe and North Qinling faults) in the graben. Given the limit of InSAR measurements (∼1 mm/yr in the line-of-sight direction), the rate map suggests that the slip rates of the faults are small (on the order of 1–3 mm/yr). Since it is not possible to measure small slip rates using modern geodetic techniques, I combine geomorphology and palaeoseismology, which record motion over longer time periods, to study active faulting in the graben, and to produce an estimate of average slip rate.

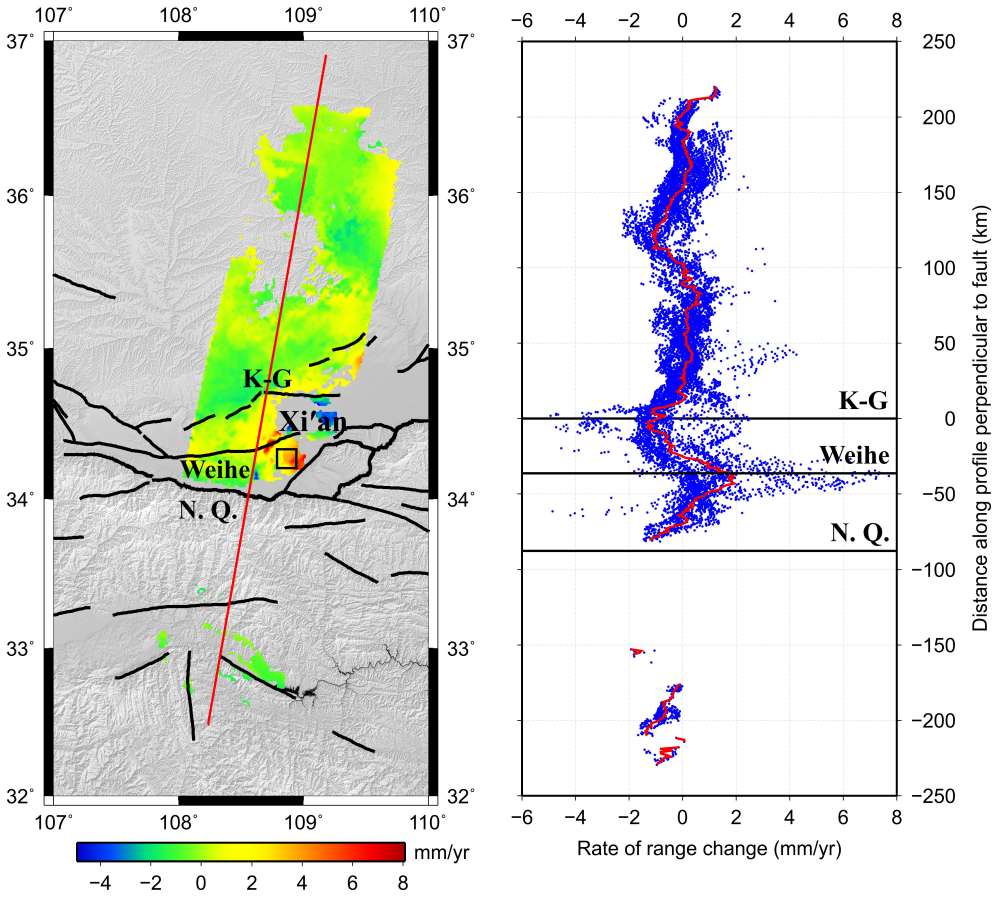


Figure 6.5: (left) Rate map from stacking the interferograms shown in Figure 6.4, after correcting for the orbital and topographically-correlated atmospheric errors. (right) Profile of the line-of-sight displacement rate. K-G: Kouzhen-Guanshan fault. Weihe: Weihe fault. N. Q.: North Qinling fault. These faults are normal faults. There is no clear change across the major faults in the graben. The apparent displacements (red regions in the left panel) are caused by groundwater exploration in Xi′an (*Qu et al.*, 2014).

6.3 The 1556 Huaxian Earthquake

The damaging effects of the 1556 earthquake are well known due to extensive historical records, but the source parameters of the earthquake itself are less well known. Isoseismals reconstructed from primary historic sources and field surveys of historic buildings are shown in Table 6.1 and Figure 6.6 (*Yuan and Feng*, 2010). Strong shaking was experienced across the entire Weihe graben, with a zone of intensity X that was ∼100 km long, and with intensity VIII shaking across most of the Weihe graben. The greatest levels of damage (11.5-12 based on the Chinese seismic intensity scale) were experienced in the Huaxian and Weinan regions, suggesting that the earthquake ruptured the nearby Huashan and Weinan tableland faults (Figure 6.6). An ∼8 m scarp along these faults has been assumed to be the 1556 earthquake scarp, though this has not been shown conclusively (*Zhang*

et al., 1989, 1995a; *Hou et al.*, 1998; *Yuan and Feng*, 2010; *Rao et al.*, 2015). Following the empirical relationship between the maximum intensity of the epicentral area (I_0) and magnitude (M): $M = 0.58I_0 + 1.523$, the magnitude of the 1556 earthquake was estimated to be M = 8.25–8.5 (*Yuan and Feng*, 2010).

On the other hand, the Huashan and Weinan tableland faults have a combined length of ∼90 km (Figure 6.7), and applying empirical scaling relationships between magnitude and fault rupture length yields a magnitude estimate of M_w 7.5 (*Wells and Coppersmith*, 1994). This estimate is significantly smaller than that inferred from the intensity scaling relationship. This could be because (1) M 8.25–8.5 is an overestimate of the size of the 1556 earthquake due to amplification effects within the graben sediments (*Middleton et al.*, 2016); (2) the seismogenic depth and slip are very large; (3) the rupture extends further than the currently mapped extent. Since the geomorphology of the epicentral area has been degraded by widespread agriculture and relatively rapid weathering and erosion, it has been challenging to investigate the 1556 earthquake rupture. However, within some of the river catchments crossing the two faults a discontinuous scarp of ∼7-8 m height is observed in fluvial/alluvial surfaces, e.g. *Yuan and Feng* (2010). Modification of the landscape by heavy industry has also obscured much of the longer-term geomorphology of the range-fronts, leaving only a small number of sites where relatively undisturbed late Pleistocene/Holocene geomorphology is preserved.

This study focusses on the Chishui river catchment (Figure 6.7). This site is important, as it is one of the few where the 7-8 m scarp is present, and where multiple higher terraces are also well preserved. During the study, the river terrace and gravels were quarried, providing an opportunity to combine our study of the surface geomorphology with a cross-section through the fault zone.

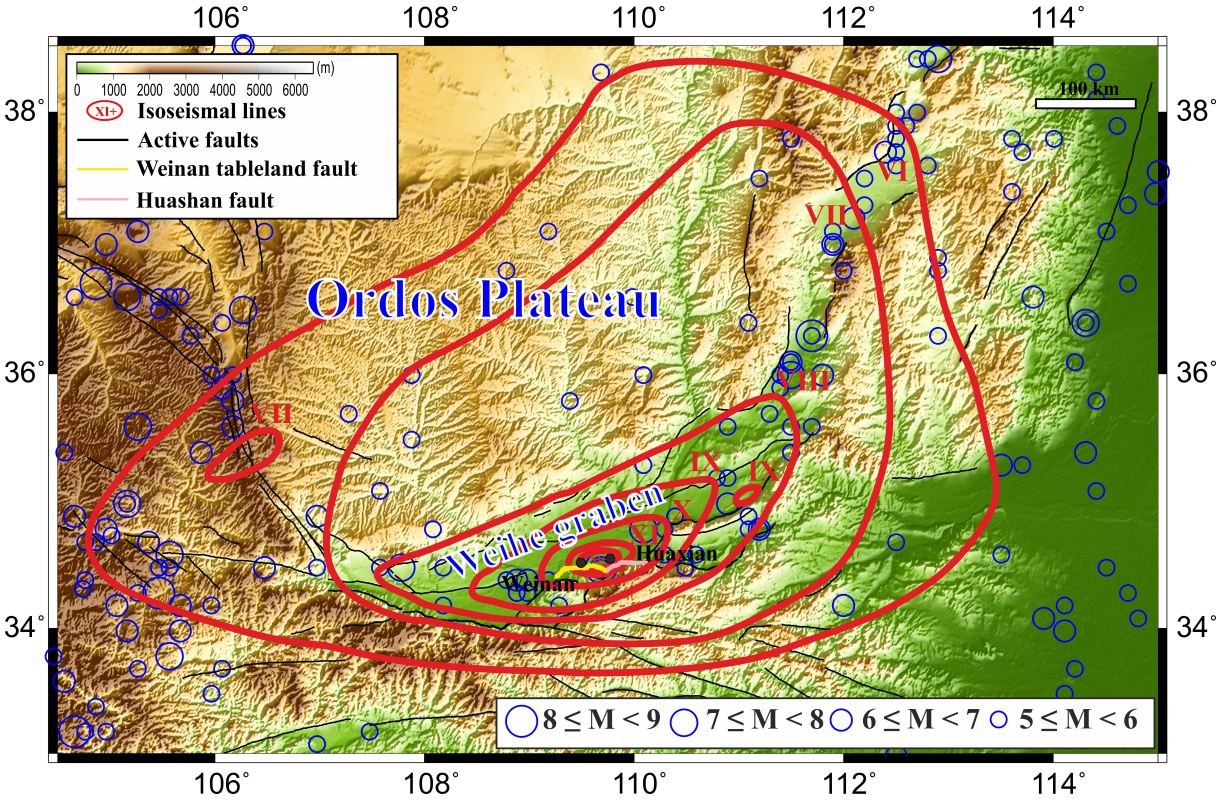


Figure 6.6: Isoseismal map of the 1556 Huaxian earthquake. Intensity (greater than 4) was mapped by *Yuan and Feng* (2010). Intensity scale is summarised in Table 6.1. Black dots mark Weinan and Huaxian. Blue circles indicate epicentres of historical earthquakes (greater than M 5), from *Song* (2012).

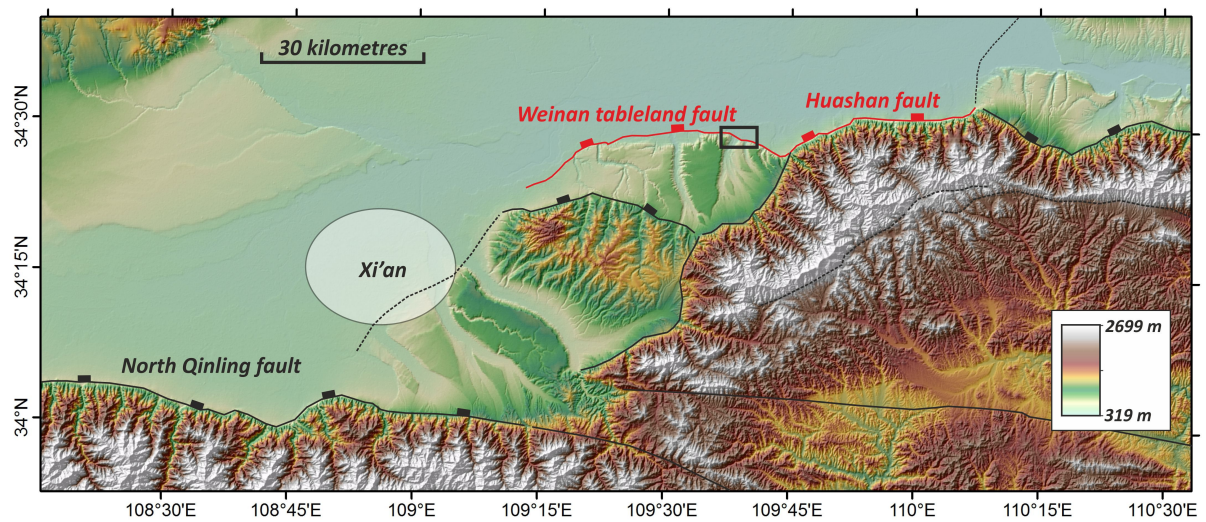


Figure 6.7: SRTM shaded-relief topography of Xi′an and the eastern Weihe graben. Black polygon marks the coverage of Figure 6.9, centred on the Chishui river cathcment.

Table 6.1: Intensity scale for the 1556 Huaxian earthquake, translated and summarised from *Yuan and Feng* (2010). The damage associated with each intensity level for the 1556 earthquake is based on extensive historical records and field investigations.

Intensity	Houses			Structures				Surface phenomena	Casualties
	Type I	Type II	Type III	City walls	Towers	Graves (upright stones)	Bridges		
VI	Many houses damaged. Roof tiles dislodged.	Minor damage.		No or minor damage.	Minor damage to tower made of bricks and stones.	Minor damage.	Handrails were damaged.		<10
VII	Most houses were damaged. A few collapsed.	Many houses were damaged. A few were severely damaged.	Minor damage to most houses.	Damage to unsolid walls.	Damage to the tops of towers.	A few were damaged.	Cracked.	Many cracks on wet and loose soil. Landslides in mountainous areas.	10-100
VIII	Most were severely damaged. Many collapsed.	Many were severely damaged. A few collapsed.	Minor damage to most houses. A few were severely damaged.	A few walls collapsed.	Towers were damaged. Tops of towers collapsed.	Many were damaged.	Some collapsed.	Centimetre-scale cracks at the surface and water released. A few mudflows and landslides occurred in mountainous areas.	100-10,000
IX	Most collapsed.	Many collapsed.	Many severely damaged. A few collapsed.	Many walls were severely damaged.	Towers were severely damaged. Some collapsed.	Most collapsed.	Completely destroyed.	Many,surface cracks up to 10 cm wide. Many mudflows and landslides occurred in the mountains.	
X	All collapsed.		Most collapsed. Very few temples and palaces survived.	All collapsed.	Most collapsed.	All collapsed.	Damage to bridges on hard bedrock.	Surface cracks can be tens of cm wide. Some cracks wider than 1 m. Crack zones extend for a few kilometres on soft alluvium. Large number of landslides in mountainous areas, blocking river channels and forming barrier lakes.	
XI					No records.		Bridges on bedrock collapsed.	Bedrock landslides. Surface scarps up to a few metres high. Ubiquitous surface cracking up to a few metres wide. Water sprayed from cracks and rivers were diverted.	>10,000
XII					No records.		No records.	Dramatic changes to surface topography. River systems completely destroyed resulting in flooding. Large numbers of landslides and land subsidence, killing most plants and animals.	No records.

Abbreviations:
House Type: I is for normal dwellings; II includes schools, government buildings and solid houses; III is for palaces and temples.

6.4 Geomorphology of the Chishui Catchment

To interpret the geomorphology of the Chishui river catchment, I combined field investigation with analysis of a 1-m digital elevation model (DEM) constructed from 0.5 m resolution Pleiades stereo satellite imagery. The imagery was acquired in winter, to minimise vegetation cover. A close-up of the 1-m Pleiades DEM where the Chishui river catchment crosses the Weinan tableland fault is shown in Figure 6.9. A patchwork of river terraces covers the southern half of the image. Chishui village sits above the western bank of the river on the footwall of the fault. A collection of industrial buildings and a deep gravel quarry excavation are present in the northern half of the image. The geomorphology of the Chishui site has been described by several authors, each of which have made differing interpretations of the terrace stratigraphy (*SSB*, 1988; *Kaizuka et al.*, 1992; *Rao et al.*, 2015). Radiocarbon samples were collected from the Chishui site in order to investigate the timing of the earthquakes on the Weinan tableland fault. All the radiocarbon material, ages and calibration for samples were summarised in Appendix E.

6.4.1 Generation and Validation of the Pleiades DEM

Pleiades stereo imagery (0.5 m resolution) was acquired on 30 December 2013 by Pleiades-1A, with a stereo angle of 30 degrees. Global Positioning Systems (GPS) measurements were collected in the field (listed in Table 6.2) using the network Real Time Kinematics (RTK) from the CEA Shaanxi Province to calibrate and evaluate the Pleiades DEM. Pleiades data were processed using the Leica Photogrammetry Suite (LPS). 28 tie points and 2 GPS measurements taken from crossroads (Figure 6.8) were used to refine the original rational function model (RFM) (see Section 2.4.1 in Chapter 2). After refining the RFM, a pixel-by-pixel matching procedure was implemented, with a relatively small window size of 5×5 pixels to avoid strong smoothing of the topographic surface (readers are referred to Chapters 2 and 3 for details of methods). The resulting point cloud from the pixel-by-pixel matching was filtered by averaging within a block of 1 m and then gridded with a pixel spacing of 1 m (WGS84 UTM 49N) using the continuous curvature splines in tension. Compared to the RTK measurements (see Table 6.2), the resulting Pleiades DEM has an error of -0.1±0.3 m, -0.4±0.5 m and -0.5±0.3 m in X, Y and Z

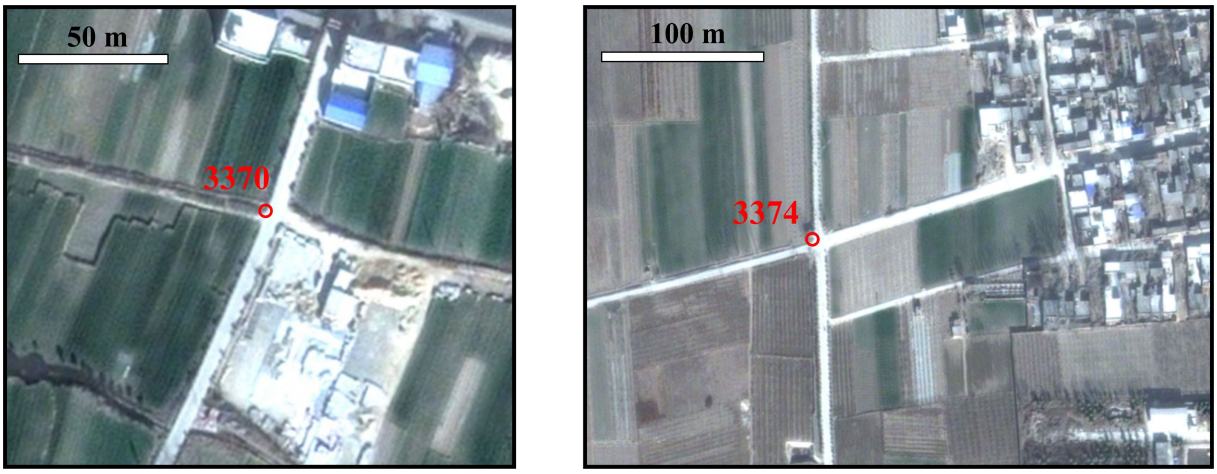


Figure 6.8: GPS measurements taken from crossroads were used as ground control points (GCPs) in the generation of the Pleiades DEM.

Table 6.2: Comparison between the RTK measurements and Pleiades DEM. The 11 GCPs taken from crossroads were identified in the orthorectified Pleiades imagery.

ID	RTK GPS			Pleiades DEM		
	X (m)	Y (m)	Z (m)	ΔX (m)	ΔY (m)	ΔZ (m)
3370	374,462.79	3,817,629.02	328.013	0.2	0.4	-0.3
3371	374,464.17	3,817,633.04	327.875	0.2	-0.8	-0.5
3372	374,069.73	3,818,890.14	311.727	-0.2	-1.4	-0.7
3373	374,061.24	3,818,893.54	311.593	-0.6	-0.2	-0.8
3374	377,098.64	3,817,991.89	325.531	-0.0	-0.1	-0.5
3375	377,098.92	3,818,002.72	325.846	-0.1	-0.4	-0.7
3376	377,751.65	3,817,320.68	327.165	-0.4	-0.8	-0.6
3377	377,758.26	3,817,320.39	327.208	0.5	-0.7	-0.4
3379	379,242.85	3,817,293.41	337.498	0.0	-0.7	-0.8
3380	379,243.18	3,817,304.72	337.144	-0.2	-0.1	0.1
3381	379,237.62	3,817,303.73	337.074	-0.2	0.2	-0.1

directions respectively.

6.4.2 Geomorphic Analysis and Geological Dating

The Weinan tableland fault is visible as a steep scarp running from top-left to lower-right of the third panel in Figure 6.9. The fault outcrops in both banks of the active channel (e.g. *Rao et al.* (2015)), and also in the walls of an extension to the gravel quarry that was excavated in 2014, allowing us to precisely locate the buried fault trace. A series of topographic profiles from the Pleiades DEM show 4 river terraces (T0, T1, T2 and T3,

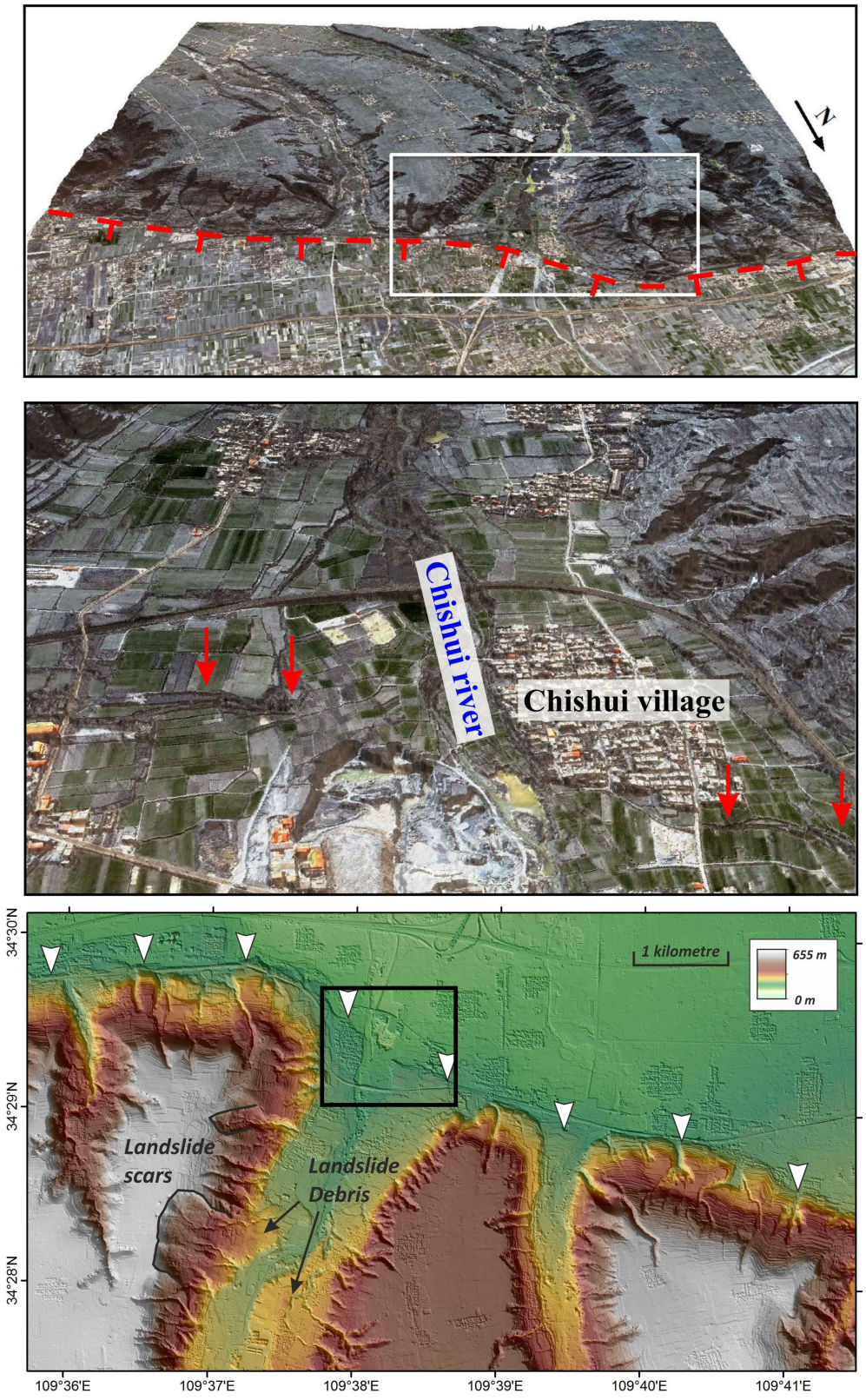


Figure 6.9: (top) 3D perspective view of Pleiades imagery (0.5 m resolution). See Figure 6.7 for location. The white polygon shows the area of the lower image. Dashed red line indicates the Weinan tableland fault. (middle) A close-up view of the Chishui catchment. Red arrows mark fault scarps. (bottom) Pleiades shaded-relief topography of the Chishui river catchment. White arrows indicate preserved scarps along the Weinan tableland fault. Black box shows the location of Figure 6.10.

Figure 6.10). The surface of the youngest terrace (T0) is not displaced across the fault and its deposition thus postdates the last slip event on the fault. The Chishui river has incised into the surface of T0 to occupy a narrow channel. Two steps in height of ∼1 m appear to show channel positions during progressive incision into the T0 surface. Risers marking the edges of T0 deposition on the downthrown (northern) side of the fault are inferred from ∼1 m steps in the height of the terraced land surface. South of the fault the T0 surface is farmed and ∼1 m of silty soil has developed above the fluvial gravels.

T0 is flanked by older terraces (T1 and T2) that are displaced by the fault, and by a higher terrace (T3) in the hanging-wall that is not preserved at the fault trace itself (Figure 6.10). The surface of T1 is offset vertically by ∼7.5 m across the fault (profiles E1-E1′ and E3-E3′ in Figure 6.10). T1 is best preserved on the western side of the active river channel, but fragments are also preserved at the eastern edge of the T0 surface, and also as a small outlier within T0 (Figure 6.10). Exposures through the T1 terrace deposits are visible directly east of Chishui village in the T0-T1 riser, which has been refreshed for the digging of an irrigation channel (Figure 6.10). At this location, the surface of T1 is ∼5.5 m above the surface of T0 (profile A-A′ in Figure 6.10), with an exposed stratigraphy composed of ∼3 m of silty soil with occasional rounded clasts (Figure 6.11). The soil overlies fluvial gravels. Detrital charcoals (RC3 & 4) from the base of the soil yield ages of 2254.5±63.5 and 2260.5±64.5 calibrated years BP (Figure 6.11).

Terrace T2 is best preserved along the eastern side of the Chishui valley where it forms an ∼13 m scarp at the fault (profiles E2-E2′, and E4-E4′ on the western side in Figure 6.10). We found exposures through the T2 deposits at location RC1 & 2 in Figure 6.10 in excavations made for an irrigation canal. Fluvial gravels are covered by ∼5 m of silty soil (Figure 6.11). Near the base of the soil we found a cultural layer containing bone and ceramic objects typical of the Banpo culture (∼5-8 ka, Figure 6.12). The cultural objects were mixed with abundant detrital charcoal, of which two samples yielded ages of 5841.5±66.5 and 5820.5±57.5 calibrated years BP (Figure 6.11). *Rao et al.* (2015) also visited this (or a nearby) exposure, obtaining a single age of 5300±30 calibrated years BP from organic-rich soil that they state is situated within the alluvial layers.

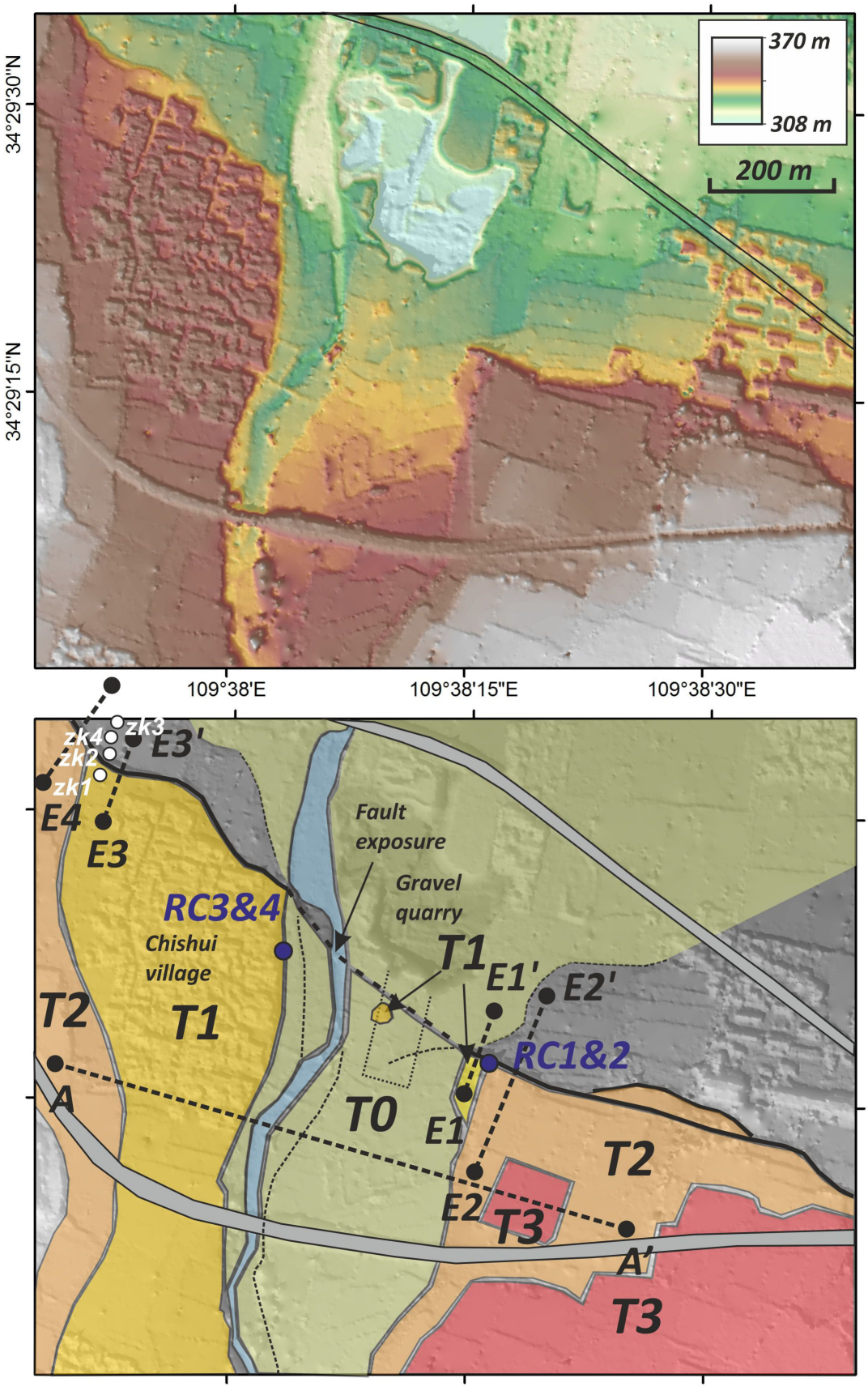


Figure 6.10: (top) Pleiades shaded-relief topography of the Chishui catchement with footwall terraces labelled from T0 (youngest) to T3 (oldest). (bottom) Surface geomorphology of the Chishui catchment. A-A′, E1-E1′, E2-E2′, E3-E3′, and E4-E4′ are topographic profiles. "RC" stands for radiocarbon samples. Dashed polygon indicates the extension of the quarry exposure. White dots are boreholes (zk1–zk4).

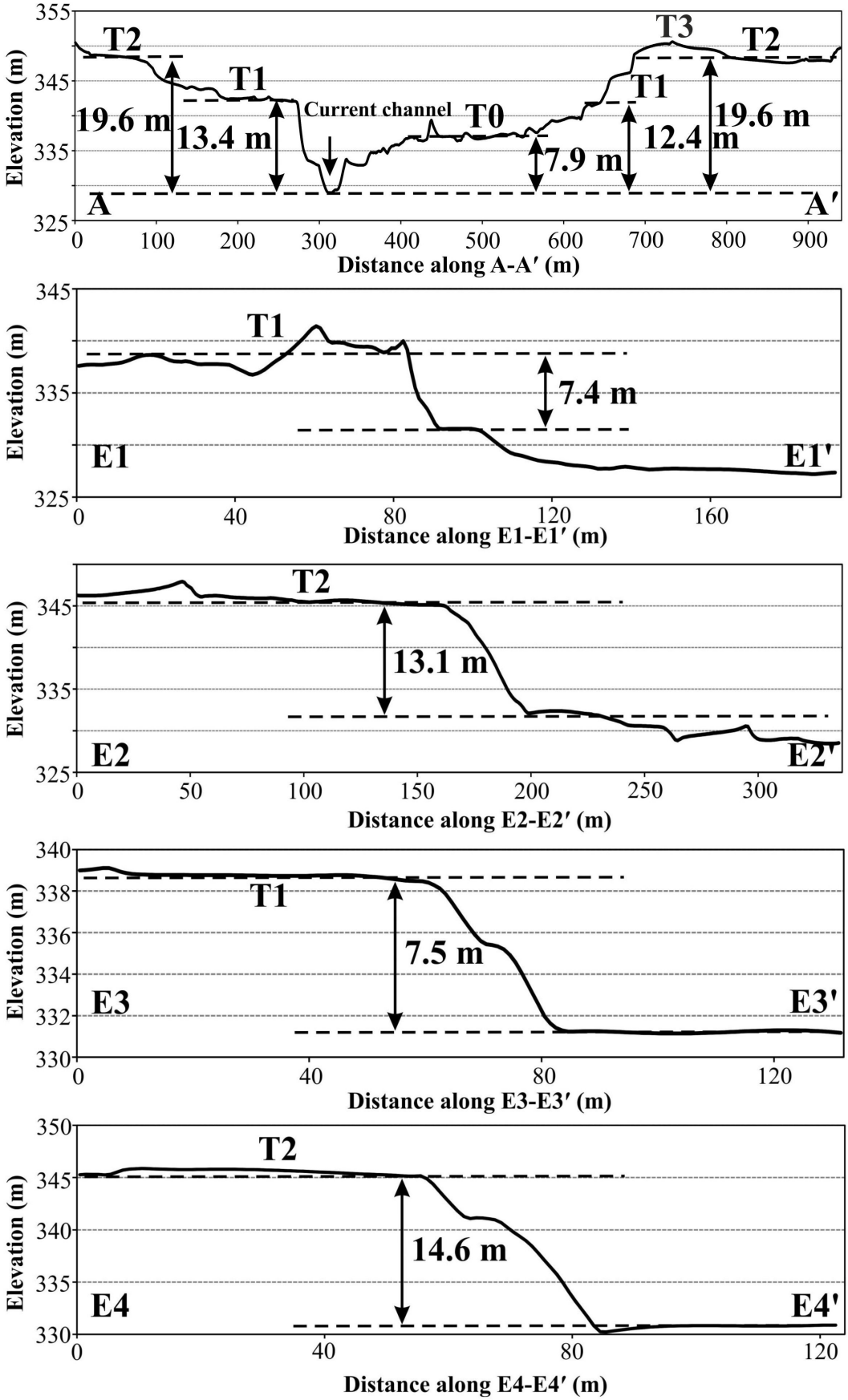


Figure 6.10 Cont.: Topographic profiles showing river terraces and scarps heights.

There are no remnants of terrace T3 at the fault scarp. It is ∼1-2 m higher than T2 and occurs in two fragments (Figure 6.10). The riser between T2 and T3 has obviously been heavily modified for agricultural use. We speculate that the distribution of T3 may represent pre-earthquake channel incision into the T2 surface.

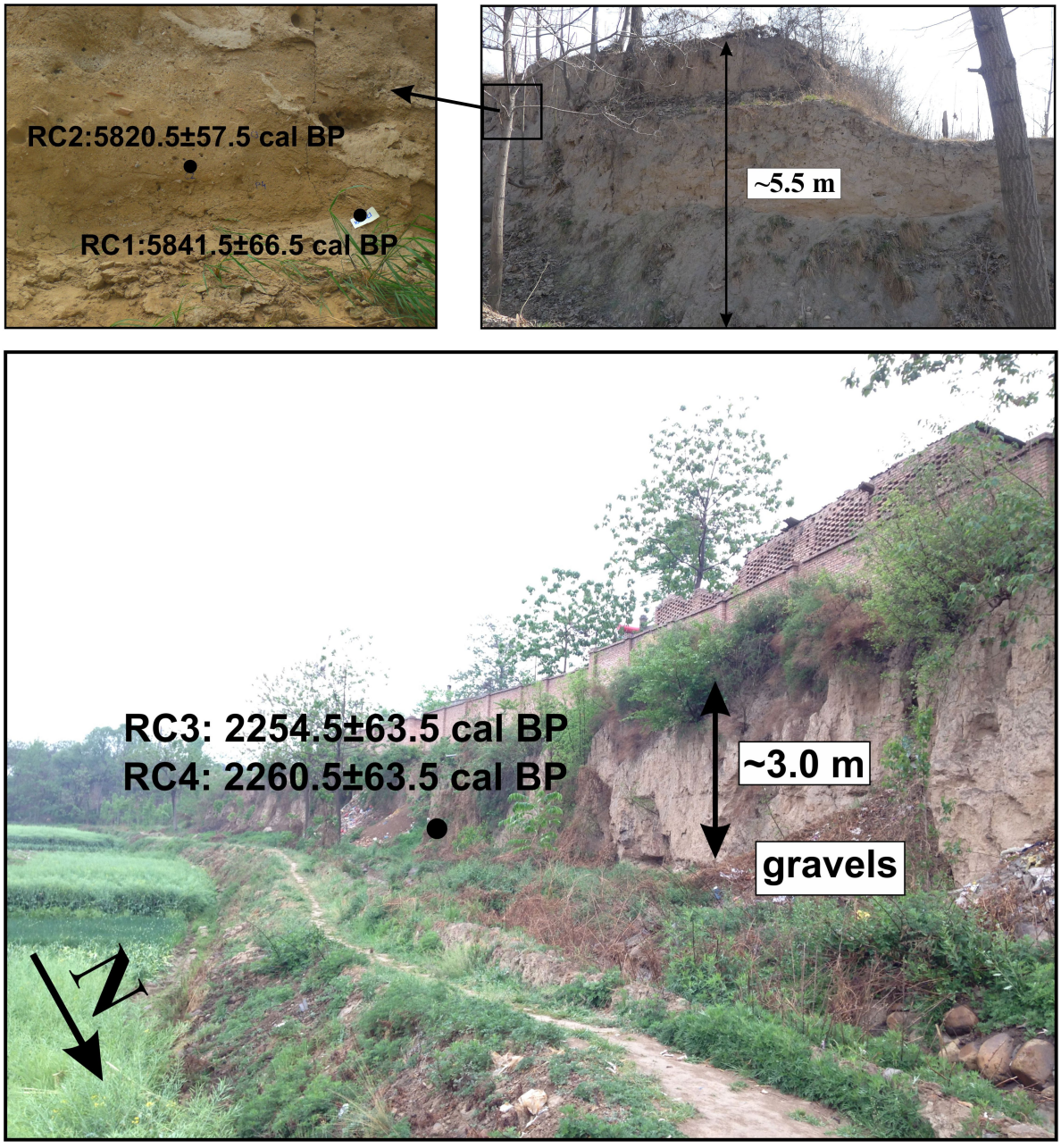


Figure 6.11: (top) Radiocarbon samples RC1 and RC2 were taken from a yellowish sandy clay layer (∼5.5 m below the surface of T2) on top of a river gravel layer in T2. Looking east. (bottom) Radiocarbon samples RC3 and RC4 collected from a silt layer that overlies gravels at a depth of ∼3 m below the surface of T1. Looking south. See Figure 6.10 for location.



Figure 6.12: (top) Pottery and bones collected from T2. (bottom) Identification of the cultral objects. Similar pieces displayed in the Shaanxi Archaeological Museum were used to compare with ours (personal communications with an archaeologist), which suggests that the pottery and bones are likely to be from the same age, ~5-8 ka.

6.4.3 Quarry Exposure

After acquisition of the Pleiades data gravel quarrying was extended southwards from the footwall across the fault beneath the T0 (post-earthquake) surface. See Figure 6.10 for location. A 3D model of the quarry exposure (110 m × 30 m × 11 m) was constructed from 287 field photographs using the Structure from Motion (SfM) technique (Figure 6.13). Four GPS measurements were collected in the trench and used as GCPs to estimate the absolute positions of the points. Readers are referred to Chapter 2 for methodology. Orthorectified photo-mosaics of the eastern and western walls were also produced.

The quarry extension exposed a main north-dipping fault plane, along with the upper 10 m of the footwall and hanging-wall stratigraphy (Figures 6.14 and 6.15). The fault dips 45-55°N, and striations indicate normal faulting, with a slight left-lateral component (*Rao et al.*, 2015). The stratigraphy and fault zone morphology varies between the western and

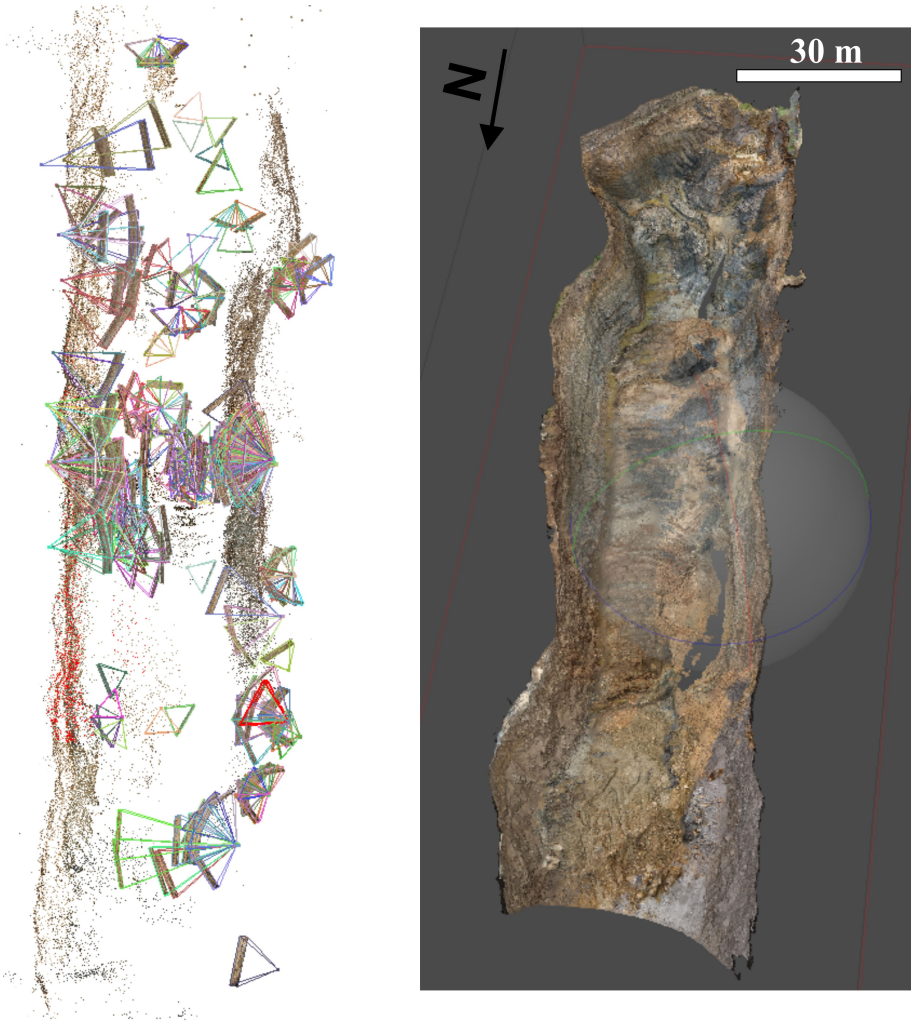


Figure 6.13: 3D model of the quarry exposure (110 m × 30 m × 11 m, looking down from above) near Chishui village, constructed from SfM. (left) Sparse reconstruction solves for the orientation parameters of all the cameras, and generates a sparse point cloud. (right) Dense point cloud.

eastern walls, at a distance of ∼30 m along strike.

On both quarry walls the hanging-wall stratigraphy is composed of coarse river gravels, with occasional thin (10-20 cm) discontinuous bands of finer material. The footwall stratigraphy is composed of Pleistocene lacustrine muds and silts overlain by ∼3 m of fluvial gravels. Boreholes in the graben interior have encountered similar lacustrine sediments at depths of ∼150 m (*Dai and Feng*, 2004). The top of the Pleistocene fine-grained sediments have been eroded, channelized, and unconformably overlain by the coarse gravels. Limited age control is provided by radiocarbon dates from detrital charcoals and from bulk organic-rich sediment. In the following we document footwall and hanging-wall stratigraphy and describe the observed deformation.

Western wall stratigraphy and structure

Two main faults were encountered in the western wall, which together define a fissure or graben (infilled by unit 8) ∼5 m wide (Figure 6.14). Unit 8 (orange gravels) has a similar stratigraphy to unit 9, so we infer it collapsed from the footwall as a coherent block. Fault F1w separates the Pleistocene lacustrine deposits from Holocene gravels and dips ∼45°N. F2w is near vertical and is interpreted as the margin of a fissure into which sediment subsequently collapsed. Between F1w and F2w the sediments are faulted along multiple steeply-dipping planes (F3w-F5w) that are defined by zones of rotated clasts. North of F2w the upper part of the hanging-wall sequence is faulted on two steeply south-dipping planes with displacements of ∼10 cm that are visible due to the offset of thin silt beds. It is likely that other minor fractures exist, but are not identified due to the absence of offset marker beds.

The footwall of F1w is made up of ∼6 m of banded blue-grey muds and silts (unit 1). We interpret these deposits to have formed within a predominantly lacustrine environment, either due to localised ponding, or at a time of lake formation within the main Weihe graben. Similar deposits of early Pleistocene age are found at depths of ∼150 m in the Weihe graben (*Dai and Feng*, 2004), though we cannot confirm whether the exposed muds are of the same age. The muds are overlain by several coarse sand to coarse gravel units (units 9 and 10), each of which have channelised bases showing erosion into the underlying units. The lower gravel units (units 2a-2d) have a distinct blue-grey colour from the reworking and incorporation of the underlying lacustrine sediment within their matrices. The blue-grey fluvial units are in turn overlain by dark-orange gravels (unit 3). Clasts within the upper part of the orange gravels are coated with an organic-rich black mud, providing an opportunity for dating, as well as providing an excellent marker horizon. The western quarry wall cuts through a small mound (∼10 m long, 2–3 m high) within the present-day agricultural fields that we interpret as a small remnant of terrace T1 (Figure 6.16). The mound contains coarse brown fluvial gravels with no discernible layering. Younger deposits (units 10-12) overlying unit 8 are not deformed by faulting, and we assume that they represent post-earthquake incision of the uplifted footwall, followed by aggradation of sediment within the river basin. Above unit 3, the transition from

silt/sand to coarse gravel probably represents times of active channel migration. A light-brown soil (unit 13) of ∼1 m thickness covers the uppermost gravel layer. The present-day land surface is used for maize farming.

The hanging-wall sequence (north of fault F2w, right-hand side of the log) is predominantly gravel. The quarry floor likely represents the top of the blue/grey muds (unit 1). The lowermost parts of the exposure are blue/grey gravels, which are overlain by orange gravels containing the organic-rich marker horizon, see Figure 6.16. Unit 4 is a sequence of fluvial gravels and silts, with layering picked out within the relatively well-sorted gravels by variations in the clast size. The silt beds (units 5-7) are truncated at fault F2w, and displaced by additional minor south-dipping faults.

Eastern wall stratigraphy and structure

F1e and F2e are the two main faults in the eastern wall, which together define a fault zone (Figure 6.15). The ∼1 m wide fault zone, infilled by rotated clasts with no bedding retained (unit 15), separates the Pleistocene lacustrine deposits (unit 1) from Holocene gravels (unit 4) (Figure 6.15). South of F1e, the middle part of the footwall sequence is faulted by a 50°N dipping fault (F3e), with displacements of ∼40 cm that are visible due to the offset of thin blue-grey silt beds.

The footwall stratigraphy exposed in the eastern wall is similar to that in the western wall. The banded blue-grey muds and silts (unit 1) are overlain by ∼1 m thickness of a blue-grey fluvial unit (unit 3) which has been incised and infilled by a unit of fluvial gravels and silts (unit 9). Unit 4 has a thickness of ∼8 m in the hanging-wall sequence (north of fault F2e, left-hand side of the log). The lowermost parts of unit 4 in the hanging-wall are coated with organic-rich black muds. A silt layer (unit 14) is truncated at fault F2e. The whole system is covered by a continuous silt layer (unit 10) with a thin layer of organic-rich rootlets in a palaeosol, which is in turn covered by fluvial gravels (unit 12); therefore units 10 and 12 must postdate the earthquake. Above unit 1, the stratigraphy also shows a transition from silt/sand (unit 3) to coarse gravel (unit 12).

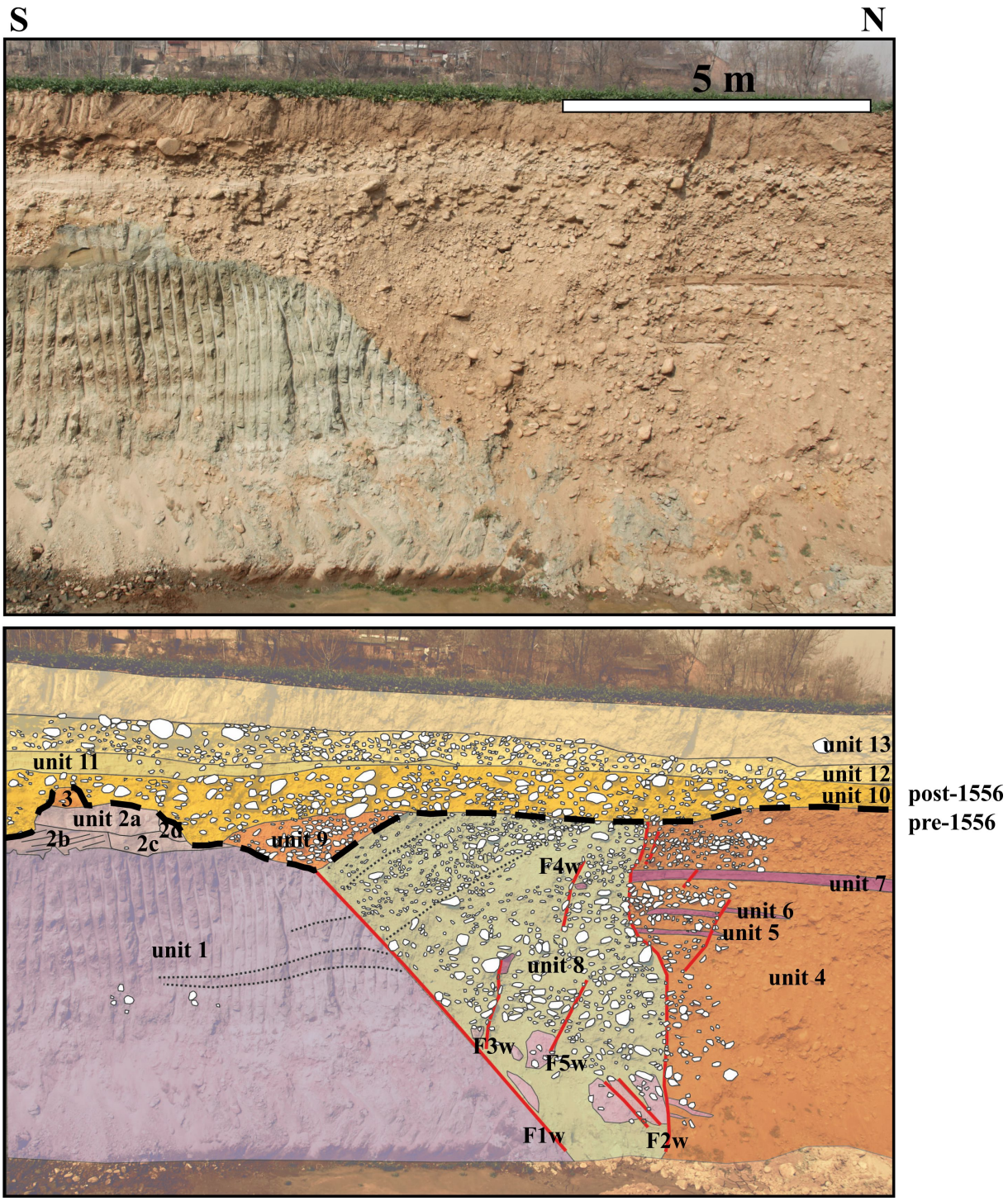


Figure 6.14: Western wall of the trench at the Chishui site (see Figure 6.10 for location). (top) Original photo. (bottom) Trench log. F1w and F2w are the main faults. White filled polygons are gravels.

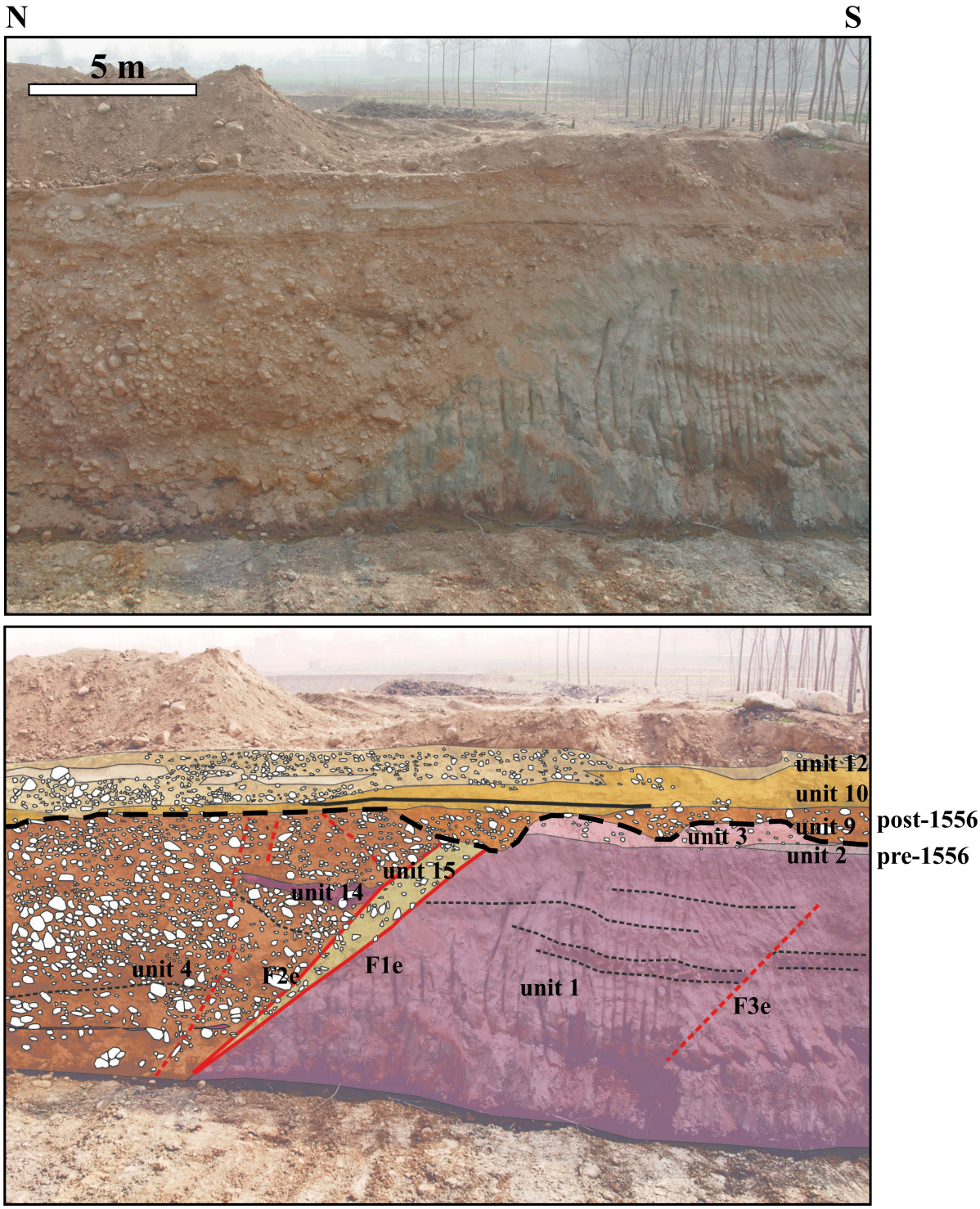


Figure 6.15: Eastern wall of the trench at the Chishui site (see Figure 6.10 for location). (top) Original photo. (bottom) Trench log. F1e and F2e (solid red lines) are the main faults. White filled polygons are gravels. Solid black line is a layer of organic-rich muds.

Age constraints from the trench

We took six samples from the western trench wall, and five from the eastern wall for radiocarbon dating (Figure 6.16). All the radiocarbon ages were summarised in Appendix E. Before describing the dates from the trench, we first summarise the stratigraphy of both walls.

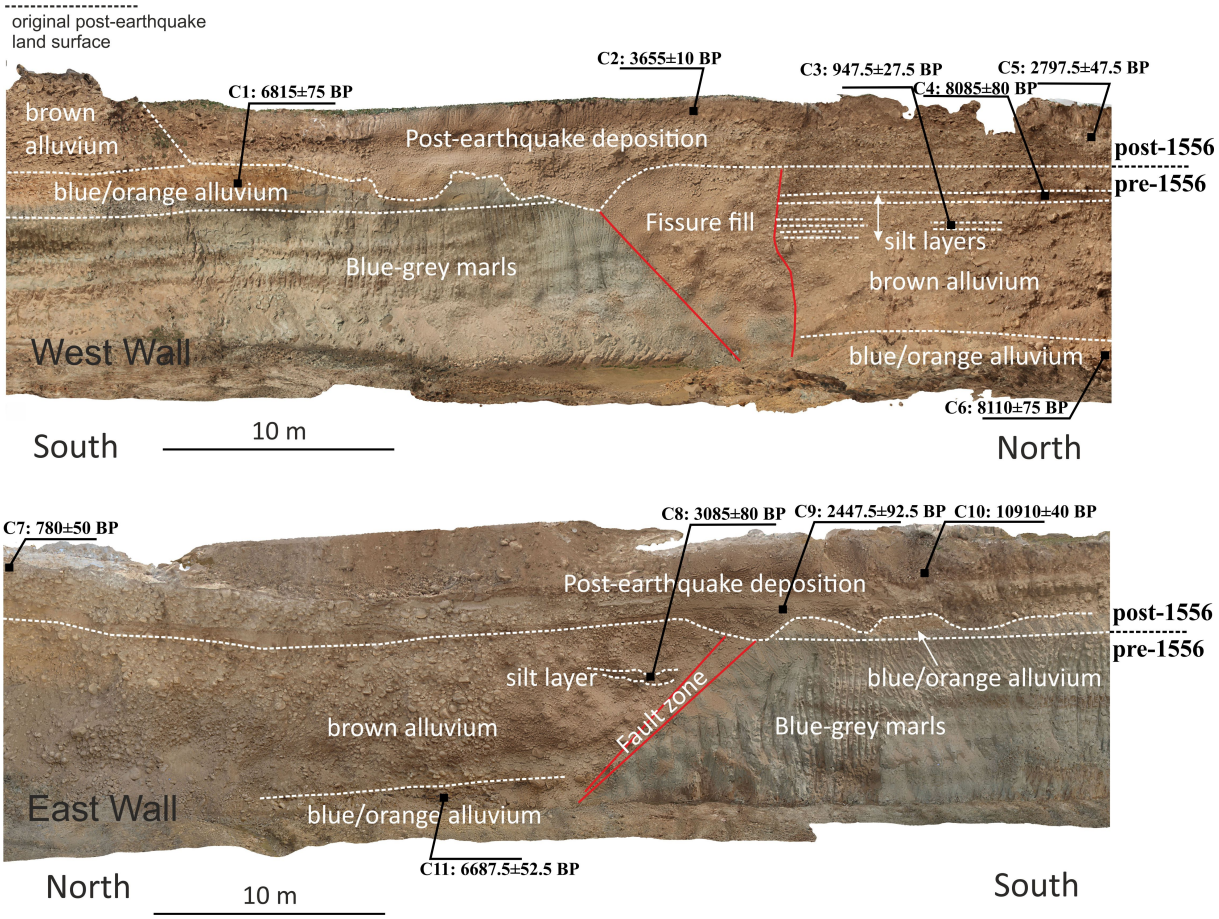


Figure 6.16: Radiocarbon samples collected from the Chishui trench. Six samples were collected from the western wall, and five from the eastern wall. Interpretation of the trench is presented in Figures 6.14 and 6.15.

In the western wall, unit 8 is a single coherent block and retains the stratigraphy, providing evidence for one event. Units 5–7 are truncated at fault F2w, and therefore must predate this event. The basal unit of the post-earthquake sequence is unit 9, a distinct unit due to the uniform light-coloured coating on the boulders, and the angular unconformity with underlying units within the fault zone. In the eastern wall, the silt layer (unit 14) is truncated at fault F2e, and should predate the last event. The top units (units 9, 10 and 12) overlie the system without interruption and therefore postdate the last event.

Sample C3 from unit 6 in the western wall has an age of 947.5±27.5 years BP, and C8

from unit 14 in the eastern wall gave an age of 3085±80 years BP. Both units should predate the last surface rupturing event. We therefore assume that the younger of the two values most immediately predates the earthquake. If 947.5±27.5 years BP is close to the actual date of the earthquake, this earthquake must be the 1556 Huaxian earthquake as it is the only event large enough in the historical records. Sample C1 was taken from the base of a blue/orange alluvium in the footwall (Figure 6.16), and yields an age of 6815±75 years BP, similar to C6 from the base of the hanging-wall exposure. It is likely that the two layers were offset by the 1556 earthquake, which indicates a vertical slip of 7.2 m, and thus giving a slip of ∼10 m on the 45°N dipping fault.

Other samples were collected from the unfaulted units and should all postdate the 1556 earthquake. However, all of the ages appear to be old. They are also inconsistent with the stratigraphy. We note that the 1556 earthquake caused widespread landsliding upstream of the fault (*Yuan and Feng*, 2010), which is evident in Figure 6.9. It is plausible that the deposits that overlie the fault zone incorporate detrital material from upstream, and thus yield ages that are older than expected.

6.5 Borehole Cross-section

Four boreholes (zk1-zk4) were drilled across the fault scarp at the western side of the Chishui river catchment (Figure 6.10). The boreholes, with depths of 71.3 m (zk1), 38.0 m (zk2), 20.0 m (zk4) and 50.7 m (zk3) respectively, exposed three fault splays (Figure 6.17). F1 offset the upper layer, made up of gravels and silt clays (unit 1 in zk1 and unit 2 in zk2) by 7.15–8.05 m, suggesting that the most recent rupture occurred on F1. The vertical offset from the boreholes agrees well with the 7.5 m fault scarp on the T1 surface. The sequence of units below unit 1 are predominantly lacustrine sediments, the same deposits as we saw in the quarry exposure (Figures 6.14 and 6.15). We did not find clear evidence for offset features on fault F2, but the silt clay layer (unit 4 in zk4) is much thicker than the same sediment in zk 2 (unit 3), which suggests that unit 3 in zk 2 was uplifted and has been eroded since then, whereas the same layer in zk4 in the hanging-wall has been preserved. Above unit 3, the gravel layer that was offset by F1 was not affected by F2, i.e. unit 2 is continuous in zk2 and zk4, indicating that faulting

on F2 was earlier than F1. The earliest rupture (F3) offset unit 4 in zk4 and unit 5 in zk3 (predominantly made up of silts) by 10.3 m. The three fault splays show that the earthquake ruptures are not co-located along the borehole section line. Although we do not have any dates from the boreholes, the stratigraphy exposed in zk1 is very similar to the quarry exposure, ~8 m thick orange gravels overlying banded blue-grey muds and silts. The vertical offset is also similar (~7-8 m), suggesting that the event on fault F1 is the 1556 earthquake.

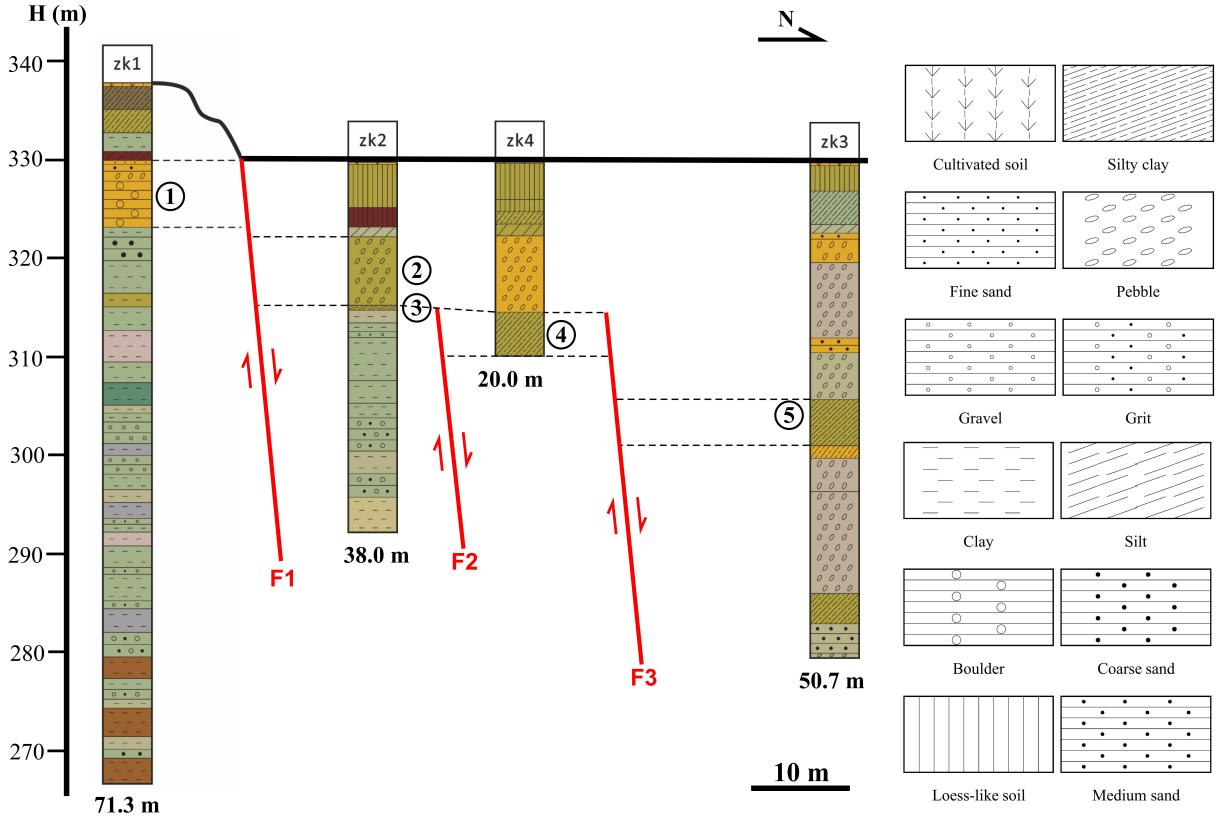


Figure 6.17: Borehole cross-section at the Chishui site (see Figure 6.10 for location). Four boreholes (zk1–zk4) were drilled, with a depth of 71.3 m (zk1), 38.0 m (zk2), 20.0 m (zk4) and 50.7 m (zk3) respectively. The stratigraphy of the four boreholes exposed three fault splays, F1, F2 and F3.

6.6 Discussion

6.6.1 Landscape Evolution of the Chishui River Catchment

Analysis of the Pleiades DEM shows scarp heights of 7.5 m and 14 m adjacent to the T1 and T2 terraces respectively. The scarp in the central part of the catchment has

been almost entirely removed by fluvial erosion after the most recent earthquake. The available age control on the displaced terraces T1 and T2 comes solely from the overlying soil layers, and hence for both we only postdate the time at which fluvial deposition ended. The fluvial gravels of the youngest displaced terrace had been removed from the active river system by ∼2250 years BP, much earlier than the 1556 earthquake. However, the ages are explained if the development of T1 and T2 occurred in a similar manner to that seen for the youngest terrace (T0).

In this scenario, an initial aggradation of river gravel within the Chishui catchment (Figure 6.18a), potentially at the last glacial-interglacial transition (*Rost*, 2000), was followed by downcutting of the active channel, leaving behind T3 and T2, and allowing farming and soil development on the abandoned terrace treads by ∼6 ka. The highest observed terrace (T3) may represent remnants of the original post-glacial fluvial surface that was dissected by river down-cutting in the same way as observed for T0. T2 and T3 were offset by ∼7-8 m in the penultimate earthquake, and then abandoned (Figure 6.18b). This may have happened sometime around 6 ka, and was followed by thick soil development with the Banpo cultural objects on top of the T2 and T3 surface. Meanwhile, downcutting of the active channel had removed most of T2 and T3 on its western side. Farming and soil development started on T1 since it was removed from the active river system by channel entrenchment around ∼2 ka (Figure 6.18c). The 1556 Huaxian earthquake offset terrace T1, and enlarged the offset of T2 and T3, and was accompanied by widespread landsliding in the upstream (Figure 6.18d). The two earthquake ruptures appear not to be co-located in the western part of the study area, as the boreholes exposed three fault splays, ∼65 m apart and the quarry exposure appears to show only one earthquake. However, in the eastern part of the study area, the development of a 14 m scarp in T2 indicates rupture along a single trace in two earthquakes. Since the 1556 earthquake, the footwall was eroded, leaving remnants of T1, followed by aggradation of sediment on T0 (Figure 6.18e). Evidence of landslides and remnants of the preserved T1 surface in T0 are visible in the present-day imagery (Figure 6.18f).

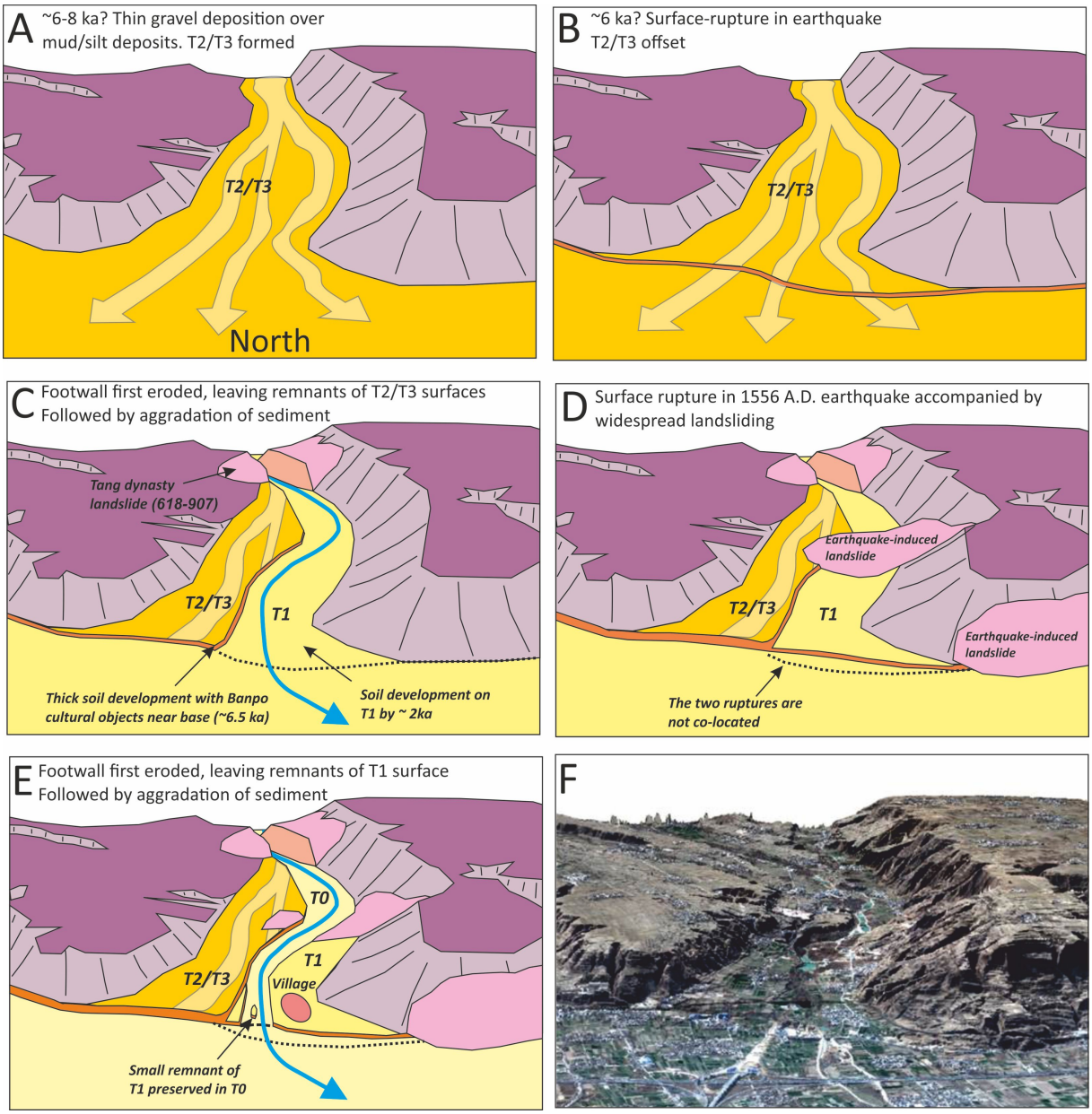


Figure 6.18: Cartoon showing the landscape evolution of the Chishui river catchment. (a) T2/T3 started to form. (b) Penultimate earthquake offset T2/T3. (c) Footwall was eroded, leaving remnants of T2/T3 surfaces followed by aggradation of sediment. (d) Surface rupture in the 1556 Huaxian earthquake, causing widespread landsliding. (e) Footwall was eroded. (f) 3D perspective view of the present-day land surface.

6.6.2 Re-estimating the Magnitude

In this section, I re-estimate the magnitude for the 1556 earthquake based on observations made in this study (Table 6.3). I also consider the upper bounds on all the fault parameters in order to estimate the likely maximum magnitude for the 1556 earthquake (Table 6.3). The causative faults have a combined length of ∼90 km (Figure 6.7). Microseismic data in the Weihe graben show a seismogenic thickness of ∼20 km (*Yuan and Feng*, 2010) and I took 30 km as the upper bound. Fault dip (45°) and surface slip were measured from the

Table 6.3: Fault parameters and magnitude estimates.

Parameter	Best Estimate	Upper Bound
Fault Paramters		
Fault length (km)	90	/
Seismogenic thickness (km)	20	30
Fault dip (°)	45	/
Down-dip width (km)	28	42
Fault area (km^2)	2520	3780
Maximum slip (m)	10	/
Average slip (m)	10	/
Magnitude Estimates		
M_w from fault length	7.3	/
M_w from fault plane area	7.4	7.6
M_w from maximum slip	7.4	/
M_w from average slip	7.5	/
M_w from M_0=$\mu A\bar{u}$	7.9	8.0

quarry exposure. I assumed that the dip at the surface is the same as the dip at depth. The 10 m slip was assumed to be the maximum slip. As I do not have a slip distribution, and a few ∼7–8 m scarps were also observed at other places along the causative faults (*Yuan and Feng*, 2010), I also used 10 m as the average slip.

Applying scaling relationships between moment magnitude and each of fault length, fault plane area, maximum slip, and average slip (*Wells and Coppersmith*, 1994), I obtained M_w 7.3, M_w 7.4 (with an upper bound of M_w 7.6), M_w 7.4 and M_w 7.5, respectively (Table 6.3). I also calculated seismic moment (M_0) using M_0=$\mu A\bar{u}$, with a modulus of rigidity of 3×10^{10} Pa, and obtained a seismic moment of 8.32×10^{20} Nm with an upper bound of 1.13×10^{21} Nm, which correspond to a moment magnitude ($M_w = \frac{2}{3}\log_{10} M_0 - 6.03$) of 7.9 with an upper bound of 8.0.

The results suggest that the previously proposed magnitude of 8.25–8.5 may be an overestimate of the size of the 1556 Huaxian earthquake. Based on the various magnitude estimates, I suggest a preferred magnitude in the range M_w 7.3–7.9. Historical records of earthquakes (such as damage) can provide valuable information about active faulting, but sometimes the intensity of shaking and amount of damage may be biased by sedimentary effects resulting in overestimation, e.g. the 1739 Yinchuan earthquake (*Middleton et al.*, 2016).

6.7 Conclusions

Detailed analysis based on the high-resolution Pleiades DEM of the surface geomorphology at the Chishui river catchment, along with a recent fault exposure in a nearby quarry excavation and borehole cross-section, allow us to conclude that the vertical component of slip in the 1556 Huaxian earthquake is ∼7.5 m. The discontinuous ∼7–8 m scarps along the Weinan tableland and Huashan faults (*Yuan and Feng*, 2010) are from 1556. Given a fault dip of 45° (measured in the field, Figure 6.14), the slip of the 1556 event is ∼10 m. Our magnitude estimate for the 1556 earthquake, M_w 7.3–7.9, is smaller than previously inferred (M 8.25–8.5) based on historical records of shaking and damage, suggesting that the size of the earthquake may have been overestimated.

The heights of terraces T1 (∼7–8 m) and T2 (∼13–14 m) show two earthquakes with a similar magnitude. Ages of the radiocarbons samples and cultural objects from the clay layer on top of a river gravel layer in T2 suggest that the penultimate earthquake may have occurred ∼6–8 ka. Assuming a characteristic slip of ∼10 m and a recurrence interval of 5.5–7.5 ka, the slip rate of the Weinan tableland fault over the last two earthquake cycles is estimated to be 1.3–1.8 mm/yr. This small rate is expected from the InSAR observations (less than 3 mm/yr across the Weihe graben).

This study of the 1556 earthquake in the Weihe graben also demonstrates the importance of combining modern VHR imagery and geological data to reexamine past earthquakes. The landscape in this part of the world can be modified dramatically; as a result, it is difficult and often impossible to delineate the extent and slip of surface ruptures in continental interiors. Identification and documentation of active faulting is increasingly urgent for the assessment of earthquake hazard, especially given that rapid urban development in recent decades can easily erase the evidence of fault activity (e.g. fault scarps, uplifted river terraces, etc.) within years or even a few days. For example, a few weeks after our fieldwork, the trench structures were destroyed by road works. Our SfM work preserves the site, showing the usefulness of the technique for digital preservation. And our Pleiades DEM preserves the terraces prior to quarrying. It is necessary and timely to work on such regions and make archives in order to quantify the seismic activity of regions where millions of people are living. For example, the North Qinling fault at the

southern margin of the Weihe graben ruptured around 780 BC, but very little is known about it. Palaeoseimological and geomorphological studies are needed to investigate this fault (as well as other faults in the graben) in the future.

6.8 Contributions

I processed the InSAR and Pleiades data, and constructed the 3D trench model. R. Walker advised on trench interpretation. Radiocarbon samples in the trench were collected by X. Feng and J. Ma. X. Feng provided the borehole cross-section. I wrote the chapter, which was commented on by R. Walker.

Chapter 7

Conclusions and Discussion

In this thesis, I have explored the potentials of high-resolution optical imagery for measuring 3D displacements in earthquakes. I have assessed the capability of Pleiades stereo imagery in determining coseismic vertical motion (Chapter 3). In the case of the 2013 Balochitan, Pakistan earthquake, I have demonstrated the value of obtaining vertical motion so as to better constrain fault kinematics (Chapter 4). The study of the 1978 Tabas earthquake highlights the usefulness of historical imagery in investigating past earthquakes, thus providing new information about faulting in continental regions (Chapter 5). Finally, in the case of the 1556 Huaxian earthquake, I have shown the improvement in understanding of earthquakes and tectonic geomorphology that can be gained by combining high-resolution topographic data, fieldwork and geological dating techniques (Chapter 6).

In this chapter, I compile a list of earthquakes that have been studied with optical image matching and compare the results to the previous InSAR estimates. I discuss the future work that could be done on measuring earthquake deformation. One of the main aims of the project was to assess the potentials and establish the techniques of using high-resolution optical imagery to study past and present earthquakes. Therefore, I examine the earthquake catalogue and discuss the events that have not yet been studied but could possibly be investigated with the methodology presented in this thesis.

7.1 Compilation of Earthquake Deformation Studied with Optical Image Matching

Unlike InSAR, which has been extensively used to study earthquake deformation since the 1992 Landers earthquake (*Massonnet et al.*, 1993), the application of optical image matching is relatively recent, with the first example presented by *Michel and Avouac* (2002). 17 earthquakes have been studied with optical image matching by others, or in this thesis. These earthquakes are summarised in Table 7.1, where I list the data used and the measured surface displacements. Most of the earthquakes have also been studied with InSAR, except for the 2013 Balochistan earthquake where there is little InSAR data (Envisat lost contact on the 8th April 2012 whereas Sentinel-1 was launched on 3 April 2014), so I also list the corresponding InSAR-derived slip for comparison.

7.1.1 Image Resolution and Surface Displacement

Optical image matching is capable of capturing surface displacement with sub-pixel accuracy (*Leprince et al.*, 2007). The minimum measured coseismic displacement reported in the published papers is ∼0.6 m in the 2001 Bhuj earthquake, in which *Copley et al.* (2011) used 10-m resolution SPOT-4 images. Previous studies have attempted to measure smaller surface displacements, but it appears that any displacements less than 1/20 of the image resolution are not detectable. For example, in the case of the 2003 Altai earthquake with small surface displacements, *Barbot et al.* (2008) cannot locate the fault location precisely based on the displacement field derived from SPOT-5 images.

Table 7.1: Compilation of earthquake deformation studied with optical image matching

#	Location	M_w	Date	Fault Type	Data Type		Surface slip	$\bar{\mu}$ (m)	References
					Pre-earthquake	Post-earthquake			
1	Tabas, Iran	7.3	16/09/1978	TH	KH-9 (26/11/1974)	SPOT-2 (06/09/1991)	3.4 m shortening (coseismic + postseismic)	No data	*Zhou et al.* (2016b)
					Aerial (13/08/1956)	SPOT-6 (29/12/2013)	4.7 m vertical (coseismic + postseismic)		
2	Landers, USA	7.3	28/06/1992	SS	Aerial (07/1989)	Aerial (05/1994)	1.52±0.70 m (mean), 5.58±0.14 m (max)	2.97	*Milliner et al.* (2015)
3	Izmit, Turkey	7.4	17/08/1999	SS	SPOT-1 (22/07/1999)	SPOT-2 (31/08/1999)	Karamursel-Golcuk segment: 3.2 ±0.5 m	3	*Michel and Avouac* (2002)
							Golcuk-Izmit segment: 3.4±0.4 m	3	
					SPOT-2 (27/07/1998)	SPOT-2 (16/09/1999)	Izmit-Sapanca segment: 3.5±0.2 m	3.3	
							Sapana-Akyazi segment: 2.2±0.6 m	2.5	
4	Chi-Chi, Taiwan	7.6	21/09/1999	TH	SPOT (29/01/1999)	SPOT (23/11/1999)	4–5 m E-W 5.6 m N-S	7-8	*Dominguez et al.* (2003)
5	Hector Mine, USA	7.1	16/10/1999	SS	SPOT-4 (17/08/1998)	SPOT-2 (10/08/2000)	Up to 6 m N-S Up to 3.5 m E-W	5.6	*Leprince et al.* (2007)
6	Bhuj, India	7.6	26/01/2001	TH	SPOT-4	SPOT-4	<0.4 m N-S 0.6 m E-W + uplift	4	*Copley et al.* (2011)
7	Kokixili, China	7.8	14/11/2001	SS	Landsat-7 (26/10/2001)	Landsat-7 (15/05/2002)	1.5-8.1 m, 4.8 m (mean)	3.2	*Liu and Haselwimmer* (2006)
						Landsat-7 (26/08/2002)			
					SPOT-1 (29/09/1989)	SPOT-4 (30/11/2002)	3.5 m (mean), 4.5-5 m (maximum)		*Rosu et al.* (2015)
8	Denali, USA	7.9	23/11/2002	SS/NF	SPOT-4 (03/09/2002)	SPOT-4 (20/06/2004)	7.5±1.12 m (in the east) 5.5±0.67 (in the west)	5.7	*Taylor et al.* (2008)
9	Altai, Russia	7.2	29/09/2003	SS	SPOT-5 (09/09/2003)	SPOT-5 (17/01/2004)	No precise fault location	1.7	*Barbot et al.* (2008)
10	Bam, Iran	6.5	26/12/2003	SS	SPOT-5 (16/10/2003)	SPOT-5 (28/02/2004)	1.2±0.15 m (max), 0.77+/0.05 m (mean)	0.88	*Binet and Bollinger* (2005)
11	Kashmir, Pakistan	7.6	08/10/2005	TH	ASTER (14/11/2000)	ASTER (27/10/2005)	4 m (mean), 7 m (maximum)	7.4	*Avouac et al.* (2006)
12	Mozambique, east Africa	7.0	22/02/2006	NF	SPOT-5 (03/08/2001)	SPOT-5 (26/08/2008)	∼1 m of left-lateral strike-slip motion	2.6 (N), 3.4 (S)	*Copley et al.* (2012)
13	Yutian, China	7.1	21/03/2008	NF	SPOT-5 (25/08/2002)	SPOT-5 (26/06/2008)	2.7 m	4	*Rosu et al.* (2015)
14	Baja, Mexico	7.2	04/04/2010	SS/NF	SPOT-5 (26/05/2009)	SPOT-5 (08/04/2010)	2 m strike-slip (mean)		*Wei et al.* (2011)
					LiDAR (08/2006)	Pleiades (17/03/2014)	1.1 m vertical (mean)		*Zhou et al.* (2015b)
15	Darfield, New Zealand	7.1	04/09/2010	SS	GeoEye (23/10/2009)	WorldView (21/09/2010)	5 m (E-W), one profile	2.5	*Barnhart et al.* (2011)
16	Ahar, Iran	6.4 + 6.3	11/08/2012	SS	WorldView (24/12/2010)	WorldView (19/08/2012)	1.5±0.5 m (mean, overestimated)	0.65	*Copley et al.* (2013)
17	Balochistan, Pakistan	7.7	24/09/2013	SS	Landsat-8 (10/09/2013)	Landsat-8 (26/09/2013)	6 m (mean), 10 m (maximum)	No data	*Avouac et al.* (2014)
					WorldView	WorldView	17.6 m (maximum)		*Barnhart et al.* (2015)
					SPOT-5	SPOT-5	Strike-slip: 8 m (mean), 14 m (maximum) Shortening: up to 6–7 m (locally)		*Vallage et al.* (2015)

Abbreviations:
Fault Type: SS = Strike-Slip, TH = Thrust, NF = Normal Fault
Data Type: KH-9 – 6-9 m resolution, Aerial – 1 m resolution, SPOT-6 – 1.5 m resolution, SPOT-5 – 5 m resolution, SPOT-1–4 – 10 m resolution, Landsat-7–8 & ASTER – 15 m resolution, WorldView, GeoEye & Pleiades – 0.5 m resolution
$\bar{\mu}$ = average slip over fault plane from InSAR solutions, summarised in *Elliott* (2009) (except for 4, 12 and 14–17)

Assuming that 1/20 of the image resolution is the limit for the measurable surface displacement by the optical image matching method, I calculate the minimum moment magnitude of earthquakes that could be studied with this technique using the empirical earthquake scaling relations (*Wells and Coppersmith*, 1994):

$$\mathbf{M} = 6.93 + 0.82 \log_{10}(\mathbf{AD}) \tag{7.1}$$

where **M** is the moment magnitude, **AD** means the average surface displacement.

From Equation 7.1, the earthquakes to be studied with KH-9 (6–9 m resolution), SPOT-1–4 (10 m resolution) and Landsat-7–8 (15 m resolution) images should have a minimum moment magnitude of M_w 6.7–6.9. With images at 2.5 m (SPOT-5), 1.5 m (SPOT-6) and 0.5 m (Pleiades, WorldView and GeoEye) resolutions, this technique could in principle be applicable to earthquakes with a moment magnitude of M_w ~6.0.

It is interesting to note that in the 2013 Balochistan earthquake, images at different resolutions yielded slightly different surface displacements. I plot these different results in Figure 7.1 for comparison. The displacements from WorldView imagery (*Barnhart et al.*, 2015) have higher peaks than those from SPOT-5 (*Vallage et al.*, 2015) and Landsat-8 (*Avouac et al.*, 2014). In places where the WorldView-derived displacements are smaller than the Landsat-derived results, surface rupture is not a single trace but a wide zone of cracks. It is because low resolution images (e.g. 15 m for Landsat-8) will smooth out some image features, and thus resulting in smoother measurements, whereas at higher resolutions, images can preserve local features, so the matching result may reflect more localised deformation.

7.1.2 Coseismic Shallow Slip Deficit?

Fialko et al. (2005) observed that coseismic slip in many strike-slip earthquakes decreases in magnitude towards the surface and proposed the 'shallow slip deficit' model, as shown in Figure 7.2. Such model remains arguable because the slip distribution inverted based on InSAR observations is usually not well constrained due to severe decorrelation in the near field in the coseismic interferograms (Figure 1.6 for example). Optical image matching

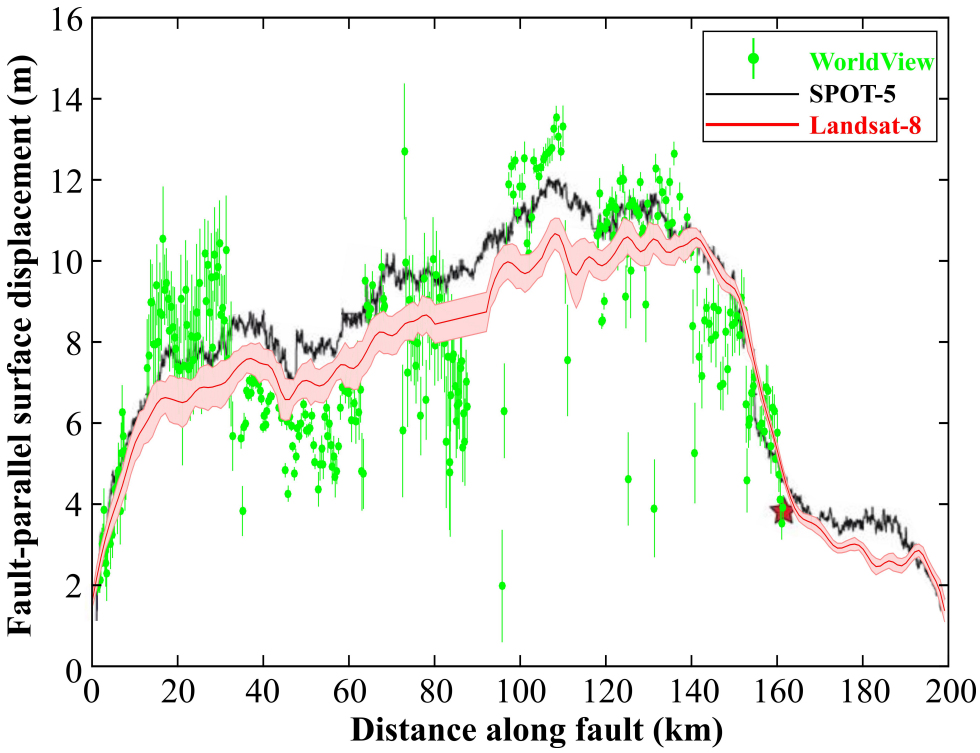


Figure 7.1: Comparison of far-field surface displacements from different images in the 2013 Balochistan earthquake. Red star indicates the epicentre. Green dots are measurements from cross-correlating pre- and post-earthquake 0.5 m resolution WorldView images (*Barnhart et al.*, 2015). Black line is from 2.5 m resolution SPOT-5 images (*Vallage et al.*, 2015) and red band from 15 m resolution Landsat-8 images (*Avouac et al.*, 2014).

provides complementary measurements to InSAR. In Figure 7.2, I replaced the data points between 0–2 km inverted from InSAR with the average surface slip measured by optical image matching, and re-plot the slip distribution for the earthquakes that have been claimed to show shallow slip deficit. It appears that none of these strike-slip earthquakes shows a significant difference between slips in the uppermost crust and at seismogenic depths (4–10 km), within the error of the measurements. In Table 7.1 where more strike-slip earthquakes are listed, I found that the surface slip measured from image matching is also similar to the InSAR-derived average slip across the fault plane, which suggests that shallow slip deficit in strike-slip earthquakes may primarily be artefacts of the InSAR measurements whereas a few events with shallow slip deficit are exceptional (*Vallage et al.*, 2015). *Xu et al.* (2016) improved the static coseismic slip inversion for the 1992 Landers, 1999 Hector Mine and 2010 El MayorCucapah earthquakes using InSAR, GPS and optical imagery, and found that the previously observed 'coseismic shallow slip deficit' in large strike-slip earthquakes may be artificial. I also notice that in thrust earthquakes, the

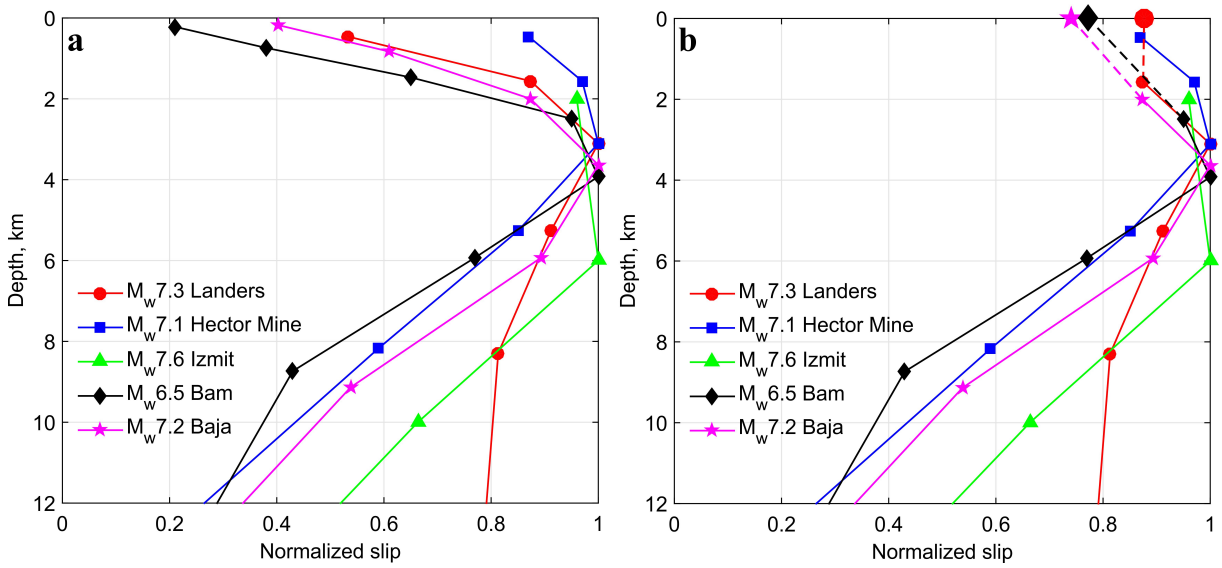


Figure 7.2: Distribution of coseismic slip for several $M_w \geq 7$ strike-slip earthquakes. (a) Inverted from InSAR or a combination of InSAR and GPS, modified from *Fialko et al.* (2005) and *Kaneko and Fialko* (2011). (b) After replacing the data points between 0–2 km inverted from InSAR in (a) with the average surface slip measured by optical image matching in Table 7.1.

surface displacements are smaller than the average slip, e.g. the 2001 Bhuj and 2005 Kashmir earthquakes. It might be because optical image matching can only measure 2D displacements, whereas a large fraction of the fault slip is in the vertical direction in thrust earthquakes. Therefore, to investigate the 'coseismic shallow slip deficit' problem, InSAR and image matching in 3D should be combined to better constrain the inversion of slip distribution (*Xu et al.*, 2016).

7.2 Future Work and Possibilities

Optical image matching has become increasingly popular in studying earthquake deformation in recent years. When I started to work on my thesis, earthquake deformation was mostly measured in 2D. High-resolution stereo imagery provides new possibilities of measuring sub-metre surface displacements in 3D, which has been well demonstrated in this thesis, so in the years to come, I expect that it will come to be in common usage in the following areas.

7.2.1 Towards 3D Mapping of Earthquake Deformation

3D surface motion can help to fully characterise fault kinematics. Previous studies of earthquakes based on 2D surface displacements may have limited our ability to understand fault behaviour and thus earthquake mechanics in continental regions. For example, in the 2013 Balochistan earthquake, horizontal displacements from image matching have led to a wide range of unconventional kinematic models, but these models were found to be unnecessarily over-complicated due to a lack of observations on the vertical motion. I presented methods of mapping 3D coseismic surface slips using modern VHR stereo imagery in Chapter 3. To achieve the goal of 3D mapping of earthquake deformation, both pre- and post-earthquake high-resolution stereo imagery are needed. This requires (1) space agencies to fund stereo satellites and reduce the price for scientific research, and (2) spacecraft operators and research institutes to acquire data for regions of active faulting and high seismic hazard systematically, as pre-earthquake data sets are rare at present.

7.2.2 Historical Earthquakes

Earthquakes provide the most valuable source of information for describing and understanding continental tectonics. However, as the recurrence intervals of large earthquakes within continental regions are often very long due to the relatively slow strain accumulation, only a limited sample of events that contained within the recent seismic record have been well studied. This thesis presents a method that uses declassified KH-9 images to investigate historical earthquakes (Chapter 5). As discussed in Section 7.1.1, it is possible to employ KH-9 imagery to measure surface deformation of earthquakes with a moment magnitude of M_w $\geq$6.9. Many of those earthquakes between 1974 and 1997 have only been studied by seismology and field observations. No reliable estimates of earthquake slip exist. Using the method in Chapter 5, we could potentially investigate some of the events back to the 1970s. For example, I used pre- (27th July, 1976) and post-earthquake (7th July, 1980) KH-9 images and measured the surface displacement from the 24th November, 1976 M_w 7.3 Chaldiran, Turkey earthquake (Figure 7.3). When combined with InSAR to measure postseismic deformation, it can advance our understanding

of continental deformation through the seismic cycle and thus the nature of continental tectonics.

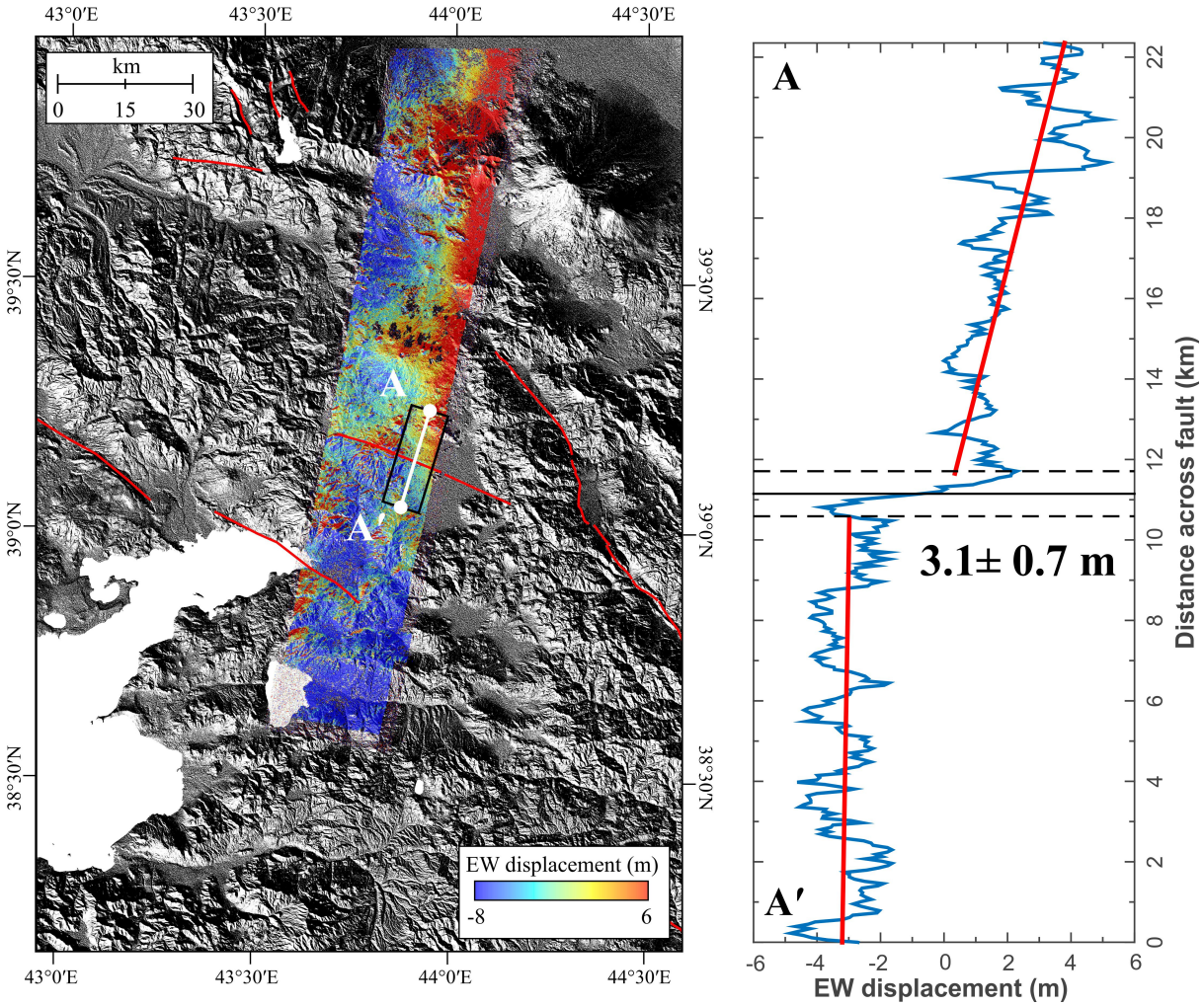


Figure 7.3: (left) E-W displacement field of the 1976 M_w 7.3 Chaldiran, Turkey earthquake, imaged from pre- and post-earthquake KH-9 images. (right) Profile A-A' shows an E-W displacement of 3.1±0.7 m by fitting two lines (red) on each side of the fault. Field measurements show a minimum strike-slip of 3.0 m (*Toksöz et al.*, 1977). Long-wavelength film distortions are evident in the displacement field.

Bibliography

Abdel-Aziz, Y. (1971), Direct linear transformation from comparator coordinates in close-range photogrammetry, in *ASP Symposium on Close-Range Photogrammetry in Illinois, 1971*. 2.2.1

Ader, T., J.-P. Avouac, J. Liu-Zeng, H. Lyon-Caen, L. Bollinger, J. Galetzka, J. Genrich, M. Thomas, K. Chanard, S. N. Sapkota, S. Rajaure, and P. Shrestha (2012), Convergence rate across the Nepal Himalaya and interseismic coupling on the Main Himalayan Thrust: Implications for seismic hazard, *Journal of Geophysical Research: Solid Earth (1978–2012)*, *117*(B4), doi:10.1029/2011JB009071. 4.2

Anderson, E. M. (1905), The dynamics of faulting, *Transactions of the Edinburgh Geological Society*, *8*(3), 387–402. 1.3.2, 1.3.3

Astrium (2013), SPOT 6 & SPOT 7 Imagery User Guide, *Astrium GEO-Information Services, Toulouse, France*, p. 120. 5.3.1

Avouac, J.-P., and G. Peltzer (1993), Active tectonics in southern Xinjiang, China: Analysis of terrace riser and normal fault scarp degradation along the Hotan-Qira Fault System, *Journal of Geophysical Research: Solid Earth (1978–2012)*, *98*(B12), 21,773–21,807. 3.1

Avouac, J.-P., F. Ayoub, S. Leprince, O. Konca, and D. V. Helmberger (2006), The 2005, M_w 7.6 Kashmir earthquake: Sub-pixel correlation of ASTER images and seismic waveforms analysis, *Earth and Planetary Science Letters*, *249*(3), 514–528. 1.4.3, 3.1, 7.1

Avouac, J.-P., F. Ayoub, S. Wei, J.-P. Ampuero, L. Meng, S. Leprince, R. Jolivet, Z. Duputel, and D. Helmberger (2014), The 2013, M_w 7.7 Balochistan earthquake, energetic strike-slip reactivation of a thrust fault, *Earth and Planetary Science Letters*, *391*, 128–134. 1.5, 3.1, 4.1, 4.2, 4.3.1, 4.3, 4.3.2, 4.3.3, 4.6, 4.4.2, 4.7, 4.4.3, 4.5, 7.1, 7.1.1, 7.1

Ayoub, F., S. Leprince, and L. Keene (2009), Users Guide to COSI-CORR Co-registration of Optically Sensed Images and Correlation, *California Institute of Technology: Pasadena, CA, USA*, p. 38. 3.5.2, 5.3.2, C

Ballard, D. H., and C. M. Brown (1982), Computer vision, *Prenice-Hall, Englewood Cliffs, NJ*. 2.2.1

Barbot, S., Y. Hamiel, and Y. Fialko (2008), Space geodetic investigation of the coseismic and postseismic deformation due to the 2003 M_w 7.2 Altai earthquake: Implications for the local lithospheric rheology, *Journal of Geophysical Research: Solid Earth (1978–2012)*, *113*(B3), doi:10.1029/2007JB005063. 7.1.1, 7.1

Barišin, I., A. Hinojosa-Corona, and B. Parsons (2015), Co-seismic vertical displacements from a single post-seismic lidar DEM: example from the 2010 El Mayor-Cucapah earthquake, *Geophysical Journal International*, *202*(1), 328–346. 1.4.3, 1.7, 3.5.2, 3.5.3, 3.5.3, 5.3.2

Barnhart, W., R. Briggs, N. Reitman, R. Gold, and G. Hayes (2015), Evidence for slip partitioning and bimodal slip behavior on a single fault: Surface slip characteristics of the 2013 M_w 7.7 Balochistan, Pakistan earthquake, *Earth and Planetary Science Letters*, *420*, 1–11. 1.4.3, 1.5, 2.1, 4.1, 4.3.1, 4.3.2, 4.3.3, 4.6, 4.4.2, 4.4.3, 4.4.3, 4.5, 7.1, 7.1.1, 7.1

Barnhart, W. D., M. J. Willis, R. B. Lohman, and A. K. Melkonian (2011), InSAR and optical constraints on fault slip during the 2010–2011 New Zealand earthquake sequence, *Seismological Research Letters*, *82*(6), 815–823. 3.1, 7.1

Barnhart, W. D., G. P. Hayes, R. W. Briggs, R. D. Gold, and R. Bilham (2014), Ball-and-socket tectonic rotation during the 2013 M_w 7.7 Balochistan earthquake, *Earth and Planetary Science Letters*, *403*, 210–216. 1.5, 4.1, 4.4.2, 4.4.3, 4.5

Bennett, R. A., W. Rodi, and R. E. Reilinger (1996), Global Positioning System constraints on fault slip rates in southern California and northern Baja, Mexico, *Journal of Geophysical Research: Solid Earth (1978–2012)*, *101*(B10), 21,943–21,960. 3.2

Berberian, M. (1979), Earthquake faulting and bedding thrust associated with the Tabas-e-Golshan (Iran) earthquake of September 16, 1978, *Bulletin of the Seismological Society of America*, *69*(6), 1861–1887. 1.3.2, 5.1, 5.2, 5.2, 5.3.2, 5.5.2, 5.5.3, 5.9, 5.11

Berberian, M. (1981), Active faulting and tectonics of Iran, *Zagros Hindu Kush Himalaya Geodynamic Evolution*, pp. 33–69. 5.1, 5.2

Berberian, M. (1982), Aftershock tectonics of the 1978 Tabas-e-Golshan (Iran) earthquake sequence: a documented active 'thin-and thick-skinned tectonic' case, *Geophysical Journal International*, *68*(2), 499–530. 5.1, 5.5.3

Berberian, M., I. Asudeh, R. Bilham, C. Scholz, and C. Soufleris (1979), Mechanism of the main shock and the aftershock study of the Tabas-e-Golshan (Iran) earthquake of September 16, 1978: A preliminary report, *Bulletin of the Seismological Society of America*, *69*(6), 1851–1859. 5.1, 5.2, 5.5.3

Bernard, M., D. Decluseau, L. Gabet, and P. Nonin (2012), 3D capabilities of Pleiades satellite, *ISPRS International Archives of the Photogrammetry, Remote Sensing and Spatial Information Sciences*, *39*, 553–557. 2.1, 3.1

Berthier, E., C. Vincent, E. Magnússon, Á. Gunnlaugsson, P. Pitte, E. Le Meur, M. Masiokas, L. Ruiz, F. Pálsson, J. Belart, et al. (2014), Glacier topography and elevation changes derived from Pléiades sub-meter stereo images, *The Cryosphere*, *8*(6), 2275–2291. 2.1, 3.1

Besl, P. J., and N. D. McKay (1992), Method for registration of 3-D shapes, in *Robotics-DL tentative*, pp. 586–606, International Society for Optics and Photonics. 3.4.2

Beyer, H. (1992), Accurate calibration of CCD-cameras, in *Computer Vision and Pattern Recognition, 1992. Proceedings CVPR'92., 1992 IEEE Computer Society Conference on*, pp. 96–101, IEEE. 2.2.1

Biggs, J., T. Wright, Z. Lu, and B. Parsons (2007), Multi-interferogram method for measuring interseismic deformation: Denali Fault, Alaska, *Geophysical Journal International*, *170*(3), 1165–1179. 6.2, 6.2

Bilham, R., S. Lodi, S. Hough, S. Bukhary, A. M. Khan, and S. Rafeeqi (2007), Seismic hazard in Karachi, Pakistan: uncertain past, uncertain future, *Seismological Research Letters*, *78*(6), 601–613. 4.2

Binet, R., and L. Bollinger (2005), Horizontal coseismic deformation of the 2003 Bam (Iran) earthquake measured from SPOT-5 THR satellite imagery, *Geophysical Research Letters*, *32*(2). 1.4.3, 3.1, 7.1

Bird, P. (2003), An updated digital model of plate boundaries, *Geochemistry, Geophysics, Geosystems*, *4*(3), doi:10.1029/2001GC000252. 1.2

Bolles, R. C., H. H. Baker, and D. H. Marimont (1987), Epipolar-plane image analysis: An approach to determining structure from motion, *International Journal of Computer Vision*, *1*(1), 7–55. 2.4.2

Brock, F., T. Higham, P. Ditchfield, and C. Bronk Ramsey (2010), Current pretreatment methods for AMS radiocarbon dating at the Oxford Radiocarbon Accelerator Unit (ORAU), *Radiocarbon*, *52*(1), 103–12. E

Brown, D. C. (1971), Close-range camera calibration, *Photogrammetric Engineering & Remote Sensing*, *37*, 855–866. 2.2.1, 2.2.1, 5.5.1

Burbank, D. W., and R. S. Anderson (2011), *Tectonic Geomorphology*, John Wiley & Sons. 5.1

Bürgmann, R., and G. Dresen (2008), Rheology of the lower crust and upper mantle: Evidence from rock mechanics, geodesy, and field observations, *Annual Review of Earth and Planetary Sciences*, *36*(1), 531. 1.1, 1.2

Burnett, M. G. (2012), Hexagon (KH-9)– Mapping camera program and evolution, *National Reconnaissance Office (NRO), Center for the Study of National Reconnaissance (CSNR), Chantilly, VA, USA*, p. 395. 2.4.2, 5.1, 5.3.2

Butler, R., G. S. Stewart, and H. Kanamori (1979), The July 27, 1976 Tangshan, China earthquakea complex sequence of intraplate events, *Bulletin of the Seismological Society of America*, *69*(1), 207–220. 6.1

Byrne, D. E., L. R. Sykes, and D. M. Davis (1992), Great thrust earthquakes and aseismic slip along the plate boundary of the Makran subduction zone, *Journal of Geophysical Research: Solid Earth (1978–2012)*, *97*(B1), 449–478. 4.2

Çakir, Z., S. Ergintav, H. Özener, U. Dogan, A. M. Akoglu, M. Meghraoui, and R. Reilinger (2012), Onset of aseismic creep on major strike-slip faults, *Geology*, *40*(12), 1115–1118. 5.5.2

Campbell, G., R. Walker, K. Abdrakhmatov, J. Jackson, J. Elliott, D. Mackenzie, T. Middleton, and J.-L. Schwenninger (2015), Great earthquakes in low-strain-rate continental interiors: an example from SE Kazakhstan, *Journal of Geophysical Research: Solid Earth*, *120*(8), 5507–5534. 3.1

Chen, W.-P., and P. Molnar (1983), Focal depths of intracontinental and intraplate earthquakes and their implications for the thermal and mechanical properties of the lithosphere, *Journal of Geophysical Research*, *88*(B5), 4183–4214. 1.1

Conrady, A. E. (1919), Decentred lens-systems, *Monthly notices of the Royal Astronomical Society*, *79*(5), 384–390. 2.2.1

Copley, A. (2014), Postseismic afterslip 30 years after the 1978 Tabas-e-Golshan (Iran) earthquake: observations and implications for the geological evolution of thrust belts, *Geophysical Journal International*, doi:10.1093/gji/ggu023. 5.1, 5.2, 5.2, 5.3.2, 5.5.1, 5.5.1, 5.5.2, 5.5.3, 5.8

Copley, A., J.-P. Avouac, J. Hollingsworth, and S. Leprince (2011), The 2001 M_w 7.6 Bhuj earthquake, low fault friction, and the crustal support of plate driving forces in India, *Journal of Geophysical Research: Solid Earth (1978–2012)*, *116*(B8), doi:10.1029/2010JB008137. 6.1, 7.1.1, 7.1

Copley, A., J. Hollingsworth, and E. Bergman (2012), Constraints on fault and lithosphere rheology from the coseismic slip and postseismic afterslip of the 2006 M_w 7.0 Mozambique earthquake, *Journal of Geophysical Research: Solid Earth*, *117*(B3), doi:10.1029/2011JB008580. 7.1

Copley, A., M. Faridi, M. Ghorashi, J. Hollingsworth, J. Jackson, H. Nazari, B. Oveisi, and M. Talebian (2013), The 2012 August 11 Ahar earthquakes: consequences for tectonics and earthquake hazard in the Turkish–Iranian Plateau, *Geophysical Journal International*, doi:10.1093/gji/ggt379. 7.1

Cowgill, E. (2007), Impact of riser reconstructions on estimation of secular variation in rates of strike–slip faulting: Revisiting the Cherchen river site along the Altyn Tagh Fault, NW China, *Earth and Planetary Science Letters*, *254*(3), 239–255. 3.1

Cunningham, W., and P. Mann (2007), Tectonics of strike-slip restraining and releasing bends, *Geological Society, London, Special Publications*, *290*(1), 1–12. 4.4.1

D'Agostino, N., D. Cheloni, S. Mantenuto, G. Selvaggi, A. Michelini, and D. Zuliani (2005), Strain accumulation in the southern Alps (NE Italy) and deformation at the northeastern boundary of Adria observed by CGPS measurements, *Geophysical Research Letters*, *32*(19), doi:10.1029/2005GL024266. 1.4.1

Dai, W., and X. Feng (2004), Lateral migration of fault activity in Weihe basin, *Acta Seismologica Sinica*, *2*. 6.4.3, 6.4.3

Dawson-Howe, K. M., and D. Vernon (1994), Simple pinhole camera calibration, *International Journal of Imaging Systems and Technology*, *5*(1), 1–6. 2.2.1

de Lussy, F., P. Kubik, D. Greslou, V. Pascal, P. Gigord, and J. P. Cantou (2005), PLEIADES-HR image system products and quality-PLEIADES-HR image system products and geometric accuracy, in *Proceedings International Society for Photogrammetry and Remote Sensing Hannover Workshop*, pp. 17–20. 2.1, 3.1

de Lussy, F., P. Gigord, and S. Airault (2006), The Pleiades-HR mosaic system product, in *ISPRS International Archives of the Photogrammetry, Remote Sensing and Spatial Information Sciences*, pp. 537–542. 3.3.1

Di, K., R. Ma, and R. X. Li (2003), Rational functions and potential for rigorous sensor model recovery, *Photogrammetric Engineering & Remote Sensing*, *69*(1), 33–41. 2.2.2

Dixon, T. H. (1991), An introduction to the Global Positioning System and some geological applications, *Reviews of Geophysics*, *29*(2), 249–276. 1.4.1

Dolan, J. F., and B. D. Haravitch (2014), How well do surface slip measurements track slip at depth in large strike-slip earthquakes? The importance of fault structural maturity in controlling on-fault slip versus off-fault surface deformation, *Earth and Planetary Science Letters*, *388*, 38–47. 4.3.1

Dominguez, S., J.-P. Avouac, and R. Michel (2003), Horizontal coseismic deformation of the 1999 Chi-Chi earthquake measured from SPOT satellite images: Implications for the seismic cycle along the western foothills of central Taiwan, *Journal of Geophysical Research: Solid Earth (1978–2012)*, *108*(B2), doi:10.1029/2001JB000951. 3.1, 7.1

Dowman, I., and J. T. Dolloff (2000), An evaluation of rational functions for photogrammetric restitution, *International Archives of Photogrammetry and Remote Sensing*, *33*(B3/1; PART 3), 254–266. 2.2.2, 2.2.2

Efron, B. (1979), Bootstrap methods: another look at the jackknife, *The Annals of Statistics*, pp. 1–26. B

Eisenbeiss, H., E. Baltsavias, M. Pateraki, and L. Zhang (2004), Potential of Ikonos and QuickBird imagery for accurate 3D point positioning, orthoimage and DSM generation, *International Archives of the Photogrammetry, Remote Sensing and Spatial Information Sciences*, *35*(B3), 522–528. 2.1

Elliott, J. (2009), Strain accumulation & release on the Tibetan Plateau measured using InSAR, Ph.D. thesis, Oxford University. 7.1

Elliott, J., J. Biggs, B. Parsons, and T. Wright (2008), InSAR slip rate determination on the Altyn Tagh Fault, northern Tibet, in the presence of topographically correlated atmospheric delays, *Geophysical Research Letters*, *35*(12), doi:10.1029/2008GL033659. 6.2

Elliott, J., E. Nissen, P. England, J. A. Jackson, S. Lamb, Z. Li, M. Oehlers, and B. Parsons (2012), Slip in the 2010–2011 Canterbury earthquakes, New Zealand, *Journal of Geophysical Research: Solid Earth (1978–2012)*, *117*(B3). 1, 1.4.4, 3.1, 4.1

England, P., and R. Bilham (2015), The Shillong Plateau and the great 1897 Assam earthquake, *Tectonics*, *34*(9), 1792–1812. 6.1

England, P., and J. Jackson (2011), Uncharted seismic risk, *Nature Geoscience*, *4*(6), 348–349. 1, 1.1, 3.1, 5.1, 6.1

England, P., and P. Molnar (1997), Active deformation of Asia: from kinematics to dynamics, *Science*, *278*(5338), 647–650. 1.1

Farr, T. G., P. A. Rosen, E. Caro, R. Crippen, R. Duren, S. Hensley, M. Kobrick, M. Paller, E. Rodriguez, L. Roth, D. Seal, S. Shaffer, J. Shimada, J. Umland, M. Werner, M. Oskin, D. Burbank, and D. Alsdorf (2007), The Shuttle Radar Topography Mission, *Reviews of Geophysics*, *45*(2), doi:10.1029/2005RG000183. 2.5, 4.10

Fattahi, H., F. Amelung, E. Chaussard, S. Wdowinski, and T. Dixon (2014a), Characterizing seismic and aseismic deformation along the Chaman fault system with InSAR, in *AGU Fall Meeting Abstracts*, vol. 1, p. 0463. 4.2, 4.5

Fattahi, M., R. Walker, M. Talebian, R. Sloan, and A. Rasheedi (2014b), Late Quaternary active faulting and landscape evolution in relation to the Gowk Fault in the South Golbaf Basin, SE Iran, *Geomorphology*, *204*, 334–343, doi:10.1016/j.geomorph.2013.08.017. 5.2

Fialko, Y., M. Simons, and D. Agnew (2001), The complete (3-D) surface displacement field in the epicentral area of the 1999 M_w 7.1 Hector Mine Earthquake, California, from space geodetic observations, *Geophysical Research Letters*, *28*(16), 3063–3066. 3.1

Fialko, Y., D. Sandwell, M. Simons, and P. Rosen (2005), Three-dimensional deformation caused by the Bam, Iran, earthquake and the origin of shallow slip deficit, *Nature*, *435*(7040), 295–299. 1, 1, 5.1, 7.1.2, 7.2

Fischler, M. A., and R. C. Bolles (1981), Random sample consensus: a paradigm for model fitting with applications to image analysis and automated cartography, *Communications of the ACM*, *24*(6), 381–395. 2.4.2

Fleck, M. M. (1995), Perspective projection: the wrong imaging model, *Department of Computer Science, University of Iowa*, pp. 1–27. 2.2.1

Fletcher, J. M., O. J. Teran, T. K. Rockwell, M. E. Oskin, K. W. Hudnut, K. J. Mueller, R. M. Spelz, S. O. Akciz, E. Masana, G. Faneros, E. Fielding, S. Leprince, A. Morelan, J. Stock, D. Lynch, A. Elliott, P. Gold, J. Liu-Zeng, A. Gonzalez-Ortega, A. Hinojosa-Corona, and J. Gonzalez-Garcia (2014), Assembly of a large earthquake from a complex fault system: Surface rupture kinematics of the 4 April 2010 El Mayor–Cucapah (Mexico) M_w 7.2 earthquake, *Geosphere*, *10*(4), 797–827. 1.7, 1.8, 3.2, 3.1, 3.5.3

Foroutan, M., B. Meyer, M. Sébrier, H. Nazari, A. Murray, K. Le Dortz, M. Shokri, M. Arnold, G. Aumaître, D. Bourlès, and K. Keddadouche (2014), Late Pleistocene-Holocene right slip rate and paleoseismology of the Nayband fault, western margin of the Lut block, Iran, *Journal of Geophysical Research: Solid Earth*, *119*(4), 3517–3560, doi:10.1002/2013JB010746. 5.2, 5.5.4

Fraser, C., G. Dial, and J. Grodecki (2006), Sensor orientation via RPCs, *ISPRS Journal of Photogrammetry and Remote Sensing*, *60*(3), 182–194. 2.2.2, 2.2.2, 2.2.2, 2.2.2

Fraser, C. S. (1997), Digital camera self-calibration, *ISPRS Journal of Photogrammetry and Remote Sensing*, *52*(4), 149–159. 2.2.1

Fraser, C. S., and H. B. Hanley (2005), Bias-compensated RPCs for sensor orientation of high-resolution satellite imagery, *Photogrammetric Engineering & Remote Sensing*, *71*(8), 909–915. 2.2, 2.2.2, 2.2.2, 2.2.2, 2.2.2, 3.3.2, 3.3.2

Fraser, C. S., and M. Ravanbakhsh (2009), Georeferencing accuracy of GeoEye-1 imagery, *Photogrammetric Engineering & Remote Sensing*, *75*(6), 634–638. 2.1, 3.1

Freed, A. M., R. Bürgmann, E. Calais, and J. Freymueller (2006), Stress-dependent power-law flow in the upper mantle following the 2002 Denali, Alaska, earthquake, *Earth and Planetary Science Letters*, *252*(3), 481–489. 5.5.2

Funning, G. J., B. Parsons, T. J. Wright, J. A. Jackson, and E. J. Fielding (2005), Surface displacements and source parameters of the 2003 Bam (Iran) earthquake from Envisat advanced synthetic aperture radar imagery, *Journal of Geophysical Research: Solid Earth*, *110*(B9), doi:10.1029/2004JB003338. 1, 5.1

Furukawa, Y., and J. Ponce (2010), Accurate, dense, and robust multiview stereopsis, *Pattern Analysis and Machine Intelligence, IEEE Transactions on*, *32*(8), 1362–1376. 2.4.2, 2.4.2

Furukawa, Y., B. Curless, S. M. Seitz, and R. Szeliski (2010), Towards internet-scale multi-view stereo, in *Computer Vision and Pattern Recognition (CVPR), 2010 IEEE Conference on*, pp. 1434–1441, IEEE. 2.3, 2.4.2, 2.4.2

Glennie, C. L., A. Hinojosa-Corona, E. Nissen, A. Kusari, M. E. Oskin, J. R. Arrowsmith, and A. Borsa (2014), Optimization of legacy lidar data sets for measuring near-field earthquake displacements, *Geophysical Research Letters*, *41*(10), 3494–3501. 1.8, 3.2, 3.5.1, 3.5.2

Gold, R. D., and E. Cowgill (2011), Deriving fault-slip histories to test for secular variation in slip, with examples from the Kunlun and Awatere faults, *Earth and Planetary Science Letters*, *301*(1), 52–64. 3.1

Gonzales, R. C., R. E. Woods, and S. L. Eddins (2004), *Digital image processing using MATLAB*, Pearson Prentice Hall. 2.4.1

Gratier, J. P., F. Renard, and B. Vial (2014), Postseismic pressure solution creep: Evidence and time-dependent change from dynamic indenting experiments, *Journal of Geophysical Research: Solid Earth*, *119*(4), 2764–2779, doi:10.1002/2013JB010768. 5.5.2

Gremban, K. D., C. E. Thorpe, and T. Kanade (1988), Geometric camera calibration using systems of linear equations, in *Robotics and Automation, 1988. Proceedings., 1988 IEEE International Conference on*, pp. 562–567, IEEE. 3.3.2

Grodecki, J., and G. Dial (2003), Block adjustment of high-resolution satellite images described by rational polynomials, *Photogrammetric Engineering & Remote Sensing*, *69*(1), 59–68. 2.2.2, 3.3.2

Haghipour, N., J.-P. Burg, F. Kober, G. Zeilinger, S. Ivy-Ochs, P. W. Kubik, and M. Faridi (2012), Rate of crustal shortening and non-Coulomb behaviour of an active accretionary wedge: The folded fluvial terraces in Makran (SE, Iran), *Earth and Planetary Science Letters*, *355*, 187–198. 4.2

Hanks, T. C., R. C. Bucknam, K. R. Lajoie, and R. E. Wallace (1984), Modification of wave-cut and faulting-controlled landforms, *Journal of Geophysical Research: Solid Earth (1978–2012)*, *89*(B7), 5771–5790. 3.1

Hanssen, R. F. (2001), *Radar Interferometry: Data Interpretation and Analysis*, Kluwer Acad., Norwell, Mass. 1.4.2

Harris, R. A. (2004), Numerical simulations of large earthquakes: Dynamic rupture propagation on heterogeneous faults, *Pure and Applied Geophysics*, *161*(11-12), 2171–2181. 4.5

Hartley, R., and A. Zisserman (2003), *Multiple view geometry in computer vision*, Cambridge University Press. 2.3

Hashimoto, C., A. Noda, T. Sagiya, and M. Matsuura (2009), Interplate seismogenic zones along the Kuril–Japan trench inferred from GPS data inversion, *Nature Geoscience*, *2*(2), 141–144. 6.1

Hauksson, E., J. Stock, K. Hutton, W. Yang, J. A. Vidal-Villegas, and H. Kanamori (2011), The 2010 M_w 7.2 El Mayor-Cucapah Earthquake Sequence, Baja California, Mexico and Southernmost California, USA: Active Seismotectonics along the Mexican Pacific Margin, *Pure and Applied Geophysics*, *168*(8-9), 1255–1277. 3.2

Heikkila, J., and O. Silvén (1997), A four-step camera calibration procedure with implicit image correction, in *Computer Vision and Pattern Recognition, 1997. Proceedings., 1997 IEEE Computer Society Conference on*, pp. 1106–1112, IEEE. 2.2.1, 2.2.1

Heki, K., S. Miyazaki, and H. Tsuji (1997), Silent fault slip following an interplate thrust earthquake at the Japan Trench, *Nature*, *386*, 595–598. 6.1

Hessami, K. (2002), Tectonic history and present-day deformation in the Zagros fold-thrust belt, *Acta Universitatis Upsaliensis*. 5.2

Hollingsworth, J., S. Leprince, F. Ayoub, and J.-P. Avouac (2012), Deformation during the 1975–1984 Krafla rifting crisis, NE Iceland, measured from historical optical imagery, *Journal of Geophysical Research: Solid Earth (1978–2012)*, *117*(B11), doi:10.1029/2012JB009140. 1.4.3, 3.5.2, 5.1, 5.3.2

Hou, J.-J., M.-K. Han, B.-L. Chai, and H.-Y. Han (1998), Geomorphological observations of active faults in the epicentral region of the Huaxian large earthquake in 1556 in Shaanxi Province, China, *Journal of Structural Geology*, *20*(5), 549–557. 6.3

Hsu, Y.-J., M. Simons, J.-P. Avouac, J. Galetzka, K. Sieh, M. Chlieh, D. Natawidjaja, L. Prawirodirdjo, and Y. Bock (2006), Frictional afterslip following the 2005 Nias-Simeulue earthquake, Sumatra, *Science*, *312*(5782), 1921–1926. 1.4.1

Hu, Y., V. Tao, and A. Croitoru (2004), Understanding the rational function model: methods and applications, *International Archives of Photogrammetry and Remote Sensing*, *20*(6). 2.2.2, 3.3.2

Hubbard, J., and J. H. Shaw (2009), Uplift of the Longmen Shan and Tibetan plateau, and the 2008 Wenchuan (M = 7.9) earthquake, *Nature*, *458*(7235), 194–197. 5.1

Jackson, J. (2001), Living with earthquakes: know your faults, *Journal of Earthquake Engineering*, *5*(spec01), 5–123. 3.1, 5.1

Jackson, J., J. Haines, and W. Holt (1995), The accommodation of Arabia-Eurasia plate convergence in Iran, *Journal of Geophysical Research: Solid Earth (1978–2012)*, *100*(B8), 15,205–15,219. 5.2

Jenkins, F. A., and H. E. White (1957), *Fundamentals of optics*, Tata McGraw-Hill Education. 2.2.1

Johnson, K., E. Nissen, S. Saripalli, J. R. Arrowsmith, P. McGarey, K. Scharer, P. Williams, and K. Blisniuk (2014), Rapid mapping of ultrafine fault zone topography with structure from motion, *Geosphere*, *10*(5), 969–986. 2.1

Jolivet, R., Z. Duputel, B. Riel, M. Simons, L. Rivera, S. Minson, H. Zhang, M. Aivazis, F. Ayoub, S. Leprince, S. Samsonov, M. Motagh, and E. J. Fielding (2014), The 2013 M_w 7.7 Balochistan earthquake: Seismic potential of an accretionary wedge, *Bulletin of the Seismological Society of America*, *104*(2), 1020–1030. 4.1, 4.3.1, 4.3.3, 4.4.2, 4.5

Jonsson, S., P. Segall, R. Pedersen, and G. Björnsson (2003), Post-earthquake ground movements correlated to pore-pressure transients, *Nature*, *424*(6945), 179–183. 1.2

Kaizuka, S., T. Matsuda, K. Oike, et al. (1992), Active faults in the Weihe basin and ground fissures in Xi′an city, Shaanxi Province, China, *A report on the Japan-China cooperative studies on earthquake prediction (1987-1989)*. 6.4

Kaneko, Y., and Y. Fialko (2011), Shallow slip deficit due to large strike-slip earthquakes in dynamic rupture simulations with elasto-plastic off-fault response, *Geophysical Journal International*, *186*(3), 1389–1403. 7.2

King, G., and J. Nábělek (1985), Role of fault bends in the initiation and termination of earthquake rupture, *Science*, *228*(4702), 984–987. 4.4.1

Kirby, S. H. (1983), Rheology of the lithosphere, *Reviews of Geophysics*, *21*(6), 1458–1487. 5.5.2

Klinger, Y., K. Sieh, E. Altunel, A. Akoglu, A. Barka, T. Dawson, T. Gonzalez, A. Meltzner, and T. Rockwell (2003), Paleoseismic evidence of characteristic slip on the western segment of the North Anatolian Fault, Turkey, *Bulletin of the Seismological Society of America*, *93*(6), 2317–2332. 4.4.2

Klinger, Y., X. Xu, P. Tapponnier, J. Van der Woerd, C. Lasserre, and G. King (2005), High-resolution satellite imagery mapping of the surface rupture and slip distribution of the M_w 7.8, 14 November 2001 Kokoxili earthquake, Kunlun fault, northern Tibet, China, *Bulletin of the Seismological Society of America*, *95*(5), 1970–1987. 3.1

Klinger, Y., M. Etchebes, P. Tapponnier, and C. Narteau (2011), Characteristic slip for five great earthquakes along the Fuyun fault in China, *Nature Geoscience*, *4*(6), 389–392. 1, 4.4.2

Kruskal, J. B. (1956), On the shortest spanning subtree of a graph and the traveling salesman problem, *Proceedings of the American Mathematical Society*, *7*(1), 48–50. 6.2

Kukowski, N., T. Schillhorn, E. R. Flueh, and K. Huhn (2000), Newly identified strike-slip plate boundary in the northeastern Arabian sea, *Geology*, *28*(4), 355–358. 4.2

Lawrence, R., R. Yeats, S. Khan, A. Farah, and K. DeJong (1981), Thrust and strike slip fault interaction along the Chaman transform zone, Pakistan, *Geological Society, London, Special Publications*, *9*(1), 363–370. 4.4.3

Lee, C., H. J. Theiss, J. S. Bethel, and E. M. Mikhail (2000), Rigorous mathematical modeling of airborne pushbroom imaging systems, *Photogrammetric Engineering & Remote Sensing*, *66*(4), 385–392. 2.2.1

Leprince, S., S. Barbot, F. Ayoub, and J.-P. Avouac (2007), Automatic and precise orthorectification, coregistration, and subpixel correlation of satellite images, application to ground deformation measurements, *Geoscience and Remote Sensing, IEEE Transactions on*, *45*(6), 1529–1558. 1.4.3, 3.1, 3.4.2, 3.5.2, 5.4.1, 7.1.1, 7.1, C

Leprince, S., J. Lin, F. Ayoub, F. Herman, and J. Avouac (2013), 3D high resolution tracking of ice flow using mutli-temporal stereo satellite imagery, Franz Josef Glacier, New Zealand, in *AGU Fall Meeting Abstracts*, vol. 1, p. 07. 3.6

Lin, A., B. Fu, J. Guo, Q. Zeng, G. Dang, W. He, and Y. Zhao (2002), Co-seismic strike-slip and rupture length produced by the 2001 M_s 8.1 Central Kunlun earthquake, *Science*, *296*(5575), 2015–2017. 4.1

Lin, Y., R. Jolivet, M. Simons, P. Agram, H. Martens, Z. Li, and S. Lodi (2015), High interseismic coupling in the Eastern Makran (Pakistan) subduction zone, *Earth and Planetary Science Letters*, *420*, 116–126. 4.2, 4.1, 4.5

Liu, J., and C. Haselwimmer (2006), Co-seismic ruptures found up to 60 km south of the Kunlun fault after 14 November 2001, M_s 8.1, Kokoxili earthquake using Landsat-7 ETM+ imagery, *International Journal of Remote Sensing*, *27*(20), 4461–4470. 7.1

Lowe, D. G. (1999), Object recognition from local scale-invariant features, in *Computer vision, 1999. The proceedings of the seventh IEEE international conference on*, vol. 2, pp. 1150–1157, IEEE. 2.4.2

Lowe, D. G. (2004), Distinctive image features from scale-invariant keypoints, *International Journal of Computer Vision*, *60*(2), 91–110. 2.12, 2.4.2, 2.4.2, 2.4.2

Luhmann, T., S. Robson, S. Kyle, and I. Harley (2006), *Close range photogrammetry: Principles, methods and applications*, Whittles. 2.2.1

Massonnet, D., M. Rossi, C. Carmona, F. Adragna, G. Peltzer, K. Feigl, and T. Rabaute (1993), The displacement field of the Landers earthquake mapped by radar interferometry, *Nature*, *364*(6433), 138–142. 1, 1.4.2, 7.1

McGlone, C. (1996), Sensor modeling in image registration, *Digital Photogrammetry: An Addendum to the Manual of Photogrammetry*, pp. 115–123. 2.2

McKenzie, D., J. Jackson, and K. Priestley (2005), Thermal structure of oceanic and continental lithosphere, *Earth and Planetary Science Letters*, *233*(3), 337–349. 1.1

McKenzie, D. P., and R. L. Parker (1967), The North Pacific: an example of tectonics on a sphere, *Nature*, *216*, 1276–1280. 1.1

Meyer, B., and K. Le Dortz (2007), Strike-slip kinematics in central and eastern Iran: Estimating fault slip-rates averaged over the Holocene, *Tectonics*, *26*(5), doi:10.1029/2006TC002073. 5.2

Michel, R., and J.-P. Avouac (2002), Deformation due to the 17 August 1999 Izmit, Turkey, earthquake measured from SPOT images, *Journal of Geophysical Research: Solid Earth (1978–2012)*, *107*(B4), doi:10.1029/2000JB000102. 1.4.3, 3.1, 7.1, 7.1

Michel, R., and J.-P. Avouac (2006), Coseismic surface deformation from air photos: The Kickapoo step over in the 1992 Landers rupture, *Journal of Geophysical Research: Solid Earth*, *111*(B3), n/a–n/a, doi:10.1029/2005JB003776, b03408. 1.4.3

Middleton, T., R. Walker, B. Parsons, Q. Lei, Y. Zhou, and Z. Ren (2016), A major, intraplate, normal-faulting earthquake: the 1739 Yinchuan event in northern China, *Journal of Geophysical Research*, *121*, 293–320, doi:10.1002/2015JB012355. 2.1, 6.3, 6.6.2

Mikhail, E. M., J. S. Bethel, and J. C. McGlone (2001), *Introduction to modern photogrammetry*, vol. 1, John Wiley & Sons Inc. 2.2.1

Milliner, C. W., J. F. Dolan, J. Hollingsworth, S. Leprince, F. Ayoub, and C. Sammis (2015), Quantifying near-field and off-fault deformation patterns of the 1992 M_w 7.3 Landers earthquake, *Geochemistry, Geophysics, Geosystems*, doi:10.1002/2014GC005693. 7.1

Mitchell, G., and K. MacNabb (2010), High resolution stereo satellite elevation mapping accuracy assessment, in *ASPRS Annual Conference, San Diego, California*. 2.1, 3.1

Mohadjer, S., R. Bendick, A. Ischuk, S. Kuzikov, A. Kostuk, U. Saydullaev, S. Lodi, D. Kakar, A. Wasy, M. Khan, P. Molnar, and R. Bilham (2010), Partitioning of India-Eurasia convergence in the Pamir-Hindu Kush from GPS measurements, *Geophysical Research Letters*, *37*(4), doi:10.1029/2009GL041737. 4.2

Mollberg, B., and B. Schardt (1988), Mission report on the Orbiter Camera Payload System (OCPS) Large Format Camera (LFC) and Attitude Reference System (ARS). 5.3.2

Molnar, P. (1988), Continental tectonics in the aftermath of plate tectonics, *Nature*, *335*(6186), 131–137. 1.1, 1.1

Molnar, P., and H. Lyon-Caen (1989), Fault plane solutions of earthquakes and active tectonics of the Tibetan Plateau and its margins, *Geophysical Journal International*, *99*(1), 123–153. 5.1

Molnar, P., and P. Tapponnier (1975), Cenozoic tectonics of Asia: effects of a continental collision, *Science*, *189*(4201), 419–426. 1.1, 3.1

Molnar, P., T. J. Fitch, and F. T. Wu (1973), Fault plane solutions of shallow earthquakes and contemporary tectonics in Asia, *Earth and Planetary Science Letters*, *19*(2), 101–112. 5.1

Mousavi, Z., A. Walpersdorf, R. Walker, F. Tavakoli, E. Pathier, H. Nankali, F. Nilfouroushan, and Y. Djamour (2013), Global Positioning System constraints on the active tectonics of NE Iran and the South Caspian region, *Earth and Planetary Science Letters*, *377*, 287–298. 5.2

Nissen, E., A. K. Krishnan, J. R. Arrowsmith, and S. Saripalli (2012), Three-dimensional surface displacements and rotations from differencing pre- and post-earthquake LiDAR point clouds, *Geophysical Research Letters*, *39*(16), doi:10.1029/2012GL052460. 3.4.2

Nissen, E., T. Maruyama, J. R. Arrowsmith, J. R. Elliott, A. K. Krishnan, M. E. Oskin, and S. Saripalli (2014), Coseismic fault zone deformation revealed with differential lidar: Examples from Japanese M_w ∼7 intraplate earthquakes, *Earth and Planetary Science Letters*, *405*(0), 244 – 256. 1.4.4, 3.1

Northrup, C., L. Royden, and B. Burchfiel (1995), Motion of the Pacific plate relative to Eurasia and its potential relation to Cenozoic extension along the eastern margin of Eurasia, *Geology*, *23*(8), 719–722. 6.2

Novak, K. (1992), Rectification of digital imagery, *Photogrammetric Engineering & Remote Sensing*, *58*(3), 339–344. 2.5, 2.19

OGC (1999), The OpenGIS Abstract Specification- Topic 7: The Earth Imagery Case, http://www.opengis.org/techno/specs.htm, [Open GIS Consortium (Online); accessed 5th May 2011]. 2.2, 2.2.2, 2.2.2, 2.2.2, 2.5, 2.2.2

Oh, J., and C. Lee (2014), Automated bias-compensation of rational polynomial coefficients of high resolution satellite imagery based on topographic maps, *ISPRS Journal of Photogrammetry and Remote Sensing*, *100*(14-22). 3.4.2

Okada, Y. (1985), Surface deformation due to shear and tensile faults in a half-space, *Bulletin of the Seismological Society of America*, *75*(4), 1135–1154. 3.5.2, 5.5.1, 5.5.1, 5.10, 5.5.4, 5.12

Oskin, M. E., K. Le, and M. D. Strane (2007), Quantifying fault-zone activity in arid environments with high-resolution topography, *Geophysical Research Letters*, *34*(23), doi:10.1029/2007GL031295. 3.1

Oskin, M. E., J. R. Arrowsmith, A. H. Corona, A. J. Elliott, J. M. Fletcher, E. J. Fielding, P. O. Gold, J. J. G. Garcia, K. W. Hudnut, J. Liu-Zeng, and O. J. Teran (2012), Near-field deformation from the El Mayor–Cucapah earthquake revealed by differential LIDAR, *Science*, *335*(6069), 702–705. 1, 1.4.4, 1.5, 3.1, 3.2, 3.4.2, 3.5, 3.5.1, 3.9, 3.5.2, 3.5.3, 3.6, 4.1, 4.3.1, 5.1

Ozawa, S., T. Nishimura, H. Suito, T. Kobayashi, M. Tobita, and T. Imakiire (2011), Coseismic and postseismic slip of the 2011 magnitude-9 Tohoku-Oki earthquake, *Nature*, *475*(7356), 373–376. 6.1

Peacock, D., and D. Sanderson (1991), Displacements, segment linkage and relay ramps in normal fault zones, *Journal of Structural Geology*, *13*(6), 721–733. 4.4.1

Poli, D., and T. Toutin (2012), Review of developments in geometric modelling for high resolution satellite pushbroom sensors, *The Photogrammetric Record*, *27*(137), 58–73. 2.1, 2.2.2, 2.2.2, 2.2.2, 3.1, 4.3.1

Pollitz, F. F. (2005), Transient rheology of the upper mantle beneath central Alaska inferred from the crustal velocity field following the 2002 Denali earthquake, *Journal of Geophysical Research: Solid Earth (1978–2012)*, *110*(B8). 1.2, 5.5.2

Pollitz, F. F., C. Wicks, and W. Thatcher (2001), Mantle flow beneath a continental strike-slip fault: Postseismic deformation after the 1999 Hector Mine earthquake, *Science*, *293*(5536), 1814–1818. 1.4.2

Qu, F., Q. Zhang, Z. Lu, C. Zhao, C. Yang, and J. Zhang (2014), Land subsidence and ground fissures in Xi'an, China 2005–2012 revealed by multi-band InSAR time-series analysis, *Remote Sensing of Environment*, *155*, 366–376. 6.2, 6.5

Ramsey, C. B., and S. Lee (2013), Recent and planned developments of the program OxCal, *Radiocarbon*, *55*(2–3), 720–730. E

Ramsey, C. B., T. Higham, and P. Leach (2004), Towards high-precision AMS: progress and limitations, *Radiocarbon*, *46*(1), 17–24. E

Rao, G., A. Lin, and B. Yan (2015), Paleoseismic study on active normal faults in the southeastern Weihe Graben, central China, *Journal of Asian Earth Sciences*, *114*, 212–225. 6.3, 6.4, 6.4.2, 6.4.3

Regard, V., O. Bellier, R. Braucher, F. Gasse, D. Bourlès, J. Mercier, J.-C. Thomas, M. Abbassi, E. Shabanian, and S. Soleymani (2006), ^{10}Be dating of alluvial deposits from Southeastern Iran (the Hormoz Strait area), *Palaeogeography, Palaeoclimatology, Palaeoecology*, *242*(1), 36–53. 5.2

Reid, H. F. (1910), *The mechanics of the earthquake*, vol. 2, Carnegie institution of Washington. 1.2, 1.3

Reimer, P. J., E. Bard, A. Bayliss, J. W. Beck, P. G. Blackwell, C. Bronk Ramsey, C. E. Buck, H. Cheng, R. L. Edwards, M. Friedrich, et al. (2013), IntCal13 and Marine13 radiocarbon age calibration curves 0-50,000 years cal BP. E

Ren, Z., Z. Zhang, T. Chen, S. Yan, J. Yin, P. Zhang, W. Zheng, H. Zhang, and C. Li (2015), Clustering of offsets on the Haiyuan fault and their relationship to paleoearthquakes, *Geological Society of America Bulletin*, pp. B31,155–1. 3.1

Rost, K. T. (2000), Pleistocene paleoenvironmental changes in the high mountain ranges of central China and adjacent regions, *Quaternary International*, *65*, 147–160. 6.6.1

Rosu, A.-M., M. Pierrot-Deseilligny, A. Delorme, R. Binet, and Y. Klinger (2015), Measurement of ground displacement from optical satellite image correlation using the free open-source software MicMac, *ISPRS Journal of Photogrammetry and Remote Sensing*, *100*, 48–59. 1.4.3, 7.1

Savage, J., and J. Svarc (1997), Postseismic deformation associated with the 1992 M_w 7.3 Landers earthquake, southern California, *Journal of Geophysical Research: Solid Earth (1978–2012)*, *102*(B4), 7565–7577. 1.2

Scholz, C. H. (1982), Scaling laws for large earthquakes: consequences for physical models, *Bulletin of the Seismological Society of America*, *72*(1), 1–14. 5.2

Segall, P., R. Bürgmann, and M. Matthews (2000), Time-dependent triggered afterslip following the 1989 Loma Prieta earthquake, *Journal of Geophysical Research: Solid Earth (1978–2012)*, *105*(B3), 5615–5634. 1.2, 5.2, 5.5.2

Seitz, S. M., B. Curless, J. Diebel, D. Scharstein, and R. Szeliski (2006), A comparison and evaluation of multi-view stereo reconstruction algorithms, in *Computer vision and pattern recognition, 2006 IEEE Computer Society Conference on*, vol. 1, pp. 519–528, IEEE. 2.4.2

Shen, Z.-K., J. Sun, P. Zhang, Y. Wan, M. Wang, R. Bürgmann, Y. Zeng, W. Gan, H. Liao, and Q. Wang (2009), Slip maxima at fault junctions and rupturing of barriers during the 2008 Wenchuan earthquake, *Nature Geoscience*, *2*(10), 718–724. 1.5, 6.1

Sieh, K., M. Stuiver, and D. Brillinger (1989), A more precise chronology of earthquakes produced by the San Andreas fault in southern California, *Journal of Geophysical Research: Solid Earth*, *94*(B1), 603–623. 6.1

Smith, W., and P. Wessel (1990), Gridding with continuous curvature splines in tension, *Geophysics*, *55*(3), 293–305. 3.3.2

Snavely, N., S. M. Seitz, and R. Szeliski (2006), Photo tourism: exploring photo collections in 3D, in *ACM transactions on graphics (TOG)*, vol. 25, pp. 835–846, ACM. 2.4.2

Snavely, N., S. M. Seitz, and R. Szeliski (2008a), Skeletal graphs for efficient structure from motion., in *Proc. IEEE Conf. on Computer Vision and Pattern Recognition*, vol. 1, p. 2. 2.1

Snavely, N., S. M. Seitz, and R. Szeliski (2008b), Modeling the world from internet photo collections, *International Journal of Computer Vision*, *80*(2), 189–210. 2.4.2, 2.4.2

Song, Z. (2012), *Global earthquake catalogue*, Seismological press, Beijing. 4.1, 6.2, 6.6

SSB (1988), *Active fault system around Ordos Massif*, State Seismology Bureau, Seismological Press, Beijing. 6.2, 6.4

Stein, R. S., G. C. King, and J. Lin (1992), Change in failure stress on the southern San Andreas fault system caused by the 1992 magnitude= 7.4 Landers earthquake, *Science*, *258*(5086), 1328–1332. 6.1

Stein, S., and E. A. Okal (2005), Seismology: Speed and size of the Sumatra earthquake, *Nature*, *434*(7033), 581–582. 6.1

Stumpf, A., J.-P. Malet, P. Allemand, and P. Ulrich (2014), Surface reconstruction and landslide displacement measurements with Pléiades satellite images, *ISPRS Journal of Photogrammetry and Remote Sensing*, *95*, 1–12. 2.1, 3.1, 3.3.2

Suito, H., and J. T. Freymueller (2009), A viscoelastic and afterslip postseismic deformation model for the 1964 Alaska earthquake, *Journal of Geophysical Research: Solid Earth (1978–2012)*, *114*(B11), doi:10.1029/2008JB005954. 5.5.2

Sun, J. (2015), A strike-slip dominated fault rupture of the Sept. 24, 2013 M_w 7.7 Awaran, Pakistan earthquake and its first-year post-seismic deformation revealed by Landsat-8 imagery and TerraSAR-X data, in *ESA FRINGE workshop*. 4.5

Surazakov, A., and V. Aizen (2010), Positional accuracy evaluation of declassified Hexagon KH-9 mapping camera imagery, *Photogrammetric Engineering & Remote Sensing*, *76*(5), 603–608. 5.3.2

Szeliga, W., R. Bilham, D. M. Kakar, and S. H. Lodi (2012), Interseismic strain accumulation along the western boundary of the Indian subcontinent, *Journal of Geophysical Research: Solid Earth (1978–2012)*, *117*(B8), doi:10.1029/2011JB008822. 4.2, 4.1, 4.4.2, 4.4.3

Tao, C. V., and Y. Hu (2002), 3D reconstruction methods based on the rational function model, *Photogrammetric Engineering & Remote Sensing*, *68*(7), 705–714. 2.2, 2.2.2, 2.2.2, 2.2.2, 2.4.1, 2.4.1, 2.5

Tapponnier, P., and P. Molnar (1977), Active faulting and tectonics in China, *Journal of Geophysical Research*, *82*(20), 2905–2930. 1, 6.2

Tapponnier, P., B. Meyer, J. P. Avouac, G. Peltzer, Y. Gaudemer, S. Guo, H. Xiang, K. Yin, Z. Chen, S. Cai, and H. Dai (1990), Active thrusting and folding in the Qilian Shan, and decoupling between upper crust and mantle in northeastern Tibet, *Earth and Planetary Science Letters*, *97*(3), 382–403. 5.1

Tatar, M., D. Hatzfeld, J. Martinod, A. Walpersdorf, M. Ghafori-Ashtiany, and J. Chéry (2002), The present-day deformation of the central Zagros from GPS measurements, *Geophysical Research Letters*, *29*(19), 33–1. 5.2

Taylor, M. H., S. Leprince, J.-P. Avouac, and K. Sieh (2008), Detecting co-seismic displacements in glaciated regions: An example from the great November 2002 Denali earthquake using SPOT horizontal offsets, *Earth and Planetary Science Letters*, *270*(3), 209–220. 7.1

Tearpock, D. J., and R. E. Bischke (2002), *Applied subsurface geological mapping with structural methods*, Pearson Education. 4.3.3

Teran, O. J., J. M. Fletcher, M. E. Oskin, T. K. Rockwell, K. W. Hudnut, R. M. Spelz, S. O. Akciz, A. P. Hernandez-Flores, and A. E. Morelan (2015), Geologic and structural controls on rupture zone fabric: A field-based study of the 2010 M_w 7.2 El Mayor–Cucapah earthquake surface rupture, *Geosphere*, *11*(3), 899–920. 1.7, 1.8, 3.2, 3.5.3

Toksöz, M. N., E. Arpat, and F. Saroglu (1977), East Anatolian earthquake of 24 November 1976, *Nature*, *270*, 423–425. 7.3

Tong, X., S. Liu, and Q. Weng (2010), Bias-corrected rational polynomial coefficients for high accuracy geo-positioning of Quickbird stereo imagery, *ISPRS Journal of Photogrammetry and Remote Sensing*, *65*(2), 218–226. 2.1, 2.2.2, 2.2.2, 2.2.2

Toutin, T. (2006), Comparison of 3D physical and empirical models for generating DSMs from stereo HR images, *Photogrammetric Engineering & Remote Sensing*, *72*(5), 597–604. 2.2.2

Triggs, B., P. F. McLauchlan, R. I. Hartley, and A. W. Fitzgibbon (2000), Bundle adjustment– a modern synthesis, in *Vision algorithms: theory and practice*, pp. 298–372, Springer. 2.4.2

Turcotte, D. L., and G. Schubert (2014), *Geodynamics*, Cambridge University Press. 1.1, 1.1, 1.3

Tuytelaars, T., and K. Mikolajczyk (2008), Local invariant feature detectors: a survey, *Foundations and Trends in Computer Graphics and Vision*, *3*(3), 177–280. 2.4.2

Vallage, A., Y. Klinger, R. Grandin, H. Bhat, and M. Pierrot-Deseilligny (2015), Inelastic surface deformation during the 2013 M_w 7.7 Balochistan, Pakistan, earthquake, *Geology*, *43*(12), 1079–1082. 7.1, 7.1.1, 7.1, 7.1.2

Vernant, P., F. Nilforoushan, J. Chery, R. Bayer, Y. Djamour, F. Masson, H. Nankali, J.-F. Ritz, M. Sedighi, and F. Tavakoli (2004a), Deciphering oblique shortening of central Alborz in Iran using geodetic data, *Earth and Planetary Science Letters*, *223*(1), 177–185. 5.2

Vernant, P., F. Nilforoushan, D. Hatzfeld, M. Abbassi, C. Vigny, F. Masson, H. Nankali, J. Martinod, A. Ashtiani, R. Bayer, et al. (2004b), Present-day crustal deformation and plate kinematics in the Middle East constrained by GPS measurements in Iran and northern Oman, *Geophysical Journal International*, *157*(1), 381–398. 5.2

Walker, R., and J. Jackson (2004), Active tectonics and late Cenozoic strain distribution in central and eastern Iran, *Tectonics*, *23*(5), doi:10.1029/2003TC001529. 5.2

Walker, R., J. Jackson, and C. Baker (2003), Surface expression of thrust faulting in eastern Iran: source parameters and surface deformation of the 1978 Tabas and 1968 Ferdows earthquake sequences, *Geophysical Journal International*, *152*(3), 749–765. 5.1, 5.2, 5.1, 5.5.1, 5.5.3, 5.5.3, 5.11

Walker, R., P. Gans, M. Allen, J. Jackson, M. Khatib, N. Marsh, and M. Zarrinkoub (2009), Late Cenozoic volcanism and rates of active faulting in eastern Iran, *Geophysical Journal International*, *177*(2), 783–805. 5.2, 5.5.4

Walker, R., M. Khatib, A. Bahroudi, A. Rodés, C. Schnabel, M. Fattahi, M. Talebian, and E. Bergman (2013), Co-seismic, geomorphic, and geologic fold growth associated with the 1978 Tabas-e-golshan earthquake fault in eastern Iran, *Geomorphology*, *237*, 98–118. 5.1, 5.2, 5.2, 5.5.3, 5.5.4

Walker, R. T. (2006), A remote sensing study of active folding and faulting in southern Kerman province, SE Iran, *Journal of Structural Geology*, *28*(4), 654–668. 1

Walker, R. T., and M. Fattahi (2011), A framework of Holocene and Late Pleistocene environmental change in eastern Iran inferred from the dating of periods of alluvial fan abandonment, river terracing, and lake deposition, *Quaternary Science Reviews*, *30*(9), 1256–1271. 4.4.3

Wallace, R. E. (1977), Profiles and ages of young fault scarps, north-central Nevada, *Geological Society of America Bulletin*, *88*(9), 1267–1281. 3.1

Walpersdorf, A., D. Hatzfeld, H. Nankali, F. Tavakoli, F. Nilforoushan, M. Tatar, P. Vernant, J. Chéry, and F. Masson (2006), Difference in the GPS deformation pattern of North and Central Zagros (Iran), *Geophysical Journal International*, *167*(3), 1077–1088. 5.2

Walpersdorf, A., I. Manighetti, Z. Mousavi, F. Tavakoli, M. Vergnolle, A. Jadidi, D. Hatzfeld, A. Aghamohammadi, A. Bigot, Y. Djamour, and H. Nankali (2014), Present-day kinematics and fault slip rates in eastern Iran, derived from 11 years of GPS data, *Journal of Geophysical Research: Solid Earth*, *119*(2), 1359–1383, doi:10.1002/2013JB010620. 5.2

Wang, H., T. Wright, and J. Biggs (2009), Interseismic slip rate of the northwestern Xianshuihe fault from InSAR data, *Geophysical Research Letters*, *36*(3), doi:10.1029/2008GL036560. 6.2

Wang, J., F. Shi, J. Zhang, and Y. Liu (2008), A new calibration model of camera lens distortion, *Pattern Recognition*, *41*(2), 607–615. 2.2.1, 2.2.1

Wang, J.-M. (1987), The Fenwei rift and its recent periodic activity, *Tectonophysics*, *133*(3), 257–275. 6.1

Wang, Q., P.-Z. Zhang, J. T. Freymueller, R. Bilham, K. M. Larson, X. Lai, X. You, Z. Niu, J. Wu, Y. Li, and J. Liu (2001), Present-day crustal deformation in China constrained by global positioning system measurements, *Science*, *294*(5542), 574–577. 1.4.1

Watson, G. (2006), Computing helmert transformations, *Journal of Computational and Applied Mathematics*, *197*(2), 387–394. 2.4.2

Wei, S., E. Fielding, S. Leprince, A. Sladen, J.-P. Avouac, D. Helmberger, E. Hauksson, R. Chu, M. Simons, K. Hudnut, T. Herring, and R. Briggs (2011), Superficial simplicity of the 2010 El Mayor-Cucapah earthquake of Baja California in Mexico, *Nature Geoscience*, *4*(9), 615–618. 3.1, 3.2, 3.5.2, 3.5.3, 7.1

Wells, D. L., and K. J. Coppersmith (1994), New empirical relationships among magnitude, rupture length, rupture width, rupture area, and surface displacement, *Bulletin of the Seismological Society of America*, *84*(4), 974–1002. 6.3, 6.6.2, 7.1.1

Weng, J., P. Cohen, and M. Herniou (1992), Camera calibration with distortion models and accuracy evaluation, *IEEE Transactions on Pattern Analysis & Machine Intelligence*, (10), 965–980. 2.2.1

Wesnousky, S., L. Jones, C. Scholz, and Q. Deng (1984), Historical seismicity and rates of crustal deformation along the margins of the Ordos block, north China, *Bulletin of the Seismological Society of America*, *74*(5), 1767–1783. 6.2

Wesnousky, S. G. (2006), Predicting the endpoints of earthquake ruptures, *Nature*, *444*(7117), 358–360. 4.4.1

Wesnousky, S. G., S. Kumar, R. Mohindra, and V. Thakur (1999), Uplift and convergence along the Himalayan Frontal Thrust of India, *Tectonics*, *18*(6), 967–976. 3.1

Westoby, M., J. Brasington, N. Glasser, M. Hambrey, and J. Reynolds (2012), Structure-from-Motion photogrammetry: A low-cost, effective tool for geoscience applications, *Geomorphology*, *179*, 300–314. 2.1

Wright, T., B. Parsons, and E. Fielding (2001), Measurement of interseismic strain accumulation across the North Anatolian Fault by satellite radar interferometry, *Geophysical Research Letters*, *28*(10), 2117–2120. 6.2

Wright, T. J., Z. Lu, and C. Wicks (2004a), Constraining the slip distribution and fault geometry of the M_w 7.9, 3 November 2002, Denali fault earthquake with interferometric synthetic aperture radar and global positioning system data, *Bulletin of the Seismological Society of America*, *94*(6B), S175–S189. 4.1

Wright, T. J., B. Parsons, P. C. England, and E. J. Fielding (2004b), InSAR observations of low slip rates on the major faults of western Tibet, *Science*, *305*(5681), 236–239. 1, 1.4.2

Xu, C., Y. Liu, Y. Wen, and R. Wang (2010), Coseismic slip distribution of the 2008 M_w 7.9 Wenchuan earthquake from joint inversion of GPS and InSAR data, *Bulletin of the Seismological Society of America*, *100*(5B), 2736–2749. 1.6

Xu, X., X. Tong, D. T. Sandwell, C. W. Milliner, J. F. Dolan, J. Hollingsworth, S. Leprince, and F. Ayoub (2016), Refining the shallow slip deficit, *Geophysical Journal International*, *204*(3), 1867–1886. 7.1.2

Yang, X. (2000), Accuracy of rational function approximation in photogrammetry, in *Proc. ASPRS Annual Conference, Washington DC*, pp. 22–26. 2.2.2

Yu, S.-B., Y.-J. Hsu, L.-C. Kuo, H.-Y. Chen, and C.-C. Liu (2003), GPS measurement of postseismic deformation following the 1999 Chi-Chi, Taiwan, earthquake, *Journal of Geophysical Research: Solid Earth*, *108*(B11), doi:10.1029/2003JB002396. 5.5.2

Yuan, T., and X. Feng (2010), *The great 1556 Huaxian earthquake*, Seismological Press, Beijing. 6.1, 6.3, 6.6, 6.1, 6.4.3, 6.6.2, 6.7

Zhang, A., Z. Yang, J. Zhong, and F. Mi (1995a), Characteristics of Late Quaternary activity along the southern border fault zone of Weihe graben basin, *Quaternary International*, *25*, 25–31. 6.3

Zhang, A.-L., F.-S. Mi, and J. Chong (1989), Deformation relics of the 1556 Huaxian (Shaanxi, China) great earthquake and the study of palaeoseimicity on the frontal fault zone of the Huashan MTS, *Seismology and Geology*, *3*, 010. 6.3

Zhang, P., Q. Deng, G. Zhang, J. Ma, W. Gan, W. Min, F. Mao, and Q. Wang (2003), Active tectonic blocks and strong earthquakes in the continent of China, *Science in China Series D: Earth Sciences*, *46*(2), 13–24. 6.2

Zhang, P.-Z. (2013), Beware of slowly slipping faults, *Nature Geoscience*, *6*(5), 323–324. 3.1, 5.1, 6.1

Zhang, Y. Q., J. L. Mercier, and P. Vergély (1998), Extension in the graben systems around the Ordos (China), and its contribution to the extrusion tectonics of south China with respect to Gobi-Mongolia, *Tectonophysics*, *285*(1), 41–75. 6.2

Zhang, Z. (2000), A flexible new technique for camera calibration, *Pattern Analysis and Machine Intelligence, IEEE Transactions on*, *22*(11), 1330–1334. 2.2.1

Zhang, Z., R. Deriche, O. Faugeras, and Q.-T. Luong (1995b), A robust technique for matching two uncalibrated images through the recovery of the unknown epipolar geometry, *Artificial intelligence*, *78*(1), 87–119. 2.3, 2.3, 2.3

Zhou, Y., C. Zhou, E. Dongchen, and Z. Wang (2014), A Baseline-Combination Method for Precise Estimation of Ice Motion in Antarctica, *Geoscience and Remote Sensing, IEEE Transactions on*, *52*(9), 5790–5797. 1.6

Zhou, Y., J. R. Elliott, B. Parsons, and R. T. Walker (2015a), The 2013 Balochistan earthquake: An extraordinary or completely ordinary event?, *Geophysical Research Letters*, *42*(15), 6236–6243. 1.6, 2.1, 3.1, 4.6, 5.1, 5.5.4

Zhou, Y., B. Parsons, J. R. Elliott, I. Barisin, and R. T. Walker (2015b), Assessing the ability of Pleiades stereo imagery to determine height changes in earthquakes: A case study for the El Mayor-Cucapah epicentral area, *Journal of Geophysical Research: Solid Earth*, pp. 8793–8808, doi:10.1002/2015JB012358. 1.6, 2.1, 2.2.2, 4.3.3, 7.1

Zhou, Y., C. Zhou, F. Deng, D. E, H. Liu, and Y. Wen (2015c), Improving InSAR elevation models in Antarctica using laser altimetry, accounting for ice motion, orbital errors and atmospheric delays, *Remote Sensing of Environment*, *162*, 112–118. 1.6, 6.2

Zhou, Y., R. T. Walker, J. R. Elliott, and B. Parsons (2016a), Mapping 3D fault geometry in earthquakes using high-resolution topography: Examples from the 2010 El Mayor-Cucapah (Mexico) and 2013 Balochistan (Pakistan) earthquakes, *Geophysical Research Letters*, doi:10.1002/2016GL067899. 1.6, 3.5.3

Zhou, Y., R. T. Walker, J. Hollingsworth, M. Talebian, X. Song, and B. Parsons (2016b), Coseismic and postseismic displacements from the 1978 M_w 7.3 Tabas-e-Golshan earthquake in eastern Iran, *Earth and Planetary Science Letters*, doi:10.1016/j.epsl.2016.07.38. 1.2, 1.6, 2.4.2, 7.1

Zinke, R., J. Hollingsworth, and J. F. Dolan (2014), Surface slip and off-fault deformation patterns in the 2013 M_w 7.7 Balochistan, Pakistan earthquake: Implications for controls on the distribution of near-surface coseismic slip, *Geochemistry, Geophysics, Geosystems*, *15*(12), 5034–5050. 4.1, 4.2, 4.3.1, 4.3.2, 4.4.2, 4.4.3, 4.5

Zoback, M. D., M. L. Zoback, V. S. Mount, J. Suppe, J. P. Eaton, J. H. Healy, D. Oppenheimer, P. Reasenberg, L. Jones, C. B. Raleigh, and I. Wong (1987), New evidence on the state of stress of the San Andreas fault system, *Science*, *238*(4830), 1105–1111. 1.1

Appendix A

Cumulative Surface Slip along the Hoshab Fault

Additional examples of cumulative surface slip along the Hoshab fault (Sites 3–6 in Table 4.1 in Chapter 4).

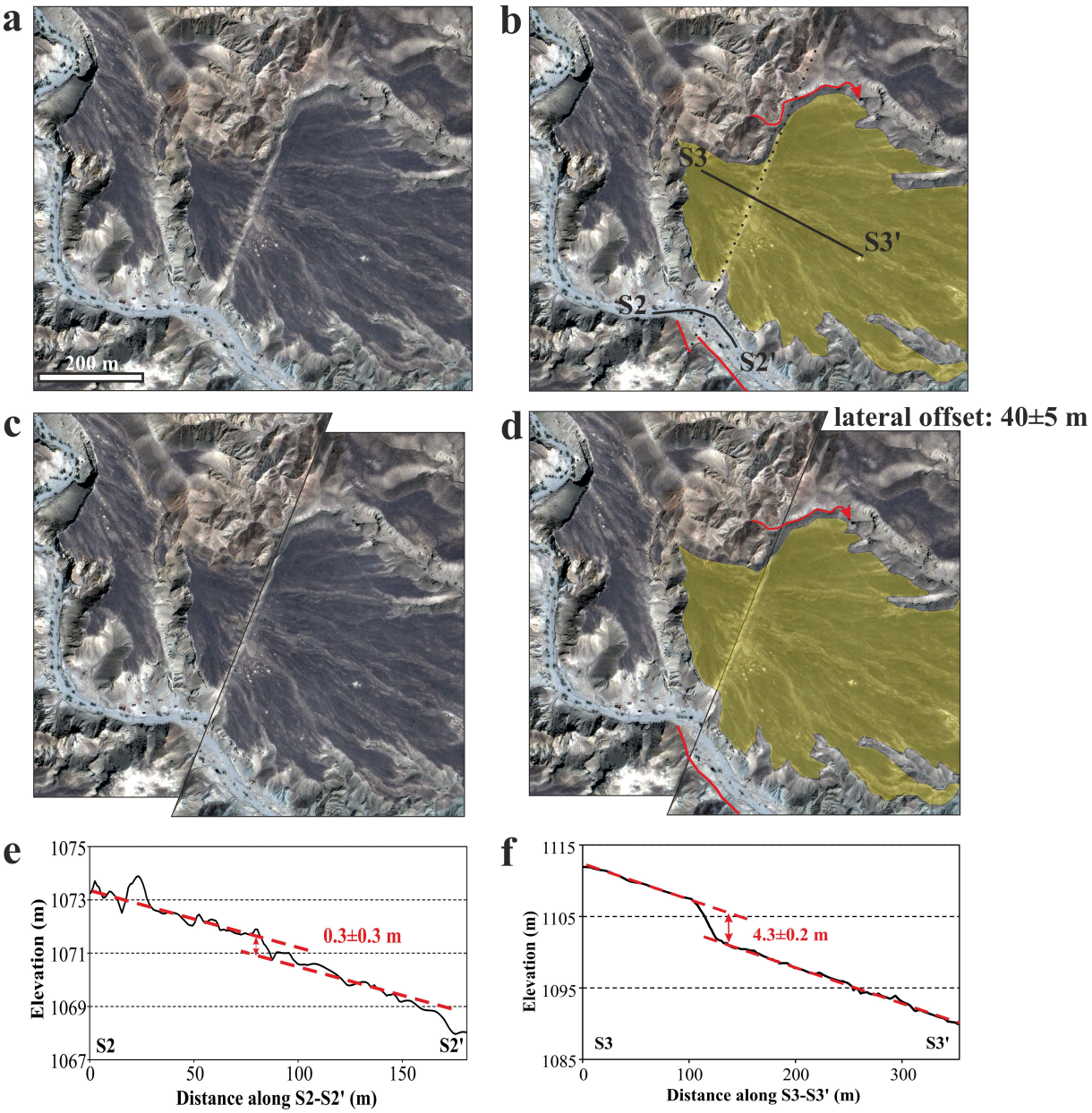


Figure A.1: Cumulative displacements along the Hoshab fault (Site 3 in Table 4.1). (a) Post-earthquake Pleiades imagery. (b) Annotation showing the offset alluvial fan surface (yellow polygon) and gully (red line). (c) Restoration of the alluvial fan surface and gully. (d) The cumulative lateral offset at this site is 40 m. (e) Elevation profile S2-S2′ across the river channel shows the vertical offset in the 2013 event at this site is 0.3 m (north-side-up). (f) Elevation profile S3-S3′ across the fan surface shows the cumulative vertical offset at this site is 4.3 m (north-side-up). Lateral displacement of the 2013 event (3.3 m) was measured 3 km west of this location.

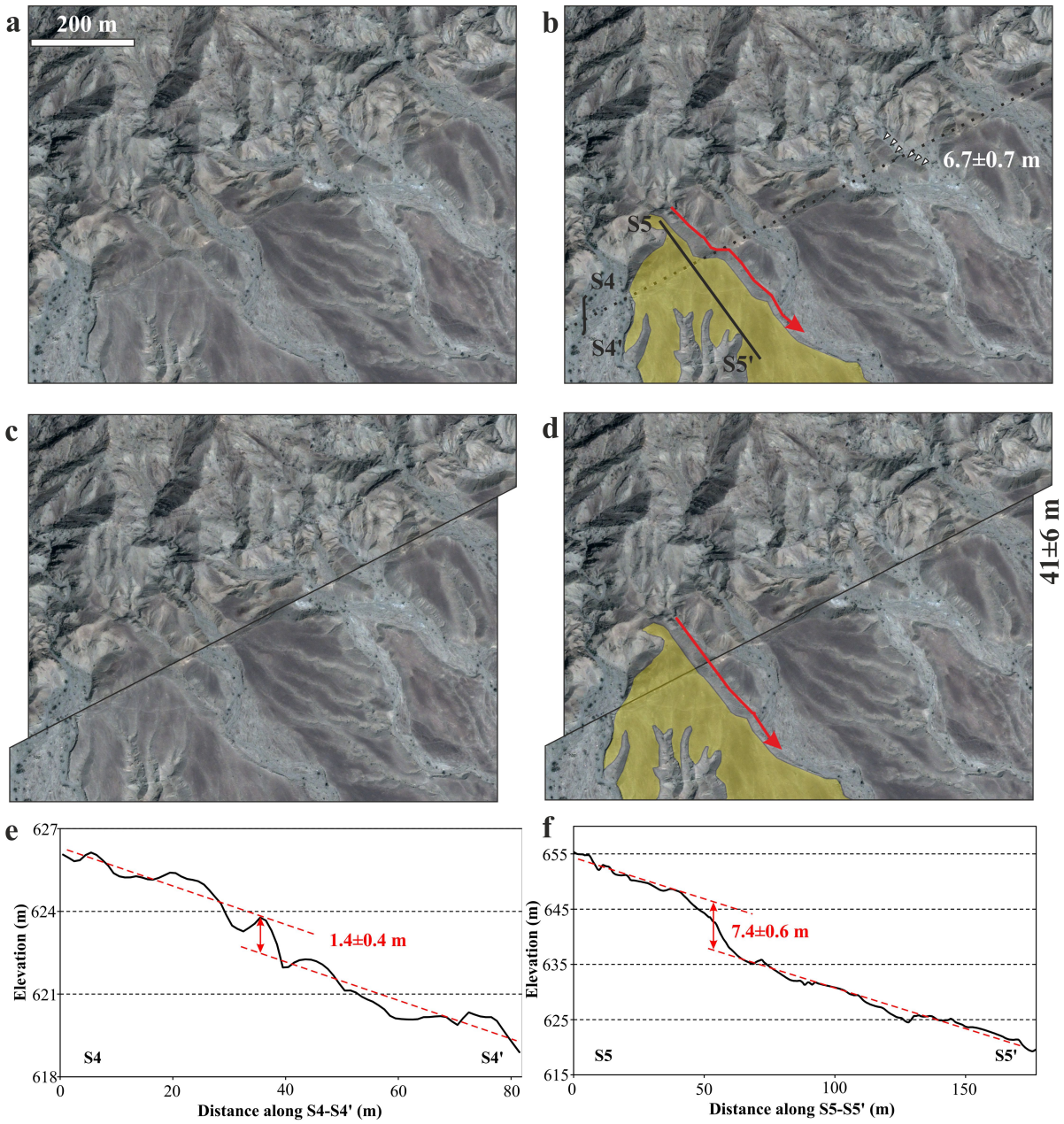


Figure A.2: Cumulative displacements along the Hoshab fault (Site 4 in Table 4.1). (a) Post-earthquake Pleiades imagery. (b) Annotation showing the offset alluvial fan surface (yellow polygon) and river channel (red line). The 2013 earthquake offset an alluvial fan by 6.7 m (white arrows). (c) Restoration of the alluvial fan surface and river channel. (d) The cumulative lateral offset at this site is 41 m. (e) Elevation profile S4-S4′ across the river channel shows the vertical offset in the 2013 event at this site is 1.4 m (north-side-up). (f) Elevation profile S5-S5′ across the fan surface shows the cumulative vertical offset at this site is 7.4 m (north-side-up).

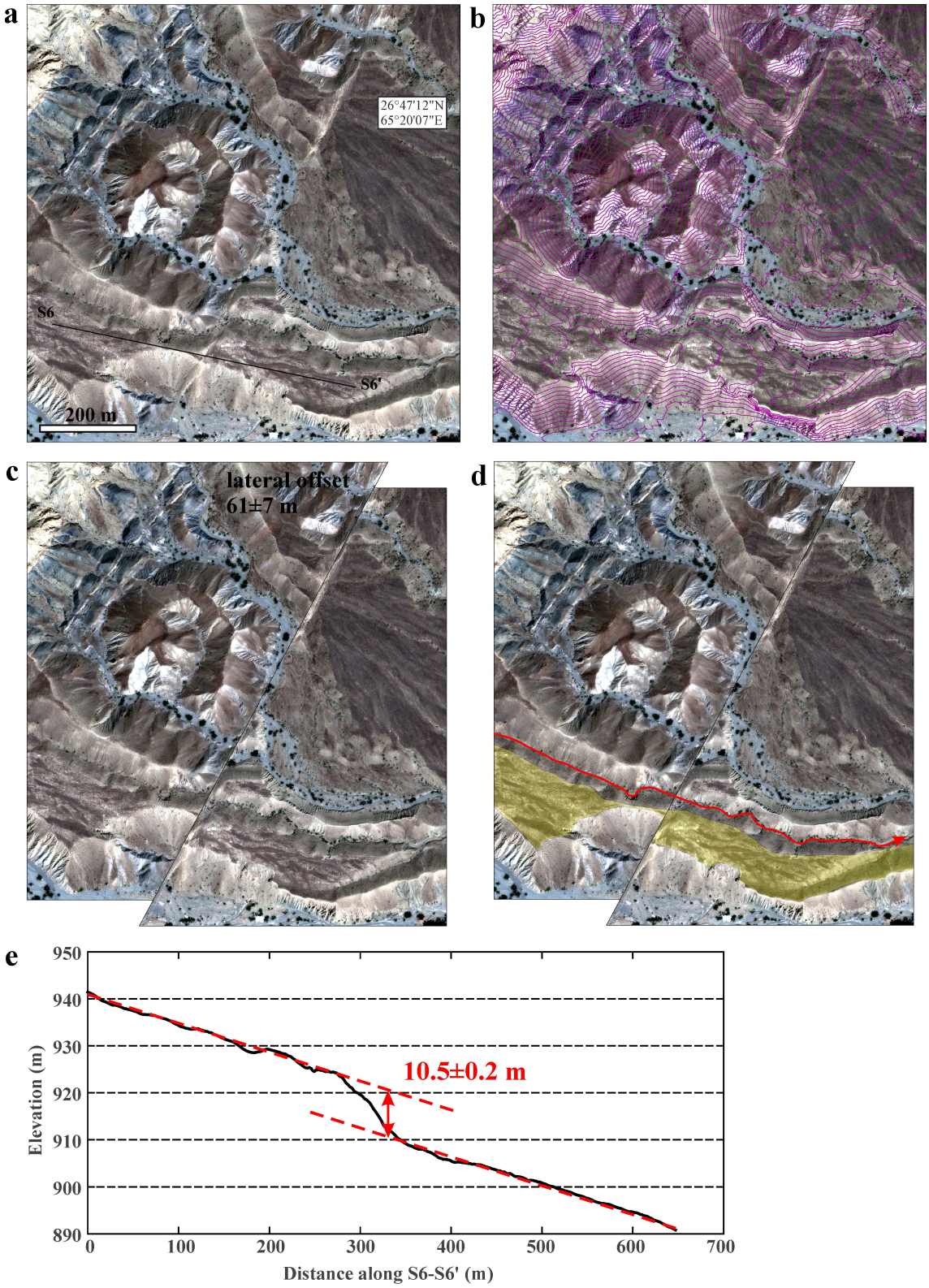


Figure A.3: Cumulative displacements along the Hoshab fault (Site 5 in Table 4.1). (a) Post-earthquake Pleiades imagery. (b) Contour map (purple lines) superimposed on the imagery showing river channels and alluvial fans. The contour interval is 5 m. (c) Restoration of the alluvial fan surface and river channel. (d) The cumulative lateral offset at this site is 61 m. (e) Elevation profile S6-S6′ across the fan surface shows the cumulative vertical offset at this site is 10.5 m (north-side-up). Surface displacement of the 2013 event (10.0 m lateral and 1.4 m vertical) was measured 1 km northeast of this location.

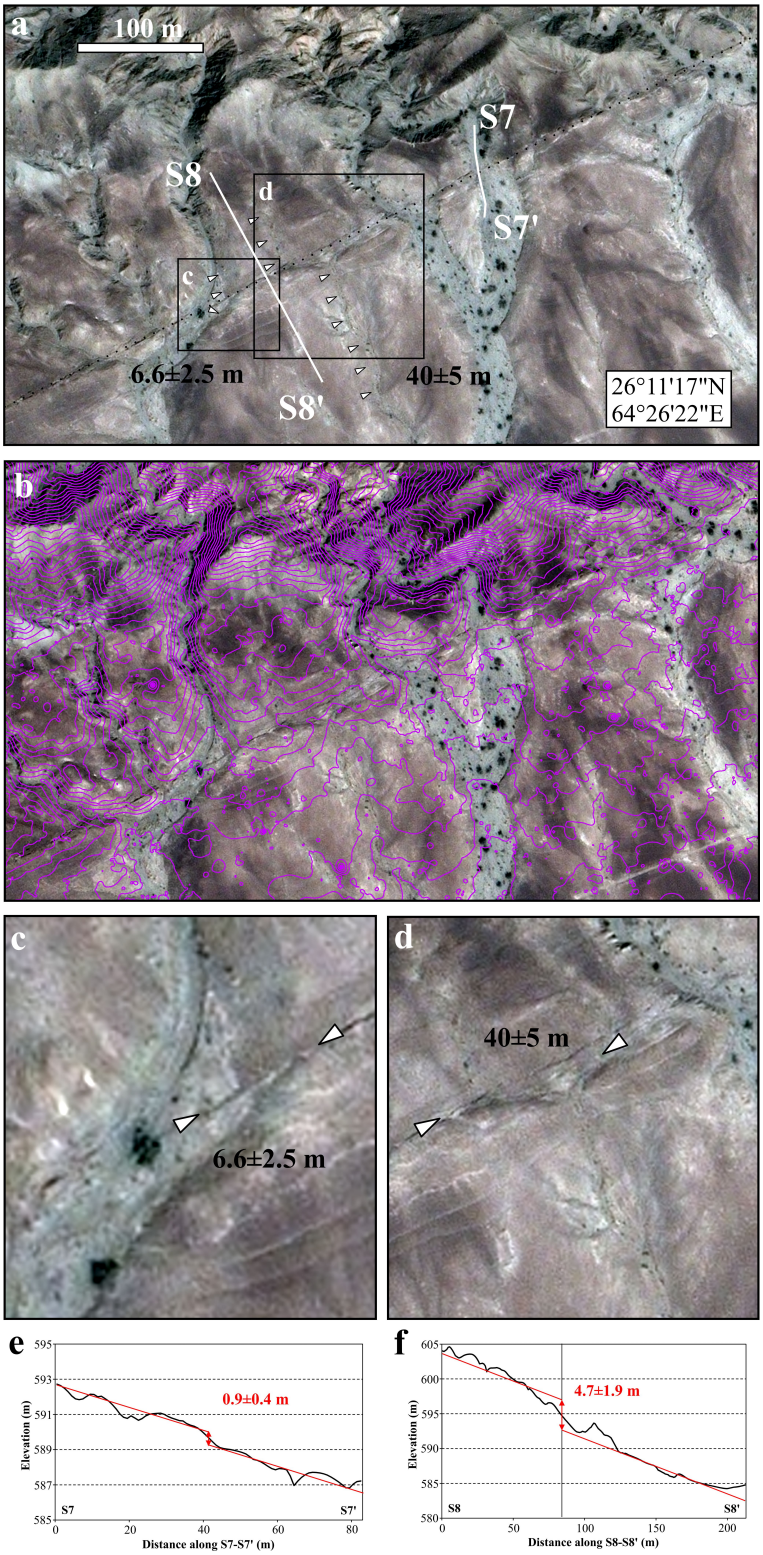


Figure A.4: Cumulative displacements along the Hoshab fault (Site 6 in Table 4.1). (a) Post-earthquake Pleiades imagery. (b) Contour map (purple lines) showing bedrock (steeper topography with denser contour lines) and alluvial fans (sparser contour lines). The contour interval is 2 m. (c) The lateral offset in the 2013 earthquake at this location is 6.6 m. (d) A gully within an older fan surface is laterally offset by 40 m. (e) Elevation profile S7-S7′ shows that the vertical displacement in the 2013 earthquake at this location is 0.9 m (north-side-up). (f) Elevation profile S8-S8′ along the old fan surface shows a cumulative vertical displacement of 4.7 m (north-side-up).

Appendix B

Estimating Fault Dip with High-resolution Topography

An earthquake rupture is the result of rapid slip on a fault. Assuming that the fault is planar and the rupture reaches the surface, the fault plane will intersect with the undulating topography (Figures B.1a and B.1b). The intersection is presented as the surface trace of an earthquake rupture. Knowing the 3D coordinates of the intersection, we can estimate fault dip (θ in Figure B.1a) by using the plane equation:

$$A \cdot x + B \cdot y + C \cdot z + D = 0 \tag{B.1}$$

where (x, y, z) are the coordinates of the points along the surface rupture, and A, B, C and D are unknown constants to be determined.

The orthogonal distance d_i of a point (x_i, y_i, z_i) to the plane is given by:

$$d_i = \frac{|A \cdot x_i + B \cdot y_i + C \cdot z_i + D|}{\sqrt{A^2 + B^2 + C^2}} \tag{B.2}$$

We minimise the sum of the orthogonal distance of each point measured at the surface to the plane using a least squares regression to solve the plane equation, i.e. to estimate the parameters A, B, C and D. The dip of the fault (θ) can then be estimated via Equation

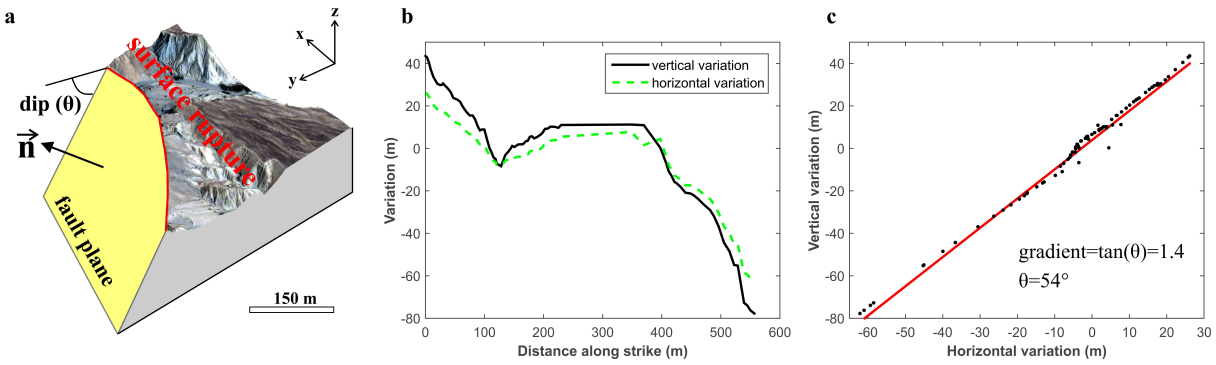


Figure B.1: Measuring fault dip by fitting a plane (in yellow) to the surface rupture. (a) Cartoon showing a fault plane dipping at an angle θ to the horizontal. The normal vector of the fault plane is $\vec{\mathbf{n}} = (\frac{A}{\sqrt{A^2+B^2+C^2}}, \frac{B}{\sqrt{A^2+B^2+C^2}}, \frac{C}{\sqrt{A^2+B^2+C^2}})$, where A, B, C and D are the constants in Equation B.1. (b) Vertical (black line) and horizontal (green dashed line) variation about the mean strike along the surface rupture. (c) Vertical variation is a linear function of horizontal variation about the mean strike (black dots are measurements from the 3D point cloud). The gradient of the linear function (red line) is $\tan\theta$. This example is from the Balochistan earthquake (S24 in Table B.1).

(B.3).

$$\theta = \frac{\pi}{2} - \tan^{-1}\frac{C}{\sqrt{A^2+B^2}} \tag{B.3}$$

As the surface rupture trace lies on the fault plane, for each point along the trace, the vertical variation is a linear function of the horizontal variation about the mean strike (i.e. $\tan^{-1}\frac{A}{B}$), the gradient of which is $\tan\theta$ (Figures B.1b and B.1c). This classic method has been successfully applied in structural geology, using three points to determine the horizontal and vertical variations, and estimate the fault dip. Recent advances in high-resolution imagery and digital elevation models (DEMs) allow us to improve our capability in structural analysis, by expanding the number of observations to more reliably solve for the fault plane using a least squares minimisation.

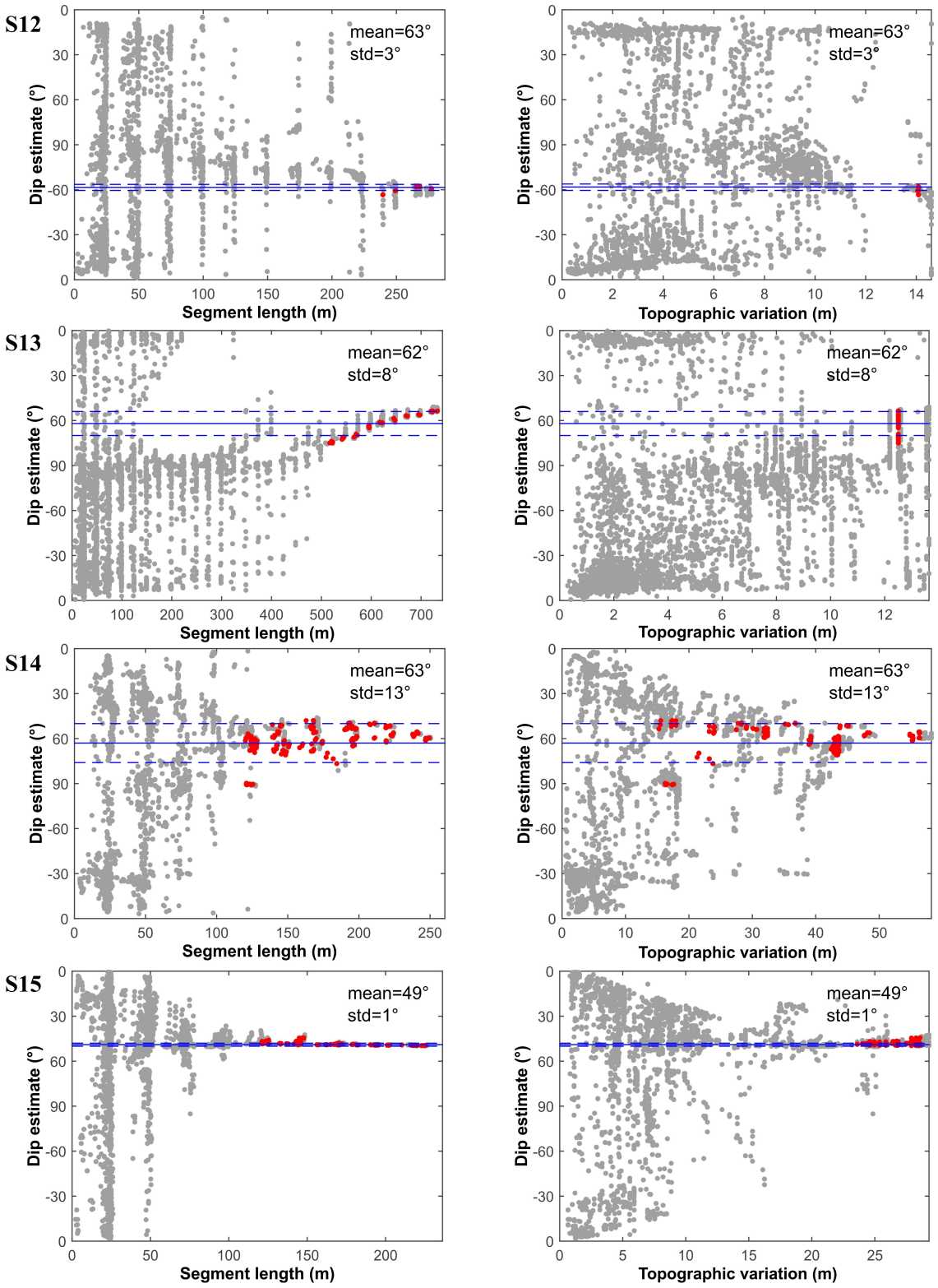
For a fault segment, we applied the following steps to estimate the dip. We started with a polygon 25 m long (L) and 0.5 m wide (W), centred on the rupture trace. We randomly chose 100 positions along the rupture and generated a new same-sized polygon for extracting 3D points beginning at each new position, given that the trace of the fault along irregular topography is not the same. The dip and topographic variation (elevation difference between the highest and lowest points) were estimated for each set of points. We also determined the distance between the most extreme points in the point cloud that

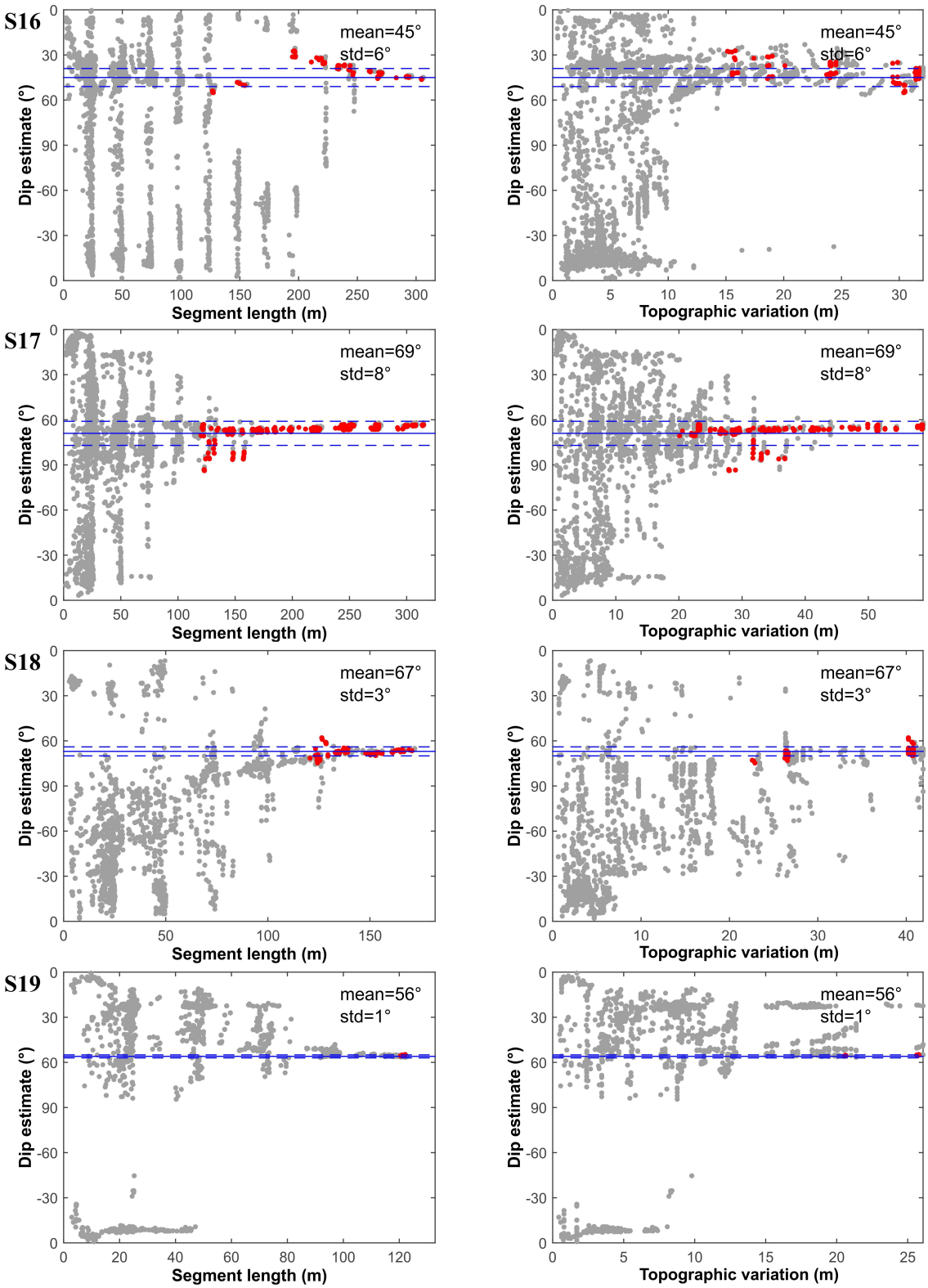
Table B.1: Fault dip estimated by determining the best-fitting planes to the fault trace. See Figure B.2 for details.

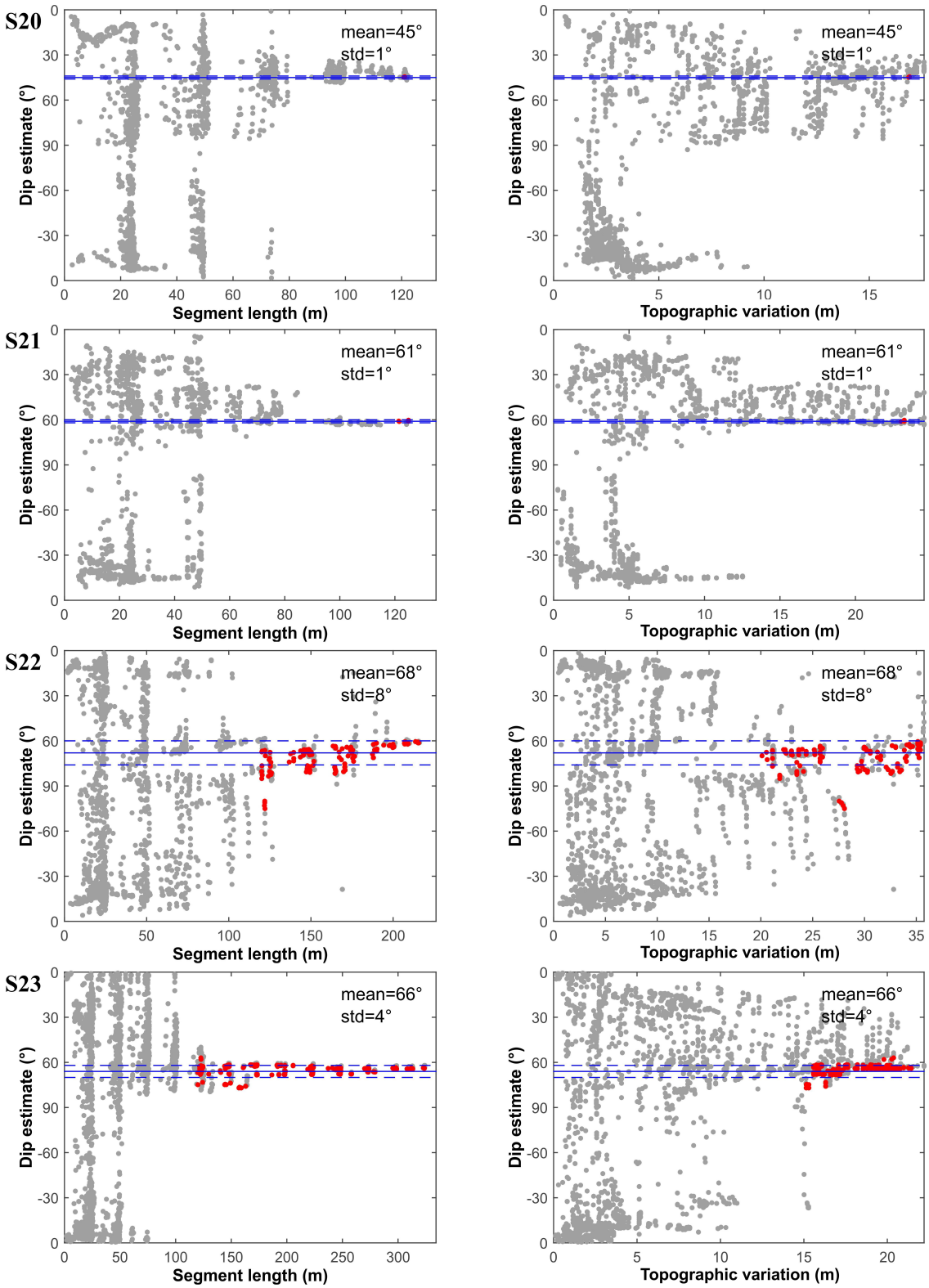
ID	Latitude (°)	Longitude (°)	Segment length (m)	Topographic variation (m)	dip (°)
S12	26.1163	64.2048	310	15	-63±3
S13	26.1230	64.2287	841	13	62±8
S14	26.3452	64.7506	275	52	63±13
S15	26.4760	64.9732	256	29	49±1
S16	26.6066	65.1664	358	30	45±6
S17	26.6997	65.2657	350	56	69±8
S18	26.6683	65.2322	190	40	67±3
S19	26.6867	65.2521	140	26	56±1
S20	26.6749	65.2402	135	16	45±1
S21	26.6713	65.2360	125	22	61±1
S22	26.6584	65.2217	240	35	68±8
S23	26.8690	65.3813	364	22	66±4
S24	26.7208	65.2868	561	55	54±12
S25	26.7503	65.3115	626	24	61±6
S26	27.0015	65.4419	339	18	66±1
S27	27.1047	65.4908	385	28	69±8

were included within the polygon each time. We then repeated the calculation varying L from 25 m in steps of 25 m and varying W from 0.5 m to 5 m in steps of 0.5 m, placing our polygon in 100 random locations for each polygon size. If our polygon was more than 25 m longer than the distance between the two most extreme points included within that polygon, then that estimate was discarded; these estimates are already likely to be included in previous calculations with smaller L. The estimates of dip vary significantly from 10° to 90° for segments shorter than 100 m (these short segments also have a low topographic variation of <10 m). As the length and topographic variation increase, the estimate becomes increasingly consistent. We used the standard deviation of all the estimates from the subsampling segments as the error bounds (i.e. bootstrapping in regression problems (*Efron*, 1979)).

Dip estimates along the Hoshab fault are shown in Table B.1 and Figure B.2.


S12
mean=63°
std=3°
Dip estimate (°)
Segment length (m)
Topographic variation (m)
S13
mean=62°
std=8°
S14
mean=63°
std=13°
S15
mean=49°
std=1°


S16
mean=45°
std=6°
S17
mean=69°
std=8°
S18
mean=67°
std=3°
S19
mean=56°
std=1°
Dip estimate (°)
Segment length (m)
Topographic variation (m)


S20
mean=45°
std=1°
S21
mean=61°
std=1°
S22
mean=68°
std=8°
S23
mean=66°
std=4°
Dip estimate (°)
Segment length (m)
Topographic variation (m)

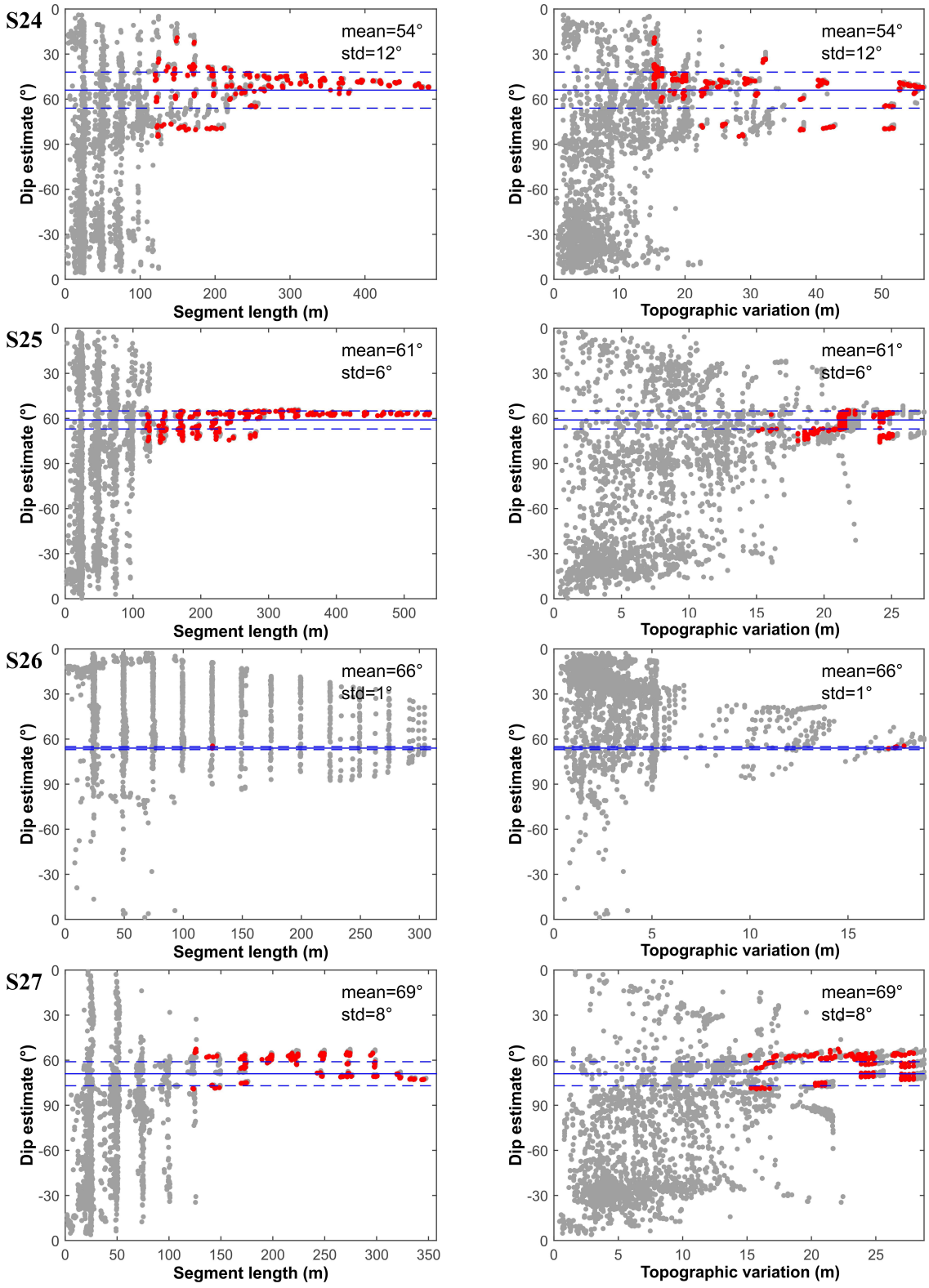


Figure B.2: Estimates of fault dip by subsampling all the segments in Table B.1. Red dots indicate the estimates from the elevation points (the topographic variation of these points is ≥15 m, except for S13 where we used 12.5 m as the threshold) extracted with polygons longer than 120 m and narrower than 2 m. Grey dots are the estimates from other segments. The mean estimates are the average of all the red dots. Positive dip indicates north dipping and negative indicates south dipping. Blue solid and dashed lines are the mean and standard deviation of the dip estimates indicated by the red dots.

Appendix C

Additional Correlation Results for the 1978 Tabas-e-Golshan Earthquake

Figure C.1 shows the displacement maps from cross-correlating the KH-9 and SPOT-6 images. In this study, we focused on the Tabas fold as the thrust motion is almost purely E-W (Figure C.1a). The N-S displacement field was heavily contaminated by scan artifact and optical distortions in the KH-9 image.

Figure C.2 shows the displacement maps using different parameters in COSI-Corr, including initial and final window size, robustness and step in the frequency correlator (*Leprince et al.*, 2007), and window size and step in the statistical correlator (based on the intensity of pixels). The definition of these parameters can be found in *Ayoub et al.* (2009). They all show a similar dislocation (∼3 m) at the deformation front.

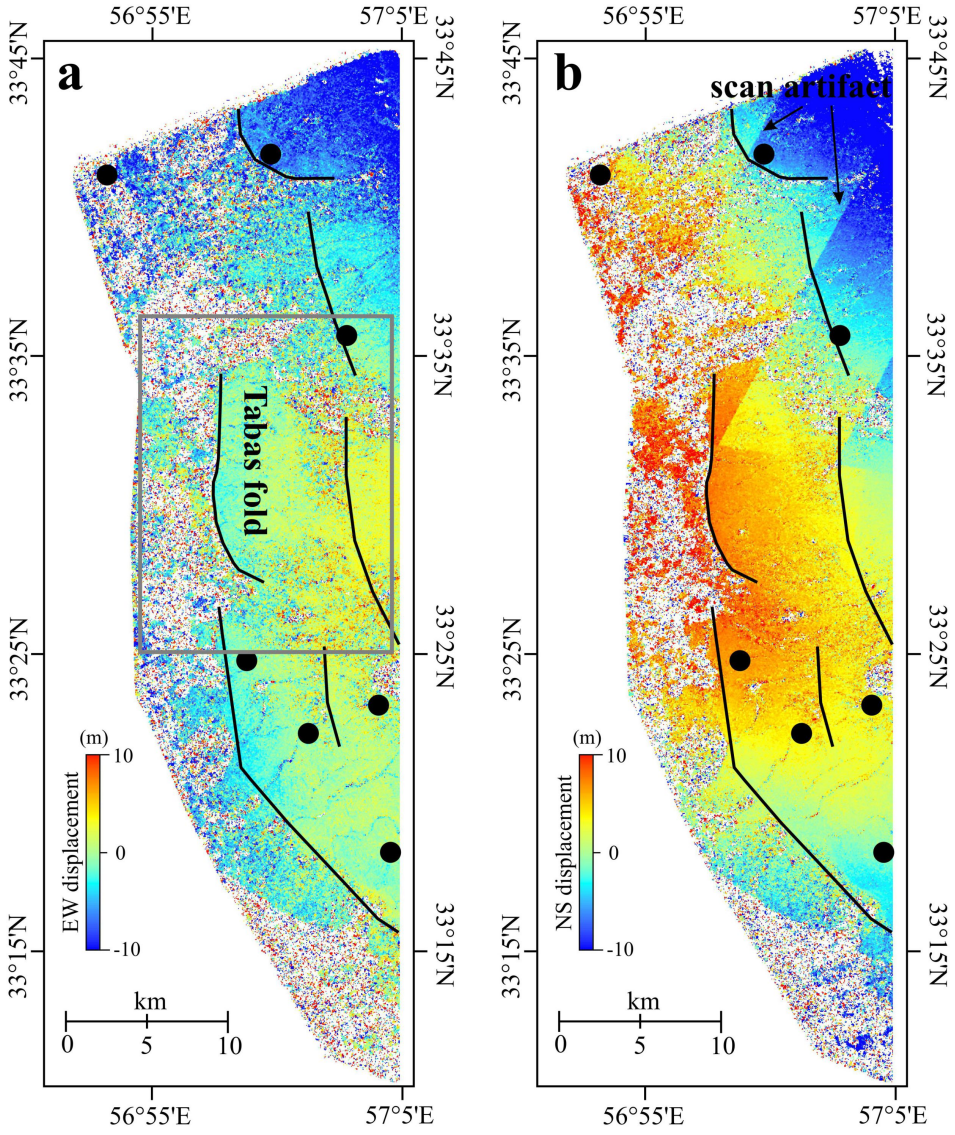


Figure C.1: Displacement fields from cross-correlating the pre-earthquake KH-9 and post-earthquake SPOT-6 images. (a) E-W displacement field. (b) N-S displacement field. Black dots indicate the tie points used to co-register the KH-9 image to the SPOT-6 image. Black lines denote active faults in the region.

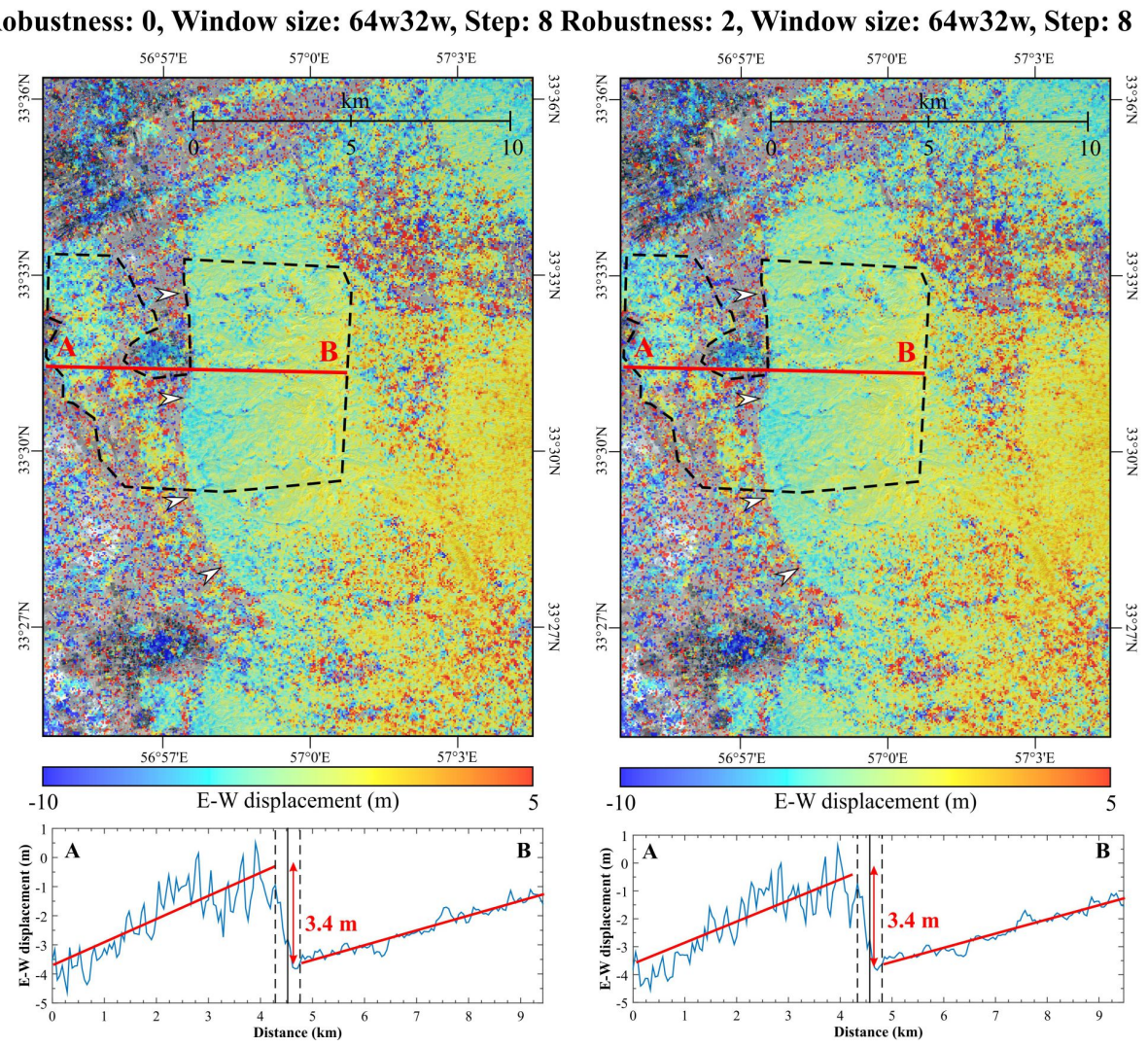


Figure C.2: Cross-correlation results using different parameters in COSI-Corr. The results from the frequency correlator are more reliable than those from the statistical correlator, but they all show a similar EW displacement (∼3 m). "Robustness" is the number of times per measurement the frequency mask should be adaptively re-computed, which contributes to reducing the noise level. "Window size": 64w32w means the initial matching was done with a window size of 64 pixels × 64 pixels, and decreased to 32 pixels × 32 pixels for the final matching. "Step" means step between two sliding windows.

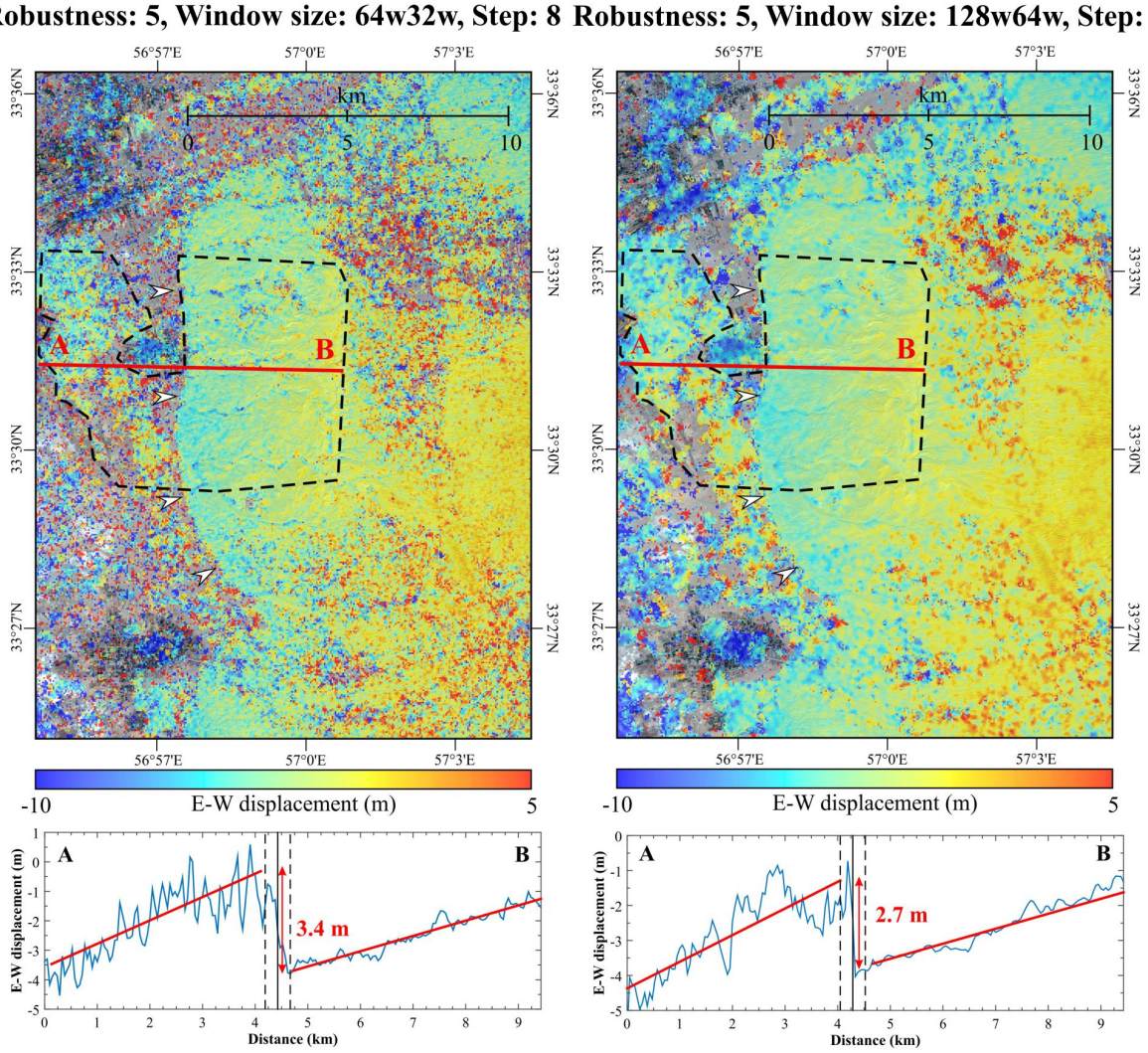


Figure C.2 (Continued).

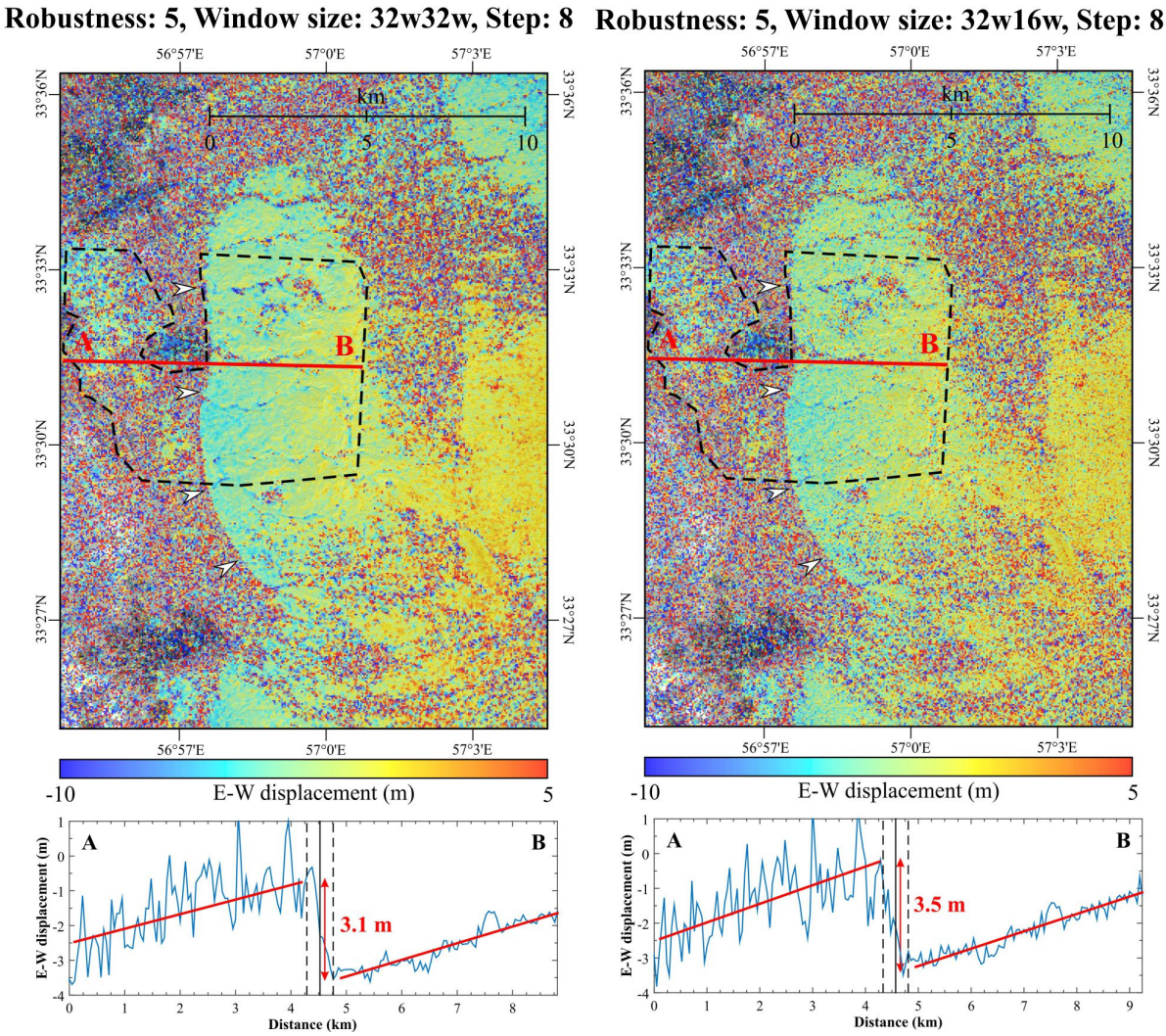


Figure C.2 (Continued).

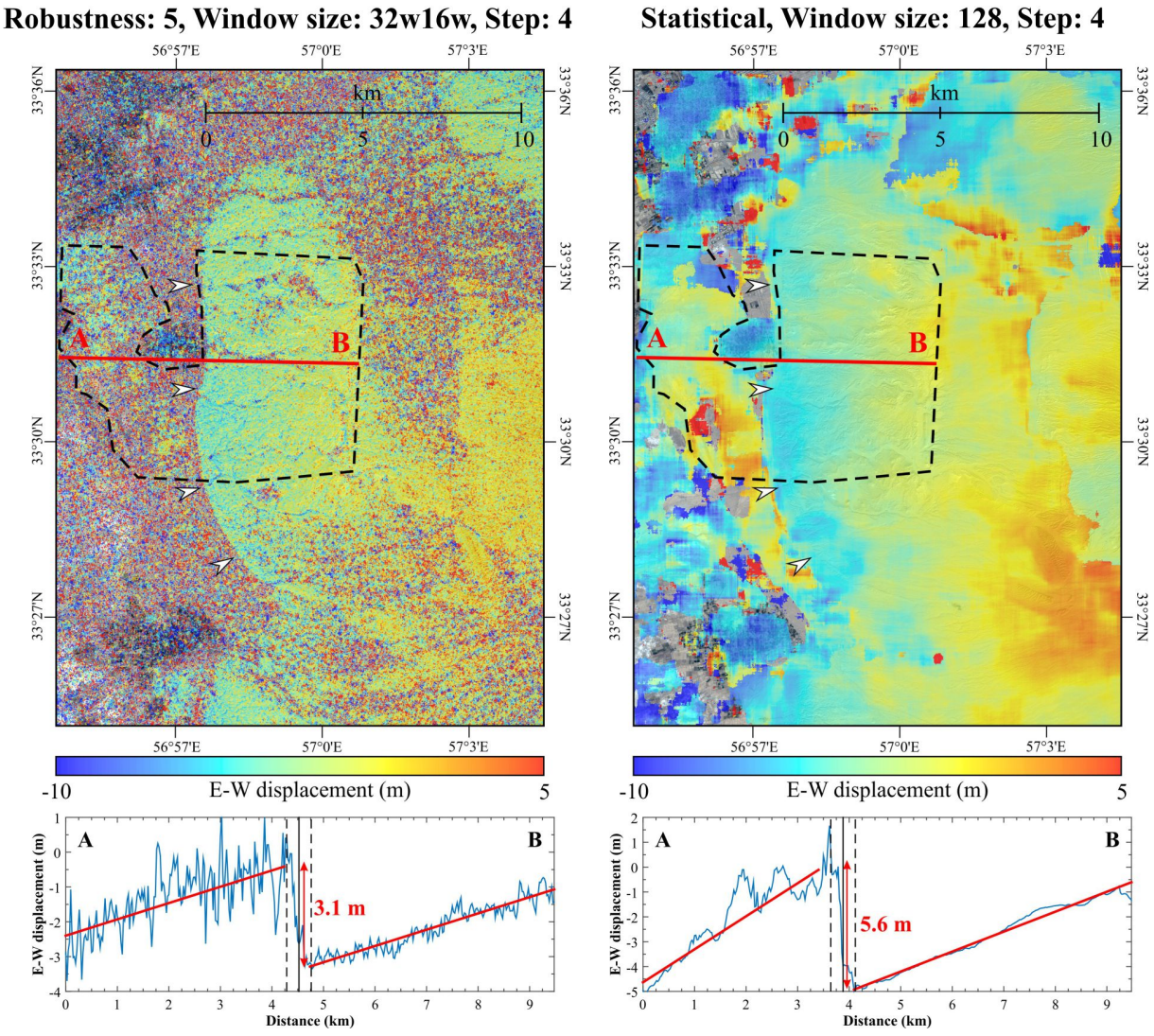


Figure C.2 (Continued).

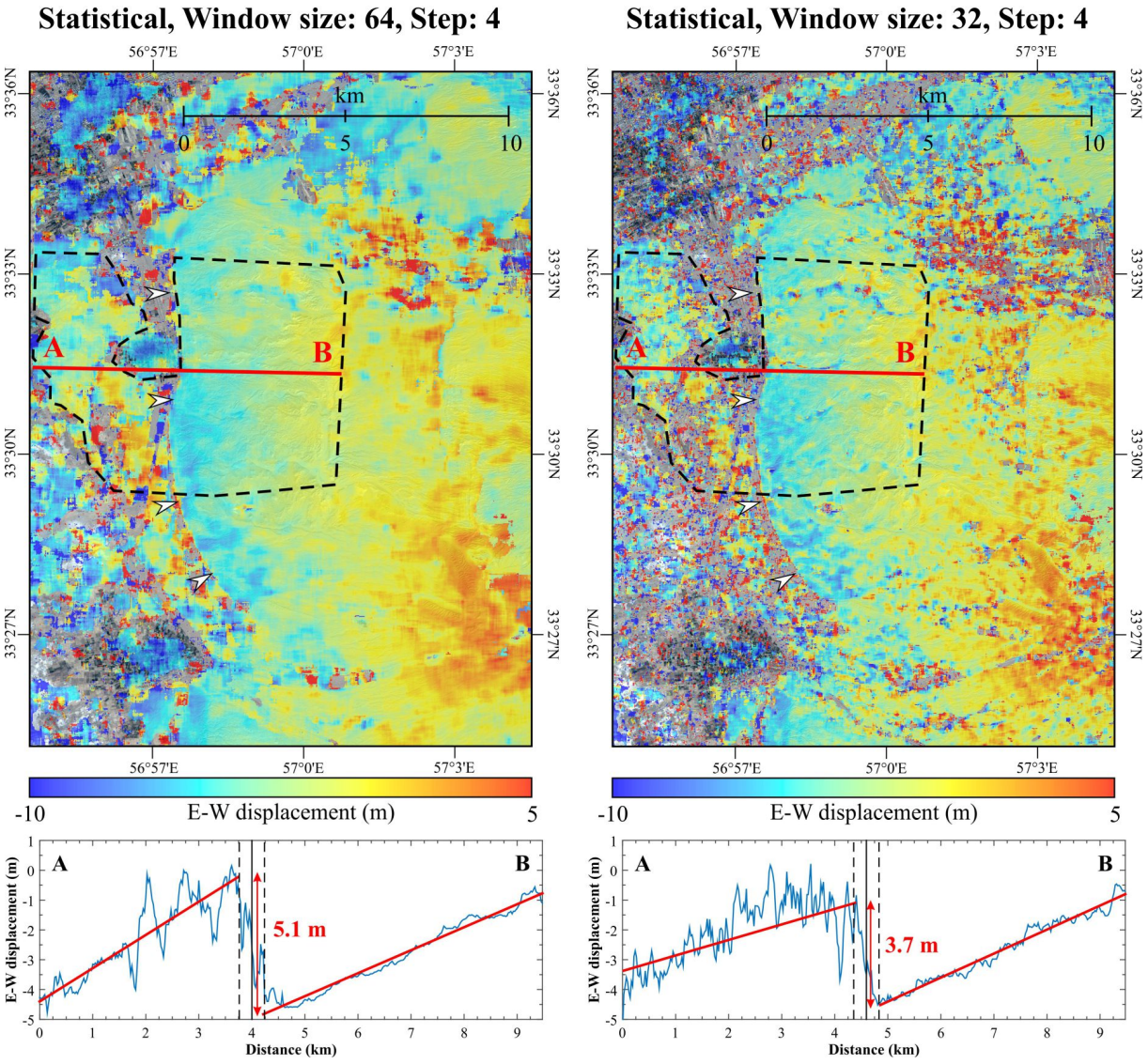


Figure C.2 (Continued).

Appendix D

Orthorectification-induced Horizontal Displacement

In Chapter 5, because we used the post-earthquake DEM for orthorectifying the pre-earthquake KH-9 imagery, any vertical displacement will result in an apparent horizontal signal. As shown in Figure S3, the vertical displacement at location **A** is $\mathbf{\Delta h}$. If an appropriate pre-earthquake DEM is available, object at **A** should be **a** in the orthoimage. However, since we used a post-earthquake DEM, $\mathbf{A}'$, rather than **A**, was treated as the object and the corresponding image point $\mathbf{a}'$ was obtained after orthorectification. The apparent displacement is $\mathbf{a}'\mathbf{a}$. In the following section, we derive the relationship between $\mathbf{a}'\mathbf{a}$ and $\mathbf{\Delta h}$.

In triangle **MOP**, we have:

$$\tan(\theta + i) = \frac{\mathbf{MP}}{\mathbf{H}} \tag{D.1}$$

where i is the rotation of the film (equivalent to the incidence angle), **H** is the flight height and

$$\tan\theta = \frac{\mathbf{a}'\mathbf{c}}{f} \tag{D.2}$$

Here **c** is the centre of the KH-9 image and f is the focal length.

Then we can calculate **MA** by

$$\mathbf{MA} = \mathbf{MP} \cdot \frac{\mathbf{\Delta h}}{\mathbf{H}} = \mathbf{\Delta h} \tan(\theta + i) \tag{D.3}$$

Hence

$$\begin{aligned}\alpha &= \tan^{-1}\frac{\mathbf{H}}{\mathbf{AP}} \\ &= \tan^{-1}\frac{\mathbf{H}}{\mathbf{MP}-\mathbf{MA}} \\ &= \tan^{-1}\frac{\mathbf{H}}{(\mathbf{H}-\mathbf{\Delta h})\tan(\theta+i)}\end{aligned} \tag{D.4}$$

Note that $\beta = \alpha - (90° - (\theta + i))$ and $\gamma = \theta - \beta$.

We can get

$$\mathbf{ca} = f \cdot \tan\gamma \tag{D.5}$$

The apparent displacement $\mathbf{a'a}$ can be determined by:

$$\begin{aligned}\mathbf{a'a} &= \mathbf{a'c} - \mathbf{ca} \\ &= \mathbf{a'c} - f\cot(\tan^{-1}\frac{\mathbf{H}}{(\mathbf{H}-\mathbf{\Delta h})\tan(\tan^{-1}\frac{\mathbf{a'c}}{f}+i)})\end{aligned} \tag{D.6}$$

Given the modelled earthquake slip of 7 m in Section 5.5.1 in Chapter 5, the vertical slip at the fault would be ∼5 m (a maximum of ∼4 m uplift on the hanging wall and ∼1 m subsidence on the footwall). The flight height of the KH-9 image is ∼160 km (with a rotation angle of <0.5°) and the distance from the Tabas fold to the image centre is ∼13 km (each image footprint measures 125 km × 250 km). Combining these figures (i.e. i =0.5°, $\mathbf{H}$ =160 km, f=30.5 cm, $\mathbf{a'c}$=2.76 cm), the orthorectification-induced horizontal displacement is estimated to be ∼0.4 m (maximum) on the hanging wall and ∼0.1 m (maximum) on the footwall, which would not have a significant influence on the tectonic signal (∼3.5 m).

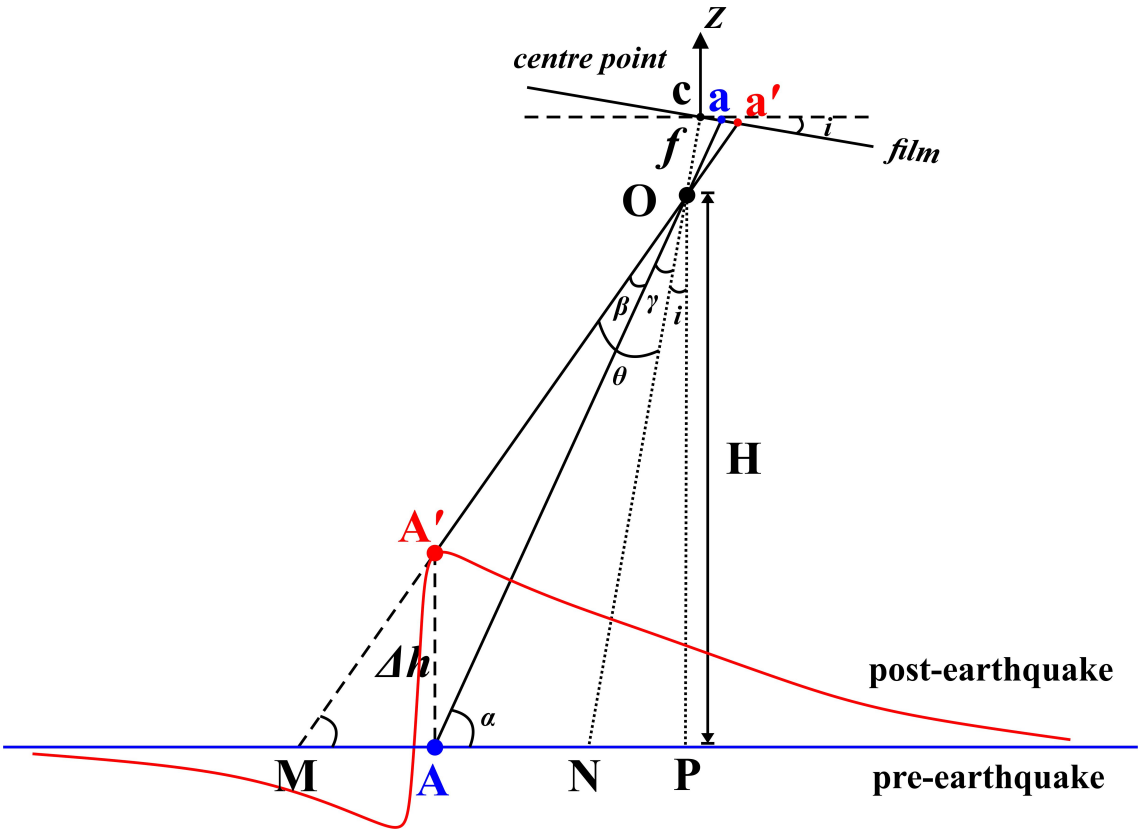


Figure D.1: Apparent horizontal displacement due to vertical motion. If a post-earthquake DEM is used to orthorectify the pre-earthquake image, the vertical displacement $\mathbf{\Delta h}$ at location **A** would yield an error in the orthoimage, resulting in an apparent horizontal signal $\mathbf{a'a}$, which can be determined from the flight height **H** and the distance $\mathbf{a'c}$ (see Equation D.6).

Appendix E

Radiocarbon Samples from the Chishui Site

In Chapter 6, we collected 15 radiocarbon samples in order to investigate the timing of the earthquakes on the Weinan tableland fault. 4 samples (RC1–4) were from the river terraces and dated at the Oxford Radiocarbon Accelerator Unit (ORAU) at the Research Laboratory for Archaeology and the History of Art (RLAHA). The other 11 samples (C1–11) were from the quarry exposure and dated by Beta Analytic Inc. Ages were then calibrated using the OxCal program (*Ramsey and Lee*, 2013) applying the atmospheric curve of *Reimer et al.* (2013). All the radiocarbon ages are summarised in Table E.1. Readers are referred to *Ramsey et al.* (2004) and *Brock et al.* (2010) for details of the dating methods.

Table E.1: Radiocarbon material, ages, and calibration for samples collected at the Chishui site. The raw data were presented in Figures E.1–E.15

Sample	Lab Code	Site	Material	^{14}C Age (BP)	Calibrated Range (95%)	Age (Cal Years BP)
RC1	OxA-28025	T2 surface	Charcoal	5127±31	Cal BC 3988 to 3909 Cal BC 3879 to 3802	5841.5±66.5
RC2	OxA-28026	T2 surface	Charcoal	5056±30	Cal BC 3954 to 3785	5820.5±57.5
RC3	OxA-28027	T1 surface	Charcoal	2240±27	Cal BC 390 to 346 Cal BC 321 to 206	2254.5±63.5
RC4	OxA-28028	T1 surface	Charcoal	2250±26	Cal BC 391 to 349 Cal BC 310 to 209	2260.5±63.5
C1	Beta-376664	Western wall	Organic clay	5980±30	Cal BC 4940 to 4790	6815±75
C2	Beta-396732	Western wall	Organic clay	3480±30	Cal BC 1885 to 1735 Cal BC 1715 to 1695	3655±10
C3	Beta-387332	Western wall	Charcoal	1030±30	Cal AD 975 to 1030	947.5±27.5
C4	Beta-387330	Western wall	Organic clay	7260±30	Cal BC 6215 to 6055	8085±80
C5	Beta-396731	Western wall	Organic clay	2680±30	Cal BC 895 to 800	2797.5±47.5
C6	Beta-399728	Western wall	Organic sediment	7320±30	Cal BC 6235 to 6085	8110±75
C7	Beta-392747	Eastern wall	Charred material	880±30	Cal AD 1045 to 1095 Cal AD 1120 to 1220	780±50
C8	Beta-381225	Eastern wall	Charcoal	2920±30	Cal BC 1215 to 1015	3085±80
C9	Beta-396733	Eastern wall	Organic clay	2430±30	Cal BC 750 to 685 Cal BC 665 to 640 Cal BC 590 to 405	2447.5±92.5
C10	Beta-387331	Eastern wall	Organic clay	9650±30	Cal BC 9230 to 9120 Cal BC 9000 to 8920	10910±40
C11	Beta-381224	Eastern wall	Charcoal	5860±30	Cal BC 4790 to 4685	6687.5±52.5

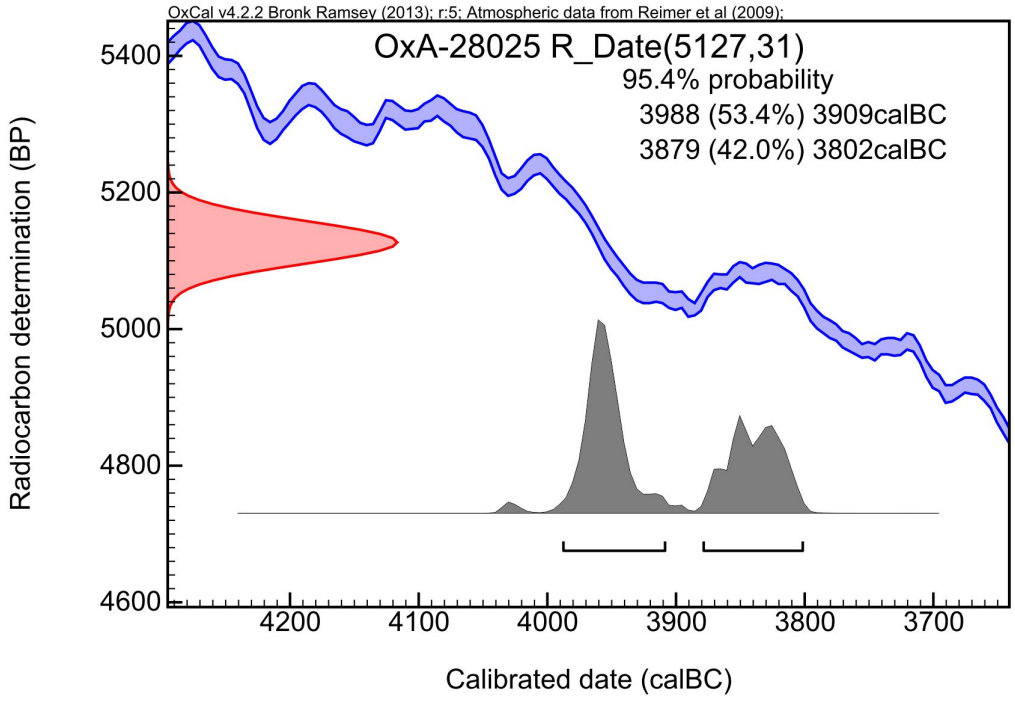


Figure E.1: Calibrated age ranges (95%) for sample RC1.

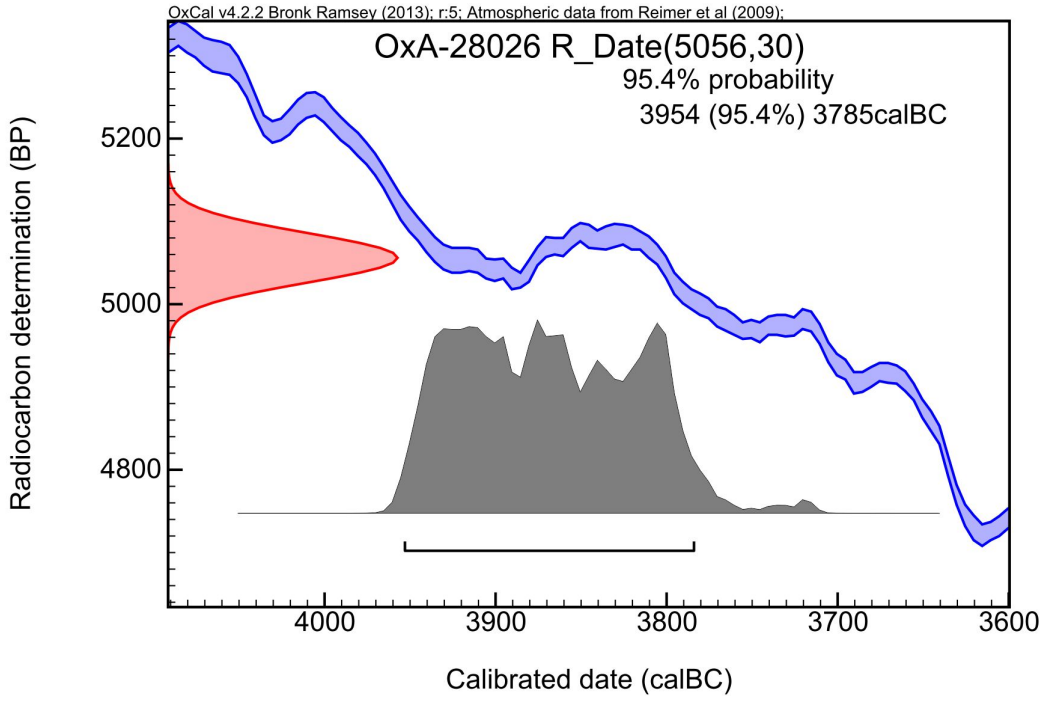


Figure E.2: Calibrated age ranges (95%) for sample RC2.

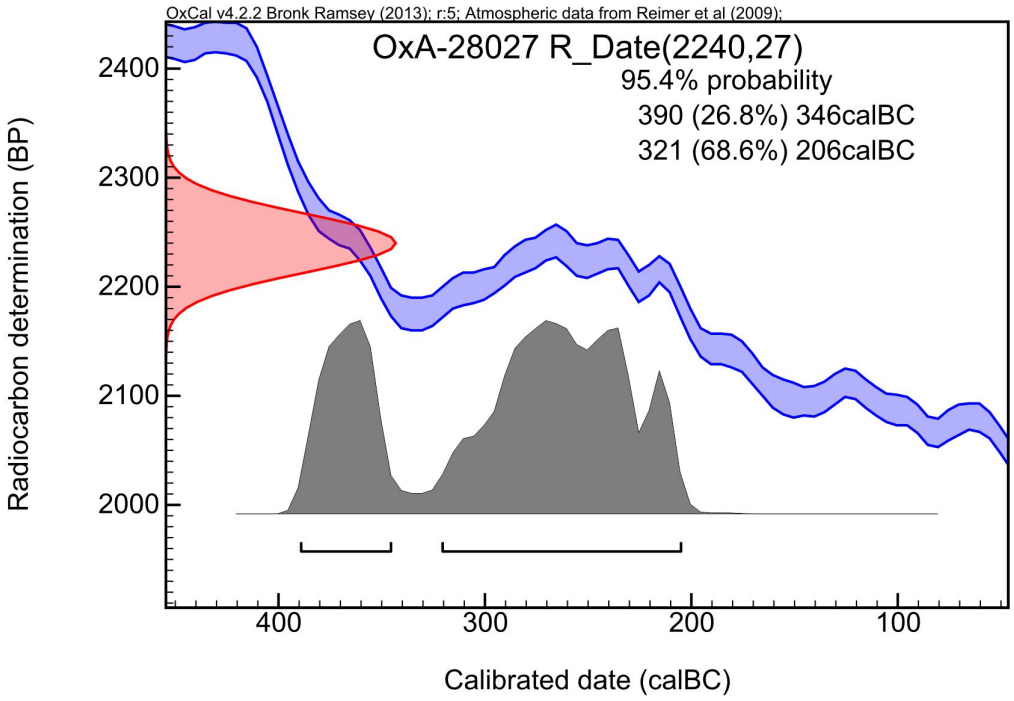


Figure E.3: Calibrated age ranges (95%) for sample RC3.

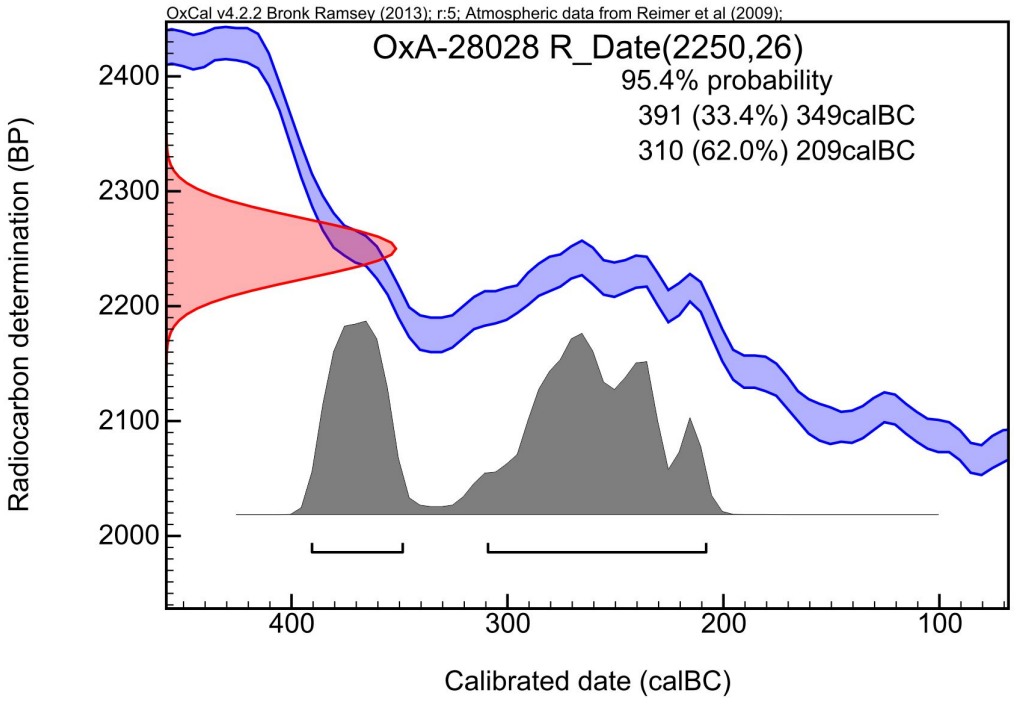


Figure E.4: Calibrated age ranges (95%) for sample RC4.

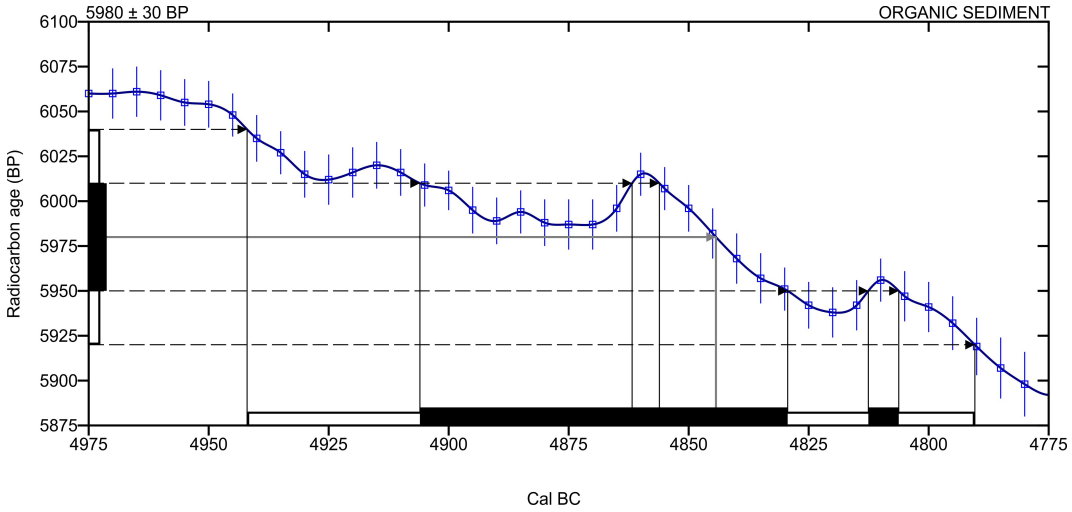


Figure E.5: Calibrated age ranges (95%) for sample C1.

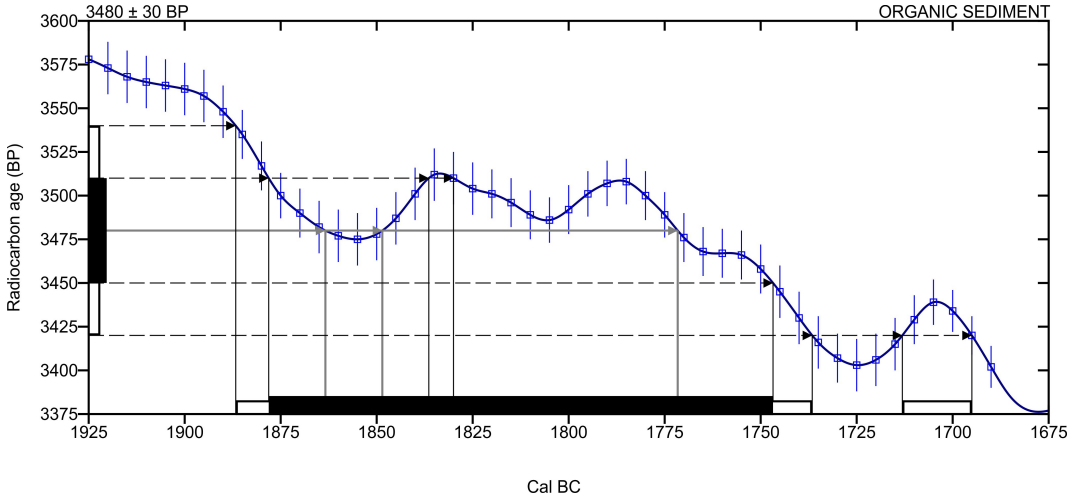


Figure E.6: Calibrated age ranges (95%) for sample C2.

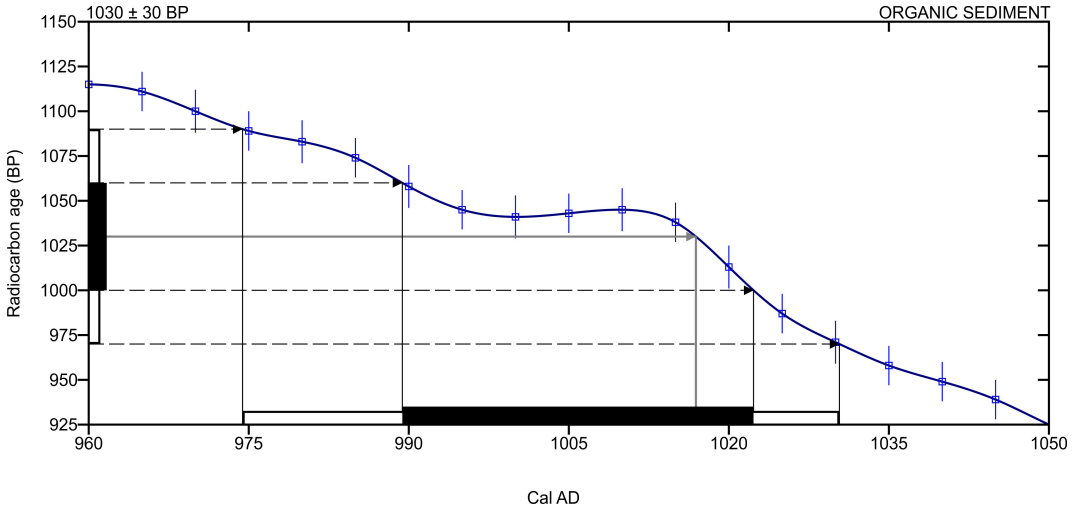


Figure E.7: Calibrated age ranges (95%) for sample C3.

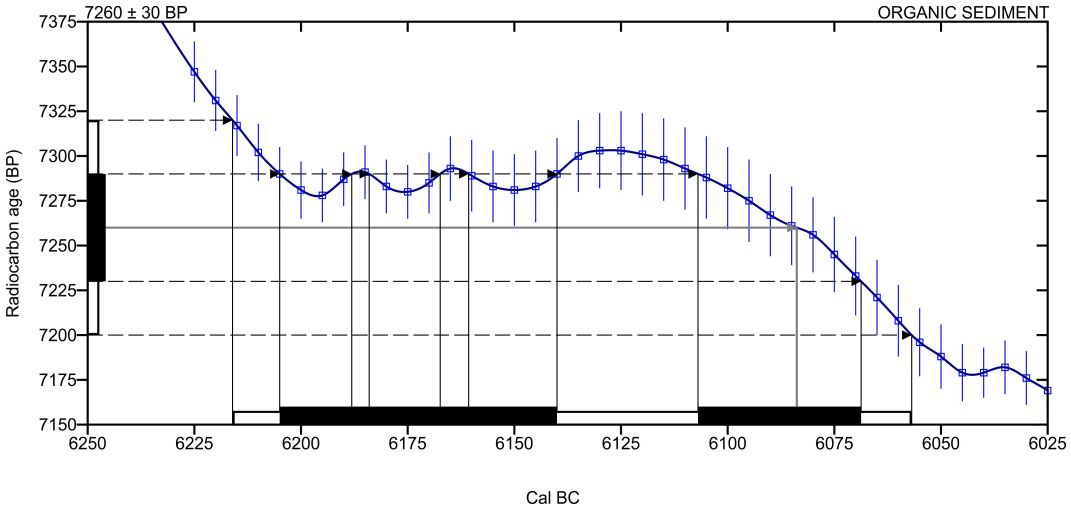


Figure E.8: Calibrated age ranges (95%) for sample C4.

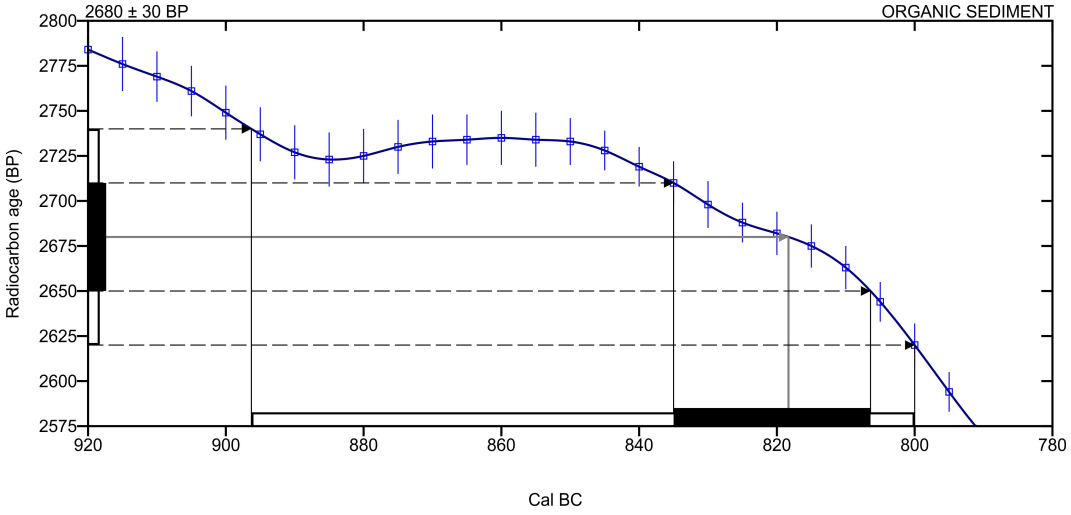


Figure E.9: Calibrated age ranges (95%) for sample C5.

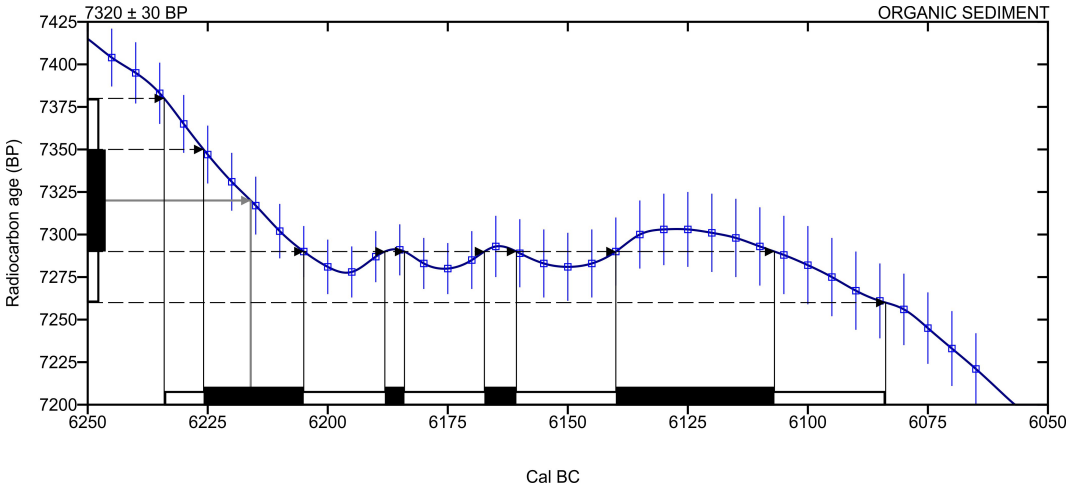


Figure E.10: Calibrated age ranges (95%) for sample C6.

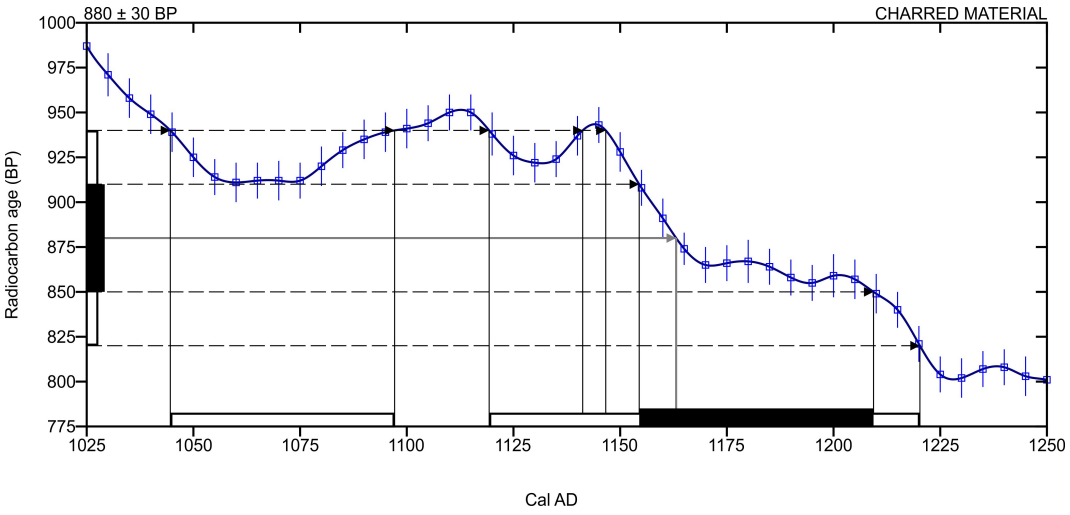


Figure E.11: Calibrated age ranges (95%) for sample C7.

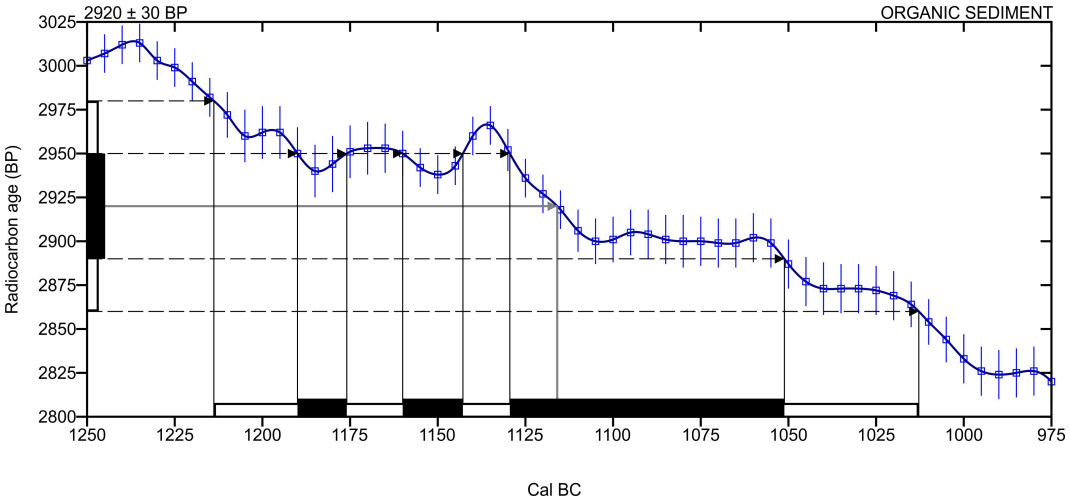


Figure E.12: Calibrated age ranges (95%) for sample C8.

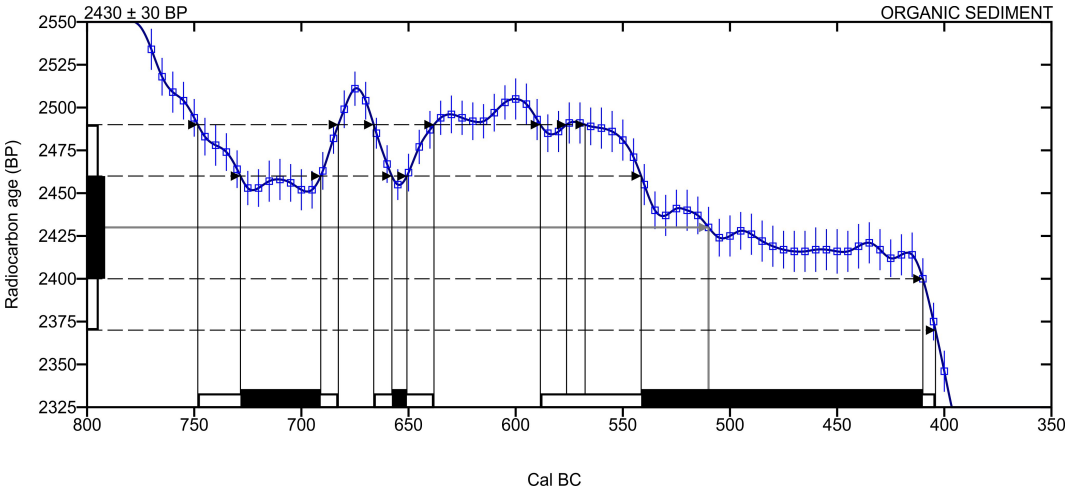


Figure E.13: Calibrated age ranges (95%) for sample C9.

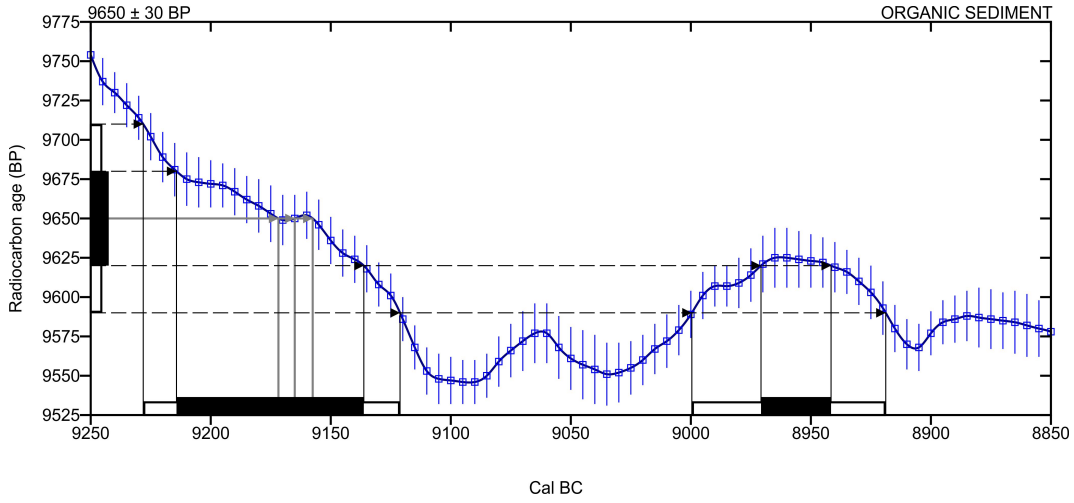


Figure E.14: Calibrated age ranges (95%) for sample C10.

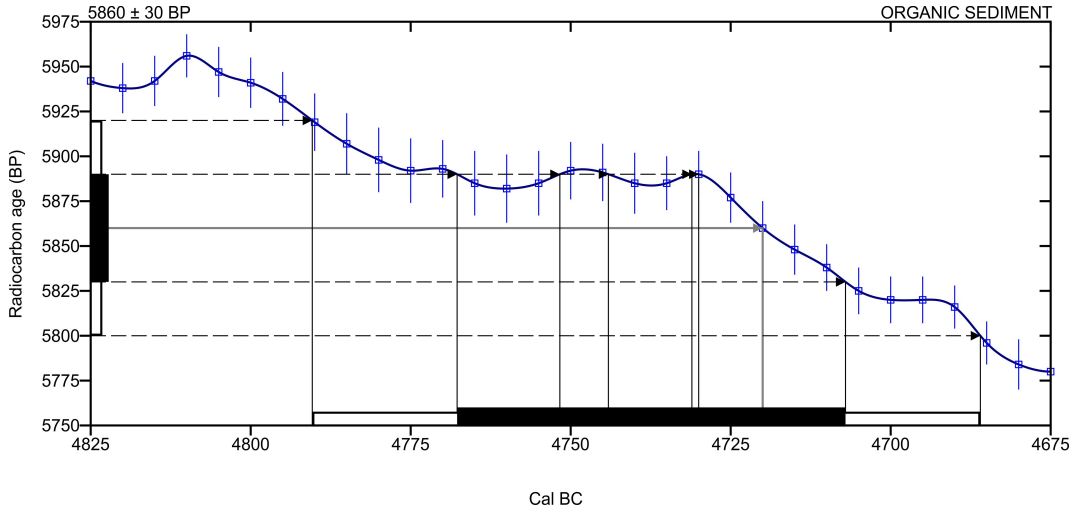


Figure E.15: Calibrated age ranges (95%) for sample C11.